Titre: Title:	Resting State Hemodynamics in Cardiovascular Disease
Auteur: Author:	Maria Elisabeth Bakker
Date:	2025
Type:	Mémoire ou thèse / Dissertation or Thesis
Référence: Citation:	Bakker, M. E. (2025). Resting State Hemodynamics in Cardiovascular Disease [Ph.D. thesis, Polytechnique Montréal]. PolyPublie. https://publications.polymtl.ca/68602/

URL de PolyPublie: PolyPublie URL:	https://publications.polymtl.ca/68602/
Directeurs de recherche: Advisors:	Frédéric Lesage, & Matthieu Vanni
Programme: Program:	Génie biomédical

POLYTECHNIQUE MONTRÉAL

affiliée à l'Université de Montréal

Resting state hemodynamics in cardiovascular disease

MARIA ELISABETH BAKKER

Institut de génie biomédical

Thèse présentée en vue de l'obtention du diplôme de *Philosophiæ Doctor*

Génie biomédical

Août 2025

POLYTECHNIQUE MONTRÉAL

affiliée à l'Université de Montréal

Cette thèse intitulée :

Resting state hemodynamics in cardiovascular disease

présentée par **Maria Elisabeth BAKKER**

en vue de l'obtention du diplôme de *Philosophiæ Doctor*

a été dûment acceptée par le jury d'examen constitué de :

Ravi RUNGTA, président
Frédéric LESAGE, membre et directeur de recherche
Matthieu VANNI, membre et codirecteur de recherche
Jean PROVOST, membre
Sebastien FOULQUIER, membre externe

ACKNOWLEDGEMENTS

First of all, I’d like to thank my two supervisors, Matthieu Vanni and Frédéric Lesage. Although I started this adventure blindly, I could not have been more lucky than to have you as supervisors.

Thank you to my parents, René and Annemiek Bakker, for the endless support and trust, and the safe, calm home where I can always recharge. Thank you Pim Bakker, for the fishbowl-calls and being my brother.

Thank you to all the lab members; Patrick Delafontaine-Martel for the support during experiments and the lessons in Quebec language and music; Enzo for giving me much more confidence after winning the marathon, and also for all the good (silent) coffees we had together; Frans Irgolitsch for the support during difficult times and the great food at home. Thank you Samuel Bélanger, for always being there for me and helping me with everything that I needed, and Joël Lefebvre for the discussions about all our creative projects.

Thank you Simon Sabatino for all the French classes and bike rides that were very necessary for my sanity. Thank you Rosanne Pronk, because I can talk to you and you always understand. Our bike holidays and pie/cake moments have been indispensable. Thank you Evelien Kalisvaart for the Eefcasts, Laila van Emden-Andres for your energy, Marieke Wemmers for the walk and talk sessions, Marike Breed for understanding my weird sides and Femke Roig Kuhn for the unending stream of good books. Thank you Wael Al Enezi and Adel Ahmadihosseini for the gaming sessions and letting me infiltrate in the McGill social life.

RÉSUMÉ

L’activité des différentes régions du cerveau sont connectées d’une manière spécifique, appelée le réseau au repos (resting state network – RSN). Ce RSN est perturbé dans nombre de conditions, et l’interprétation usuelle est celle d’une dysfonction neuronale. Toutefois, il est difficile de mesurer l’activation neuronale directement et ce sont des mesures hémodynamiques qui sont souvent utilisées comme proxy, facilitées par le couplage neurovasculaire (neurovascular coupling - NVC), qui suppose que l’activité neuronale cause une augmentation de flux sanguin. Il n’est pas encore clair si ce couplage reste intact quand l’activité cardiovasculaire est perturbée. Afin d’étudier cette question, cette thèse combine des techniques pour mesurer l’activité neuronale et hémodynamique simultanément. J’y présente deux articles et une recherche en cours qui montrent que la relation entre l’activité neuronale et les fluctuations hémodynamiques n’est pas toujours simple.

Dans le premier article, l’imagerie optique intrinsèque (IOI) et l’imagerie calcique (GCaMP) ont été combinées pour déterminer l’effet de l’hypoxie globale sur les fluctuations hémodynamiques et l’activité neuronale au repos. Nous avons observé que sur une période de 10 minutes, le niveau de la saturation en oxygène dans le cerveau retourne au niveau normal. Néanmoins, le RSN neuronal était modifié de manière significative. Dans le deuxième article, on a posé l’hypothèse qu’une artère plus rigide est associée à un dommage du système vasculaire et une réduction de NVC, avec une déconnexion entre les RSN neuronaux et hémodynamiques comme conséquence. Cependant, on n’a pas trouvé une différence significative, ainsi les mesures hémodynamiques représentent l’activation neuronale avec justesse, même avec une artère plus rigide. Par contre, on a trouvé une différence petite mais significative de NVC entre les régions du cerveau. Finalement, on a utilisé l’imagerie ultrarapide à deux photons pour étudier l’effet de l’hypertrophie du ventricule gauche sur la pulsatilité du système vasculaire cérébral. Les résultats préliminaires indiquent que la pulsatilité artérielle pourrait être légèrement plus élevée, alors que cela ne semble pas être le cas dans les capillaires.

En somme, mes investigations ont montré que la validité d’utilisation des mesures hémodynamiques comme approximation de l’activité neuronale dépend de la situation. Il faut être prudent avant de tirer des conclusions sur la base des hémodynamiques concernant l’activité neuronale, puisque le NVC n’est pas un mécanisme qui reste le même dans chaque situation ou région du cerveau.

ABSTRACT

The activity of the brain at rest forms a specific set of connections, called the resting state network (RSN), which is disturbed in a number of diseases and conditions. Since it is difficult to directly measure neuronal activation, hemodynamic activity is often used as a proxy. This is possible because neuronal activity provokes a local increase in blood flow, called neurovascular coupling (NVC). Whether NVC stays intact upon conditions that alter cardiovascular activity is insufficiently studied. Exploiting tools that can monitor both neural activity and blood flow changes, this thesis aimed to investigate this question. In the following, I present two articles and a work in progress that show that the connection between neuronal activation and hemodynamics is not always straightforward.

In the first article, we combined intrinsic optical imaging with calcium imaging (GCaMP) to study the effects of global hypoxia on hemodynamics and neuronal activity during rest. We found that within a 10 minute hypoxia period, although the oxygen saturation levels in the brain came back to baseline, the neuronal RSN was significantly altered. In the second article, we investigated the impact of stiffer arteries on RSN. We hypothesized that artery rigidification would be associated with damaged vasculature and an altered NVC, resulting in a disconnect between the neuronal and hemodynamic RSN. However, the results showed no significant differences, and the hemodynamic measurements accurately represented the underlying neuronal activation, even with a stiffer carotid artery. Interestingly, we did find small but significant differences in NVC dynamics between brain areas. Lastly, we used ultrafast 2-photon imaging to investigate the effect of left-ventricle hypertrophy on pulsatility in cerebral vasculature. Primary results indicate that the pulsatility in arteries might be slightly higher, whereas this does not seem to be the case in capillaries.

In conclusion, my investigations show that the validity of using hemodynamics as a proxy for neuronal activity depends on the circumstances. Care should be taken in drawing conclusions on hemodynamics alone, since NVC is not a “one size fits all” mechanism that is guaranteed to remain uniform over brain areas and conditions.

TABLE OF CONTENTS

LIST OF TABLES

LIST OF FIGURES

LIST OF SYMBOLS AND ABBREVIATIONS

(f)MRI	(Functional) Magnetic Resonance Imaging
(f)NIRS	(Functional) Near-Infrared Spectroscopy
(f)US	(Functional) Ultrasound
1P	One-photon
2P	Two-photon
AD	Alzheimer's Disease
BBB	Blood Brain Barrier
BOLD	Blood Oxygenation Level Dependent
CA	Cerebral Autoregulation
CAA	Cerebral Amyloid Angiopathy
CBF	Cerebral Blood Flow
CPP	Cerebral Perfusion Pressure
CSF	Cerebrospinal Fluid
CVD	Cardiovascular Disease
CVR	Cerebrovascular Resistance
DMN	Default Mode Network
EEG	Electroencephalography
ERKO	Estrogen Receptor Knockout
FACED	Free-space Angular-Chirp-Enhanced Delay
FITC	Fluorescein Isothiocyanate
FDR	False Discovery Rate (Correction)
GECI	Genetically Encoded Calcium Indicator
GEVI	Genetically Encoded Voltage Indicator

GFP	Green Fluorescent Protein
GSR	Global Signal Regression
HbO	Oxyhemoglobin
HbR	De-oxyhemoglobin
HbT	Total hemoglobin
ICP	Intracranial Pressure
IOI	Intrinsic Optical Imaging
LED	Light Emitting Diode
LVH	Left Ventricle Hypertrophy
MAP	Mean Arterial Pressure
MCI	Mild Cognitive Impairment
MEG	Magnetoencephalography
ML	Motor area, Left
MR	Motor area, Right
MWU	Mann Whitney U
NVC	Neurovascular Coupling
NVU	Neurovascular Unit
PAI	Photoacoustic Imaging
PET	Positron Emission Tomography
PMT	Photomultiplier Tube
PP	Pulse Pressure
PWV	Pulse Wave Velocity
RBC	Red Blood Cell
RL	Retrosplenial area, Left

ROI	Region Of Interest
ROS	Reactive Oxygen Species
RR	Retrosplenial area, Right
RS	Resting State
RSN	Resting State Network
SEM	Standard Error of the Mean
SL	Sensory area, Left
SMC	Smooth Muscle Cell
sO2	Oxygen saturation
SPECT	Single Photon-Emission Computed Tomography
SR	Sensory area, Right
TAC	Transverse Aortic Constriction
VL	Visual area, Left
VR	Visual area, Right

LIST OF APPENDICES

CHAPTER 1 INTRODUCTION

Although the cardiovascular system is imperative for the function of every single body part, a special focus is placed on the brain, especially in situations where oxygen is scarce. Not surprising, since loss of consciousness due to lack of oxygen can occur within a minute, and thus a continuous blood flow to the brain is crucial for survival. Additionally, with 20% of the total oxygen consumption at rest [2], the brain is the most "hungry" organ of the human body, and thus requires a solid system to fulfill its metabolic demands.

To maintain function, cerebral blood flow is subject to specific regulation. This so-called cerebral autoregulation facilitates a constant blood flow in the brain, even when cerebral perfusion pressure (CPP) changes (usually as a result of changes in blood pressure [3]). The constant cerebral blood flow (CBF) is maintained by altering the cerebrovascular resistance (CVR), which can also be written as:

$$CBF = \frac{CPP}{CVR} \tag{1.1}$$

The resistance is actively regulated by constricting or dilating arterial blood vessels. When the blood pressure increases, so does the transmural pressure of the vessels, which triggers vasoconstriction and increased myogenic tone. The smooth muscle cells (SMC) in the vessel wall contract, and the cerebrovascular resistance increases. Since capillary walls do not contain SMC, this task falls on the arteries and arterioles. The process is reversed with a decrease in blood pressure.

Besides (global) cerebral autoregulation, there are more local mechanisms for distributing blood as well, which are necessary for the sufficient nourishment of neurons. Neuronal activation or "firing" requires a lot of energy and oxygen [4]. Although some of these resources can be stored locally, prolonged activation calls for a direct increase in energy supply, which is facilitated by a local increase in blood flow. In this thesis, I will refer to this as neurovascular coupling (NVC), but throughout the literature it has many names[1], including flow-metabolism coupling [5-8], metabolic

---

[1] How these terms are used and what their exact definition is differs. However, they are all used to indicate a necessary increase of blood flow to facilitate neuronal firing.

hypothesis [3, 9] (both especially used in older literature), and functional hyperemia [10, 11]. Although the idea of NVC seems simple, the mechanisms of it are manifold, and the field is continuously expanding and improving.

Proper regulation of blood flow is also important to protect the smallest vessels. The capillaries in the brain are not elastic and can be damaged if the pressure or the pulsatility on the vessel walls is too high [12]. Damage of the capillaries can severely impair the ability of the vascular system to deliver sufficient nutrients to the neurons. Furthermore, since the brain is particularly susceptible to foreign factors such as bacteria and viruses, the blood vessels in the brain form a blood-brain barrier (BBB) that lets the nutritional components through but hinders any harmful substances to enter the tissue. This differs from the more permeable blood vessel walls in the rest of the body. The functioning of the BBB is dependent on the integrity of the vessel walls, and thus a damaging of capillaries often results in a weakened BBB and a decreased defense towards neuro-inflammation [12-14].

Since both the protection and the nutrition of the brain are dependent on healthy vasculature, it is no surprise that the disruption of it can have widespread consequences. There has been an increasing amount of evidence showing that the hindrance of NVC and blood flow through vascular damage connects cardiovascular diseases and cognitive deficits [15-22]. Even diseases that on face value seem purely neurological can be closely related to cerebral blood flow regulation. The most striking example of this is Alzheimer’s disease (AD). AD patients show a severely disturbed autoregulation and NVC [22-24]. Moreover, there is evidence that AD is heavily exacerbated by a decreased functionality of blood vessels [25, 26], caused by an increase in pulsatility [27, 28]. The reverse is also true, where diseases that seem mostly cardiovascular have a significant impact on the brain and cognitive function. For example, atherosclerosis [29], hypertension [30] and general non-stroke cardiovascular disease [31, 32] have all been linked to a decrease in cognitive functioning. Cerebral small vessel disease, which has been closely associated with pulsatility [33-37], contributes to cognitive impairment as well [34].

Neurological research, NVC studies included, is often done by offering a stimulus and measuring the response of neurons, blood flow, or both. However, studies without stimulus can provide very interesting information as well. The activity of the brain at rest is not random and can inform about connectivity between brain areas in a manner that stimulus-evoked responses might not. Resting state correlations between brain areas form a resting state network (RSN), that tends to be robust over healthy individuals [38]. Originally, RSN were discovered with the help of functional magnetic resonance imaging (fMRI) in human subjects [39]. fMRI does not directly measure neuronal activation, but instead is sensitive to the increase of hemoglobin that accompanies neuronal activation, and thus effectively uses NVC to draw conclusions on brain function. The original study therefore indicated a hemodynamic RSN, but this doesn’t definitively tell us about a neuronal RSN [40]. Later studies with other methods such as PET [41], EEG and MEG [42], and GCaMP (in animals) [43] have shown that the neuronal RSN did exist, but studies investigating both neuronal and hemodynamic measurements simultaneously remain relatively rare [41, 44, 45].

Resting state experiments have generated a lot of interest over the years. These studies are especially useful for research into conditions that inconvenience standard research methods. For example, newborns or individuals with severe autism or dementia might not be able to follow the instructions necessary for stimulus-related research. RSN have also been shown to be affected in conditions such as Alzheimer’s [46, 47], cerebral small vessel disease [48] and autism [49]. Furthermore, the alterations in RSN can be used to better quantify the disease, for example to distinguish between mild cognitive impairment and Alzheimer’s [50, 51] or between subtypes of Alzheimer’s [52]. It could also be used as diagnostic tool or even as a prediction factor [53-55].

Objectives

Given the importance of blood flow not only in brain function itself, but also in neuroscientific research, understanding cerebral hemodynamics is crucial. Methods relying on NVC are often used to research RSN, but both these factors can be altered in cardiovascular diseases. To untangle these factors, and clarify the interplay between vascular, metabolic and neural function at rest, the main question will be:

> *How do the effects of cardiovascular diseases influence the resting state hemodynamics in the brain?*

The focus here will be more on consequences of cardiovascular diseases rather than one specific condition. For example, researching global hypoxia, rather than stroke or anemia, and an increased pulse wave pressure rather than a general rigidification of all arteries.

Objective 1: Investigate the effect of global hypoxia on large-scale hemodynamics and neuronal activation (article 1).

A major function of NVC is the delivery of sufficient oxygen. A lack of oxygen over the whole brain can occur in cerebral hypoperfusion, anemia and vascular dementia, or, looking outside the cardiovascular domain, in cases of sleep apnea, asthma, chronic obstructive pulmonary disease, and altitude sickness. A local hypoxia can also take place because of a stroke. By inducing acute hypoxia, we aimed to investigate the effects of insufficient oxygen delivery on the global cerebral blood flow. More specifically, the effects on both the hemodynamic and neuronal RSN, and if they stayed in sync or if an uncoupling took place between the two modalities. By cutting off oxygen abruptly but temporarily, we could investigate both the neuronal and hemodynamic RSN without the long-term effects that cardiovascular diseases often bring. In other words, we could see the effects of a diminished oxygen delivery, without the effects of damaged vessels, increased pulsatility or neuroinflammation. We hypothesized that a neurovascular decoupling would occur, and that a change in hemodynamic RSN does not necessarily bring the same change in neuronal RSN.

Objective 2: Investigate possible differences in neurovascular coupling as a result of a rigidified carotid artery (article 2).

The rigidification of arteries often occurs in cardiovascular diseases, with the most obvious being atherosclerosis. The effects of arteries with reduced flexibility can be severe, damaging capillaries and disturbing cerebral autoregulation and NVC. In the second article, we therefore used a mouse model where we rigidified the carotid artery, increasing the pulse wave velocity entering the brain. We hypothesized that a rigidified carotid artery would disturb neurovascular coupling.

Objective 3: Determine the effects of aortic constriction on the microvasculature in the brain, in terms of increased pulsatility and microbleeds (article 3).

Lastly, we wanted to zoom in on the effects of the increased pulse wave velocity of paper 2. In the model of paper 2, we saw an effect that was quite mild, and so in this research we opted for a more severe mouse model, with a clearer effect on the pulse wave velocity. We hypothesized that cardiac hypertrophy would increase the pulsatility to such an extent that it will be noticeable in the cerebral capillaries. As a consequence of that increased stress, we hypothesized an increase in microbleeding throughout the brain. Since not all data is acquired for this project yet, the article has not been submitted to a journal. However, the in vivo results, as well as some preliminary ex vivo results, will be presented in Chapter 6.

To investigate these subjects, an interplay between biology and engineering was necessary, and thus many different techniques were used. The practical side of these procedures are discussed in the methods sections of the corresponding articles. However, to paint a more complete picture regarding the background, Chapter 3 covers the context of these methods as well.

CHAPTER 2 GENERAL BACKGROUND AND LITERATURE REVIEW

2.1 Cardiovascular system

2.1.1 Arteries

In a healthy cardiovascular system, the heart pumps oxygenated blood at regular intervals through the aorta. The blood flow towards the brain arrives via the common carotid arteries (that split into the internal and external carotid arteries) and the vertebral arteries (Figure 2.1A). The internal carotid arteries and vertebral arteries feed into the Circle of Willis, from which the blood is distributed over several pial arteries (anterior, middle and posterior cerebral arteries) that envelop the brain[2]. Then, plunging arterioles penetrate deeper into the tissue, and branch out into capillaries. All arteries and arterioles contain arterial endothelial cells and arteriolar smooth muscle cells [56].

Since the heart is a rhythmic pump, the blood that is propagated from the left ventricle arrives in pressure pulse waves, and travels through the vascular system as a “ripple” with a certain velocity (pulse wave velocity – PWV). Especially in the brain, the attenuation of PWV is important, since it is encapsulated by bone, and thus effectively a rigid box. Conduit arteries [57] have the ability to stretch, and thus accommodate for this pulse (Windkessel effect). They serve as local, temporary blood reserves by stretching at the influx of blood from the systolic phase of the heartbeat. During the diastolic phase, the conduit arteries can slowly contract back to the diameter that they had at the start of systole, so the blood is pushed into the rest of the system at a more constant velocity throughout the heart cycle. Vessels such as the aorta and carotid arteries play a crucial role in this. Important components of conduit arteries are elastin, collagen, and vascular smooth muscle cells (SMC) (Figure 2.1B). Elastin is very compliant, while collagen is more rigid, and prevents damage through overextension [57, 58]. Further from the heart, there is less elastin compared to collagen, and more SMC per unit volume [57].

Larger arteries are mostly passive in their role, while smaller arteries and arterioles more actively determine the local blood flow (more on this in cerebral autoregulation). Arteries that regulate the

---

[2] The cerebellum and pons have their own blood supply, regulated by superior, anterior inferior and posterior inferior cerebellar arteries and pontine arteries.

resistance within the brain are called resistance arteries. They are between 500-100 um in diameter, and contain several layers of smooth muscle cells (SMC), that enable them to contract and thus increase resistance within the system [59]. They feed into smaller resistance arterioles, that are <100 um and only have a single layer of SMC [59, 60]. Terminal arterioles are the last arteries before going into the capillary bed.

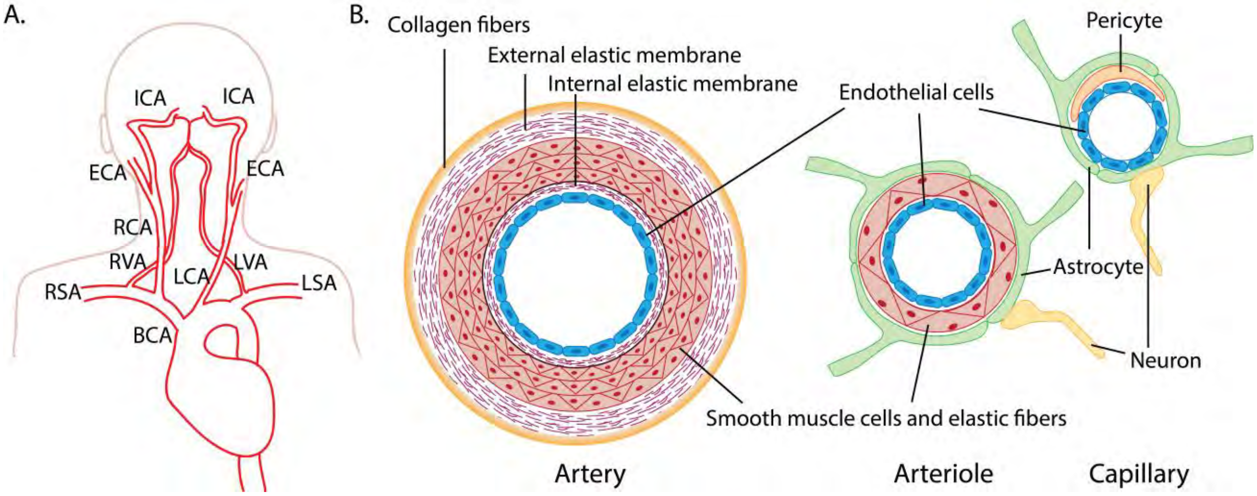

Figure 2.1: Cardiovascular system.

A. Vasculature from the heart leading the blood supply in the brain. ICA: internal carotid artery, ECA: external carotid artery, (R/L)VA: (right/left) vertebral artery, (R/L)CA: (right/left) common carotid artery, (R/L)SA: (right/left) subclavian artery, BCA: brachiocephalic artery. B. Schematic cross sections of an artery, arteriole and capillary.

2.1.2 Capillaries

Starting at the heart, the arteries of the blood circulation system become narrower with each branching off, until the diameter is just several microns wide. Capillaries are the smallest vessels of the circulatory system, measuring less than 10 µm, and generally only have a single file of red blood cells flowing through them, since the average RBC size in humans is roughly 7 µm (6 µm in mice) [61]. The bulk of nutrient exchange from the circulatory system to the tissue happens in these blood vessels.

The trade-off in permeability of the blood vessels in the brain is a delicate balance between letting nutrients in and keeping toxins and diseases out, as regulated by the Blood Brain Barrier (BBB). The BBB is highly dependent on endothelial cells which are present in all blood vessels (but differ in phenotype) [56]. They are connected with tight junction proteins, which enable them to form a firm wall between the blood vessel and the brain tissue [62]. Capillaries do not contain any SMCs in their vessel wall, but instead have pericytes and astrocytic end feet embedded in between their endothelial cell, stabilizing the endothelial cells [60] (Figure 2.1B). The lack of SMC and the simple, single layer of endothelium cells makes the BBB much more penetrable than in the arteries and arterioles, enabling nutrient exchange but also making capillaries relatively vulnerable.

2.1.3 Veins

After the exchange of nutrients in the capillary bed, the blood is drained through venules and veins. The variability of the location of cerebral veins is much higher than that of arteries [62, 63]. From the capillary bed, cerebral veins ascend to the surface, feeding into cortical veins. Many cortical veins are connected to the superior sagittal sinus, and all veinous blood is eventually drained via the jugular veins that travel parallel to the carotid arteries.

Veins have a more passive role than arteries [63]. Although their vessel walls contain SMC, they are of a different phenotype than arteries [56]. They can contract to regulate blood flow and myogenic tone, but have fewer SMC, contract less, and contribute less than arteries in this aspect [60, 63]. They have a large compliance, and they hold a larger volume of blood than arteries to facilitate the return of blood towards the heart.

2.2 Cerebrovascular autoregulation

Cerebrovascular autoregulation (or cerebral autoregulation - CA) refers to the ability to keep the cerebral blood flow (CBF) constant even if the cerebral perfusion pressure (CPP) changes [64]. This negative feedback system is achieved by alteration of the cerebrovascular resistance (CVR) (see equation 1.1), regulated by resistance arteries [65, 66]. However, since CPP is difficult to measure, it is often approximated with the help of the mean arterial pressure (MAP) and intracranial pressure (ICP) [3] such that:

$$CBF = \frac{MAP - ICP}{CVR} \tag{2.1}$$

It works effectively between a lower and upper limit of CPP, which have been estimated at 50 and 150 mm Hg [3, 64, 67] (although recent discoveries indicate a narrowed range [68]). Below the lower limit of CPP, the vessels will collapse and the CVR will rise, resulting in a low CBF [69], while above the upper limit, the pressure will forcefully dilate the vessels, and CBF will rise [3]. However, within the thresholds, the CBF remains relatively constant. Both an excessive CBF (hyperperfusion) and inadequate CBF (hypoperfusion) can be dangerous [67].

The pressure that the blood is exerting on the vessel walls will elicit a myogenic response. An increase in arterial pressure (and thus tangential wall stress) causes the SMC that are present in the vascular wall to stretch and in response contract, leading to vasoconstriction [67, 70]. The myogenic tone refers to the constant contractile activity of the SMC in response to the pressure. Even though the first description of the myogenic response is as old as 1902 [71], the sensing of pressure changes and subsequent response happens via extensive pathways that are not clear yet, and might differ per vessel type or vasculature bed [59], and diameter [66]. However, the myogenic tone is likely dependent on the depolarization of the SMC membrane, activation of voltage gated calcium channels, an influx of intracellular calcium, and phosphorylation of myosin light chain 20 [8, 59, 67, 68, 70]. Endothelial cells likely also play a role, sensing the shear stress and subsequently signalling the SMC [72, 73]. Larger conduit arteries do not show a myogenic response, but rather exhibit the Windkessel effect to regulate blood flow [67].

The distinction between cerebrovascular autoregulation and neurovascular coupling (discussed in the next section) is not always clear. Some researchers include a local increase of blood flow mediated by neurotransmitters and the vasodilatory effect of an increase of CO^2 in cerebrovascular autoregulation [3, 68], while others separate them from autoregulation and group them under neurovascular coupling [8, 60, 65, 67, 74, 75]. Here, the term cerebrovascular autoregulation will solely be used to refer to maintaining a constant CBF despite changes in pressure.

2.3 Neurovascular coupling

2.3.1 Vessels

Although cerebral autoregulation keeps a stable blood flow to the brain, more local variations are necessary as well for delivery of oxygen and glucose. Following local brain activation, blood flow to that area increases to deliver these products, resulting in an overshoot of oxygen (functional hyperemia). This process, called neurovascular coupling (NVC), has been known to exist for a long time [76]. Interestingly, NVC occurs at activation of both excitatory and inhibitory neurons, even when inhibitory neurons can cause a net decrease in neuronal activity [77-79]. NVC works both retrograde and anterograde, with signalling components travelling both upstream and downstream [60].

The neurovascular unit (NVU), consisting of vascular cells (SMC, endothelial cells, pericytes) and parenchymal cells (neurons, glial cells, astrocytes) regulates the relationship between brain cells and blood flow by altering vascular diameter. The NVC pathway works on several levels of the vascular tree [11], and the specifics of the NVU and its interactions differ per vessel type and location in the vascular tree [60].

Pial arteries, which lie on the surface of the brain, and penetrating arterioles, which deliver the blood into the brain, can be activated to facilitate an increase in blood flow [80]. These vessels contain SMC, and can thus constrict or dilate. However, NVC is spatially specific, so a more local regulation of blood flow takes place as well. When vessels transform from arterioles to capillaries, the SMC that were present in the vessel wall are replaced with pericytes. Precapillary arterioles have ensheathing pericytes that have characteristics of both pericytes and SMC [81]. Pericytes can contract and dilate capillaries, and thus influence blood flow [82, 83]. The role of pericytes and capillaries in NVC however is a topic of controversy to this day. Pericyte degeneration has been shown to decrease NVC and cause BBB leakage [84], and relatively recently, Hall et al. [82] have shown that pericytes dilate capillaries even before SMC have an effect on arterioles and arteries. Alarcon-Martinez et al. found that pericytes communicate with each other, and blocking of this communication impairs NVC [85]. However, other studies have shown that the arterioles leading into the capillary bed are responsible for local blood flow, and the contribution of capillaries and pericytes could be minimal on NVC [86]. Pericytes within the capillary network differ from each other [87], and the difficulty in distinguishing capillaries and arterioles from precapillary arterioles might explain some of the contradictory results that were found [79].

2.3.2 Signals and mediators

The pathways that lead to vasodilation upon neuronal activation are still subject to research. Studies have found roles of ions (such as K^+, H^+, and Ca^{2+}) which are directly released by neurons during action potentials, metabolites (such as CO^2 and adenosine), neurotransmitters (including dopamine, acetylcholine and GABA), and more (see [23] and [79] for a review). Moreover, a multitude of cell types are considered to be involved, such as pericytes (as explained above), astrocytes (their role is controversial) [88], interneurons and endothelial cells, as well as neurons directly. Given the extensivity and complexity of the NVC pathways, I will here focus on the role of O^2 (relating to hypoxia, Chapter 4), and endothelial cells (which might be damaged with increased pulsatility, Chapter 5 & 6).

Endothelial cells have been identified as important mediators of NVC especially in the upstream vasodilation that is further from the site of activation [89, 90]. A current theory is that capillary endothelial cells can "sense" neuronal activation, although the mechanism for this is still unclear [89]. Endothelial cells can forward a signal by hyperpolarisation via the gap junctions between endothelial cells (ECs), from capillaries towards pial vessels, leading to upstream vascular tree vasodilation [90]. This mechanism is very fast, but ECs can also facilitate a slower vasodilation via the release of nitric oxide (NO) [91] and other vasodilatory factors [89]. Once arterial endothelial cells receive the signal from capillary endothelial cells, the SMC are signalled and the vessel can dilate [79].

Given that replenishing oxygen and removing waste products are main goals of NVC, the direct involvement of partial pressure of oxygen (pO^2) and carbon dioxide (pCO^2) in vasodilation makes sense. Indeed, lack of oxygen and (hypoxia) and high CO^2 levels (hypercapnia) have been shown to cause cerebral vasodilation as early as 1890 [92], and generally increase global CBF [93-95]. However, high levels of oxygen do not seem to cause any differences in NVC [96, 97], and thus oxygen deficiency cannot be the main factor for NVC [23, 68, 98].

2.3.3 fMRI

Studies regarding NVC will need to relate to hemodynamics. There are many different techniques for this. For example, Positron Emission Tomography (PET) and Single Photon-Emission Computed Tomography (SPECT) scans in combination with injections of different tracers can be used for blood flow, blood volume and metabolic rate of oxygen in the brain. Other techniques, such as functional near-infrared spectroscopy (fNIRS) and intrinsic optical imaging (IOI) rely on the intrinsic properties of blood, such as the light absorption differences between oxygenated and deoxygenated hemoglobin. The downside of these techniques is that you can only image the surface of the brain. More recently, functional ultrasound imaging (fUS) and photoacoustic imaging (PAI) have increased in popularity as well, each with their own pros (fUS: good spatial and temporal resolution, PAI: HbO and HbR measurements, non-invasive) and cons (fUS: the skull distorts the signal, PAI: limited depth). However, here, I will mainly focus on functional Magnetic Resonance Imaging (fMRI), since it is non invasive, can be used on humans as well as animals, gives an image of the whole brain, can be relatively easily combined with stimulations or tasks and is one of the most popular imaging techniques to study NVC. Furthermore, the prevalence of MRI machines in hospitals is increasing, as well as the accuracy at which they can measure.

The fMRI signal is based on the Blood Oxygenation Level Dependent signal (BOLD). The difference between the two forms of hemoglobin (diamagnetic for oxygenated, paramagnetic for deoxygenated hemoglobin) leads to microscopic changes in the homogeneity of the magnetic field when their proportion are changed in vessels during activation [99, 100]. The increased inhomogeneity, varying in time during activation, can be measured through changes in T2* in echo-planar imaging sequences, so called BOLD sequences. What results is a dynamic measure of changes in oxygenation reflecting, in space and time, the underlying activation of the brain. Crucially, this means that any inference on brain activity is dependent on neurovascular coupling.

However, to accurately assess the state of neurovascular coupling in an individual, fMRI by itself will not suffice, since this will only inform on the hemodynamics and not on neuronal activation. Even so, there are studies that claim a decrease in NVC based on hemodynamic data alone [101-104]. For example, Chen et al. [105] concluded that there was an increase in synchronized neural activity in high-altitude hypoxia. Although this data can inform about altered hemodynamic structures, the conclusions on neuronal aspects without knowing whether NVC remains intact are premature. A decrease in BOLD signal could be because of damaged vasculature impairing NVC, but it could also be a proportional response to diminished neuronal activation. This is demonstrated by a study from Rancillac et al. [106], where they performed a study on a mouse model of Alzheimer's, and found that the vasomotor responses itself were not damaged, but rather that the problem lied on the neuronal side.

Not only in situations where NVC is altered can fMRI data be inaccurate in representing neuronal activity. Usually, the analysis of BOLD data is based on a linear model, that assumes that each increase in stimulation has a linear additive effect on both neuronal activation and blood flow increase [107]. However, studies suggest that this is not necessarily an assumption that always holds [107-110]. Furthermore, NVC has been shown to differ over brain areas [108], which we have also confirmed in Article 2.

2.4 Disruptions of the status quo

Disruptions or impairments of the cardiovascular system often feed off of each other, and result in an impairment in cognition. There are many paths from cardiovascular problems to cognitive decline, and they sometimes form a negative feedback loop, where the byproducts of cognitive diseases progress the vascular damage.

A leaking BBB increases the chance of neuroinflammation, which increases the number of neutrophils in the blood stream circulation. Neutrophils are relatively big (12-15 um) [111], and thus they could get stuck in the capillaries, causing stalling of blood flow. This theory is supported by a recent finding by Yang et al. (Q. Yang et al., 2024), where APP23/PS1 mice (an AD mouse model) show cognitive impairment that was worsened by cerebral hypoperfusion, but alleviated by the autophagy inhibitor 3-methyladenine. Similarly, Cruz Hernández et al. (Cruz Hernandez et al., 2019) showed an increase in capillary stalling due to the adhesion of neutrophils and, crucially, a reinitialization of blood flow and an increase in both spatial and working memory after admission of an antibody against a neutrophils surface antigen (Ly6G-α) to reduce the number of circulating neutrophils.

Amyloid beta (Aβ) is an important biomarker for AD, and is seen as the major indicator of AD (together with hyperphosphorylated tau protein). Injection of amyloid beta induces hypertension and reduces carotid artery blood flow [112]. Aβ depositions also decrease the number of capillaries (capillary rarefaction), which naturally causes a decline in CBF and reduced clearance of Aβ, causing a negative feedback loop [30]. Furthermore, amyloid beta activates microglia, which releases inflammatory cytokines [113]. **Cerebral amyloid angiopathy (CAA)** refers to amyloid beta depositions in the vessel wall (mostly in arterioles and capillaries) [114], and is characterised by a thickening of the vessel wall and a loss of SMC [115]. CAA is caused by a soluble type of amyloid beta [115, 116], which has been found to decrease CBF [116, 117] and cause endothelial dysfunction [118] and thereby reduce vasomotor regulation [117]. A study by Dietrich et al. [116] shows that amyloid beta causes vasoconstriction and a reduction in vasodilation in penetrating arterioles, and thus impairs autoregulation and NVC. About 82-98% of Alzheimer’s patients show CAA [119]. Furthermore, amyloid beta increased reactive oxygen species (ROS) production in endothelial cells and SMC, and the vasomotor response was partially rescued by injection of a ROS scavenger [116].

ROS overproduction does not only occur in CAA, but also occurs in hypertension [120] and hypoxia [121], as well as in aging [122]. It has been shown to constrict capillaries [123] and severely damage vasculature and cause vascular dysfunction by damaging both endothelial cells and smooth muscle cells [124-126].

Endothelial cell damage or dysfunction can occur due to ROS, amyloid beta depositions and inflammation, among others. Damaged endothelial cells fail to propel neutrophils forward, which can cause capillary stalling. Eventually, endothelial apoptosis attributes to capillary regression, ultimately leading to “string vessels” or “ghost vessels”, which are thin strands of tissue remnants leftover from previous capillaries, devoid of endothelial cells [127]. Furthermore, damaged endothelial cells hinder the constriction and dilation of vessels [60], which hinders both NVC and autoregulation.

2.4.1 Hypoperfusion

When autoregulation fails to keep a sufficient CBF, hypoperfusion occurs. CBF tends to decrease with age [128, 129], but even more so in Alzheimer’s disease [128, 130]. Hays et al. [131] even argue its usefulness as a biomarker in Alzheimer’s. Hypoperfusion is also associated with MCI in humans [132, 133]. In studies concerning animal models of AD, reduced CBF is followed by a decrease in cognition [123, 134-139]. Reversely, compensating for the hypoperfusion in AD has been shown to dampen the effects of AD, although it does not alleviate the symptoms completely [140-142].

There are several hypotheses as to how CBF reduction and AD/cognitive decline are related. First, hypoperfusion has been shown to impair the integrity of the Blood Brain Barrier [143, 144], thus contributing to neuroinflammation. Next, a decrease in CBF means less efficient clearance of “waste” in the brain, importantly amyloid beta. In this case, a negative feedback loop develops, where amyloid beta causes damage to the vasculature, which worsens hypoperfusion, which means less clearance of amyloid beta [113]. Furthermore, hypoperfusion is related to endothelial damage [145] and thus neurovascular unit dysfunction [19]. The endothelial damage is at least partially due to oxidative stress [146].

2.4.2 Hypertension

If the pressure that the blood exerts on the vessel walls is consistently too high, we speak of hypertension. The impact of hypertension on the vascular system is multifold [30], with consequences overlapping those of hypoperfusion. First, it causes a decrease in the number of capillaries. The cause of this is not completely clear yet, but it could be due to the increase of Aβ damaging the vasculature, endothelial impairment or apoptosis, pericyte damage, or impaired angiogenesis [147]. Capillary rarefaction decreases CBF, and can thus cause hypoperfusion.

Next, hypertension disrupts the BBB [148]. Hypertension in aging comes with a loss of pericytes [149] which can impair the BBB and could also contribute to the microvascular rarefaction [147, 149]. Other factors in play could be endothelial oxidative stress [150, 151] and alterations in tight junctions [149]. This would cause the problems as described above, with more neuroinflammation and an increase in capillary stalling, feeding into hypoperfusion as well. Furthermore, hypertension can disrupt NVC [30, 152]. Angiotensin II is strongly involved in hypertension [153], and in mice with hypertension induced by administering Angiotensin II, NVC was diminished. Hypertension has been shown to alter the response to vasodilators and vasoconstrictors [154], which would hinder NVC as well. Furthermore, less regional influx of blood was observed upon cognitive tasks in people with chronic hypertension [155], but no neuronal data was collected in this study.

Hypertension is an important risk factor for other cardiovascular diseases, such as atherosclerosis [156] and hypertrophy [157]. These risks can be reduced by treating hypertension [34, 158-160]. Furthermore, hypertension can cause increased Aβ depositions [161, 162], and tau hyperphosphorylation [162], indicating a role in dementia. Giving anti-hypertensive drugs (telmisartan) has been shown to decrease both depositions [163]. Furthermore, hypertension is associated with the rate of cognitive decline in Alzheimer’s patients [164].

2.4.3 Rigidification of vessels

The flexibility of vessels can be affected in a number of ways, and at different levels on the vascular tree. General hardening of arterial walls is called arteriosclerosis, with atherosclerosis being a well-known subtype specifically referring to a buildup of fats and cholesterol that cause the stiffening. Atherosclerosis mostly affects the larger (conduit) arteries [57] and the branching sites of the vessels [157]. Arteriolosclerosis is used to refer to the hardening of the smaller arterioles [165].

The elasticity of a vessel is determined by the composition of the vessel wall. However, the change in diameter towards a certain change in pressure, also termed functional stiffness [166, 167], depends on the thickness of the wall and the diameter of the vessel as well. It is related to structural stiffness (Y) in the following manner:

$$E\rho \ \approx Y \times \frac{h}{r} \tag{2.2}$$

Where the thickness of the vessel is described by h and the midwall radius by r. The distensibility of a vessel is then logically described as the inverse of the functional stiffness.

Impedance describes the opposition to pulsatile blood flow [168]. This includes all components related to blood flow, like vessel rigidity, blood viscosity, inertia and reflection. Reflection of the pulsatility generated by the heart occurs when there is a change in impedance, for example at a junction, at vascular lesion sites and at locations of increased arterial stiffness. These reflections can cause differences in pulse pressure throughout the vascular system, since the pulsatility at a site will depend on the number of reflections from upcoming bifurcations, as well as on the impedance increases further in the vascular tree where the vessels are smaller and less distensible (Figure 2.2).

Since pulse pressure (PP) and pulse wave velocity (PWV) are directly related to arterial distensibility, both have been used as measurements for arterial stiffness (although PWV is more common) [57, 167, 169]. PWV describes the velocity with which the pulse wave is traveling through the vascular system, and is determined by measuring the time it takes for a pulse wave to travel a certain distance, for example between the brachial and ankle (baPWV) or the carotid and femoral (faPWV). It is proportional to the square root of Eρ [166]. The pulse pressure on the other hand is the difference between the minimum (diastolic) and maximum (systolic) pressure. Pulse pressure is the result of cardiac output, arterial stiffness, and wave reflection.

The distensibility of vessels tends to decrease with age [57, 170]. The amount of rigid collagen and number of vascular smooth muscle cells increases, while the amount of elastin decreases [57, 171]. Furthermore, the elastin that remains becomes calcified, while the collagen cross-link with each other, and thus only strengthen.

Hypertension also has a clear effect on vessel rigidification. It causes an increase in collagen in the vessel wall, and thickening of the vessel walls through medial hypertrophy, both contributing to the stiffness of the vessel [166]. In the case of hypertension, this causes a negative feedback loop, since the consequences of hypertension are aggravated by vessel rigidification. Toth et al. [149] showed that whereas young mice can still counteract the effects of hypertension via myogenic constriction, this ability is reduced in older mice.

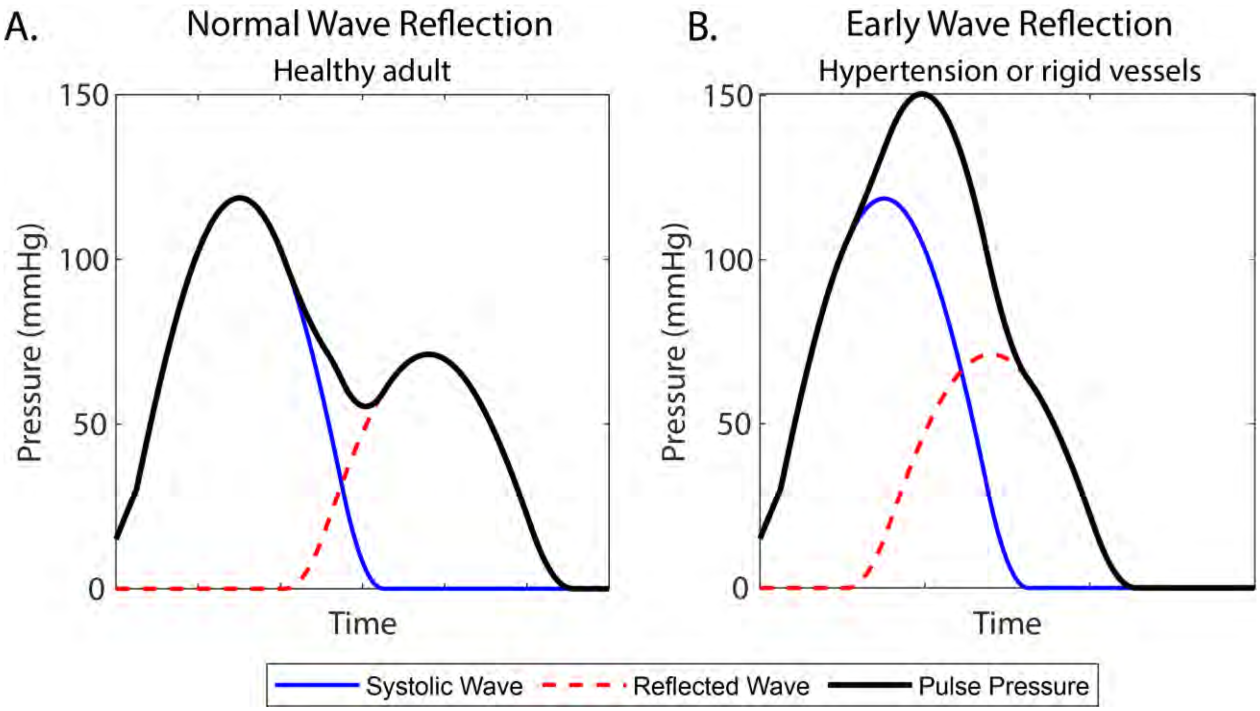

Figure 2.2: Pulse pressure and reflection.

A. Wave reflection in a healthy, young individual. The systolic wave (blue) hits a section where the impedance differs, causing a wave reflection (red dotted line). The sum of these two form the pulse pressure (black line) B. Earlier wave reflection, which causes the systolic wave and reflected wave to add to a higher value, resulting in a higher pulse pressure.

2.4.4 Left ventricular hypertrophy

Both increased mean resistance and increased impedance demand a higher workload of the heart. In situations that increase the impedance of the vascular system, such as hypertension, the heart will have to increase the force of its output, particularly the left ventricle. This is achieved by strengthening the ventricle walls, mostly affecting the left ventricle wall, leading to left ventricular hypertrophy (LVH) [172, 173]. LVH can also occur in any other setting where the heart is asked to increase the force of its output (thus increasing the pulse pressure), such as aortic valve stenosis, aortic coarctation, and very active athletes [174] and increases the risk of other cardiovascular diseases [175], including heart failure, coronary artery calcification and stroke [172, 176]. Furthermore, LVH increases the risk of atherosclerosis [177] and, vice versa, arterial stiffness contributes to LVH [178].

2.4.5 Consequences of increased PWV and PP

An increase in pulsatility is a logical consequence of cardiac hypertrophy and rigidification of vessels. The first increases the pulse of the heart, while the second fails to attenuate it. Furthermore, each worsens the other, resulting in a negative feedback loop. Increases in PWV and PP in the cerebrovascular system might lay at the base of some interactions between cardiovascular diseases and cognitive impairment, with a large body of literature to support this idea. For example, a high PWV has been shown to be a better predictor of heart disease than systolic or diastolic pressure in people over the age of 50 [167], and to be associated with all-cause and cardiovascular mortality in hypertensive patients [179]. A larger PWV has also been shown to affect the brain, giving a larger chance of dementia [180, 181] and cerebral small vessel disease [33, 36, 37, 182, 183], and is also linked to a smaller brain volume [170, 184], and general cognitive decline [37, 170, 185-187]. An increase in PP shows similar effects, with associations with cognitive decline [185, 188], dementia [189, 190] and stroke [191].

The mechanism with which increased PWV and PP affects cognition has been subject to much research. The current theory in the field [17, 27, 28, 188, 190, 192] is that the decreased attenuation of the heartbeat as caused by stiffer vessels, and the increase in pulsatility due to hypertrophy causes the pulse pressure wave to penetrate deeper into the vascular system. Increased pulsatility then damages the smaller, more fragile smaller vessels in the brain. Especially the capillary endothelial cells are sensitive to this increased pulse pressure. These damages cause BBB dysfunction and problems with blood flow, such as hypoperfusion and impaired NVC.

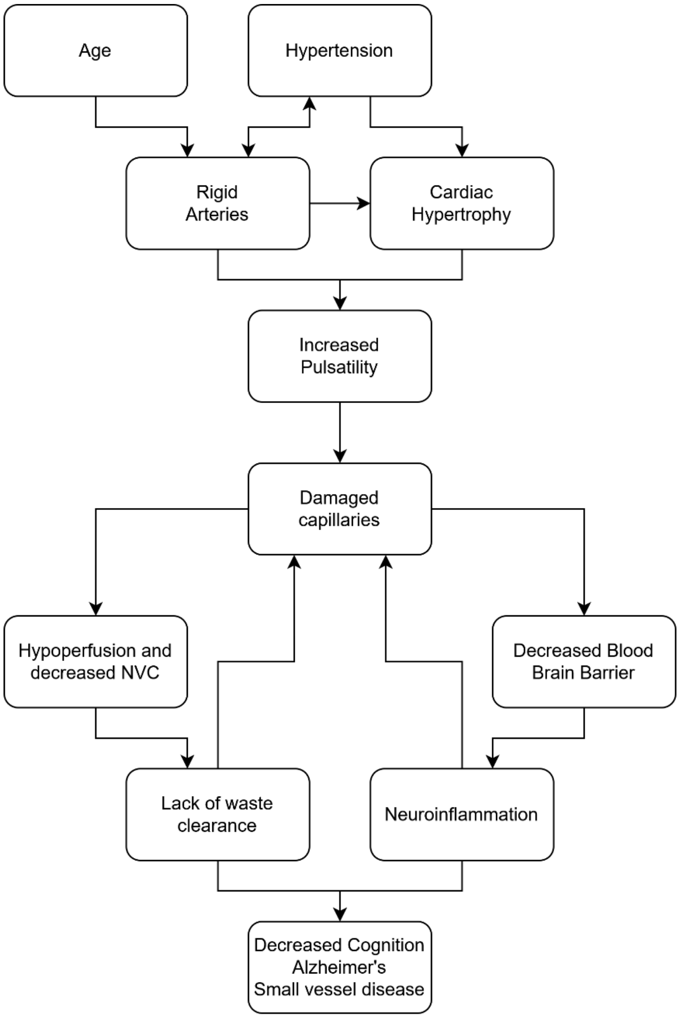

Figure 2.3: Flow chart of interactions.

Arrows indicate one aspect causing or influencing another. This flow chart does not include all interactions between cardiovascular diseases and cognitive decline, but focusses on the ones discussed in this thesis.

There is a large body of literature to support this [193]. De Montgolfier et al. [17] showed that an increase in PP damages the neurovascular unit, impairs endothelial dilatory function, weakens the BBB and causes capillary rarefaction. Muhire et al. [194] showed that carotid artery calcification in mice increased BBB permeability and impaired cerebral autoregulation. Even in healthy humans, PWV and PP are inversely correlated with endothelial cell function [192]. When exposing human endothelial cells ex vivo to pulsatility and shear stress, Garcia-Polite [12] found an alteration of the functional morphology of the endothelial cells, which thus impairs the BBB. This has led to an increased appreciation of treatment of hypertension to counteract cognitive decline [190, 195]

To summarize, hypertension, rigid arteries and cardiac hypertrophy are strongly related to each other, and often feed into each other. The end result of this is an increase in pulse wave velocity, that can damage the microvasculature of the brain, and in that manner influence cognition and brain function (Figure 2.3). Article 2 and 3 relate to this interaction. In both articles, we attempted to mimic conditions where pulsatility is increased.

2.5 Resting state and Resting State Networks

In the 90s, it was first discovered that even without any type of purposeful stimulation, the brain communicates with itself in a more or less predictable manner [39, 196]. This started with a correlated activity between left and right motor cortex, but over the years many other connections were discovered. The connections between brain areas form a Resting State Network (RSN). The largest and most prominent network is labeled the Default Mode Network (DMN) [197, 198]. It includes the posterior cingulate cortex and ventral anterior cingulate cortex [199], and shows a decrease in blood flow during cognitive tasks [198]. However, depending on the classification, many networks may be found [200], and each network is thought to be important for different types of tasks.

The study of RSN can be very useful in conditions where stimulus-driven research is difficult, for example in comatose patients, patients with Alzheimer’s disease or severe autism.

2.5.1 Disruptions of resting state networks

Exploiting resting state recordings, differences in RSN patterns in patients with Alzheimer's disease have been found by many studies [46, 47, 51, 53, 54, 201-203]. Changes in RSN can be detected very early on in cases of AD. Indeed, the changes accompanying AD when it comes to RSN are so distinct, that there has been some promising research into the topic of using RSN fMRI studies as a potential diagnostic tool [46, 50, 54], and even as prediction factor for the progression of mild cognitive impairment to Alzheimer’s disease [55]. Other diseases and conditions show an alteration in RSN as well, including Parkinson’s [204], autism [49, 205, 206], type 2 diabetes [207] and schizophrenia [208-211], among others. These findings suggest that RSN could be useful biomarkers for a myriad of diseases.

Not surprisingly, changes in the cardiovascular system also alter the RSN. Carotid artery stenosis [212, 213], hypertension [214-216] and hypoperfusion [217, 218] have all been shown to alter the RSN [212-216]. Many studies also show a connection between cardiovascular diseases, RSN and cognition [212-215, 217].

2.5.2 Neurovascular coupling in resting state

As discussed previously, fMRI is often used to reflect neuronal activation, but is dependent on NVC to make this connection. It would therefore be premature to conclude that the RSN as measured with fMRI reflects neuronal activity. Indeed, besides variability caused by heartbeat and respiration, slow oscillations in cerebral blood flow have been found, independent of neuronal activity [219]. Studies combining imaging techniques regarding resting state are therefore crucial.

The existence of a neuronal RSN has been shown with electroencephalography (EEG) and magnetoencephalography (MEG) in humans [42, 220, 221]. Furthermore, spontaneous neuronal activation and neuronal RSN has been found in animal studies with calcium sensitive reporters [222], and electrophysiological recordings [45], among others.

How the hemodynamic RSN corresponds to the neuronal RSN has also been investigated. Studies in rats [223] and mice [45, 224, 225] that looked at both neuronal activity and hemodynamics have shown that the resting state activity of both modalities are correlated. Furthermore, Shmuel et al. [226] did a study in monkeys where they recorded neuronal activation with intracortical electrodes during fMRI. They showed neuronal activity correlated with the slow fluctuations in the BOLD signal as measured during rest. Lastly, studies in humans combining fMRI and EEG [227, 228] and fMRI and electrophysiology [226, 229] also show a connection between neuronal and hemodynamic RSN. In the same line, studies have found intact neurovascular coupling during resting state in the somatosensory cortex [230] and barrel field cortex [222].

2.6 Knowledge gaps

Finally, we come to the combination of the abovementioned factors; how neurovascular coupling is impacted during resting state in cases of cardiovascular disease. Although a lot of research has been done in each of these topics individually, the mix of neurovascular coupling, resting state analysis and cardiovascular disease in a single study is relatively rare.

Li et al. [103] investigated NVC in resting state with a combination of fMRI and arterial spin labeling (ASL) which measures cerebral perfusion, and found a dysfunction in NVC in patients with cerebral small vessel disease. However, both ASL and fMRI are dependent on hemodynamics, and thus questions about the neuronal component in this aspect remain unclear. Then there are studies showing changes in RSN in either the hemodynamic component [231] or neuronal component [232] in cardiovascular diseases.

To summarize, both NVC and RSN are thought to be disrupted in many diseases and conditions, with many of them (such as Alzheimer's [23, 47], atherosclerosis [24], hypoperfusion [15, 142, 217] and hypertension [19, 216]) overlapping, but studies investigating all those components are rare. In chapters 4 and 5, I aim to address this by pairing neuronal measurements, hemodynamic measurements and alterations in the hemodynamic system in resting state recordings.

CHAPTER 3 BACKGROUND ON METHODS

3.1 Mouse models

To directly investigate the effects of an increase in pulse pressure, two mouse models were used in this thesis. The first model mimics the arterial stiffening in humans as they age, in that it increases the calcium in the artery and thereby decreases the flexibility. Of course, the timeline differs from the natural stiffening, as well as the location (only the carotid artery in this model versus the whole vascular system in nature). Since we observed a mild effect of this model, we used a model with more impact on the pulse pressure in the third article: the TAC surgery Although this is less reflective of arterial stiffening in cardiovascular diseases, it does have a much stronger impact on the cardiovascular system, and can therefore inform on the consequences of increases in pulse pressure.

3.1.1 Carotid artery rigidification/CaCl

This model was developed by Sadekova et al. [233], and has since been used in several studies [194, 234, 235]. The application of a calcium chloride (CaCl) soaked cloth to the carotid artery (Figure 3.1A) effectively stiffens it, making this a good model for studying the effect of artery rigidification and subsequent increased pulsatility. Previous studies with this model have shown a rigidification of the artery with a pressure myograph [233], and histological assessment showing an increase in intima-media thickness [233, 234]. The carotid artery showed calcium deposits, an increase in collagen [233], and an increase in pulsatility was shown with the help of a doppler OCT scan [233].

The benefit of this model is that specifically only the carotid artery is targeted. In mouse models where the arteries were stiffened by genetic mutation for example, other symptoms such as stiffening of the joints [236] and increased sensitivity to oxidative stress [237] occur. Moreover, with genetically modified models, it will be extremely difficult to determine whether the observed effects stem solely from the rigidification, and not some unexpected side-effect. Although these kinds of studies are perfect for determining the role of certain genes or clarifying molecular pathways, the impact of artery rigidification by itself is better studied with the model of Sadekova et al. Another benefit of this model is that even thought the pulsatility increased, the blood pressure remained the same, thus enabling to study the effect of rigidification independently of blood pressure [194, 233].

The CaCl mouse model has shown to cause some cerebral alterations. Sadekova et al. [233] showed in their original study that the pulsatility in the brain on the side of the affected carotid was increased, and there was more oxidative stress in the hippocampus [233, 234]. Other studies show changes in spatial organization of HbO [235] and a decrease in resting state CBF [194].

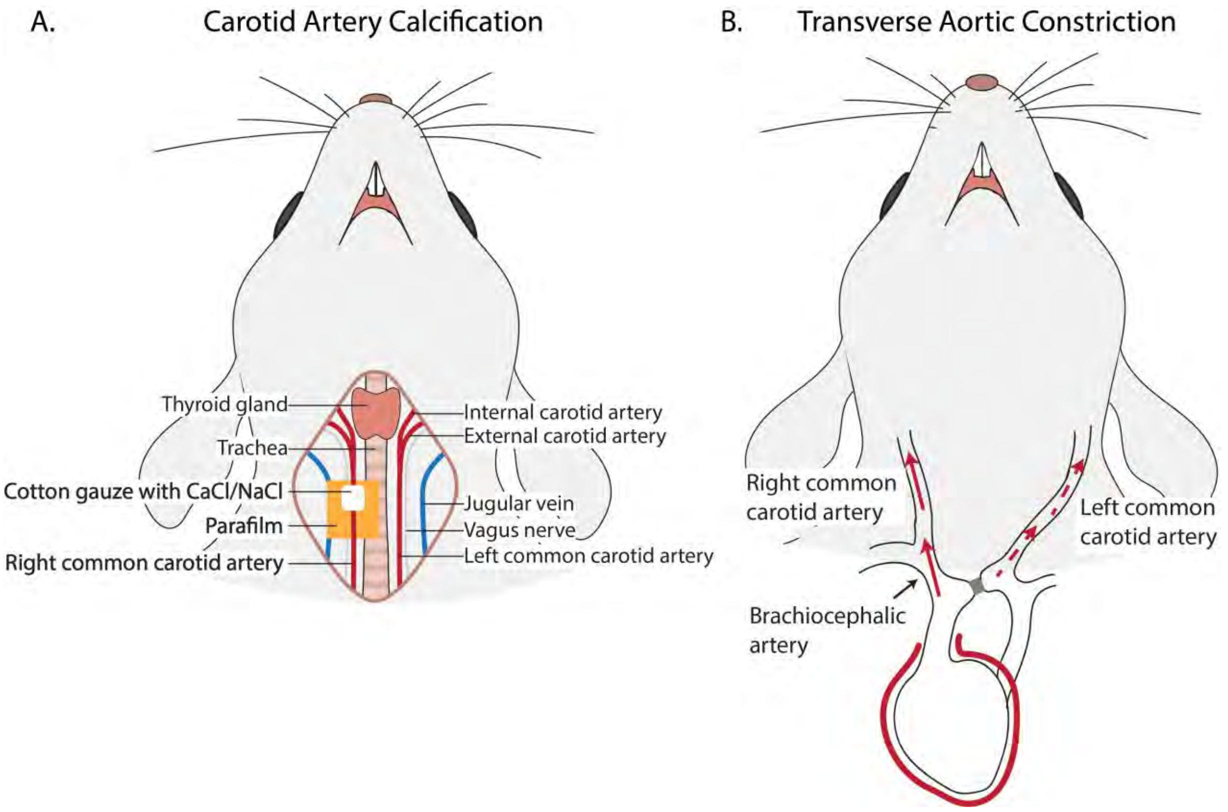

Figure 3.1: CaCl and TAC surgery.

A. Schematic overview of the carotid artery rigidification by application of calcium. During surgery, an incision is made, and a cotton gauze soaked with CaCl (or NaCl for sham) is held against the carotid artery for 20 minutes, making it more rigid. B. Overview of the transverse aortic constriction surgery. A suture is tied around the aorta, between the brachiocephalic artery and left common carotid artery, increasing the resistance that the heart has to overcome and resulting in cardiac hypertrophy.

3.1.2 Transverse Aortic Constriction

In Transverse Aortic Constriction (TAC) surgery [238], the aorta is constricted between the brachiocephalic artery (which branches off into the right carotid artery) and the left common carotid artery (Figure 3.1B). This limits the outflow of the left ventricle, causes arterial hypertension, and creates a pressure overload. The mechanical stress that this induces can result in left ventricle hypertrophy (LVH) [239]. Importantly, TAC surgery also increases pulsatility in the right carotid artery [15, 240], and has been used as a model to investigate an effect of increased pulse pressure [15]. De Montgolfier et al. [15] also found a decrease of cerebral perfusion in both hemispheres of the TAC mice, but more severely in the right hemisphere. Lastly, TAC surgery increases systolic blood pressure [16, 241].

The results of the TAC surgery depend on the severity of constriction. Most often, a 27G needle with an outside diameter of 0.4 mm is used as a gauge [242]. Furihata et al. [241] showed that a diameter of 0.4 mm induced left ventricle hypertrophy, but did not result in heart failure, while smaller gauges (0.385 mm and 0.375 mm) did. Smaller gauges unsurprisingly lead to more severe hypertrophy and a higher death rate [241-243]. Richards et al. [243] investigated the effects of 27, 26 and 25G needles, and found an increase in left ventricle/body weight, aortic pulse pressure and left ventricle diastolic volume, even in “mild” transverse aortic constriction of 25G. Cardiomyocyte area and atrial weight was increased in mice with 26G and 27G TAC surgeries, but not 25G. They conclude that TAC surgery with 25G gauge would serve as a model for hypertensive heart disease, 26G for early decompensation and, contrary to Furihata et al.[241], 27G for heart failure.

The timing from TAC surgery to imaging or sacrifice is important as well. A gauge of 0.385 mm already showed hypertrophy after one week, and this increased after 4 weeks [241]. Similarly, systolic blood pressure close to the aortic constriction was elevated after 1 week, and more so after 4 weeks.

TAC surgery might affect male and female mice differently. A study by Skavdahl et al. [244] showed that the ratio heart weight/body weight after TAC surgery in male mice showed a greater increase (64%) than in female mice (31%). Furthermore, they found a sex difference in TAC surgery induced hypertrophy on α and β estrogen receptor knockout mice (α-ERKO and β-ERKO, respectively). α-ERKO female mice showed no difference in hypertrophy compared to wildtype, while male a-ERKO mice showed less hypertrophy than wildtype TAC. Furthermore, β-ERKO had no effect on male TAC mice, while it worsened the hypertrophy in female TAC mice. However, this study did not keep into account the natural difference in aortic size between mice. Generally, smaller mice have a narrower aorta, and thus female mice tend to have narrower aortas than male mice. This would mean the restriction in percentage differs between these groups, which could be part of the reason that male mice tend to be more affected when uniform gauges are used [242, 243, 245].

In our study, the goal was to induce an increase in pulse pressure with the help of the TAC model. Given abovementioned research, we have chosen a 27G constriction of the aorta, and a period of 20-30 days between TAC surgery and imaging.

3.2 Imaging methods

All imaging methods have their benefits and limitations. I have used different imaging techniques in this thesis, depending on the purpose of the article. In chapter 4 and 5, a combination neuronal and hemodynamic imaging (GCaMP/IOI) over the whole cortex gives information about RSN and the NVC that connect them. In chapter 6, the priority was more on the temporal and spatial resolution, giving very precise data but on a much more limited field of view. In that case, an ultrafast 2-photon imaging method was used, which informed on the blood flow dynamics in vessels. To keep the imaging speed high enough to see possible pulsatility in these vessels, the field of view necessarily became quite small.

3.2.1 Mesoscale calcium and intrinsic signal imaging

Brain activity can be recorded using genetically encoded calcium indicator (GECI) such as GCaMP. There have been several generations of GCaMP, with the most recent being GCaMP8 [246]. They are the result of the fusion of a calcium-binding protein calmodulin and a green fluorescent protein (GFP). During the firing of a neuron, the amount of intracellular calcium increases, and binds with the protein calmodulin, which increases the fluorescence of the GFP [247]. GCaMP requires an excitation light of 450-490 nm [246, 247], and emits fluorescence at 500-550 nm [246, 247], which makes it possible to distinguish between reflected excitation light and actual fluorescence.

Brain function can also be imaged using genetically encoded voltage indicators (GEVI), who report the depolarization of neurons, and intensity-based glutamate-sensing fluorescent indicators (iGluSnFR) who report the activity dependant release of glutamate. The benefit of GEVI and iGluSnFR over GCaMP are mainly their speed [248, 249]. However, hemodynamic resting state dynamics tend to be slow, and since our study regarded both hemodynamic and neuronal dynamics on a slower timescale (minutes compared to milliseconds), fast imaging was not required. The specific indicator GCaMP6s provides ample speed, while also providing us with more sensitivity than GCaMP6m or GCaMP6f [247]. Furthermore, GEVI are unable to image large populations of neurons simultaneously, since they need more excitation power for the same signal to noise ratio, which induces more photobleaching [248]. GCaMP on the other hand can be imaged over the entire cortex, and has been used as such in previous literature [224, 250-252].

A great benefit of GCaMP imaging is that it can be combined with Intrinsic Optical Imaging (IOI), and can thus provide information about neuronal and hemodynamic fluctuations simultaneously. IOI requires no injection of substance since, like fMRI, the signal depends on the oxygenation of blood. IOI works by shining lights with several wavelengths onto the brain. In our implementation, this includes a red (~620 nm) and green (~535 nm) light, and can include a yellow (~590 nm) light as well (Figure 3.2). By capturing the reflected light of two or more sources, one can infer the changes in HbO and HbR over time. The absorption indexes of HbO and HbR differ from each other as well as over wavelengths [1, 253] (Figure 3.2). By alternating between red, green and blue light, it is possible to capture changes in hemodynamics and neuronal activation with just a time difference of one or two frames between the two modalities.

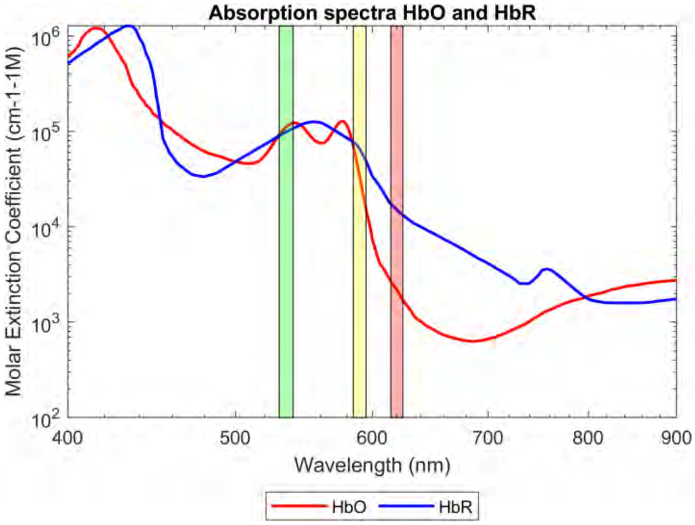

Figure 3.2: Absorption spectra HbO and HbR.

Data from Scott Prahl [1], code courtesy of Labeo Technologies inc. Coloured columns represent respective lights used in IOI. HbO (red) and HbR (blue) absorb these lights in different amounts, thus enabling estimation of changes in these compounds.

Another benefit of combining IOI and GCaMP imaging is that the hemodynamic signal can be used to clean up the neuronal signal. Changes in the amount of blood and the oxygenation of it can alter the measured GCaMP signal. Since neuronal activation is paired with an influx of blood, both the excitation light as well as the GCaMP fluorescence might be partially absorbed by the blood. Ma et al. [254] show that IOI data can be used to counteract this effect.

Both the signals of IOI and GCaMP are strong enough to be detected through the mouse skull (although in older mice a thinning of the skull is required). Since it is not necessary to remove the skull and damage or break the dura mater, the chance of infection and neuroinflammation is greatly reduced, and the natural homeostasis of the brain is kept intact. Furthermore, the optical window that is installed over the exposed skull has been shown to remain a stable quality over at least several weeks. This, in combination with the long-lasting effects of the GCaMP injection, and the intrinsic properties of IOI, enables combined IOI/GCaMP imaging over several weeks in the same mouse.

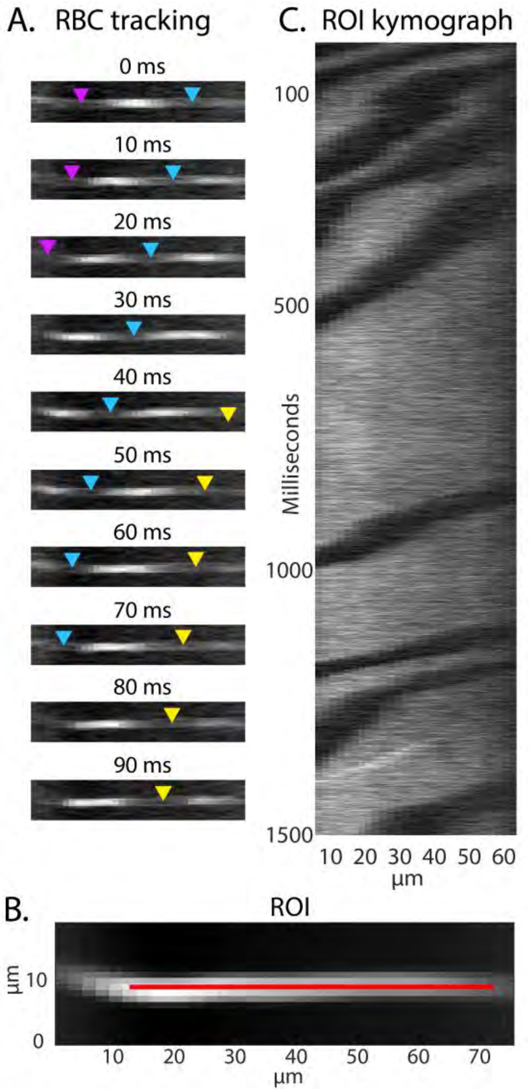

Figure 3.3: Red blood cell tracking with 2P

A. Red blood cells (RBC) can be seen as dark spots within the white vessel when the mouse was injected with rhodamine. B. Taking a region of interest (ROI) or making a linescan in the middle of the vessel allows for construction of a kymograph. C. Kymograph where RBC are seen as dark streaks.

3.2.2 2-photon imaging

Two-photon (2P) imaging is, similar to GCaMP, an imaging method that is dependent on a fluorescent molecule. However, GCaMP and other so-called “linear” microscopy techniques only require a single photon to excite the target (i.e. the amount of signal that you receive is linearly dependent on the light that you give), while 2P imaging requires 2 photons to arrive within a very short timeframe.

2P imaging requires light that is roughly twice the wavelength of typical 1 photon excitation, such as green or blue light, resulting in infrared excitation light or similar. Excitation with high wavelength light decreases the amount of phototoxicity and scattering, thus increasing accuracy [255]. This allows for imaging depths of up to 2 millimeters [256]. Furthermore, by limiting the input light to a small spot, fluorescent scattered photons can still be used to inform on activity in a limited location.

2P imaging can be used to investigate blood flow in vessels [257]. For this, a fluorescent agent needs to be injected in the blood stream, such as Texas red, fluorescein isothiocyanate (FITC) or, as we use in Chapter 6, rhodamine. During imaging, red blood cells will appear as darker spots against the fluorescing plasma (Figure 3.3 A), allowing for RBC tracking. 2D scans can be used to determine the vessel diameter (Figure 3.3 B). Drawing a region of interest over the 2D image (Figure 3.3B) allows for the construction of a kymograph (Figure 3.3C). Following the dark stripes on the kymograph, we can determine how much time (y-axis Figure 3.3B) one RBC takes to cover a certain distance (x-axis Figure 3.3B) and thus determine the blood flow velocity.

To get a 2D image, it is necessary to move the laser in both the x and y direction, and thus two galvos are needed to construct an image point by point (Figure 3.4E). The blood flow in some vessels is too fast to track with 2D imaging. In such cases, a linescan can be made along the vessel, limiting the necessary movement to one axis and thus increasing imaging speed. The vessel needs to be horizontally aligned to the imaging axis. The maximum velocity at which an RBC can be tracked depends on the width of the linescan (and thus the kymograph) and the framerate. If the linescan is not sufficiently wide, or the framerate too slow, the RBC will leave the field of view without sufficient frames capturing it to allow for tracking. Although the spatial resolution of 2P is much better than 1P, the temporal resolution has its drawbacks, and even with linescans regular 2P imaging can not keep up with the fastest vessels. Adding a free-space angular-chirp-enhanced delay (FACED) to the system circumvents this problem.

3.2.3 Ultrafast 2-photon FACED microscopy

Although 2-photon imaging has existed since 1990 [258], the ultra-fast FACED module was first published by Wu et al. in 2017 [259], and then recently used to image neurons [260] and cerebral blood dynamics [261]. The FACED module essentially splits a single strong laser pulse into many beamlets, which differ in both angle and time. This allows for imaging line-by-line instead of point-by-point, and thus drastically increases the imaging speed, allowing for tracking of individual blood cells, even in faster flowing arterioles or arteries. This system is used in Chapter 6.

The FACED module [259] consists of two mirrors that are almost parallel to each other (the misalignment angle is small, around 0.6°) (Figure 3.4 A). There are rays that enter the FACED system and have the exact same path on entrance as on exit, called cardinal rays. There are multiple paths to form cardinal rays, resulting in beamlets that are both spatially and temporally distanced. The number of beamlets (M) depends on the angle of the laser pulse into the FACED system (Δθ) and the misalignment angle of the two mirrors (α) [259]:

$$M = \frac{\Delta\theta}{\alpha} \tag{3.1}$$

The distance between the mirrors (S) influences the temporal delay between the beamlets (τ) as follows:

$$\tau \approx \frac{2S}{c} \tag{3.2}$$

Where c is the speed of light.

This line of beamlets can then be used to scan a blood vessel in the cortex. A photomultiplier tube (PMT) is used to register the intensity of the light over time (Figure 3.4 B). Since the beamlets are both temporally and spatially different, the recorded intensity can be attributed to a spatial location along the imaging line based on the time it arrives at the PMT (Figure 3.4 D). In other words, instead of scanning point by point (Figure 3.4 E), the FACED module ensures scanning line by line (Figure 3.4 F), making the repetition rate of the laser the limiting factor for the speed for a linesan. For a 2D scan, a galvo is still necessary, and thus mechanical inertia limitations need to be considered.

The width of both the x-axis of the 2D image as well as the linescan depend on the dispersion achieved with the FACED module. The more beamlets are produced, the wider the field of view. In our system, the maximum achieved width of the field of view was 80 µm, and the laser repetition rate (and thus the acquisition rate per line) was roughly 1 000 000 lines per second. An average per 100 lines was necessary to generate a good quality image, bringing our maximum linescan acquisition rate to 10 000 Hz. If we set the minimum number of frames that the RBC needs to be in the kymograph in order to track it at 10 frames (corresponding to 1 ms) over a width of 80 µm, the maximum velocity with which we can track RBC's is 80 µm/ms or 80 mm/sec. Meng et al. [261] has shown measurements of 49 mm/s for RBC tracking with this system[3].

---

[3] The theoretical maximum tracking velocity in Meng et al. was estimated at 40 m/s. However, they set the minimum number of kymograph frames that the RBC needs to be in at 2, which would make it impossible to link RBCs to their previous position. They also did not average over lines.

3.2.4 Development and Adjustments of the 2P FACED

In our research, the construction of the 2-photon FACED was modelled after the set-up in Meng et al. [261]. The system was optimized and calibrated with fluorescent beads and, at a later stage, test mice injected with rhodamine.

The placement of the mirrors was found to be particularly important. The mirror that the incoming beam hits first (bottom mirror in Figure 3.4 A) should be almost perpendicular to the incoming beam. The first hit of the beam should be as close to the border of this mirror as possible. The second mirror (top mirror in Figure 3.4 A) should then be placed as close to the entry beam as possible without cutting the light, with the reflection of the first mirror again being right on the edge. The angle of the second mirror can then be adjusted to alter the number of reflections to the maximum. Lastly, it is important to optimize all three axes of the mirrors, to maximize the number of reflections but minimize the "leakage" of the laser outside of the system (i.e. light escaping at the top, bottom or sides of the mirrors). Before each acquisition, the system was recalibrated with the use of fluorescent beads.

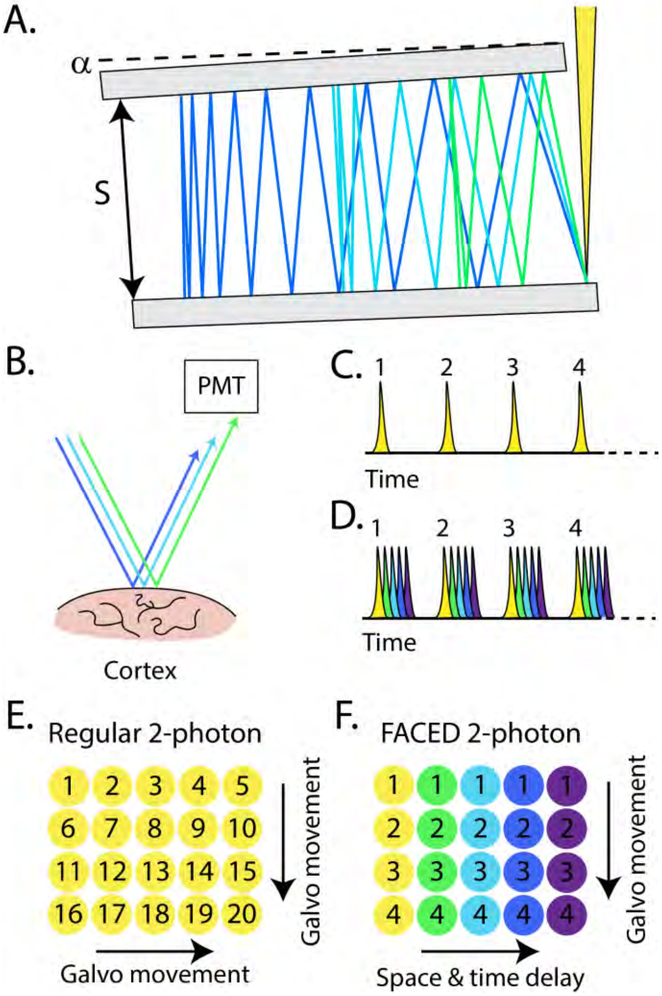

Figure 3.4: FACED vs. regular 2P.

A. FACED module with a laser beam entering and the paths of three example beamlets that exit the FACED module both spatially and temporally distanced. B. Beamlets hitting the cortex and entering the PMT at different times. C. PMT detection with regular 2P. D. PMT detection with FACED system. E. 2D image as taken with a regular 2P. The laser can scan one point per laser pulse and two galvos are responsible for moving this laser point. F. 2D image as taken with a FACED module. Each laser pulse will give a beamlet line that scans over the x-axis. A galvo is only needed for the y-axis movement.

Data analysis in the original study contained parameters that required manual input, differing per acquisition. Since no clear description of the method for calculating these parameters was given, I altered the analysis such that parameters were constant or calculated based on input data. Multiple methods of velocity calculation were tested, and compared to the expected velocities as calculated "by hand" (i.e. manually tracking movement per frames). This resulted in an altered version of the original code, including better estimation of blood flow around zero and robust outcomes regardless of kymograph width.

3.3 Articles of this thesis

Having discussed the context and methods, I will now present the research that I have done for my Ph.D. Chapters 4 and 5 present articles that have been submitted and accepted to scientific journals. However, the article in chapter 6 is still a work in progress, and therefor incomplete. I have included as much preliminary results as possible, with the consequence that these results might be slightly unpolished. Nevertheless, they give a good indication of the general direction that the results will take.

CHAPTER 4 ARTICLE 1: ALTERATION OF FUNCTIONAL CONNECTIVITY DESPITE PRESERVED CEREBRAL OXYGENATION DURING ACUTE HYPOXIA

4.1 Preamble

This article was published by Scientific Reports on August 15 2023. It focusses on the changes of both the neuronal and hemodynamic resting state networks during several levels of hypoxic hypoxia. Several levels of hypoxia were tested (12%, 10% and 8% oxygen), and the tissue oxygenation level in the brain came back to baseline within the 10 minute hypoxia period in all hypoxia levels. However, the functional connectivity levels as measured with GCaMP showed significant alterations (mostly decreases in connectivity) between seed pairs in 8% oxygen. When comparing anterior and posterior brain regions, significant decreases in connectivity were found in both 8% and 10% oxygen.

4.2 Authors

Marleen E. Bakker[1,2], Ismaël Djerourou[1], Samuel Belanger[3], Frédéric Lesage[2,4], Matthieu P. Vanni[1]

1. École d’Optométrie, Université de Montréal, Montréal, Canada
2. Institute of Biomedical Engineering, École Polytechnique de Montréal, Montréal, Canada
3. Labeo Technologies Inc., Montréal, Canada
4. Montréal Heart Institute, Montréal, Canada

4.3 Abstract

Resting state networks (RSN), which show the connectivity in the brain in the absence of any stimuli, are increasingly important to assess brain function. Here, we investigate the changes in RSN as well as the hemodynamic changes during acute, global hypoxia. Mice were imaged at different levels of oxygen (21, 12, 10 and 8%) over the course of 10 weeks, with hypoxia and normoxia acquisitions interspersed. Simultaneous GCaMP and intrinsic optical imaging allowed tracking of both neuronal and hemodynamic changes. During hypoxic conditions, we found a global increase of both HbO and HbR in the brain. The saturation levels of blood dropped after the

onset of hypoxia, but surprisingly climbed back to levels similar to baseline within the 10-minute hypoxia period. Neuronal activity also showed a peak at the onset of hypoxia, but dropped back to baseline as well. Despite regaining baseline sO2 levels, changes in neuronal RSN were observed. In particular, the connectivity as measured with GCaMP between anterior and posterior parts of the brain decreased. In contrast, when looking at these same connections with HbO measurements, an increase in connectivity in anterior-posterior brain areas was observed suggesting a potential neurovascular decoupling.

4.4 Introduction

A lack of oxygen in tissue (hypoxia) can occur in different ways, such as lack of atmospheric oxygen, inability of blood cells to bind oxygen, or a stroke. Research into the effects of hypoxia has received increased attention[262] since 2020, after discovery that COVID-19 can cause severe respiratory syndrome[263], and thus might have exposed millions of people to hypoxic episodes.

The brain response to hypoxia differs depending on the oxygen level, whether it is acute or chronic, continuous or intermittent, and as a function of age[264]. Hypoxia in the brain has a negative impact on perception, cognition and motor performance[265-267]. In cases of acute hypoxia, these changes have been shown to precede histopathological changes[264].

At the physiological level, hypoxia influences brain hemodynamics in several ways. Studies have shown an increase of cerebral blood flow (CBF)[268-275] as well as respiration rate[273, 276], depending on the severity of hypoxia. However, these adaptations were insufficient to counteract the decline in systemic oxygen saturation levels[267, 269, 270, 277-279] and cognition[265, 266, 280, 281] during hypoxic periods.

At the cellular level, changes in neuronal activity with both depolarization[282] and hyperpolarization[283] have been previously reported. However, the neuronal changes are spatially heterogeneous, showing differences not only per area, but also per neuron within area[264], with areas that are important for respiratory functions being the most spared of the detrimental effects[284]. In general, the neuronal activity tends to decrease in hypoxic conditions. During severe hypoxia (6% oxygen), the EEG signal recorded in mice was largely suppressed, together with the respiration rate[276], which the authors suggest indicates an impairment in consciousness.

Furthermore, measurements using electrically evoked action potentials in vitro show that hypoxia abolishes the evoked action potentials (in extreme hypoxic conditions: 0% oxygen, 95% nitrogen and 5% CO2)[282]. Although it would stand to reason that hypoxia has a solely detrimental effect on neuronal activity given neuron's dependence on oxygen for survival and firing ability, the effect of hypoxia on neuronal signals is far from universal and can have positive effects as well. For example, intermittent hypoxia can be an effective treatment for certain neurological dysfunctions, such as spinal cord injury[285].

Overall, the short-term molecular mechanisms associated with hypoxia are well characterized at the level of individual cells (neurons and astrocytes) but, on their own, they cannot explain the effect observed on cognition at larger scales.

The investigation of brain networks can help characterize brain function at larger scales. In particular, resting state networks (RSN) have been used to investigate activation patterns that the brain exhibits during rest [286]. This approach assumes that neural networks remain active during rest, and that their correlated activity can be used to map the functional connections without the need to perform stimulations or involve the subject in a task.

RSN are thought to be important in cognition and consciousness, and are altered in neurological dysfunctions such as Parkinson's disease[204], Alzheimer's disease[287], schizophrenia[211] and autism[49], among others. RSNs are also altered during long term exposure to hypoxia[105, 273, 288]. Patients with obstructive sleep apnea, associated with mild intermittent hypoxia each night, exhibit changes in RSNs when compared to controls[289, 290], as do people residing at a higher altitude for a longer period of time[105]. Both conditions have been associated with a decrease in cognitive performance[105, 291-293].

Most of the literature addressing the impact of hypoxia on functional connectivity has been performed during long-term exposure to low oxygen levels or high altitude. A recent exception is a study performed on mice using photoacoustic tomography during resting state[294]. This approach relies on neurovascular coupling and observed a decrease of functional connections between homotopic cortical regions during acute exposure to hypoxia. However, to better understand what underlies cognitive function impairment, investigations with more direct measures of brain function are needed. While RSNs investigated with fMRI have been shown to be altered because of hypoxia, these are not direct neuronal measurements. In this work, we aim to investigate changes in neuronal RSNs and hemodynamic signals in the mouse brain as a result of acute, global hypoxia.

With the development of highly sensitive genetically encoded calcium indicators such as GCaMP[247] it is now possible to monitor functional connections using resting state calcium activity[252, 295] in mice with high sensitivity, specificity and precision, while simultaneously imaging the hemodynamic signals with intrinsic optical imaging[254]. We exploited this approach and imaged mice at several hypoxia levels to investigate concomitant changes in large scale brain networks.

4.5 Material and Methods

4.5.1 Animals

All procedures were approved by the Animal Care Committee of the Université de Montréal (Comité de Déontologie en Expérimentation Animale, CDEA) and conformed to the Canadian Council on Animal Care and Use guidelines. Reporting of the experiments is done in line with the ARRIVE (Animal Research: Reporting in Vivo Experiments) guidelines. Eight C57/BL6 mice were used (4/4, male/female). Mice were 3-4 months of age at the first imaging session, and 4.5-6 months at the last. All mice had ad libitum access to food and water. Male and female mice formed two separate groups, with the female group preceding the male by 6 weeks. No previous data was suitable to base statistics for sample size. However, based on results previous research[277, 296, 297] we estimated the needed sample size at 8. The set-up of this study allowed normoxia and hypoxia comparisons within the same animal, and thus no control group was used. In this same line of reasoning, potential confounding factors such as difference in cage location between the groups were not controlled.

4.5.2 Virus injection and window surgery

Mice were injected with AAV.PHPeB.syn.GCaMP6s.WPRE (Canadian Neurophotonics Platform – Viral Vector Core, Québec, Canada) in the tail vein at 8 weeks of age. In contrast to other serotypes, AAV.PHPeB capsides can cross the blood brain barrier and can be injected in the blood to infect neurons[298]. At least 5 days passed between injection and window surgery. To prepare the imaging window, mice were anesthetised with isoflurane (1.5-3%) and body temperature was maintained at 37°C with a rectal probe and a heating pad. Heart rate and oxygen saturation were monitored during the surgery (Small animal physiological monitoring system, Labeo Technologies inc.). The head of the mouse was shaved followed by i.p. injection with an anti-inflammatory drug (Carprofen). A local analgesic (Lidocaine) was injected s.c. on the head and the skin was cleaned thoroughly with alcohol and iodine. The skin on top of the skull was cut away to expose the skull. A glass coverslip was secured over the exposed skull with clear dental cement (C&B Metabond)[299]. Cyanoacrylate (Vetbond) was used to bond the skin to the skull, and a titanium head bar was glued to the top of the head for fixation during imaging. After the surgery, the mice recovered for at least a week before the first habituation session (described below). The surgery was followed by three days of analgesia administration (Carprofen, 0.01 mL per gram).

One imaging window led to imaging artifacts 6 weeks after the start of imaging. The mouse was re-anesthetized, and a new window and head bar were installed with the methods described above. Following this procedure, the mouse followed the same imaging protocol as the other mice, with two weeks of delay.

4.5.3 Mesoscale imaging

Imaging was done with awake mice, since anesthesia can impact hemodynamics and calcium resting state networks[300, 301]. The mice were fixed by their head bar during imaging to avoid movements. To limit stress, mice were habituated to fixation and imaging over a period of a week, starting with 1 minute on the first day and gradually increasing the duration depending on the behaviour of the mouse (grooming/eating behaviour shortly after release), until a period of 40 minutes was reached.

Imaging was performed with a LightTrack OiS200 system (Labeo Technologies inc.) and used a time-interlaced multicolor illumination. The GCaMP reporter was excited with a 475 nm centered blue LED (CREE XPEBBL-L1) in combination with an excitation filter (Semrock FF02-472/30-25). To capture the activity, a long-pass emission filter (Semrock FF01-496/LP-25) was positioned in front of the camera (sCMOS sensor) just after the imaging objective (50 mm F#1.2, Nikkor), which collected images at a framerate of 80 Hz. This yielded a final frame rate of 20 Hz per color.

The collected images were 192x192 pixels over a 10x10 mm area of the brain, with an exposure time of 8.5 ms.

To disentangle the hemodynamic response from the calcium response, red, green and amber LEDs (OSRAM LZ4-20MA00, 535 nm, 590 nm, 620 nm respectively) were used to gather maps of absorption which were used to estimate the changes in concentrations of oxy- and deoxyhemoglobin.

To refrain whiskers from hovering above the brain and casting a shadow, we designed and 3D-printed a small cap that could be placed on the head and had an opening through which the skull could be seen and imaged. This hat also reduced the visual stimulation that the mouse received.

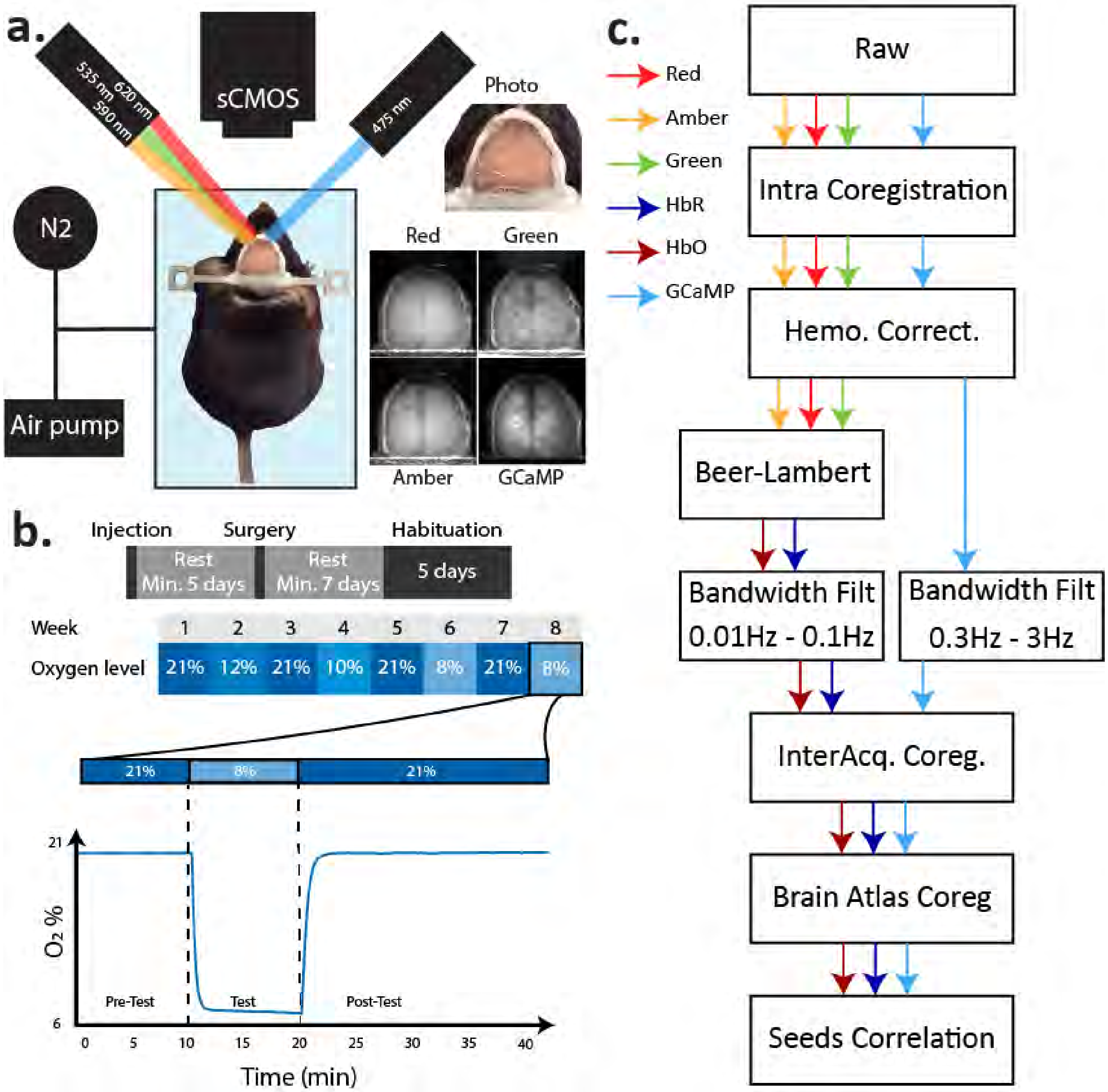

Figure 4.1: Methods of simultaneous IOI and GCaMP imaging during hypoxia.

a. Overview of the imaging set-up. The mouse is fixed by its head bar inside a container where the influx of oxygen is monitored. To excite the GCaMP molecules, blue light was used, while red, green and amber lights were used for hemodynamics calculations. b. Overview of the hypoxia protocol. Upper panel: Mice were injected with a GCaMP virus, and after a minimum of 5 days rest underwent window surgery. After a week of rest, mice were habituated to the fixation and were subsequently imaged once a week, with intermittent hypoxia and normoxia conditions. Lower panel: example of oxygen concentration for an experiment of the impact of 8% hypoxia. Oxygen levels dropped quickly after onset of nitrogen influx. c. Analysis pipeline of the imaging data.

4.5.4 Hypoxia protocol

The mouse was placed in a transparent, airtight box (19 cm x 26 cm x 7 cm) for which influxes of air and nitrogen were controlled (Figure 4.1a). During normoxia, atmospheric air was pumped into the box (1L/min). To decrease oxygen levels, the influx of nitrogen into the box was initiated and increased until the desired oxygen level was reached. Inflow was active and achieved with a pump, outflow was passive through a small tube. Oxygen levels were calibrated before the start of each acquisition with the help of an oxygen sensor (LuminOx O2 Sensor – Lox-O2-S), so that the transition from normoxia to hypoxia during imaging was fast and accurate (Figure 4.1b). Imaging was done through the transparent lid of the box.

Mice were imaged once a week. To monitor any chronic changes in resting state networks over time due to the hypoxia-manipulations, we interlaced sessions of normoxia between the hypoxia acquisitions. Thus, we started the first weekly session with normoxia, then 12% oxygen, normoxia, 10% oxygen, normoxia, 8% oxygen, normoxia, ending with another acquisition at 8% oxygen. Levels of 12, 10 and 8% oxygen correspond to partial pressure of O2 in atmosphere (pO2) at 4000, 5500, and 7000 m, respectively. Acquisitions lasted 40 minutes, starting with 10 minutes normoxia, followed by 10 minutes of the hypoxic condition (where applicable) and ending with 20 minutes normoxia (Figure 4.1b). During acquisitions, the oxygen in the box was monitored with an oxygen sensor (LuminOx Optical Oxygen Sensors connected to an Arduino Uno).

Hypoxia was started and stopped by manually flipping a switch, which could have introduced a small imprecision in timing. To minimize this impact on the quantifications, the transition periods were excluded from the analysis.

Outcome measures of this experiment were the changes in hemodynamics, as defined by an increase or decrease in oxyhemoglobin (HbO), deoxyhemoglobin (HbR), total hemoglobin (HbT) and oxygen saturation levels (sO2), and changes in the neuronal connectivity, as defined by the increase or decrease in correlation in GCaMP activity between seeds during hypoxia compared to during normoxia, as well as over time in normoxia conditions.

4.5.5 Exclusion criteria

A-priori exclusion criteria for this experiment were infection, illness, or death of the animal. Furthermore, animals that failed to express the GCaMP virus (n=1) were excluded from the functional connectivity analysis (n=7). This mouse remained included in the hemodynamic results (n=8).

Several circumstances occurred during the study that resulted in partial exclusion of acquisitions. First, one mouse displayed clear divergent GCaMP signal in the last acquisition (suspected epileptic seizure or similar). Data from this event (at 30 minutes) and after were excluded from the analysis. Second, one acquisition of 12% oxygen showed technical errors, which resulted in cutting the data of that mouse after 35 minutes from the analysis. Third, at the 10% oxygen acquisition for the female batch (n=4), the timing of the hypoxia onset occurred at 18 minutes instead of 10, so the first 8 minutes of the acquisition were discarded, and the last 8 minutes consisted of missing values. Lastly, the timing for returning to normoxia was off for one mouse at the 8% oxygen acquisition, which resulted in discarding the data after 30 minutes. None of these alterations affected the hypoxia period, nor the first normoxia period, and thus all statistics and results are concluded on a n=7 for GCaMP data and n=8 for hemodynamic data. No mice died during this study.

4.5.6 Analysis

Analysis was done with MATLAB R2020b and followed a series of steps (Figure 4.1c). Analysis was not done blindly, and the condition of the oxygen level at the acquisition was known at all times by the authors.

Co-registration. To correct for movement during the acquisition, every frame was co-registered to the first frame of the acquisition using an affine 2D transformation with the mean squared error as the optimisation parameter. Following that, a diffeomorphic transformation was computed to correct for movements or small deformations generated by the non-rigid nature of the mouse brain. With heartbeat and respiration, the vessels of the brain might have small local movements that would be better adjusted for in a non-rigid co-registration than a rigid one.

Hemodynamic correction. The fluorescence signal was corrected for hemodynamic fluctuations using reflectance measurements obtained from the red, green and yellow LEDs, as described in [250]. Shortly, the backscattering light of each one of these LEDs provides information about the variations in oxy- and deoxy- hemoglobin. Since each of the LEDs' absorption spectrum is influenced differently by the two hemoglobin variations, we can use a linear regression of the reflectance signals to remove most of the hemodynamic fluctuations from the fluorescence signal. Doing so, most of the hemodynamic influence on the fluorescence measurement was corrected. The method was initially validated using GFP expressing mice where no fluorescence fluctuations were observed. Valley et al. showed in their recent work that this method works better than using the Beer-Lambert approximation of HbO and HbR. One reason could be that there are no a priori regarding baseline concentrations or pathlength factors in the computation. In order to get quantitative values of HbO and HbR, the Beer-Lambert approximation is still necessary, but in the case of hemodynamic correction it seems that a blind approach is more efficient.

Calculation of hemodynamic signals. The absorption spectra for HbO and HbR vary as a function of wavelength. This causes different reflectance for the red, green and amber lights. The same methods as described in [250] were used, using the modified Beer-Lambert law to approximate the changes in HbO, HbR and HbT, assuming baseline values of HbO and HbR of 60µM and 40µM respectively[302-304]. To evaluate the impact of the different dynamics in HbO and HbR variations on the oxygen availability within the cortex, the cerebral oxygen saturation was calculated (sO2=HbO/HbT).

Normalisation. Normalization was applied on the fluorescence channel to obtain the percent fluorescence fluctuation (ΔF/F) measurements. A band-pass filter of 0.3-3 Hz was used to obtain the signal of interest. The baseline fluorescence signal was obtained from a low pass filter at 0.3 Hz.

Co-registration between days. The Allen Mouse Common Coordinate Framework atlas[305] was fitted on the first acquisition of each mouse using the bregma location. To ensure the consistency of the ROI placement, all acquisitions were co-registered to the first acquisition of that mouse, with the same method as described above.

Global signal regression. To underline the spatial changes caused by hypoxia, a global signal regression (GSR) was applied before the production of the seed pixel correlation maps of both the fluorescence and hemodynamic data[222]. Each pixel was normalized by the linear fit of the global signal (average of all pixels for every frame) on its own temporal dimension. Maps without GSR can be found in Appendix A.2. All quantitative and statistical analysis were done on data without GSR.

Regions of interest. Regions of interest (ROI) were identified with the Allen atlas[305]. For each mouse, an activity map was generated by summing the $\Delta F/F$ signal over the whole acquisition. The difference in baseline levels of activity of functional areas made it possible to position the atlas on the activity map. Regions of the atlas were pooled into right (R) and left (L) versions of Motor (Mot), Retrosplenial (Ret), Visual (Vis) and Somatosensory (Sen) regions (overview in Figure 4.6c). For seed analyses, the pixel at the centroid of the region was taken and expanded with a 3-pixel radius disk. The time course of the average of these pixels was calculated and compared to other regions.

Statistics. For all statistical tests, $p<0.05$ was deemed significant. If a correction for multiple testing was done (Benjamini-Hochberg False Discovery Rate - FDR[306]), corrected p-values are referred to as q-values, and similarly deemed significant if $q<0.05$.

Hemodynamics. Values of HbO and HbR that differed from the mean with more than 3 standard deviations were considered outliers and excluded from the analysis. Mean HbO, HbR, HbT and sO_2 values were calculated over the whole brain, with exclusion of the middle cerebral sinus and the edges of the brain.

For calculating dips/peaks in the dynamics of the hemodynamic data, the minimum/maximum value was found within a window around the observed dip/peak in the data, and the average and standard error of the mean (SEM) were calculated from that. The values were then compared to a normoxia period with the same time-window.

For the plateaus, the averages of minute 14.5 to minute 19.5 were calculated and compared to minutes 4.5 to 9.5 of the same acquisition. Since differences were not normally distributed (Kolmogorov-Smirnov test), a Wilcoxon-signed rank test was applied. To decrease the false discovery rate (FDR) due to the many statistical tests, a Benjamini-Hochberg FDR was applied[306].

Correlation of the seeds. Both the GCaMP and HbO time courses of the ROI were extracted from the data. To evaluate the direct change that hypoxia causes, the correlation values of each unique seed pair before and during hypoxia were transformed with the Fisher z-transformation and then subtracted from one another. For the correlation matrices, the differences in correlation values were tested for normality with a Kolmogorov-Smirnov test, and were deemed not normally distributed, so a Wilcoxon signed rank test was chosen. Again, a Benjamini-Hochberg FDR was applied.

To compare the changes in connectivity within or between macroclusters, a Fisher z-transformation was performed, and the average change in correlation of seedpairs within the same macrocluster was calculated per mouse. The same was done for seedpairs between macroclusters. After verifying normal distribution and homogeneity of variance, t-tests were done for each hypoxia level. A Benjamini-Hochberg FDR was applied.

GCaMP normoxia levels. To see long-term changes over weeks, minute 2.5 to 7.5 (normoxia) of each acquisition was compared. A Friedman test was done for each unique seed pair. The seed pairs were corrected for multiple testing with a Benjamini-Hochberg FDR. If the Friedman test resulted in significant values, a Kruskal-Wallis test was done for each week compared to week 1.

4.6 Results

4.6.1 Hemodynamic response to hypoxia

Deoxygenated hemoglobin levels. Within a minute after the start of the hypoxia period, HbR rapidly increased, and ΔHbR reached a plateau with a mean of 10.9±0.5, 13.4±0.4, 21.2±0.7 and 21.6±0.52 µM (mean±SEM) for 12%, 10%, 8% and 8% oxygen, respectively (-0.7±0.5, -1.0±0.5, 0.3±0.4 and -0.1±0.4 for normoxia conditions, Figure 4.2a). All plateaus were significantly higher than baseline (q=0.016 for all hypoxia conditions, q=0.13, 0.44, 0.74 and 0.42 for the subsequent normoxia acquisitions, n=8, Wilcoxon signed rank test, FDR corrected). Upon return to normoxia, we observed an undershoot which was more pronounced in acquisitions with lower oxygen levels.

Oxygenated hemoglobin levels. HbO shows a slower change in concentrations as a response to hypoxia compared to HbR (Figure 4.2a). At the start of hypoxia, ΔHbO levels dipped briefly before increasing and reaching a plateau. Whereas ΔHbR plateaus were generally reached within a minute after hypoxia onset, plateaus for ΔHbO were reached later, and more severe levels of hypoxia delayed the response. At 12% oxygen, ΔHbO levels reached a plateau around 4 minutes after the start of hypoxia (7.8±1.1 µM), while for 10% oxygen this was after approximately 6 minutes (20.0±0.8 µM). ΔHbO levels in 8% oxygen did not reach a plateau within the hypoxic duration of 10 minutes, but the averages over 14.5 to 19.5 minutes were 28.0±1.9 and 30.2±2.6 µM, respectively (-0.2±1.2, -0.9±0.8, -2.8±0.7, and -0.8±0.7 for normoxia acquisitions). All plateaus differed significantly from baseline (q=0.016 for all hypoxia conditions, q=1, 1, 0.24 and 0.73 for the subsequent normoxia acquisitions, n=8, Wilcoxon signed rank test, FDR corrected).

Upon return to normoxia, ΔHbO showed a quick overshoot which intensified with lower levels of oxygen, with maxima of 14.3±2.4, 29.0±6.4, 51.8±13.8 and 62.1±6.9 µM for 12%, 10%, 8% and 8% respectively, calculated by averaging the maximum value of each mouse between 20 and 21 minutes. The maxima for normoxia acquisitions were 5.1±5.4, 3.5±3.5, 5.0±2.8 and 3.9±6.2.

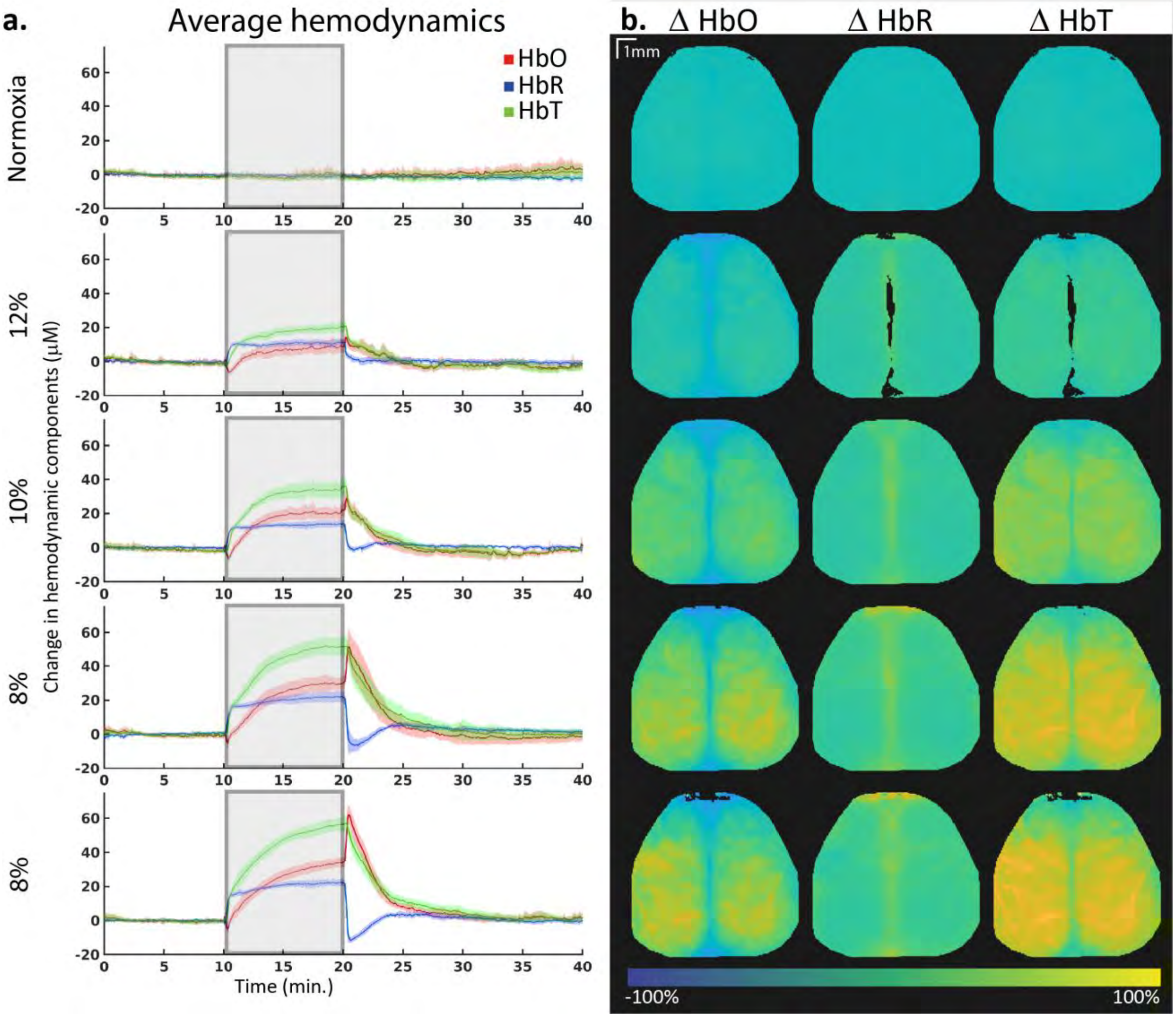

Figure 4.2: Hemodynamic changes during hypoxia.

a. Average changes in HbO, HbR and HbT concentrations over the whole brain. All mice are combined for these graphs (n=8). The solid line indicates the mean, and the shaded regions indicate 95% confidence interval. Hypoxia started 10 minutes into the acquisition and was stopped at 20 minutes, as indicated with the grey area. b. Spatial representation of changes in HbO, HbR and HbT concentrations during normoxia compared to the hypoxia period of the same acquisition (n=1).

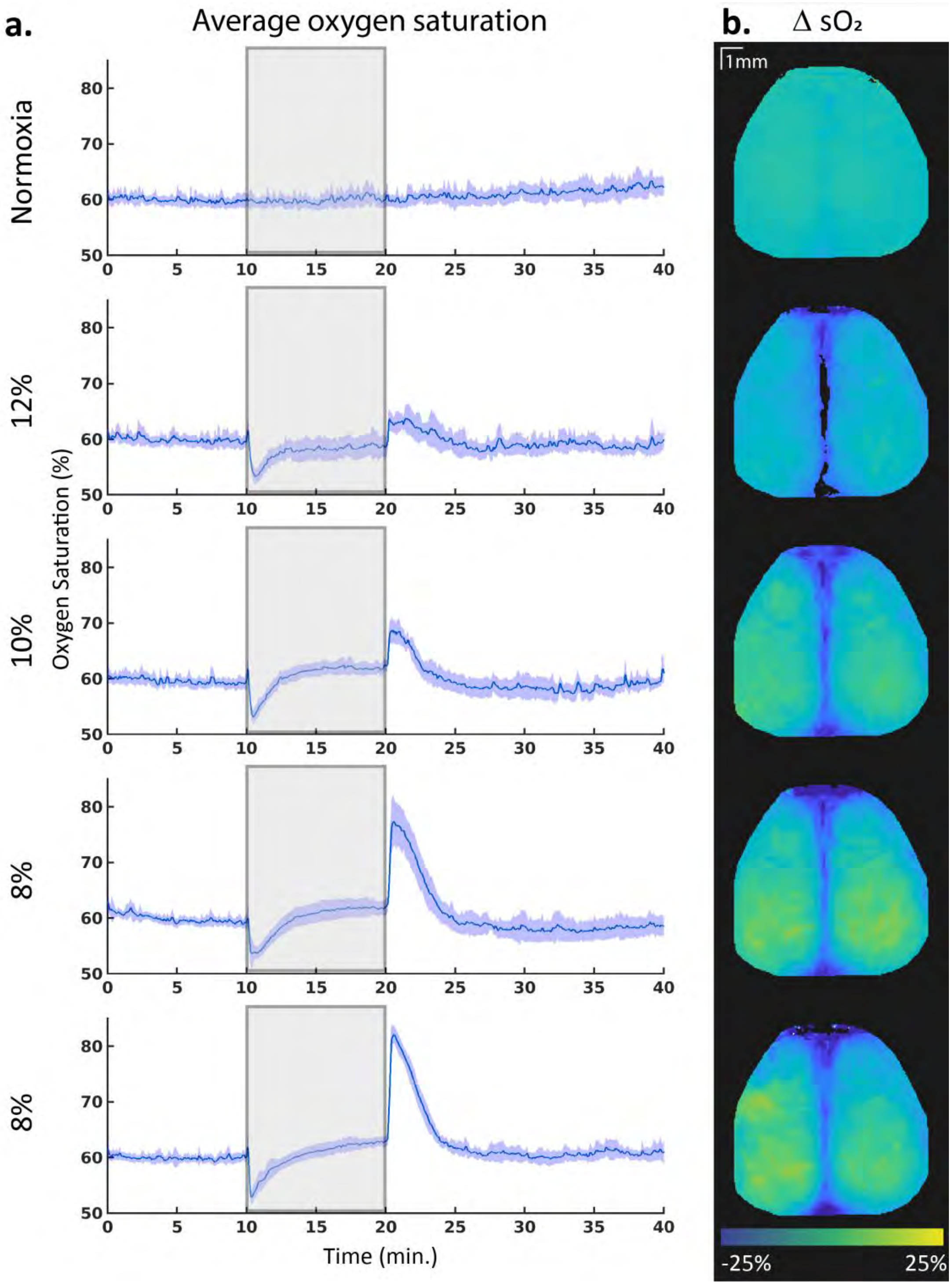

Figure 4.3: Oxygen saturation changes during hypoxia.

a. Average changes in oxygen saturation over the whole brain. All mice are combined for these graphs (n=8). The solid line indicates the mean, and the shaded regions indicate 95% confidence interval. Hypoxia started 10 minutes into the acquisition and was stopped at 20 minutes, as indicated with the grey area. b. Spatial representation of changes in oxygen saturation concentrations (sO2) during normoxia compared to the hypoxia period of the same acquisition (n=1).

Spatial distribution. The increase in HbO and HbR was not localized to a single brain region, but rather showed a similar pattern throughout the brain (Figure 4.2b). HbO was slightly more augmented in the tissue regions, while HbR showed more increase in the middle cerebral vein. This same spatial pattern was visible in the sO2 increase (Figure 4.3b), where the increase was found in tissue and not the middle cerebral vein, with no preference for a specific brain area.

Oxygen saturation. sO2 levels first dropped rapidly, dipping to consistent levels over different hypoxia levels from 60±1.5, 59±0.9, 59±0.4 and 60±0.9% during baseline (59±0.6, 59±0.8, 59±0.5, and 59±0.6 in normoxia conditions) to 54±1.0, 54±1.5, 54±2.3 and 54±1.5% for 12%, 10%, 8% and 8% oxygen, respectively (59.8±1.0, 59.6±1.1, 58..5±0.4 and 59.3±0.6 for normoxia acquisitions). This dip was reached within half a minute after the start of hypoxia and was significant compared to the baseline (q=0.013, for all hypoxia conditions, q=0.63, 0.51, 0.01 and 1 for the subsequent normoxia acquisitions, n=8, Wilcoxon signed rank test, FDR corrected, Figure 4.3a).

After this initial dip, sO2 levels slowly climbed back to baseline, and reached a plateau. Plateaus were reached later at lower levels of oxygen. Surprisingly, this saturation was slightly higher than the baseline for the 10% and 8% hypoxia conditions (plateaus 59±0.6, 62±0.3, 62±0.4 and 62±0.6%, baselines 60±0.6, 59±0.5, 59±0.4 and 60±0.4%). However, this difference was not significant in all hypoxia levels (q=0.33, 0.03, 0.15 and 0.03 for 12%, 10%, 8% and 8% oxygen, respectively, n=8, Wilcoxon signed rank test, FDR corrected), and the normoxia acquisitions showed similar values (baseline: 60±0.5, 60±0.5, 59±0.6 and 60±0,5%, plateau: 60±0.7, 60±0.5, 58±0.5 and 60±0.5%, q=0.64, 0.53, 0.16 and 0.33).

Upon return to normoxia, an overshoot could be observed that was stronger with lower oxygen levels (64±2.7, 69±2.6, 77±6.0 and 82±2.4% for 12%, 10%, 8% and 8% of oxygen, respectively, 63±2.5, 62±3.4, 63±1.7, and 62±2.8 for normoxia acquisitions). Peaks at 10% and 8% oxygen differed significantly from baseline, whereas the peak at 12% did not (q=0.13, 0.02, 0.02 and 0.02 for 12%, 10%, 8% and 8% oxygen, respectively, q=0.74, 0.33, 0.02 and 0.36 for the subsequent normoxia acquisitions, n=8, Wilcoxon signed rank test, FDR corrected).

4.6.2 Neuronal activity

Activation over time. Analysing activation directly is not possible with the normalisation and filtering that is used in the rest of the analysis. The analysis was redone without normalisation in order to depict the activation (Appendix A.1). For consistency, we will focus on the fluctuations in the data that is following the main pipeline.

For each seed, the fluctuations of the fluorescence caused by GCaMP were quantified using the standard deviation (std) within a moving window of 10 frames (500ms, Figure 4.4). Upon the onset of the hypoxia period, we observed a transient decrease in std, followed by a large increase. The transient decrease mimicked the changes seen in HbO at the onset of hypoxia (Figure 4.2). However, unlike the HbO levels, the increased fluctuations of GCaMP fluorescence did not stay consistent over the hypoxia period, but rather dropped after an initial peak. Independent of the level of hypoxia, the greatest increase in std were observed in both the right and left retrosplenial seed (shown in purple, Figure 4.4).

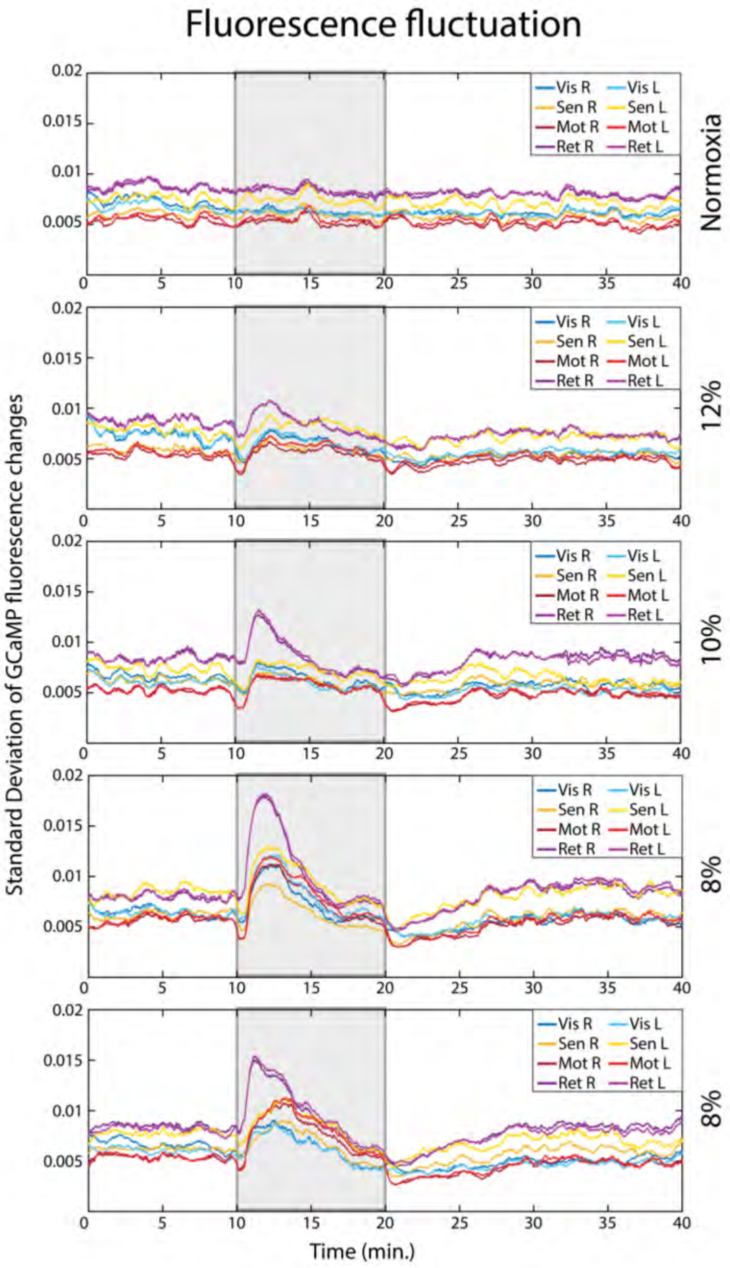

Figure 4.4: GCaMP standard deviation per cortical area.

Standard deviation over time, depicted per seed, averaged over all mice (n=7). The standard deviation was calculated with a window of 10 frames. Grey areas indicate the timing of the hypoxia period.

Seed pixel correlation maps. To explore the impact of hypoxia on the functional connectivity, the cortical fluctuation in centroids of the different ROI were correlated with the fluctuation in every other pixel over the cortex (Figure 4.5a, Appendix A.2 for maps without GSR).

As expected, these results showed strong connectivity between homotopic regions, particularly between the two visual, motor and retrosplenial cortices. At the intrahemispheric level, a strong reciprocal connection existing between the motor and somatosensory cortex was also observed. Finally, weak and even negative connections could be observed between the anterior (including motor and somatosensory cortex) and posterior (including visual and retrosplenial cortex) regions, both inter- and intrahemispherically, supporting the idea that these groups of regions are part of two independent functional clusters (hereafter referred to as macroclusters). This is also supported by the strong similarity of the correlation maps of motor and somatosensory seeds on the one hand, and visual and retrosplenial seeds on the other hand.

When comparing the seed pixel correlation maps based on GCaMP signals to the ones based on HbO fluctuations (Figure 4.5b), the resemblance was clear. The connections within anterior and posterior structures were present in both imaging methods, albeit less clearly in the hemodynamic maps. These similarities were expected since neurovascular coupling dictates that an increase in neuronal activation is accompanied by a local increase in HbO.

a. Seed pixel correlation maps - GCaMP with GSR

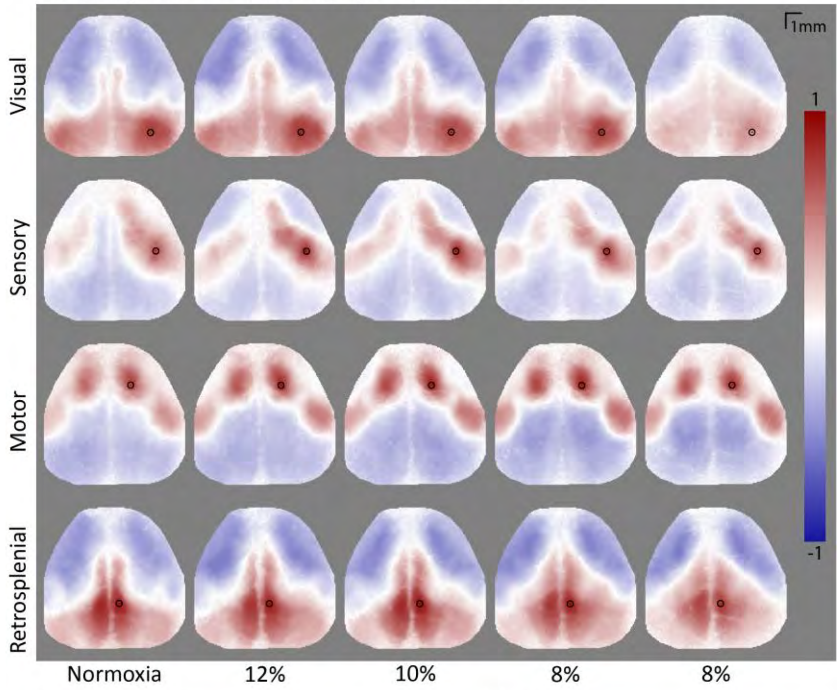

b. Seed pixel correlation maps - HbO with GSR

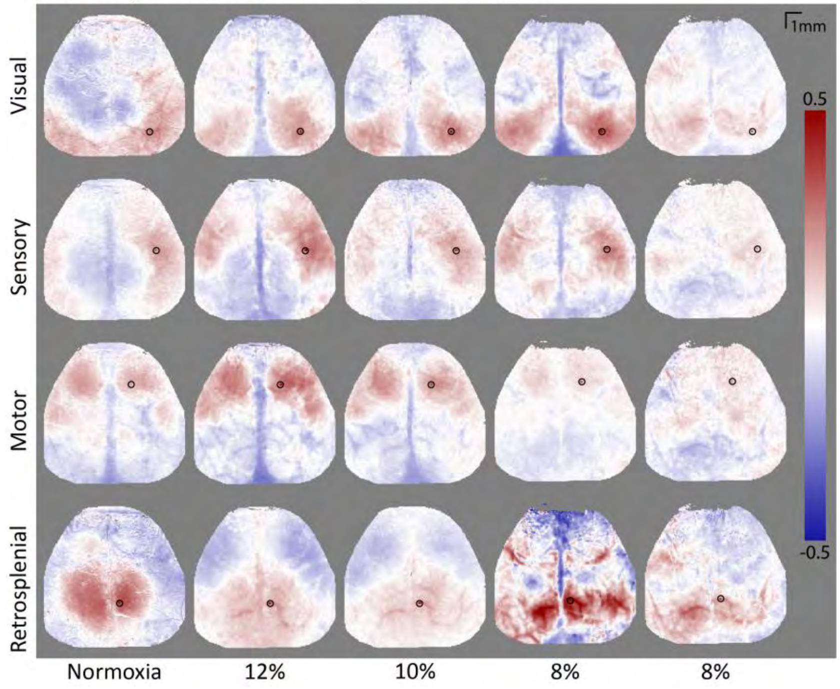

Figure 4.5: Seed pixel correlation maps over different hypoxia levels.

Seed pixel correlation maps (SPCM) over minute 12.5 to 17.5 of the first normoxia, and all hypoxia periods (n=1). A global signal regression (GSR) was applied (see Appendix A.2 for maps without GSR). The black circle indicates the chosen seed; the centroid of the region of interest. Red indicates positive correlation of the seeds timecourse to the corresponding pixel, blue indicates negative correlation. a. SPCM of fluorescence caused by GCaMP, indicating neuronal activation. b. SPCM of HbO concentrations, measured with intrinsic optical imaging.

a. GCaMP correlation during hypoxic period

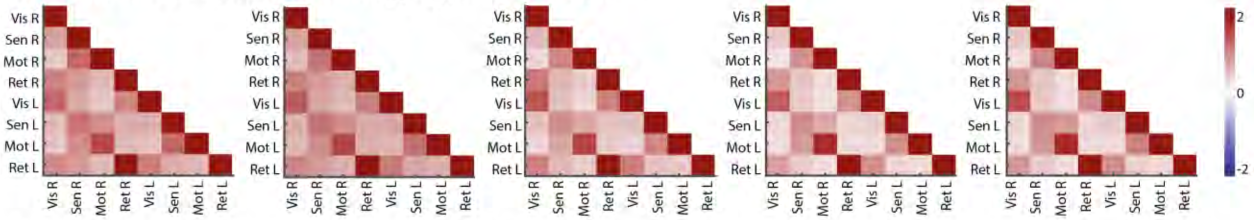

b. GCaMP difference in correlation: hypoxic period - normoxic period

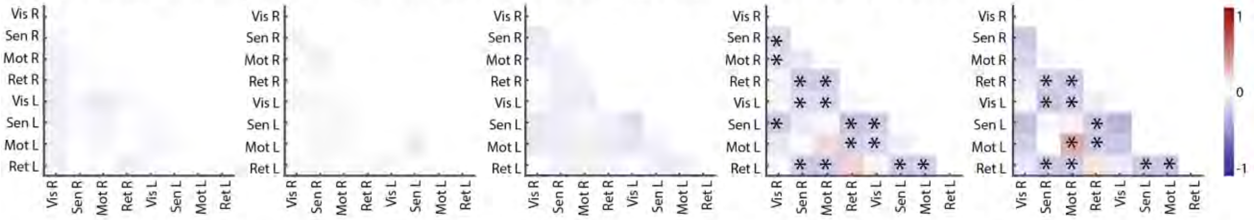

c. Overview

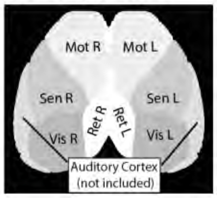

d. GCaMP difference in correlation: hypoxic period - normoxic period

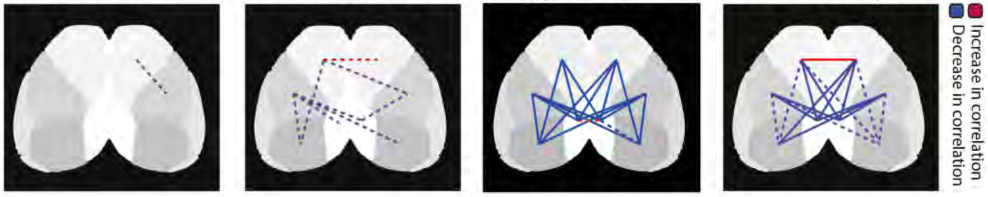

e. HbO correlation during hypoxic period

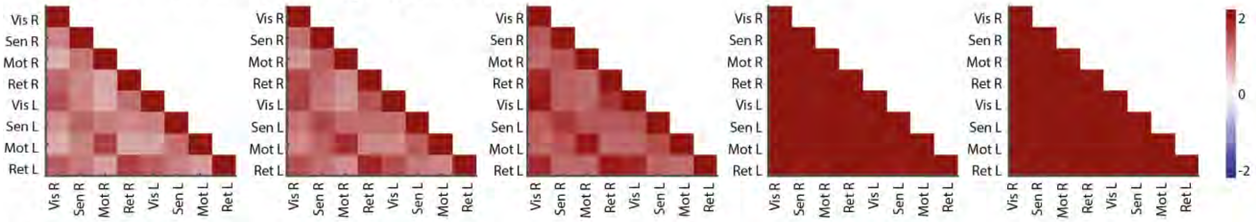

f. HbO difference in correlation: hypoxic period - normoxic period

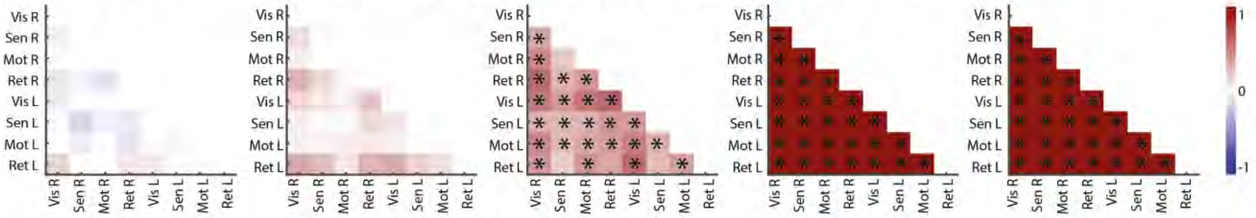

g. HbO difference in correlation: hypoxic period - normoxic period

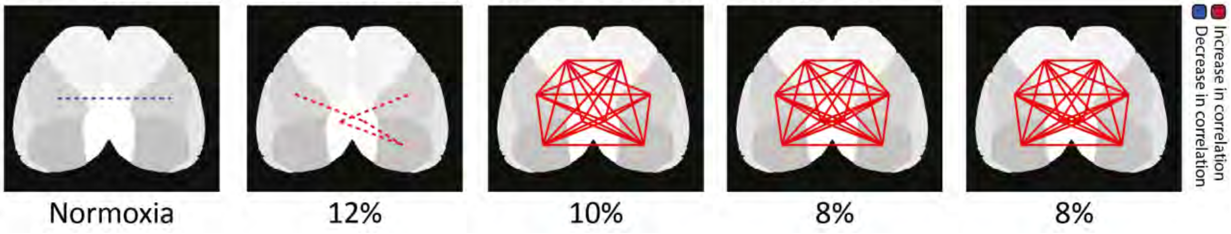

Figure 4.6: Connectivity between brain areas over different levels of hypoxia.

Correlation during hypoxia, and changes in correlation over different hypoxia levels, from normoxia (left column) to 8% oxygen (right column). a. Correlation matrices depicting the correlation of the seeds in z-score, based on the amount of fluorescence caused by GCaMP during the hypoxia period (minute 12.5 to 17.5) (n=7). b. Differences in fluorescence correlation of the seeds in z-score during hypoxia compared to the normoxia (minute 2.5 to 7.5) period of the same acquisition (n=7). Asterisks indicate $q<0.05$. c. Overview map indicating the regions used for this analysis. d. The difference in correlation of the seeds depicted in B shown on the regions of interest. Changes of the first normoxia acquisition are not shown. Dotted lines indicate $p<0.05$ before false discovery rate (FDR) adjustment, filled lines indicate $q<0.05$ after FDR adjustment. Colours indicate an increase (red) or decrease (blue) in connectivity during hypoxia compared to the normoxia period before. e. Correlation matrices depicting the correlation of the seeds in z-score based on the amount of HbO during the hypoxia period (n=8). f. Differences in HbO correlation of the seeds in z-score during hypoxia compared to the normoxia period of the same acquisition (n=8). Asterisks indicate $q<0.05$. g. The difference in correlation of the seeds depicted in F shown on the regions of interest. Dotted lines indicate $p<0.05$ before FDR adjustment, filled lines indicate $q<0.05$ after FDR adjustment. Colours indicate an increase (red) or decrease (blue) in connectivity during hypoxia compared to the normoxia period before.

Changes in connectivity during hypoxia. The correlation between the seeds was generally high in normoxic conditions, both when measured with GCaMP (Figure 4.6a) as with HbO (Figure 4.6e). As the oxygen levels dropped, we see a general decrease in connectivity based on GCaMP fluorescence (Figure 4.6a), whereas the connectivity based on HbO signal increased in all seeds (Figure 4.6e). This is seen more clearly when subtracting the correlation during normoxia from the correlation during hypoxia, within the same acquisition (Figure 4.6b and f). Both 8% oxygen acquisitions showed a significant increase in HbO correlation for all seed pairs (all q-values were 0.0078, Figure 4.6f and g). However, this increase is most likely due to a general increase in blood flow (as shown in Figure 4.2), and thus does not inform us about the relationships between the seeds to the same extent as the GCaMP data.

Using the GCaMP data, significant differences in correlation values were found in the two 8% oxygen acquisitions, although a similar pattern could be seen emerging at the 10% oxygen acquisition as well (Figure 4.6b and d). Decreases in connectivity were mainly observed between the anterior (motor and somatosensory areas) and posterior (visual and retrosplenial areas) macroclusters, with many interregional seed pairs significantly decreasing their correlation during hypoxia (Figure 4.6b and d, see Appendix A.3 for all p-values of the 8% oxygen acquisitions). Contrarily, correlation between homotopic seed pairs or seed pairs within the same macrocluster (anterior or posterior) stayed relatively stable, and the connectivity between the homotopic motor seeds even significantly increased during the second 8% hypoxia acquisition.

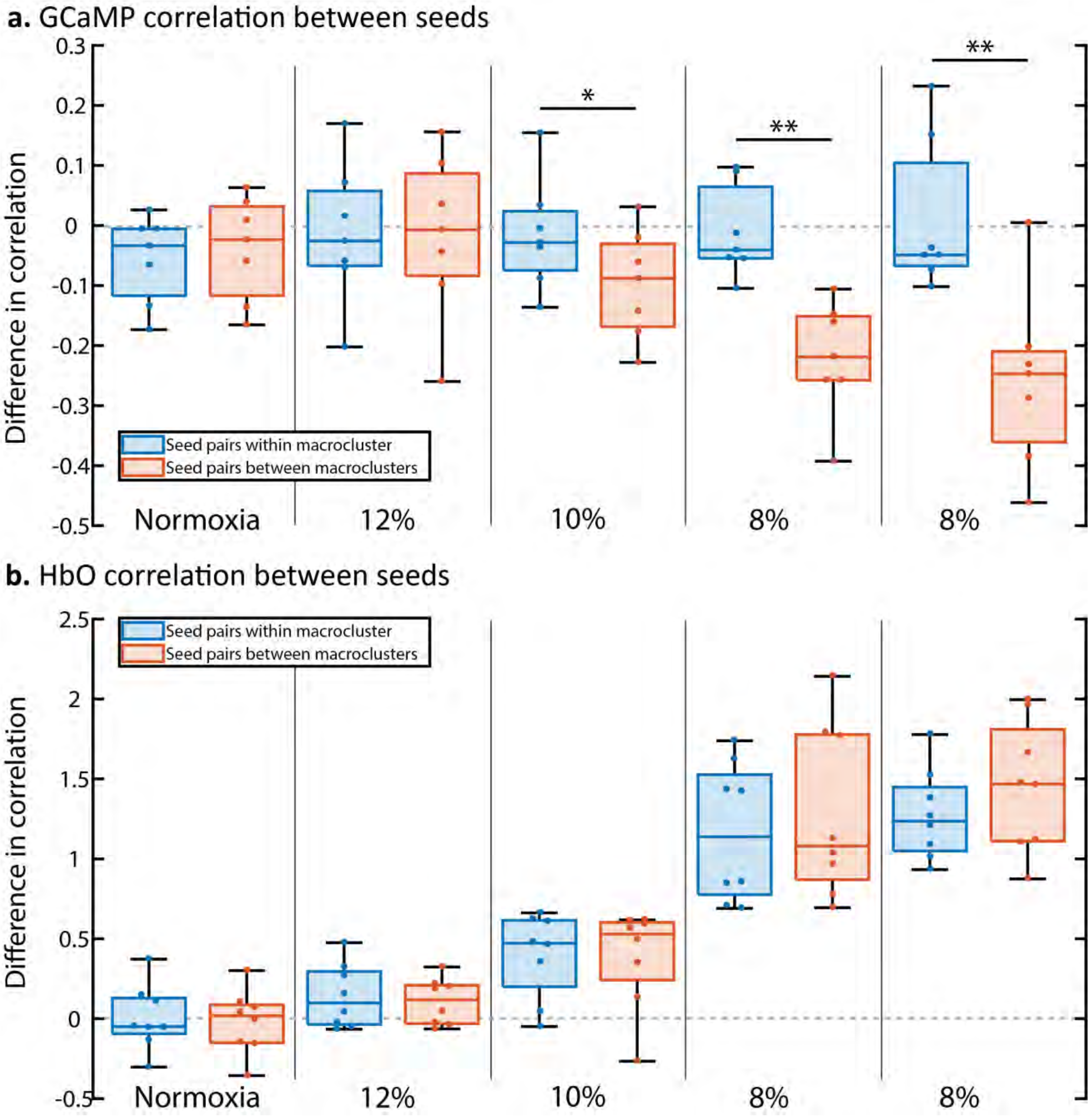

Figure 4.7: Correlations within and between macroclusters.

Differences in correlation of the seeds during hypoxia (minute 12.5 to 17.5) compared to the normoxia (minute 2.5 to 7.5) period of the same acquisition (n=7), divided in seed pairs within the same area (both seeds in anterior, or both seeds in posterior area, orange boxplots) versus changes in seed pairs with seeds coming from different areas (blue boxplots). Each datapoint corresponds to the average change in correlation for all seedpairs falling into the abovementioned groups of one mouse. Edges of the boxes indicate the upper and lower quartiles, the line within the box indicates the median value. Whiskers extend to the furthest datapoints that are not considered as outliers. * indicates a $q < 0.05$, ** indicates $q < 0.01$ (t-test, false discovery rate (FDR) corrected). a. Differences in correlation based on fluorescent (GCaMP) data, indicating neuronal activity. b. Differences in correlation based on HbO concentrations, as measured with intrinsic optical imaging.

Seed pairs within or between areas. We further investigated the specific effect of hypoxia on connectivity between seeds within or between macroclusters (Figure 4.7). The changes of connectivity differed significantly between “within” and “between” groups for the 8% acquisitions for the GCaMP (q = 0.0022 and q = 0.0022) but not the HbO (q = 0.3784 and q = 0.1031) measurements. GCaMP measurements also showed a significant difference for the 10% oxygen acquisition (q = 0.0448), whereas HbO did not (q = 0.7996). The groups did not differ significantly during the 12% oxygen acquisition (GCaMP: q = 0.9090, HbO: q = 0.4639) nor during normoxia (GCaMP q = 0.3510, HbO: q = 0.4639).

In conclusion, the GCaMP data suggests that the functional connectivity within macroclusters was relatively spared by hypoxia. On the other hand, seed pairs connecting different macroclusters showed a decrease in connectivity during hypoxia, with stronger decreases at lower oxygen levels, suggesting a decrease in communication between the anterior and posterior areas. Interestingly, the HbO data shows an opposite trend, with seed pairs connecting macroclusters increasing their correlation more than seed pairs within the same cluster.

Normoxia acquisitions. To control whether repeated exposure to hypoxia could have a longitudinal effect on connectivity states during normoxia, we depicted the connectivity of the first acquisition during baseline from minute 2.5 to minute 7.5 (Figure 4.8a), and calculated the change in correlation of all subsequent acquisitions compared to the first (Figure 4.8b). No significant changes were observed over time, suggesting that repeated exposure of hypoxia did not have a long-term impact on the connectivity in our animals.

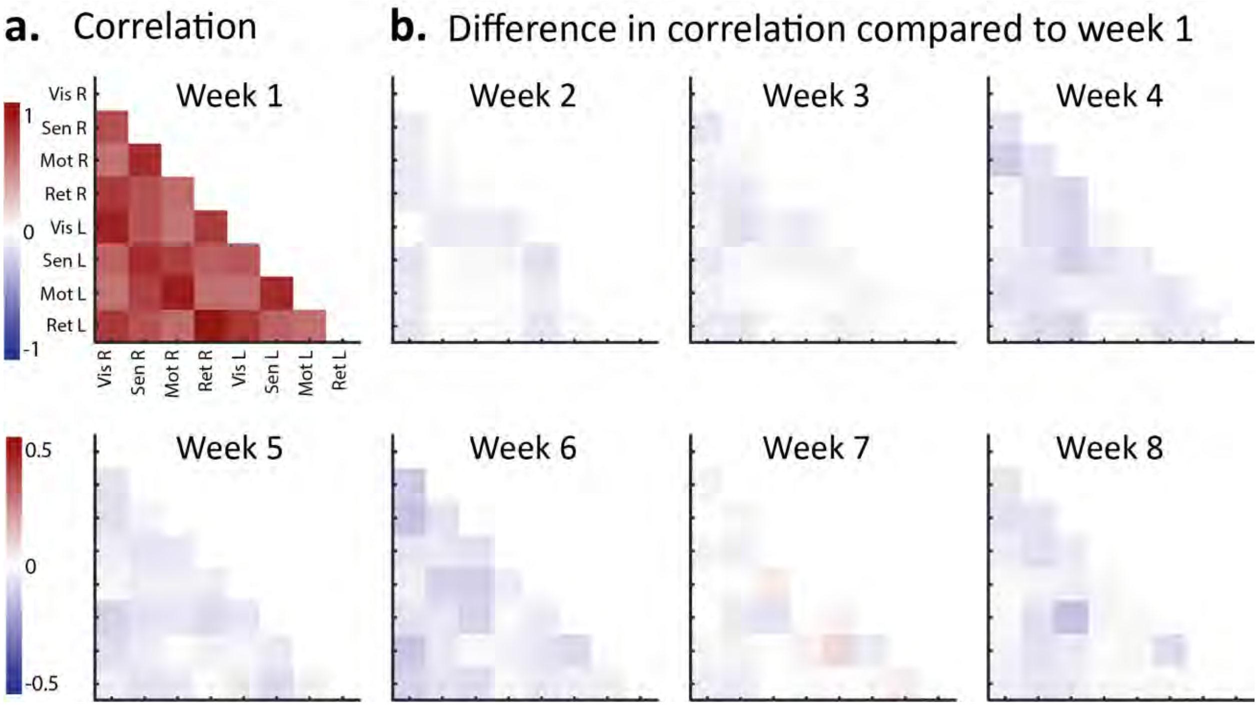

Figure 4.8: Correlation matrices of normoxic acquisitions over time.

Comparisons of normoxia acquisitions. a. Average correlation matrix for minute 2.5 to 7.5 of the first week (normoxia) for all mice (n=7). b. Difference in correlation between the normoxia period of that week (minute 2.5 to 7.5) and the normoxia period of week 1 (n=7).

4.7 Discussion

4.7.1 Hemodynamics

Increase in HbT. Hypoxia led to global brain hemodynamic changes that increased both HbO and HbR. The paradoxical increase in HbO during hypoxia can be explained by a general increase of cerebral blood flow (CBF) and cerebral blood volume (CBV), which both have been found before in hypoxic conditions[268-271, 307] and are thought to be a result of the prioritization of the brain over other organs[264]. For example, in conditions of 10% oxygen, CBF increases were about 15% in humans[270, 272]. Spatially, this increase in CBF was not homogeneous over the brain[272, 273]. However, in the present experiment, we did not observe any difference in hemodynamics between the imaged cortical regions when evaluating the complete hypoxia period (Figure 4.2), which might be explained by our relatively small sample size. Similarly, the study of Julien-Dolbec et al.[307] did not find a difference in CBV increase between brain regions, but rather a global increase during hypoxic periods. Further investigations measuring the spatial cerebral blood flow in parallel such as speckle contrast imaging[302], should help to resolve this discrepancy.

Differences in increases of HbO and HbR. The HbO levels increased by a larger amount compared to HbR. This suggest a similar arterial response as is seen during neuronal activation, since an increase in blood flow will supply oxygenated arterial blood which, despite hypoxia, has higher saturation than what is measured in the capillary bed. Following an initial overshoot, return to the same level of oxygen saturation during hypoxia as during baseline suggests physiological oxygen regulation through a feedback mechanism.

Differences were also observed in the temporal profile of hemodynamic signals. Where the HbR reach their plateau quite quickly, HbO levels increase with a slower pace. The quick increase in HbR is likely due to the brain consuming the same amount of oxygen, while this is no longer being delivered by the arteries to the same extent, since the atmospheric oxygen level is lower. HbO levels increase more slowly, likely because the compensation mechanisms such as a change in respiration rate (depending on oxygen levels, shown in literature but not measured in this study[273, 276]) are set into motion by feedback processes and need time to come into effect.

sO2 levels returning to baseline during hypoxia. The current study shows that the sO2 in the brain reaches the same levels during hypoxia as before the hypoxic episode. However, in the literature, oxygen saturation levels in blood have been found to be lower during mild hypoxic periods[269, 270, 277-279]. In humans exposed to an oxygen level of 10%, the sO2 levels decreased from 98 to 83%[270, 279] even though the oxygen consumption in the brain has been reported to remain the same[269, 271, 274, 275, 308]. However, these studies have mostly measured peripheral oxygen saturation levels[267, 269, 278, 279], whereas our study investigated cerebral sO2. Thus, a more comparable study would be that of Feng et al.[277], who also measured oxygen saturation in the brain, yet also found a decrease in sO2. However, the time scale of their study was different from ours, with a hypoxia exposure of only 3 minutes. Nevertheless, even though the sO2 in our study dips right after the onset of hypoxia, the levels are already climbing back to baseline within 3 minutes of hypoxia exposure, whereas Feng et al. show continuous low levels of oxygen saturation after the induction of 10% oxygen. This difference could be partially explained by the use of isoflurane anesthesia during their recording, which is in contrast to the present results collected in awake mice[309]. Further research into this topic would be needed to understand the different results for this parameter, especially given the relatively small sample size of both the current study and the study of Feng et al. (n=10).

4.7.2 Neuronal activity

Although the hemodynamic results seem to implicate that there are sufficient compensatory mechanisms for oxygen delivery in the brain, we still observed a difference in neuronal connectivity as measured with GCaMP imaging. During the initial decrease of oxygenation at the start of hypoxia, the fluctuations in GCaMP increased, suggesting an increase in neuronal activation (also verified in Appendix A.1). These transient increases of GCaMP fluctuations showed a similar but slower pattern compared to oxygen saturation changes, with std values returning to baseline after about 5 minutes.

An increase in neuronal activation during an episode of decreased oxygenation seems paradoxical. However, this study is not the first to report such results. Chronic hypoxia has been linked to seizures [310]. Intermittent hypoxia has been shown to increase muscle sympathetic nerve activity [311] and motoneuronal output [312], and caused hyperexcitability in pyramidal neurons and interneurons in the hippocampus [313]. Thus, the origin of the transient increases of calcium fluctuations observed in the current study could have been attributed the an increase of cortical excitability during hypoxic episodes.

4.7.3 Connectivity

Connectivity between seeds was quantified with both HbO and GCaMP measures. In normoxic conditions, the correlation matrix of these two measurements were very much alike, as expected [314]. As oxygen levels decreased, the connectivity between all seeds as measured with HbO increased. This is likely because of the increase in general blood volume in the brain. Since all seeds show an elevated HbO level, their correlation increases, with as a result that the correlation between seeds were all very close to 1 in the 8% acquisitions. This high correlation value also means that the increases measured in HbO seedpair correlation might be truncated, with naturally highly correlated seedpairs unable to show the same increase as seedpairs that were correlated to a lesser extent during normoxia.

On the other hand, correlations of seedpairs as measured with GCaMP showed opposite results. Changes consisted of decreases in connectivity, specifically between the anterior (including motor and somatosensory cortex) and posterior cluster (including visual and retrosplenial cortex) macroclusters. Changes were gradual between sessions as O2 decreased, suggesting that they indeed originate from the hypoxic condition. The changes in mild hypoxia of 12% and 10% oxygen were small, but at 8% oxygen we observed strong decreases in functional connectivity between the anterior and the posterior macroclusters. Since homotopic connections between seeds stayed relatively stable, this cannot be considered as a decrease in long range connectivity. Rather, it suggests a reduction in the interaction between modules operating distinct functions such as vision and navigation on the one hand (involving the visual and retrosplenial cortex) and sensorimotor functions on the other hand (involving the somatosensory and motor cortex)[252]. The observed increase of interhemispheric functional connections between the left and right motor seed in the last acquisition further reinforces the idea that the cortex is becoming more modular during hypoxia.

4.8 Conclusion

In this work we investigated the hemodynamic and neural changes in resting networks associated with episodic hypoxia. We observed that despite the presence of physiological compensation to maintain oxygen saturation in the brain, neural resting state networks were modified during hypoxia, bringing about a decrease in connectivity between anterior and posterior brain areas, suggesting that measures of vascular physiology alone are not sufficient to characterize brain function during hypoxia.

4.9 Acknowledgements

We are grateful to the Canadian Institute of Health Research (Grant No. 436352 to F. Lesage and M. Vanni), the Natural Sciences and Engineering Research Council of Canada (Grant No. RGPIN-2018-05056 to M. Vanni), and FRQS programme chercheur boursier J1 (Grant No. 269359 to M. Vanni), as well as the funding of a Canada Research Chair to F. Lesage. We thank Enzo Delamarre for the construction of the oxygen sensor and Marie-Eve Paquet from the Molecular Tools Platform of the CERVO brain research center for providing the AAV virus.

CHAPTER 5 ARTICLE 2: NEUROVASCULAR COUPLING OVER CORTICAL BRAIN AREAS AND RESTING STATE NETWORK CONNECTIVITY WITH AND WITHOUT RIGIDIFIED CAROTID ARTERY

5.1 Preamble

This article was published by Neurophotonics on February 4, 2025. It explores both the neuronal and hemodynamic RSN in resting state in healthy conditions as well as with a rigidified carotid artery. No significant differences were found between healthy mice and mice with a rigidified carotid artery for neurovascular coupling parameters nor in the functional connectivity of the resting state network. However, significant differences were found in NVC over brain areas in healthy mice.

5.2 Authors

Marleen E. Bakker[1,2], Cong Zhang[1,3], Matthieu P. Vanni[2], Frédéric Lesage[1,3]

1. Institute of Biomedical Engineering, École Polytechnique de Montréal, Montréal, Canada
2. École d’Optométrie, Université de Montréal, Montréal, Canada
3. Institut Cardiologie de Montréal, 5000 Rue Bélanger, Montréal, QC H1T 1C8, Canada

5.3 Abstract

Significance: Neurovascular coupling (NVC) is key to research, since hemodynamics can reflect neuronal activation and is often used in studies regarding the resting state network (RSN). However, several circumstances, including diseases that reduce blood vessel elasticity, can diminish NVC. In these cases, hemodynamic proxies might not accurately reflect the neuronal RSN.

Aim: To investigate in resting state if 1. NVC differs over brain regions, 2. NVC remains intact with a mild rigidification of the carotid artery, 3. Hemodynamic-based RSN reflect neuronal-based RSN, and 4. RSN differ with a mildly rigidified artery.

Approach: We rigidified the right common carotid artery of mice (n=15) by applying a CaCl2 soaked cloth to it (NaCl for Sham, n=17). With simultaneous GCaMP and intrinsic optical imaging, we compared neuronal activation to hemodynamic changes over the entire cortex.

Results: NVC parameters did not differ between the CaCl and Sham groups. Likewise, GCaMP and hemodynamic RSN showed similar connections in both groups. However, the parameters of NVC differed over brain regions. Retrosplenial regions had a slower response and a higher HbR peak than sensory and visual regions, and the motor cortex showed less HbO influx than sensory and visual regions.

Conclusions: NVC in resting state differs over brain regions but is not altered by mild rigidification of the carotid artery.

5.4 Introduction

Activations in specific parts of the brain can be evoked with stimuli. However, even in the absence of stimuli, the brain follows a structured pattern of activity, forming a Resting State Network (RSN) [39, 198, 203, 286, 315]. These networks are relatively similar between subjects [38], with high correlation between homotopic brain areas, and a lower correlation between brain regions underlying different functions, for example areas involved in visual and motor processing [39].

Due to the difficulty in directly measuring neuronal activation over the entire human brain, RSN studies in humans have been largely based on hemodynamic proxies of activation, such as measured with BOLD-fMRI. This method is based on the notion that there is an increase in cerebral blood flow, and an influx in oxygenated hemoglobin (HbO) accompanying neuronal activity, referred to as neurovascular coupling (NVC). It has previously been shown that neurovascular coupling might differ between brain areas [316, 317], which could be related to a difference in blood vessel structure [317]. While NVC is usually investigated as the evoked response to a stimulus, it has also been found in resting state, where spontaneous activations of neurons in awake mice were followed by an influx of HbO, with a similar response and timing to evoked neuronal activity [40, 45, 221, 314]. To our knowledge, no study towards NVC differences in resting state over cortical brain structures has been done so far.

In healthy conditions, NVC has been proven to be reliable and consistent across subjects. However, NVC can be weakened or altered in different situations, for example primary brain gliomas [101], diabetes [102, 318], and pontine infarction [319]. Not surprisingly, factors that affect the vasculature of the brain, such as hypertension [152, 320-322] and atherosclerosis [24], a disease that causes thickening and hardening of vessel walls [323], tend to decrease NVC as well. Furthermore, NVC is shown to be decreased in aging individuals, and NVC dysfunction is strongly associated with Alzheimer's disease [22, 24, 26], and dementia [24, 324], as well as cerebral small vessel disease [325], and is often suspected to be a main contributor to these diseases. One of the potential causes for NVC dysfunction is the decreased ability to attenuate the pulse wave velocity that is caused by the heartbeat [17]. In healthy, young subjects, the aorta and carotid arteries are compliant to the pulse pressure associated with each heartbeat (the Windkessel effect), thereby dampening the pulsatile flow before reaching the smaller vessels. As a consequence of the stiffening of the main blood vessels, a larger pulse wave will reach the small vessels in the brain, which has been shown to damage their structural integrity by causing endothelial dysfunction and increased blood brain barrier permeability [15, 17, 194].

Many RSN studies are done with fMRI, and thus rely on NVC to give accurate information about underlying neuronal processes. RSN have been found to be altered in neurovascular diseases such as cerebral small vessel disease [48], concussion [326] and post-concussion syndrome [327], and as a result of carotid endarterectomy [213]. Furthermore, RSN differ in patients with mild cognitive impairment and Alzheimer's disease [46, 51, 52], and this change might even show useful as a biomarker to distinguish between mild cognitive impairment and Alzheimer's [50, 53], or even a predictive factor for Alzheimer's [55]. However, since these measurements have been done with a proxy relying on NVC, it remains uncertain whether the alterations in RSN are due to change in neuronal functional connectivity, or a neurovascular decoupling that causes oxygenated blood flow to misrepresent the neuronal activity.

5.4.1 Aims

The main aim of this study is to investigate the effect of arterial stiffness on NVC and RSN connectivity. We use the mouse model as developed by Sadekova et al. [233], where the carotid artery of the mouse is rigidified. This model isolates the effect of rigidification of the artery from other factors that may combine and confound observations. Exploiting combined calcium and hemodynamic imaging, we investigated the parameters of NVC, such as timing and amount of HbO influx, over different brain regions during rest, and compared these findings with mice with a rigid carotid artery in awake conditions. Furthermore, we investigated the possible changes in RSN as a result of the rigidification of this artery.

5.5 Methods

5.5.1 Surgeries

Animals

A total of 34 C57BL/6J mice were used in this study (16 male, 18 female), obtained from Charles River (Wilmington, MA). After arrival in the animal facility, mice had at least 4 days of rest. Mice had ad libitum access to food and water and were housed under a 12-hour light/dark schedule. All procedures were approved by the Animal Research Ethics Committee of the Montreal Heart Institute and conformed to the regulations of the Canadian Council on Animal Care. A general overview of the procedures underwent by one mouse can be seen in Figure 5.1A. In all mentions of anesthesia, mice were anesthetized with isoflurane (3% induction; 1.5% surgery in pure O2) and the body temperature was controlled at 37°C with the help of an anal probe and a feedback-controlled heating pad. Heartrate, breathing and body temperature were monitored continuously in this period (Small animal physiological monitoring system, Labeo Technologies Inc.).

Calcium Rigidification & GCaMP injection

The procedure followed here was the same as in [233]. A piece of parafilm was immersed in glutaraldehyde for at least 10 hours, after which it was rinsed with sterile saline. The mouse was anesthetized, and an incision of about 1.5 cm was made at midline in the neck to allow for isolation of the right common carotid artery. A sheet of parafilm was inserted below the artery, and a sterile cotton gauze soaked in 0.3M CaCl2 solution (or 0.9% NaCl for Sham) was held to the carotid artery for 20 minutes (Figure 5.1B). After the carotid treatment, the incision was closed with sutures and tissue adhesive (VetBond). Mice were treated with the local anesthetic Bupivacaine (Marcaine, 4 mg/kg SC infiltration at the incision site), the antibiotic Trimetoprim-Sulfa (Tribrissen; 30 mg/kg

SC) and the anti-inflammatory Carprofen (Rimadyl; 5 mg/kg SC) immediately after surgery. Mice recovered for at least 2 days before GCaMP injection, for which mice were shortly anesthetized and injected with AAV2/php.eB-hSyn-GCaMP6s (CERVO molecular platform) in the tail vein with a catheter (50 µL, diluted with 150 µL saline).

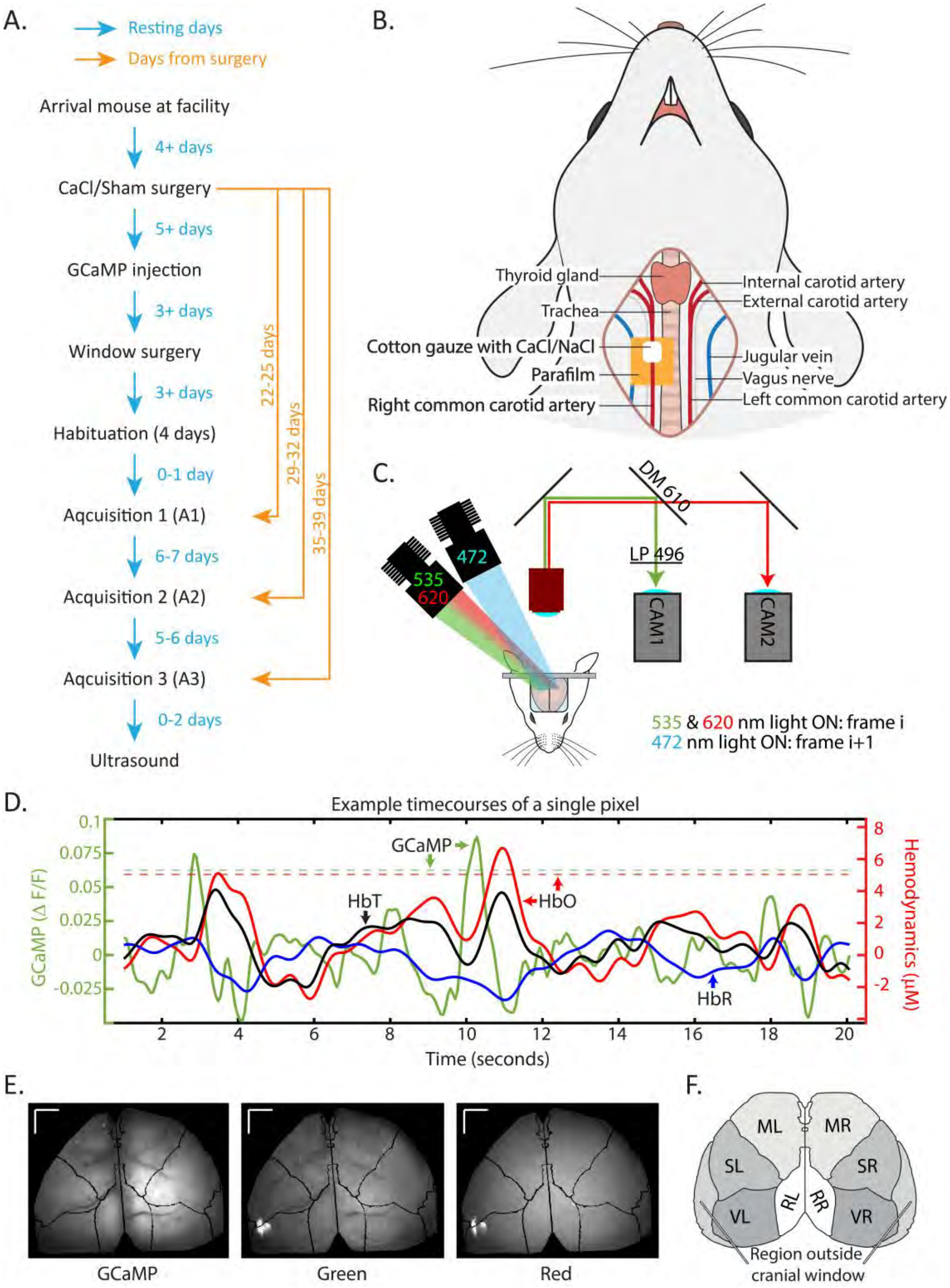

Figure 5.1: Methods of imaging and calcification surgery.

A. Overview of the procedures that the mice were subjected to. B. Schematic overview of the carotid artery calcification surgery. C. Schematic overview of the imaging system. DM = dichroic mirror, LP = long pass filter. D. Timecourses of a single pixel in the Right Sensory area, of a single mouse. The GCaMP timecourse (in green) follows the y-axis on the left, while the hemodynamic timecourses (oxygenated hemoglobin – HbO – in red, deoxygenated hemoglobin – HbR – in blue and total hemoglobin – HbT – in black) are on the right y-axis. The threshold for detecting spontaneous activation (z-score > 1.95) for this pixel is depicted as a green dotted line for GCaMP, and a red dotted line for HbO. E. Average images of the GCaMP, green and red channels of a single acquisition. Black lines show the fitted Allen Atlas. Lines in top left corner depict the scale – 1mm per line. F. Overview of the different regions of interest of the brain. VR = Right Visual Area, SR = Right Sensory Area, MR = Right Motor Area, RR = Right Retrosplenial Area, VL = Left Visual Area, SL = Left Sensory Area, ML = Left Motor Area, RL = Left Retrosplenial Area.

Window Surgery

Mice were anesthetized, ketoprofen (5 mg/kg, SC) was injected subcutaneously, and local analgesia (Lidocaine 0.2 mL of 4mg/mL, SC) was administered on the top of the head. The head was shaved and cleaned with ethanol. The skin on top of the skull was cut away and the tissue covering the skull was cleaned with a cotton swab. Vetbond was applied to the edges of the skin. A titanium headbar was fixed on the head with dental cement (C&B Metabond). The skull was covered with thin layers of cyanoacrylate glue. Carprofen (12.5 mg/kg, SC) was given right after the surgery and Ketoprofen (5 mg/kg, SC) was administered the following day. The mouse rested for at least 3 days after the surgery.

Imaging

Optical imaging was done on awake mice. To limit the stress that the mice could experience during imaging, they were habituated to head fixation and imaging over a period of 4 days, (15 min., 20 min., 30 min., and 45 min. respectively). Following habituation, intrinsic optical imaging (IOI) and GCaMP imaging were done simultaneously, at rest. IOI/GCaMP acquisitions lasted 10 minutes and were performed once per week for 3 weeks. These acquisitions will be referred to as A1, A2 and A3, and occurred on day 22-25, 29-32 and 35-39 after calcium rigidification surgery, respectively.

To excite the genetically encoded reporters, a blue LED (472 nm) combined with a bandpass filter (FF02-472/30) was used to restrain the spectral excitation (Figure 5.1C). For the intrinsic optical imaging (IOI [222]), green (535 nm) and red (620 nm) LEDs were used intermittently with the blue LED. A two camera design was chosen in order to simplify the dissociation of the 3 recorded signals. Camera 1 captures the green reflectance (~535 nm) and the GCaMP emission (~515 nm), while camera 2 captures the red reflectance (~620 nm). To separate the red from the green/GCaMP, a dichroic (610 nm) was used. A long-pass filter (FF01-496/LP) was placed in front of camera 1 to filter out the fluorescence excitation blue light. Two cameras were used (CS2100M, Thorlabs), each with a framerate of 30 Hz. This yielded a final framerate of 15 Hz per color. Images were 512 x 512 pixels. Imaging was done with a LightTrack OiS200 system (Labeo Technologies inc.). Analysis was done with the help of MATLAB (R2020b and R2023a). Code can be found on github.com/marl1bakker/CaCl_P2. The two cameras had a slight offset, which was corrected by an automatic coregistration of the first frame captured by each camera, followed by a manual verification. The system recorded images mirrored, and thus a left-right flip was administered.

5.5.2 GCaMP and Hemodynamics

Movement and Outlier removal

Mice were fixed with their head bar during acquisition and placed on a treadmill which registered locomotion (Appendix B.1). Several recordings were made , and the best session was chosen a posteriori with the help of the registered movements of the treadmill. Furthermore, during analysis, recordings of the movement of the treadmill were used to detect movement, and corresponding frames were marked, as were frames 1 second before and after the movement. These frames were excluded from the analysis. For a session to be included in analysis, the threshold for number of marked moved frames was set at 3000. All mice met this criteria for at least one session in all acquisitions. To detect frames with artefacts or movement that went undetected by the treadmill, an outlier detection was done on the processed data. All pixels over the brain were averaged per frame. Frames that diverted more than three standard deviations of the mean in either GCaMP or hemodynamic data were marked and excluded from analysis. Lastly, an outlier detection of single pixels was done to remove pixels which were marked as an outlier on 1000 frames or more. This helped detect and exclude artefacts in the window, such as bubbles or scratches.

One mouse failed to show GCaMP expression and was thus excluded from all calculations including GCaMP measurements. Since the cranial window was of good quality, and the hemodynamic measurements worked well for this mouse, it remained in the study for calculations that only included hemodynamic measurements. Two other mice showed window artefacts in acquisition 2 and 3 that hindered the imaging of hemodynamic data. Because of this, the hemodynamic measurements for one mouse were excluded from acquisition A2 and A3, and another mouse was only excluded from hemodynamic measurements of A3.

ROI selection and image alignment

Regions of interest were determined by fitting the Allen atlas [305] on top of the mouse brain, based on the location of bregma and lambda. Regions of the atlas were pooled into larger ROIs, resulting in left and right versions of Motor (M), Retrosplenial (R), Sensory (S), Visual (V) and Auditory (A) regions (Figure 5.1E and F). Auditory regions were left out of the analysis, since they often fell outside of the cranial window. To ensure the stability of the regions of interest over the distinct acquisitions over time, the Allen atlas was fitted on the first acquisition, and the second and third acquisition were coregistered to the first. Coregistration was done using an affine 2D transformation where the mean squared error was used as optimization parameter. Image registrations were checked manually. If automatic coregistration was off by more than 3 pixels, the coregistration was done by hand.

Hemodynamic correction

The influx of blood that typically accompanies an increase in neuronal activation can cause a weakened recording of the GCaMP signal by absorbing both light that activates the GCaMP molecule and by absorbing the fluorescence that this molecule emits due to neuronal firing [250]. Having information on hemodynamics allows for a correction for this alteration. Here, we used the same approach as described by Valley [250], in which a linear regression of the reflectance is used to remove the bulk of the interference.

Normalization and filtering

A lowpass filter (cutting frequency at 3Hz) is first applied to remove high frequency noise. To remove slow drifts in the signal, we then normalized it by its own low frequency content (lowpass filter with cutting frequency at 0.08Hz), to get the fluorescence fluctuations (ΔF/F).

Hemodynamic calculations

A lowpass filter of 1 Hz was applied to the green and red channels, after which it was normalized by a lowpass filter at 0.08 Hz to remove any non-functional variations from the signal. The light absorption of oxygenated hemoglobin (HbO) and deoxygenated hemoglobin (HbR) vary as a function of wavelength. The difference in reflectance of the green and red light thus allows us to calculate the changes in HbO and HbR in the same manner as [250], using the modified Beer-Lambert equation. Baseline values of HbO and HbR were set to 60 µM and 40 µM respectively [302-304]. Total hemoglobin levels (HbT) are calculated by adding HbO and HbR values.

Neurovascular coupling

Spontaneous spikes in GCaMP activation, which were not provoked by any type of stimulation, were defined as fluorescence peaks that had a z-score of 1.95 or over (Figure 5.1D). Z-score was calculated as follows:

$$z = \frac{x - \mu}{\sigma} \tag{4.1}$$

Where x is the GCaMP activation of a pixel, µ is the mean GCaMP activation of this pixel, and σ is the standard deviation of this pixel. For each spontaneous spike, the timecourses of HbO, HbR and GCaMP were obtained from 5 seconds before to 10 seconds after the spike. All spontaneous spike timecourses of a single pixel were averaged. These time series were then used to investigate NVC over the whole brain by averaging the timecourses of all pixels over the brain, and changes in NVC between regions of interest by averaging timecourses of all pixels within that region. Spontaneous spikes of HbO were calculated in a similar manner, where a z-score was calculated based on the HbO values on a pixel (x), the mean HbO activation of that pixel (µ) and the standard deviation of that pixel (σ). The threshold for a detected activation was likewise set to a z-score of

1.95 or over. The number of detected activations per brain area can be found in Appendix B.2 A and B.

Ultrasound imaging

Ultrasound imaging (US) was done on a subset of mice (n=7 CaCl, n=6 Sham), using a transducer of 30 MHz. Mice were anesthetized and placed on a heating pad in a supine position. The hair on the neck was removed. Heartrate was measured with ECG. The right carotid artery was located with the help of the B-mode and the color Doppler.

Images were required in M-mode. The diameter of the vessel was calculated as the space between the brightly appearing vessel walls (Appendix B.3A for example frame). Changes in vessel diameter were averaged over several (2-3) heartbeat cycles (green line in Appendix B.3A). The difference between the minimum and maximum diameter over this average curve was then used as measurement. Anesthetized mice were sacrificed at the end of the ultrasound acquisition.

5.5.3 Statistics

Movement

To verify that the CaCl and Sham groups did not differ in the amount of movement during acquisition, we compared the number of frames where movement was detected between the two groups. Since the data was not normally distributed, a Kruskal-Wallis test was performed for each acquisition, none of which showed significance.

NVC in Sham

To compare NVC between brain regions and groups, nine parameters were calculated and compared between regions of interest. First, the peak values of HbO, HbR and GCaMP were compared (black triangles in Figure 5.3B, and top row of Figure 5.3C). Then, increase of HbO and GCaMP were calculated as the difference between the peak and the preceding dip. For HbR, the decrease (difference between the peak and proceeding dip) was calculated (Figure 5.3B, and middle row of Figure 5.3C). Next, the time between the GCaMP peak and HbO peak was calculated, and labeled “Delay” (Figure 5.3B, and bottom left of Figure 5.3C). Lastly, the strength of the neurovascular coupling was calculated by dividing the HbO peak by the GCaMP peak (Figure 5.3C, bottom row, middle column) and by dividing the HbO increase by the GCaMP increase (Figure 5.3C, bottom row, right column).

Statistics was done on each parameter separately. First, an Anderson-darling test was done to determine if the data conformed to a normal distribution. If this was not the case, a non-parametric Friedman test was performed. Otherwise, an ANOVA was performed, and the sphericity of the assumptions were checked. If the sphericity assumption was not met, a Greenhouse-Geisser correction was performed. Because of the high number of statistical tests (especially relevant for statistics on the Correlation Matrices later in this article), there is a large chance of a false positive in the results. To correct for this, a false discovery rate correction (FDR, Benjamini-Hochberg) was performed, providing us with adjusted p-values, hereafter referred to as q-values. Pairwise comparisons (Tukey-Kramer) were calculated on p-values that retained their significance after the FDR (q-values). Appendix B.4 shows which tests were done for which parameter (A), and the p-values per seed pair of the post-hoc testing (B). Appendix B.5A shows NVC curves per mouse, per brain area.

Ultrasound

The assumption of sampling from a normal distribution was checked with an Anderson-Darling test, and homogeneity of variance was tested with a two-sample F test. Since both assumptions were met, CaCl and Sham groups were compared using a two-sample t-test (Appendix B.3B).

NVC with rigidified artery

The same parameters as NVC in Sham were calculated (Appendix B.6). A similar approach for determining correct tests as in NVC Sham was also used. However, the sample sizes between the groups differed (CaCl n = 14, Sham n = 17), and thus a Mack-Skillings [328] test (code from Pingel [329]) was used instead of a Friedman test in non-parametric instances. Which tests were used eventually can be found in Appendix B.7. None of the parameters showed a significant difference between groups, so no post-hoc tests were performed.

Correlation Matrices

The correlation value of all seed pair combinations was calculated (Appendix B.8). The use of global signal regression (GSR) has been a topic of much debate in resting state studies [330]. In this paper, presented correlation matrices and statistics are without the use of GSR, to prevent the accidental removal of signal of interest. However, correlation matrices with GSR can be found in Appendix B.9. A Fisher's z-transform was executed in order to calculate statistics [331]. The data of the correlation matrices was not normally distributed (tested with Kolmogorov-Smirnov test), and therefore a non-parametric Mann Whitney U test was performed for each ROI pair for comparisons between CaCl and Sham groups, and a Friedman test was chosen for tests over the three time points. An FDR was run on all seedpairs. To keep the possibility to see trends in the data, both p-values and q-values of the correlation matrixes can be found in Appendix B.10.

5.6 Results

5.6.1 Neurovascular Coupling in Sham – Spontaneous GCaMP Activation

The relation between neuronal activity and the hemodynamic response was investigated on the basis of the spontaneous neuronal activity using GCaMP signal fluctuation as a proxy. These spontaneous events were detected, and the timecourses of the GCaMP, HbO and HbR data from 5 seconds before to 10 seconds after each event was kept. The fluctuations were averaged over the whole brain (Figure 5.2) and over separate brain areas (Figure 5.3) for the mice in the Sham group (n = 17) during the first acquisition.

As expected, we found neurovascular coupling to be present in resting state, with a typical increase in HbO and decrease in HbR after spontaneous GCaMP activity. As seen in figure 2A (and Appendix B.5A), all mice show similar dynamics. The GCaMP signal tends to decrease before showing a quick peak. After the peak, the GCaMP shows an undershoot. This has been found before in cases without hemodynamic correction [254, 332], and could be caused by the increase in HbO hindering the GCaMP signal [332], but given that we did a correction for that in this study, this possibility is unlikely here. Lastly, the GCaMP signal fluctuates back to baseline. The GCaMP activity tends to stay much more stable around 0 in between activations, with less longer-term fluctuations as can be seen in the hemodynamic measurements. The HbO and HbT timecourses follow a very similar pattern as GCaMP, delayed by about 1 second, whereas the HbR timecourse shows an inverse pattern (Figure 5.2B). Both hemodynamic signals and the GCaMP signals are back around baseline within 5 seconds. To exclude the possibility of the oscillations being caused by a filtering effect on the data, the same analysis was done on unfiltered data, showing very similar results (Appendix B.5B-D).

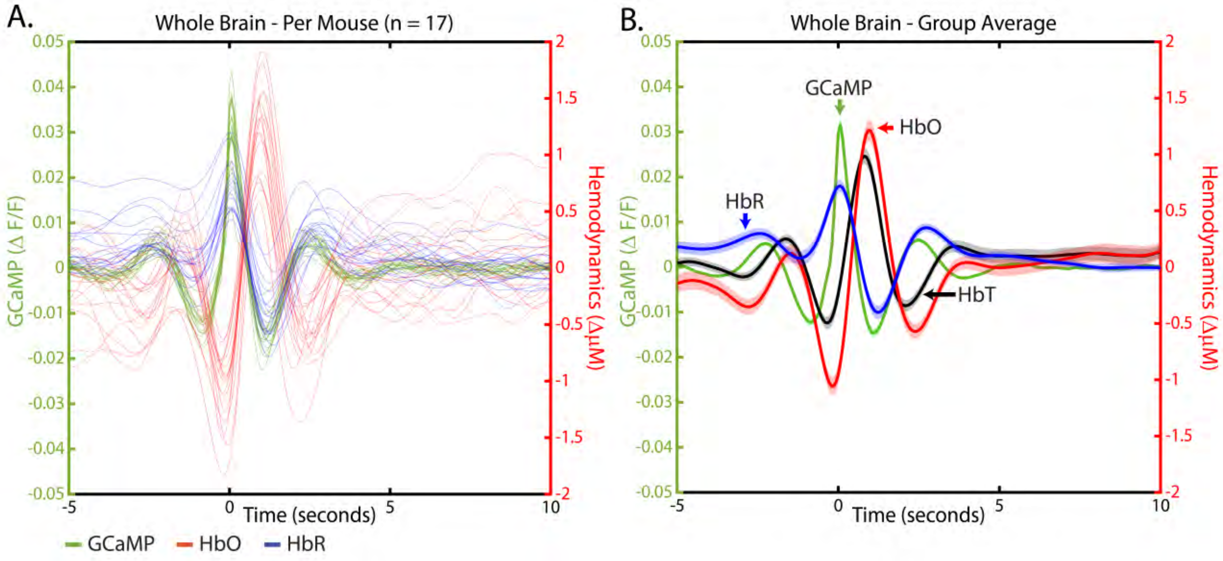

Figure 5.2: NVC in Sham mice over the whole brain.

A. Neurovascular coupling in individual mice. Each line depicts the average GCaMP, HbO and HbR fluctuations 5 seconds before to 10 seconds after a detected spontaneous GCaMP activation. Green line depicts the GCaMP signal and corresponds to the left y-axis. Red lines depict HbO, and blue lines depict HbR, both corresponding to the right y-axis. Individual HbT curves not shown to increase visibility. B. Group average of the mice depicted in A. The dark line shows the group average, the lighter patches around the line show the standard error of the mean (SEM). See Appendix B.5B-D for plots with unfiltered data.

Next, on the same group of Sham mice (n = 17), we investigated whether the NVC differed per brain area (Figure 5.3A). In order to do so, we calculated the average peaks of GCaMP, HbO and HbR per mouse, per brain area (Figure 5.3C). However, as can be seen in Figure 5.2A and Appendix B.5A, the hemodynamic values tend to fluctuate, and might start from a value that differed from 0. In order to focus on the change in hemodynamics in the moment of spontaneous GCaMP activation, without including longer term hemodynamic fluctuations, we also calculated the increase in HbO, measured from the lowest to the highest point, the decrease in HbR, measured from the highest to the lowest point (Figure 5.3B), and the increase of HbO in relation to the increase in GCaMP. Statistical testing showed a significant difference between brain areas for all 9 parameters (Appendix B.4A). Post-hoc tests were conducted, and results can be seen in Figure 5.3C (individual p-values in Appendix B.4B).

First, when looking at the detected spontaneous activation of GCaMP and the increase of GCaMP, we see that in all regions of interest the right version showed a significantly higher peak than its left homotopic counterpart. The left Motor region was significantly lower than all other left GCaMP peaks, and the same was true for the right Motor region compared to the other right regions of interest. This significance disappeared when measured by the amount of increase.

The HbO peak and HbO increase show similar results, although the increase shows more significant differences than the peaks. In general, the sensory and visual areas show an increased HbO influx compared to the motor and retrosplenial areas, where all sensory and visual areas except for the right retrosplenial area differ significantly from all motor and retrosplenial areas when measured by the HbO increase.

The retrosplenial area shows the highest peak in HbR, as well as the largest decrease. In general, although not always significantly different, the same two groups as HbO can be distinguished, with the motor and retrosplenial regions showing a higher peak and larger decrease, and the sensory and visual regions showing a lower peak and smaller decrease. Interestingly, neither HbO nor HbR results seem to show a difference between hemispheres, whereas this difference is very apparent in the GCaMP data.

The delay of the HbO peak compared to the GCaMP peak is longest in the retrosplenial area, and differed significantly from the shorter delays of the sensory and visual areas. The motor region did not differ significantly from any of the other regions.

The strength of the neurovascular coupling shows significant differences between homotopic regions of the sensory and visual areas, both when measured at the peaks and when measured by increases. Furthermore, the homotopic regions of the motor cortex show a significant difference when measured by increase. These differences reflect the differences as found in the GCaMP results.

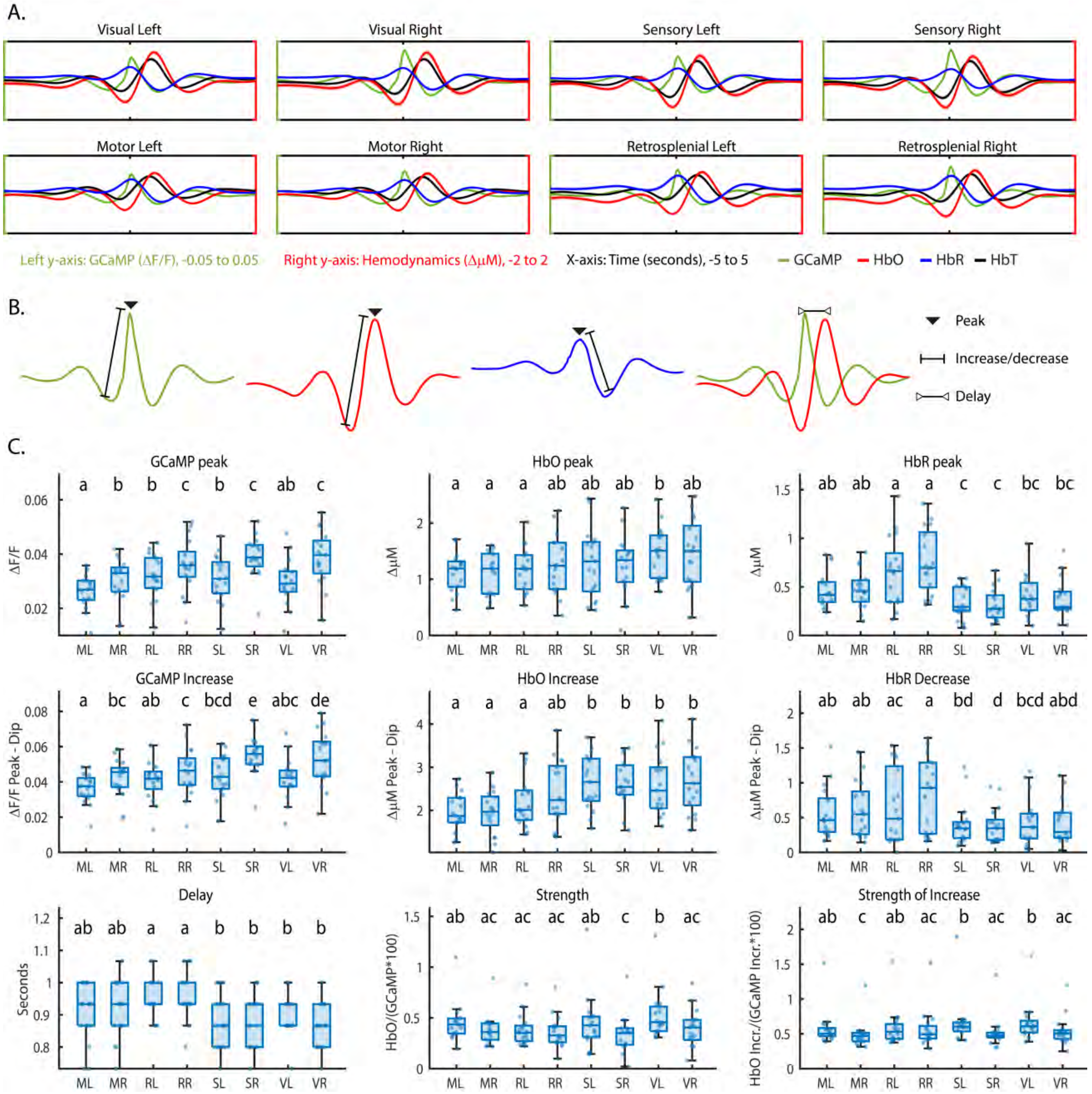

Figure 5.3: NVC in Sham mice per brain area.

A. Average curves for GCaMP (green), HbO (red), HbR (blue) and HbT (black) over different brain regions in the first acquisition of the Sham group. The left (green) y-axis depicts ΔF/F values for GCaMP, ranging from -0.05 to 0.05. The right (red) y-axis shows ΔμM for HbO, HbR and HbT values, ranging from -2 to 2. X-axis shows time, ranging from -5 to 5 seconds, with a notch at 0, where the spontaneous GCaMP activation was detected. B. Visual illustration of how the parameters in C were calculated. C. Parameters related to NVC in different brain areas in the first acquisition of the Sham group. Letters above boxplots indicate significance: if two groups do not carry at least one similar letter, they differ significantly ($p<0.05$, see Appendix B.4).

5.6.2 Neurovascular Coupling in Sham – Spontaneous HbO Activation

While we just showed that the NVC response is present in resting state, and that an activation in GCaMP is generally followed by an increase in HbO, this does not automatically mean that an increase in HbO is always preceded by a GCaMP spike. For this reason, we used the same spontaneous activity detection method on HbO data (Figure 5.4, note: the data in A is the same as in Figure 5.2B, with the axes altered to facilitate a direct comparison to HbO-detected activation).

Comparing the average curves around the detected spontaneous HbO increase, a larger hemodynamic but smaller GCaMP response can be seen. Furthermore, the oscillating effect of HbO has disappeared in favor of an increase of HbO before the GCaMP curve shows a clear divergence from zero. On average, over the whole brain, a detected spontaneous HbO activation was preceded by a GCaMP spike that went over the detection threshold in 50.5% of the cases (Sham: 49.6%, CaCl: 51.5%). On the other hand, detected spontaneous GCaMP activations were followed by a detected HbO activation 10.8% of the time (Sham: 10.6%, CaCl: 11.1%, Appendix B.2C and D). However, this can be partially explained by the difference in the number of detected spontaneous activations; GCaMP crossed the threshold about 10 times more often than HbO (Appendix B.2A and B). To be able to make a fair comparison, the number of "matches" was also calculated on random activation data. This means that for the GCaMP-detected data, the same number of activations per pixel was taken, but the timing of it was determined randomly instead of being based on the data crossing the activation threshold. The number of detected activations of the HbO data was then calculated on this randomly-timed data. A similar calculation was made on the HbO data, with preceding GCaMP activation detection. For these random cases, random GCaMP timepoints were followed by HbO activations 5.1 % of the time (Sham: 5.2%, CaCl: 5.0%), while random HbO timepoints were preceded by GCaMP activations 25.8% (Sham: 25.7%, CaCl: 26.0%, Appendix B.2E and F).

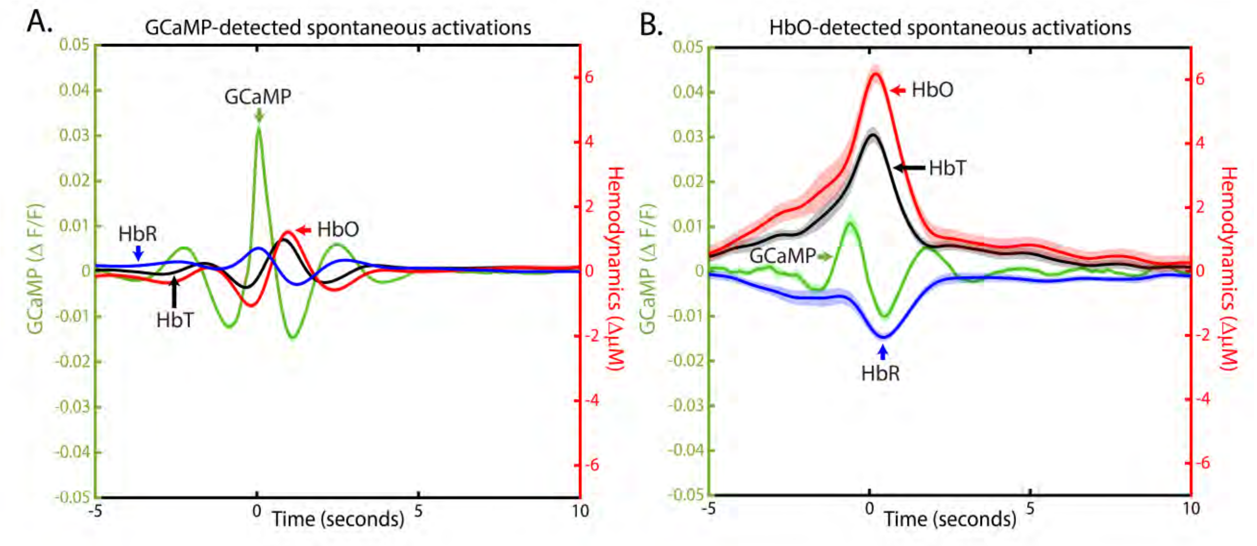

Figure 5.4: NVC in Sham mice detected on GCaMP vs. HbO.

Neurovascular coupling for all Sham mice of Acquisition 1 over the whole brain. Green line depicts the GCaMP signal and corresponds to the left y-axis. Red lines depict HbO, blue lines depict HbR, and black lines depict HbT, all corresponding to the right y-axis. The dark line shows the group average, the lighter patches around the line show the standard error of the mean (SEM). A. Curves of detected spontaneous GCaMP activations, where 0 is the time of detection based on GCaMP data. Note that this data is the same as shown in Figure 2B, with adjusted y-axes to make a direct comparison to B. B. Curves of detected spontaneous HbO activations, where 0 is the time of detection based on HbO data.

5.6.3 Neurovascular Coupling with Rigidified Artery

Ultrasound measurements on the diameter change of the right carotid artery was done on a subset of the mice, and showed significantly less diameter change during the heart pressure pulse for the CaCl group (Appendix B.3, p = 0.04). As with the calculations on NVC in Sham, the spontaneous activations of GCaMP were detected, and the timecourses of GCaMP, HbO and HbR from 5 seconds before to 10 seconds after the events were averaged over a region of interest. Since the calcification surgery was performed on the right carotid, our region of interest is the right hemisphere (Figure 5.5, for other brain regions see Appendix B.6), and the possible differences between the CaCl and Sham groups were investigated. The same parameters as shown in Figure 5.3 were calculated. Statistics show no significant difference between CaCl and Sham groups, and thus no post-hoc analysis was performed (Appendix B.7).

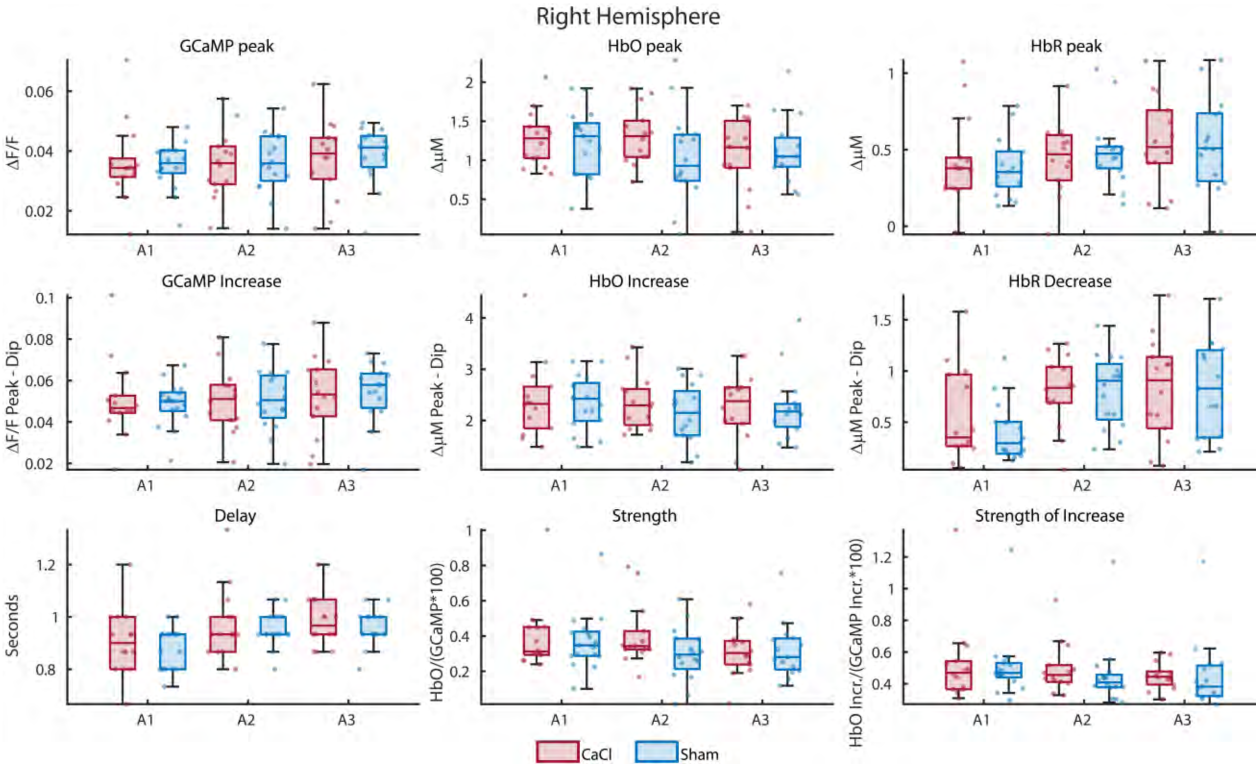

Figure 5.5: NVC parameters in CaCl vs Sham mice.

Parameters related to NVC in CaCl versus Sham treated mice over three acquisitions. Values were taken from the right hemisphere. The same parameters as in Figure 3 were calculated. None of the parameters showed a significant difference between the groups (Appendix B.7). For differences per brain area, see Appendix B.6.

5.6.4 Resting State Networks

To assess the general connectivity of the brain, the timecourses of the signals localized in centroids from the regions of interest (Figure 5.1F) were correlated with each other to produce correlation matrices for GCaMP, HbO and HbR (Figure 5.6A and Appendix B.8 and 9). We observed a similar pattern in the correlation of the GCaMP and hemodynamic data. Homotopic seeds were strongly correlated, with the retrosplenial seeds in particular showing a strong correlation in all modalities, which are not only homotopic but also very close in proximity, and thus relatively “cost-effective” in their wiring [333]. Retrosplenial and visual areas also tend to be strongly correlated to each other, whereas weaker connectivity was found between visual and motor areas. Differences between modalities can also be found. The general connectivity between seeds derived from HbR is much higher than in GCaMP or HbO. Interestingly, where sensory and motor seeds measured with GCaMP showed a strong correlation, this correlation was a lot weaker in the hemodynamic components. Lastly, the correlation matrices were very robust over time, with no significant difference over the three acquisitions (Appendix B.11).

None of the seedpair connections were greatly altered in the CaCl group versus the Sham group (Figure 5.6B). Statistics show no significant differences in any of the ROI pairs between the two groups in any of the three acquisition times and modalities (Appendix B.10 and 11). Even before multiple testing correction (FDR), only two seed pairs of GCaMP data showed a p-value below 0.05 in acquisition 3 (RR-SR: $p = 0.049$ and SL-SR: $p = 0.028$). This significance disappeared after FDR (RR-SR: $q = 0.554$ and SL-SR: $q = 0.554$) and no significance was found in other modalities or acquisition times.

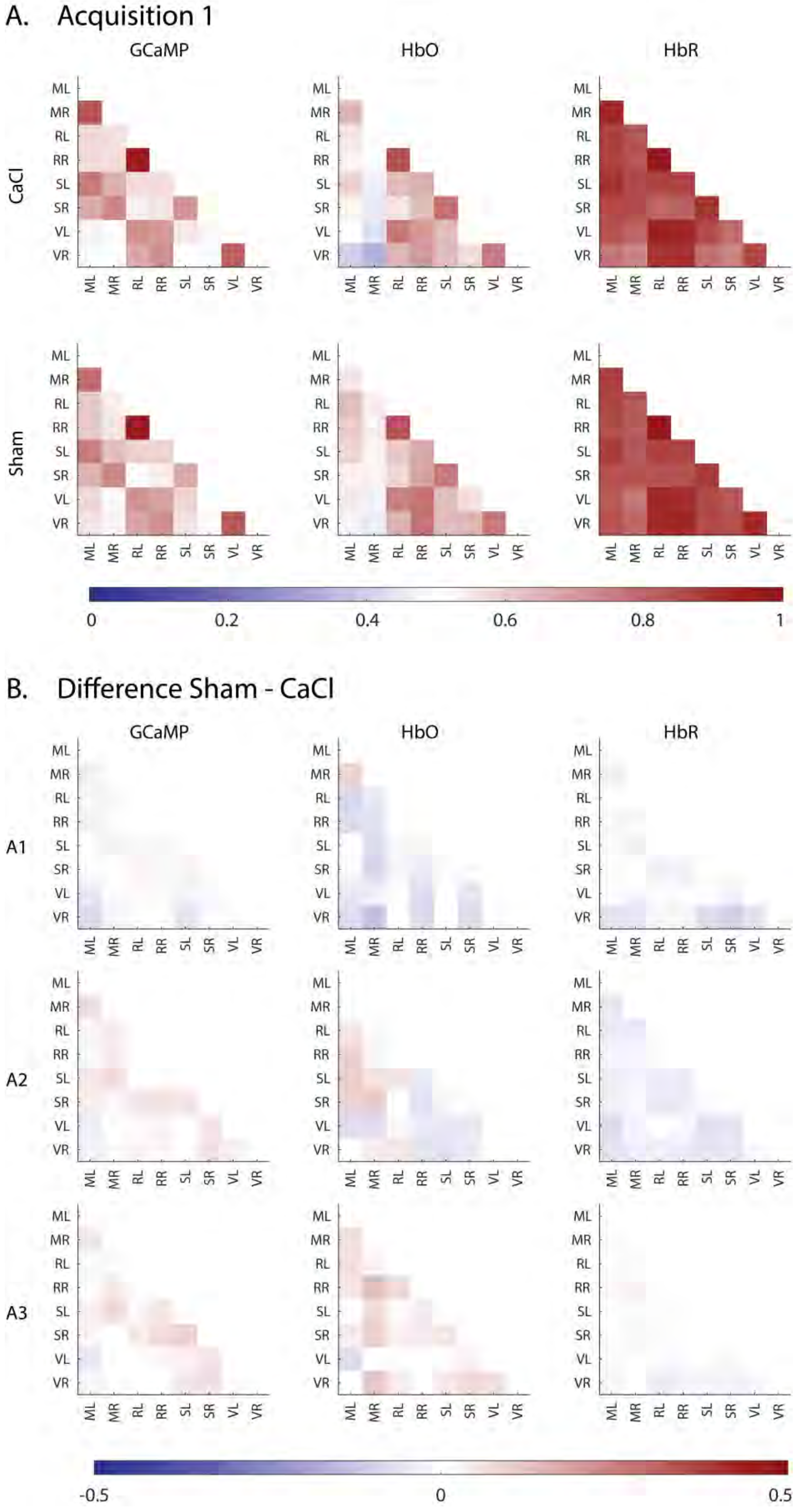

Figure 5.6: Correlation matrices of CaCl vs Sham mice.

A. Average correlation scores between seeds in different brain areas of the CaCl group (top row) and Sham group (bottom row) for GCaMP (left), HbO (middle) and HbR (right) during Acquisition 1 (other Acquisitions can be found in Appendix B.8 and B.9). B. The differences between average correlation scores of the Sham group minus the CaCl group over the three acquisitions (rows). None of the datatypes (GCaMP, HbO and HbR) nor Acquisition times showed a significant difference between Sham and CaCl groups (Appendix B.10 and B.11).

5.7 Discussion

5.7.1 NVC in Resting State in Sham

General NVC Observations

Indications of neurovascular coupling in resting state have been found in previous studies [44, 45, 222, 230, 314] as well as in the current one. Ma et al. [314] showed a clear neurovascular coupling in resting state, and our results coincide very well with theirs, in both curve-shape and timing. Additionally, Bruyns-Haylett et al. [45] found hemodynamic curves as response towards detected spontaneous activations that resembles our results very closely, albeit with a slower response. This difference might be explained by the presence of anesthesia in their study, which can alter the response [254, 334]. We found a delay of roughly 1 second between the HbO and GCaMP peaks, similar to other resting state studies and ultrashort stimuli findings [314, 335, 336]. Studies with stimulations often show a later peak in HbO [89, 337, 338]. This is likely due to the stronger or prolonged neuronal response that is evoked in comparison to resting state, requiring a greater influx of HbO that in turn takes longer to reach.

In the GCaMP-detected spontaneous activation data, we can see oscillations in both GCaMP and hemodynamic data. In general, GCaMP activation fluctuates around a baseline. Because of this, a spontaneous activation in a resting state recording is likely preceded by a dip in activity, and vice versa. Whereas a stimulus can cut into the timecourse and “demand” an activation at any point, the spontaneous activation will rely on the fluctuations around baseline and build upon the natural increase to reach the threshold. When the spontaneous fluctuation frequency of neurons differs by even a small amount, eventually the timecourses will fall out of sync and cancel each other out, which will result in an average that is back at baseline.

This oscillation is not only seen in GCaMP, but in hemodynamic data as well. The dip before the spontaneous neuronal activity is occasionally seen in other works. In our current results, the initial dip is clear, and the results resemble the preliminary results of Bruyns-Haylett very closely [45]. We can clearly distinguish it in Ma et al. [314] as well, although to a lesser extent. In Wright et al. [43] we can spot it in the example of a single timecourse. On the other hand, the undershoot after the HbO influx is much more often observed [44, 45, 230, 314, 334-336, 338]. This dip only seems to occur in detected spontaneous activations [44, 45, 254, 314] and very short and/or weak stimuli [44, 230, 254, 334-336, 338], and disappears if the stimuli get stronger [45, 334, 338].

In the HbO-detected spontaneous activations, the HbO increases several seconds before crossing the threshold. This might be due to slow-wave, background fluctuations of HbO, that have a slower frequency than the response-curve towards GCaMP. The threshold of HbO detection might only be reached if both the slow wave and higher frequency fluctuations are at their peak.

Left vs. Right Brain Area Differences

When comparing the strength of the GCaMP activations above the detection threshold, we found significantly different responses between brain areas between all homotopic areas, with the right area showing significantly higher peaks than the left. A possible explanation for this could be the imaging setup. Mice were always positioned in the same manner. The location of the researcher, angle of the LEDs to activate the GCaMP and measure the hemodynamics (acquisitions were otherwise performed in a dark room), and other factors could have had an effect on the acquisition. Interestingly, the number of times that GCaMP timecourses cross the threshold in the different areas does not show this pattern with the same intensity (Appendix B.2).

Although the GCaMP peaks are generally higher on the right side of the brain, the hemodynamics do not show this same pattern, with the homotopic regions differing significantly in neither HbO/HbR peak, nor increase/decrease between left and right regions. With a difference in GCaMP activity, but none in hemodynamics, we logically end up with a different strength in neurovascular coupling between right and left areas. This is more visible when looking at the strength as calculated with the increases, with all areas except for the retrosplenial showing a significantly stronger NVC in the left areas compared to the right.

Medial vs. Lateral Brain Area Differences

In regards to the timing differences between brain areas, we found the retrosplenial cortex to have a significantly slower response than most other brain areas. The retrosplenial areas also have the highest HbR peak, and the biggest HbR decrease. Lastly, we can generally distinguish two groups in the HbO data: the motor and retrosplenial areas with a lesser response, and the sensory and visual areas with a greater response, although these differences are not always significant. The difference in timing, HbO influx and HbR peak might all stem from the same phenomenon. The vascular density is not homogeneous over the brain [339]. The cerebral arteries feeding large parts of the more superficial parts of the brain wrap around the brain and come in laterally. This means that the middle cerebral artery comes across the sensory region, and the posterior cerebral artery feeds the visual area. The motor region and the retrosplenial area are located more medially, which might mean that the blood supply to those areas is less efficient, and thus the delay is longer and the peak in HbO values is lower. This would also explain the higher HbR peak; as we can see in the delay, the sensory and visual areas receive the needed HbO increase significantly quicker than the retrosplenial areas, while the motor areas stay in between those values.

5.7.2 Resting State Networks in Sham

RSN studies have gained interest over the years. First, because RSN information is especially useful in cases where the subject cannot be asked to perform a task, for example coma patients or young infants. Secondly, RSN have been found to be disrupted in many diseases affecting brain functions such as Alzheimer’s [55, 202, 340], schizophrenia [211], obstructive sleep apnea [290] and autism [49], among others. This opens the possibility for the usage of RSN as a biomarker to distinguish between Mild Cognitive Impairment and Alzheimer’s [50, 53], or even a predictive factor for Alzheimer’s [55].

Most of these findings have been obtained with fMRI, and are generally assumed to reflect ongoing neuronal processes. Our results show that this assumption rings true in general, but with some subtle differences between the two networks that should not be ignored. The clearest difference lies in the connection between sensory and motor areas, which is much higher in GCaMP compared to HbO. This could be related to the difference in neurovascular coupling between these two areas. In general, the motor areas show a lower GCaMP peak, lower HbO influx, larger HbR peak, and slightly (not significantly) slower response than the sensory areas.

To prevent accidental removal of relevant signal, a global signal regression (GSR) was not performed on the data in this article. However, since global factors such as changes in LED intensity can confound the data, correlation matrices after GSR are shown in Appendix B.9. Results for both methods come to the same conclusion.

5.7.3 Calcium Rigidification Effect

In this study, we used the mouse model as proposed by Sadekova et al. [233]. They demonstrated the efficiency of their method by showing an increase in carotid intima-media thickness, an increase in stiffness of the artery with a pressure myograph, and an increase in minimum to maximum speed of blood flow with a doppler OCT. Furthermore, they showed that the carotid artery radius was not different, and there was no detectable increase in systolic blood pressure compared to Sham mice. They performed these tests two weeks after the surgery. In the current study, ultrasound imaging on the carotid artery was done 3 weeks after the surgery on a subset of mice to validate that the rigidification surgery had the desired effect, which showed a significant difference between the two groups 3 weeks after the surgery. Although a limitation of this study is a lack of histological sampling and invasive verification techniques to validate the calcification surgery, in our hands, previous success rate for the surgery was found in excess of 95% suggesting that, if any, procedural variability should be small. Previous studies with this mouse model showed a decreased resting cerebral blood flow (CBF) in perirhinal and entorhinal cortices, parts of the hippocampus (CA1 and dentate gyrus) and the thalamus [194], a decrease in cerebral vessel density in the somatosensory cortex and CA1 but not in the dentate gyrus [194], and cerebral gliosis in the hippocampus [234]. Though the impact on the hippocampus seems clear, the current study focused on the effects on cortical regions. Given the impact on at least some cortical structures, as mentioned above, we hypothesized that the calcification of the carotid artery would have a detectable effect on the neurovascular coupling and resting state connectivity of cortical regions. Acquisitions were taken at three timepoints to track the effects of the surgery over time, since the potential NVC dysfunction as a result of a rigidified artery might only appear once the microvasculature is sufficiently damaged. However, the neurovascular coupling showed no significant difference in any of the measured parameters as an effect of rigidification of the carotid artery. Similarly, none of the seedpair connections or the resting state network were significantly altered in the CaCl group versus the Sham group, indicating that a (subtle) increase in carotid artery rigidity does not alter the resting state connectivity of cortical brain areas.

5.8 Conclusion

Our research indicates that hemodynamic signal remains a solid indicator of neuronal activation in resting state in mild cases of rigidification of the carotid artery, since both resting state networks and neurovascular coupling parameters indicate no differences between Sham and CaCl groups. Moreover, detected peaks in hemodynamic data are frequently preceded by detected peaks in GCaMP data in both CaCl and Sham mice. This confirms the validity of past and future studies relying on hemodynamic data to infer neuronal activation. However, further research is needed to verify whether more severe cases of large artery rigidification alters NVC. Lastly, we found subtle but significant differences between brain regions regarding resting state activations and neurovascular coupling, which can be used in future research to finetune the conclusions drawn from hemodynamic data.

5.9 Acknowledgements

This work was funded by CIHR grant #436352 to F. Lesage and M. Vanni and by a Canada Research Chair to F. Lesage.

CHAPTER 6 ULTRAFAST 2-PHOTON IMAGING OF CEREBRAL VASCULATURE IN TAC MICE

6.1 Preamble

This chapter presents work in progress that will lead to an article, and thus not all results are included yet. The most important upcoming results are a measurement of cerebral microbleeds and an improvement of red blood cell velocity calculation. The specifics of this are discussed in section 6.6.

In this research, we used a 2-photon microscope with a FACED module in order to investigate the blood flow in the cerebral vascular system, in sham mice as well as in mice that underwent TAC surgery. Since these results are preliminary, no definitive conclusions can be made. However, we saw slightly higher pulsatility in arteries in TAC mice, whereas this did not seem to be the case in capillaries.

6.2 Resume

The transverse aortic constriction (TAC) surgery has been shown to increase pulse pressure, cause cardiac hypertrophy, and damage cerebral vasculature. It has been hypothesized that the cerebrovascular damage is caused by the penetration of the pulse wave into the fragile microvasculature of the brain. Here, we investigated whether an increase in pulsatility in the cerebral capillaries can be found in mice that underwent TAC surgery compared to sham mice. We used a 2-photon microscope in combination with a FACED module. This ultrafast imaging method allowed for estimation in pulsatility in capillaries, arteries and veins. Preliminary results show that the pulsatility might be slightly increased in arteries after TAC surgery, but does not seem to differ in capillaries nor veins. This indicates that the increase in pulse pressure as caused by TAC surgery might not affect the pulsatility in capillaries, and thus the microvascular damage may be caused by other factors.

6.3 Introduction

Damages to the cerebral vasculature are thought to be linked to an increase in pulse wave velocity (PWV) [341]. This could be because the pulse propagates into the capillaries where it can damage the endothelial cells [12, 342] that are vital for the integrity of the vessels, leading to a damaged blood brain barrier (and thus more neuroinflammation) [190], and impaired neurovascular coupling [17]. An increase in PWV is associated with Alzheimer’s [27, 28], cerebral small vessel disease [343, 344], decrease in cognition [170, 181, 187, 345, 346], and Parkinson’s [347], among others [184, 348, 349].

An increase in PWV can be caused by a stiffening of the arteries or hypertrophy of the heart. Cardiac hypertrophy in mice can be induced by transverse aortic constriction (TAC) surgery, where the aorta is narrowed between the brachiocephalic artery and left common carotid artery. This increases the resistance that the heart has to overcome, and thus induces cardiac hypertrophy [241, 243] and increases PWV [240]. Previous studies utilizing TAC surgery have shown decreased microvasculature density, endothelial cell dysfunction and an increased number of microbleeds [15, 16]. However, since TAC surgery also increases blood pressure [15, 16, 243], whether this damage is caused by an increase in pressure or a propagation of the pulse into the capillaries is unclear.

While imaging arterioles, capillaries and veins with two-photon microscopy is common, investigating the pulse requires fast imaging rates. This was achieved with an elegant approach recently: free-space angular chip-enhanced delay (FACED) 2-photon imaging [259, 260]. The FACED module consists of two highly reflective mirrors that have a slight misalignment angle (α). When an angularly dispersed beam (as created here with a cylindrical lens) hits the first mirror, the reflective angle of the beamlets will differ (Figure 6.1A). A discrete number of beamlets will have the exact same path upon entrance and exit of the system (cardinal rays). Since the number of reflections within the system of these beamlets differ as well as their location, they become both spatially and temporally separated, and thus can be considered to be coming from several virtual sources. The spatial separation allows the system to acquire a line per laser pulse, leading to images with one galvo movement for a 2D scan, and without any galvo movement for a linescan, while the temporal separation ensures the proper space-time localisation of the detected signal. Exploiting this approach, Meng et al. [261] have shown the ability to track individual blood cells in vessels at high velocities, and to derive a pulsatility index from this.

In this study, we utilize a similar FACED 2 photon system to map the pulsatility in individual cerebral vessels, and the changes that occur with increased PWV as induced by transaortic constriction (TAC) surgery [243]. By imaging vessels of different sizes and speeds, we can identify which types of vessels take the lion's share of the increased pulsatility.

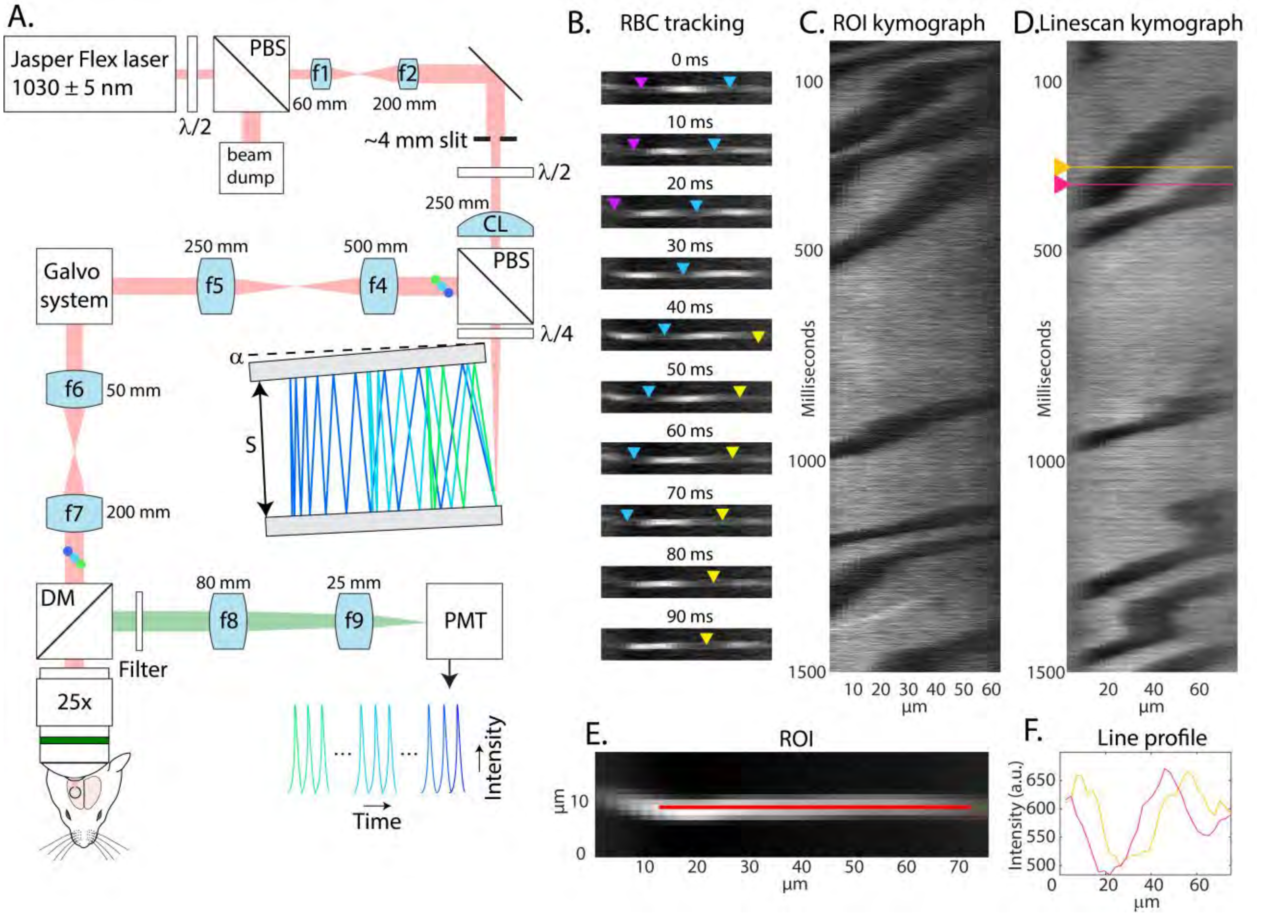

Figure 6.1: 2P FACED imaging

A. Schematic overview of the 2-photon FACED system. PBS: polarizing beam splitter, CL: cylindrical lens, DM: dichroic mirror, PMT: photomultiplier tube. B. 2D scan of capillary showing the ability to track individual RBC. Coloured arrows indicate RBC's. C. Kymograph based on a ROI drawn on a 2D scan (see E for ROI). D. Kymograph based on linescan of the same vessel as B and C. E. 2D scan with line ROI projected on top. F. Intensity profiles of the lines indicated in D. A velocity estimation is made by doing a crosscorrelation on these intensity profiles.

6.4 Methods

6.4.1 Mice

17 C57BL/6NCrl mice were used in this study (8 male, 9 female), obtained from Charles River Laboratories (Saint-Constant, Qc, Canada). One male mouse died after TAC surgery, one female TAC mouse died after the cranio surgery and two TAC mice (one male, one female) were unusable for imaging due to bleeding below the cranial window. This left 8 TAC (4 male) and 6 sham (3 male) for imaging. All surgeries and procedures were approved by the Animal Care and Use Committee of the Université de Montréal, and conformed to the regulations of the Canadian Council on Animal Care. Mice were housed with ad libitum access to food and water. Heartrate, temperature and respiration rate were monitored during both surgeries and imaging with a small animal physiological monitoring system (Labeo Technologies Inc.).

6.4.2 TAC surgery

A Transverse Aortic Constriction (TAC) [238] or sham surgery was performed on the mice. The mouse was anesthetized (1.5-2% isoflurane in pure oxygen), the fur at the incision location was removed, and the mouse was injected with Marcaine (2 mg/kg) at the site of the incision. It was then intubated, and placed in a supine position on a heating pad. The skin was cleaned with alcohol and betadine, and an incision was made between the second and the third rib. The aorta was isolated, and a 6.0 silk suture was passed under the aorta, between the brachiocephalic artery and the left common carotid artery (Figure 6.2A). In sham surgeries, the suture was then removed. For TAC surgeries, a 27G needle gauge was used [243], and the suture was tied to constrict the aorta. The incision was closed with sutures. Mice were injected with Carprofen (5 mg/kg) and Tribrissen (30 mg/kg) 24 and 48 hours after the surgery, and saline when shown signs of dehydration. Mice recuperated for 20-27 days before imaging. The hearts of the mice were weighed after sacrifice. For each mouse, the heart weight (in milligrams) was divided by the body weight as measured directly before craniotomy (in grams) as a measure of hypertrophy caused by the TAC surgery.

6.4.3 Craniotomy

To image blood vessels, a craniotomy surgery was performed on the imaging day. The mouse was anesthetized (2% isoflurane) and placed in a prone position on a heating pad. The fur on the head was removed, and the skin cleaned with betadine and alcohol. Lidocaine was locally administered, and the skin cut away to expose the skull. A titanium headbar was installed with dental cement and Vetbond to be able to fix the mouse head during imaging. A circular region (3 mm in diameter) of bone was removed over the right somato-sensory cortex with a drill. A glass coverslip was installed over the exposed region with glue and dental cement. The dura mater was not damaged or removed during the procedure. Lastly, rhodamine (20 mg/mL, 200µL) was injected in the tail vein. Mice were imaged immediately after the craniotomy, and kept under isoflurane during imaging (1% in O2).

6.4.4 Perfusion

After imaging, a perfusion was performed. Mice were intraperitoneally injected with ketamine (3.2 mg/kg) and a thoracotomy was done to reach the heart. A needle was inserted into the left ventricle, and a small incision was made in the right atrium. PBS was pumped into the heart, followed by a 4% PFA solution at the same rate. Hearts and brains were extracted and kept for further analysis.

6.4.5 Ultrafast 2-photon FACED

The imaging system design was based on the papers of Wu et al. [259] and Meng et al [261]. An overview is provided in Figure 6.1A. A Jasper Flex high power femtosecond fiber laser (Fluence technology) of 1030 nm was used at a frequency of 983 kHz at a pulse duration of 250 fs. The laser beam went through an achromatic half-wave plate (Thorlabs AHWP05M-950) and polarizing beam splitter (PBS: Thorlabs CM1-PBS252) to control the power. It then passed through a ~4x beam expander (f1: Thorlabs LA1134-B-ML and f2: Thorlabs LA1708-B-ML), and a ~4 mm-wide slit (Thorlabs VA100C/M) to control the numerical aperture into the faced module. Entry polarization was controlled via an achromatic half-wave plate (Thorlabs AHWP05M-950), after which the laser passed through a cylindrical lens (CL: Thorlabs LJ1267RM-B) to provide the optical dispersion in the axis of the faced mirrors. To distinguish incoming and outgoing beams, another polarizing beam splitter (PBS: Thorlabs CCM1-PBS253/M) was used with a quarter wave plate (Thorlabs AQWP10M-980) before entering the FACED module [259] so that the output of the module is cross-polarized compared to the input. The mirrors of the FACED module had a small misalignment angle (α). Mirrors were 18.5 cm apart (S) and had a length of 25 cm (Layertec, HR(30-45°, 1030nm)>99.9%). The apparatus configuration ensures a widening of the entrance beam by increasing optical dispersion upon each reflection. Because of the misalignment angle of the mirrors, the beamlets will eventually leave the module on the same side as they entered, with the angle and timing varying per beamlet based on the angle of entrance and the number of reflections within the system. This line of beamlets passes through a relay consisting of two lenses (f4: Thorlabs AC508-500-AB-ML and f5: Thorlabs AC508-250-B-ML), a galvo system (Thorlabs GCM102/M and GVS102TSH223186Y) to enable a 2D scan of the sample, a scan lens and tube lenses (f6: Thorlabs SL50-2P2 and f7: Thorlabs TL200-2P2) before being focused with an objective (Olympus XLPlan N 25x) on the brain. Fluorescence excitation was reflected by a dichroic mirror (DM: Thorlabs ff775-Di01) and further filtered using a shortpass emission filter (Thorlabs ff01-770SP). The light was focussed with two lenses (f8: Thorlabs AC508-080-A-ML and f9: Thorlabs LA1951-A) into a photomultiplier tube (PMT: Hamamatsu H7422A-50).

This set-up allowed for faster 2D and linescan imaging due to the inherent scanning provided by the time-dispersed beamlets. In a 2D image, the x-axis is determined by the spacing between the beamlets. Before each imaging session, the width of the field of view was calibrated, and found to be between 65-80 µm. The y-axis of the 2D image can be altered by adjusting the settings of the galvo. The framerate of the 2D images depends on the number of linescans over the y-axis, which in this work was set to 1064. For linescans, the galvo was not moved, as the line provided by the FACED stayed at the same location on the y-axis. The frequency for the linescan is then determined by the laser frequency. For each linescan, a 2D scan of the same area was made, which allowed for diameter estimations.

The power of the laser was adjusted to the depth of the imaging plane, but never exceeded 20mW at the brain surface nor 125mW deeper. The mouse was fixed with its headbar during the entire imaging session.

6.4.6 2P Analysis

Analysis was done with MATLAB R2023a and R2024b, and the code is available at github.com/marl1bakker/P3_FACED. The illumination over the FACED line was not uniform, and thus data was normalized by the illumination profile. The y-axis was averaged to result in roughly 1 pixel per micron. For linescans, an average over 100 lines was calculated. For 2D scans, a line ROI was manually drawn onto the average 2D image (Figure 6.1E). A kymograph was made for this ROI (Figure 6.1C) or over the whole image in the case of a linescan (Figure 6.1D).

To calculate velocity, frames of the kymographs were correlated. Each frame (i) was crosscorrelated with a range of frames from i+1 to i+j (Figure 6.1F), where j is the estimated number of frames that the RBC needs to cross half the kymograph. For each crosscorrelation, the maximum correlation index was used to calculate the estimated velocity. All estimated velocities for a single frame (i) were averaged to get one velocity point per frame.

Pulsatility was calculated by fitting a smoothing spline over the velocity over time. Peaks were detected with a minimal peak distance ensuring less than 700 peaks per minute to conform with expected heartbeat values. The pulsatility index is then calculated as the change in velocity over the average velocity per cardiac cycle.

6.4.7 Statistics

For all comparisons between two groups, the assumptions for a t-test were tested, and when they were not met, a Mann Whitney U (MWU) test was performed.

For statistics relating to pulsatility, the differences in variance over vessel types (arteries, capillaries and veins) was such that an ANOVA was ruled out. Sham and TAC groups were compared per vessel group, with a correction for multiple comparisons (Benjamini-Hochberg).

6.5 Results

6.5.1 TAC surgery

Mice that underwent the TAC surgery had similar weights as Sham mice on the day of imaging (26.0 grams versus 26.5 grams on average, respectively, p = 0.89, MWU, Appendix C.1). Both the weight of the heart (p = 0.008, MWU, Appendix C.1) as the heart weight over body weight (p = 0.001, MWU, Figure 6.2B) was significantly higher for the mice that underwent TAC surgery. The effect of the TAC surgery seems to be bigger in female mice than in male (Figure 6.2C). However, a two-way ANOVA showed no significant impact of sex (p = 0.17 for sex, p = 0.02 for surgery). The first images of the lightsheet analysis indicate thicker ventricle walls in the TAC mice (Figure 6.2D), but since not all hearts are imaged yet, a statistical value cannot yet be given.

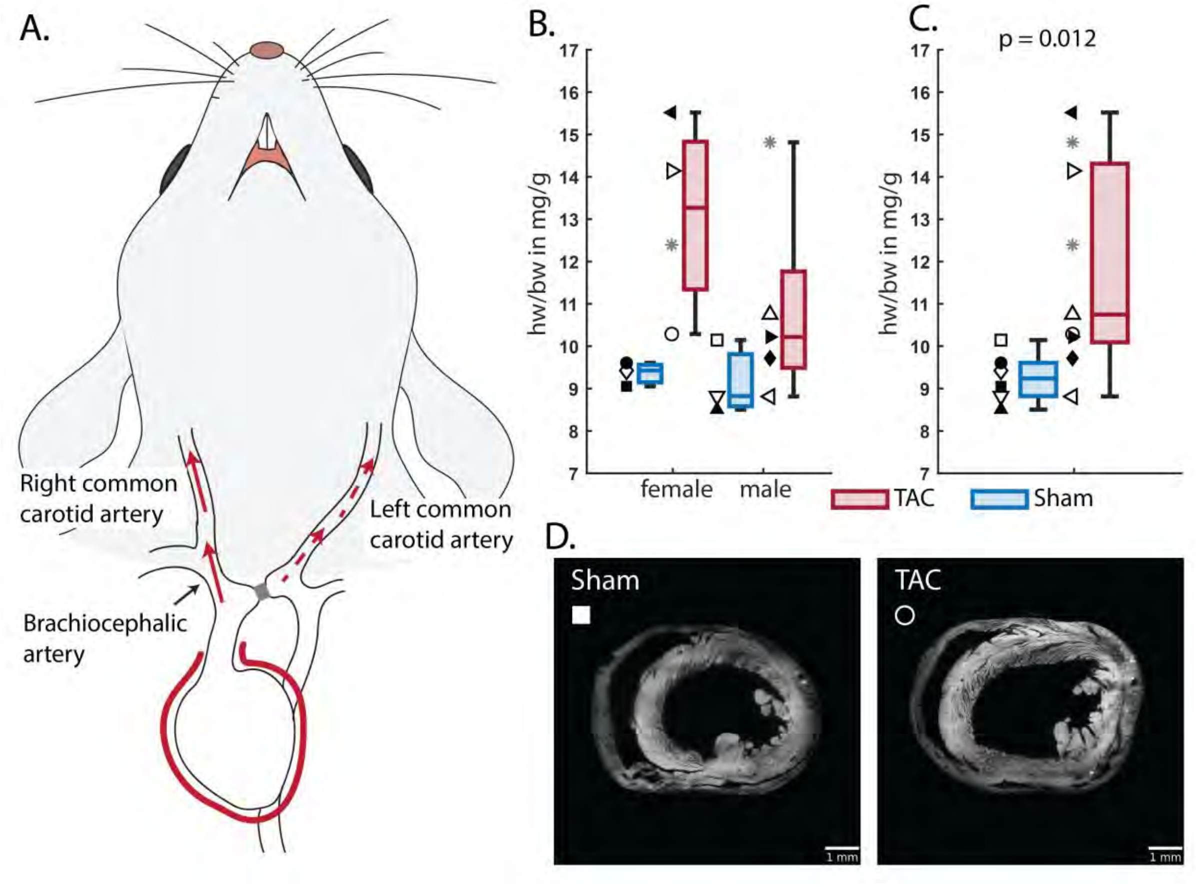

Figure 6.2: TAC surgery

A. Overview of the TAC surgery. The aorta between the brachiocephalic artery and left common carotid artery was narrowed with a suture. B. Heart weight divided by body weight for female and male Sham and TAC mice. C. Heart weight divided by body weight for all Sham and TAC mice. D. Lightsheet images of a heart from a Sham and TAC mouse. The symbols correspond with the symbols in B and C.

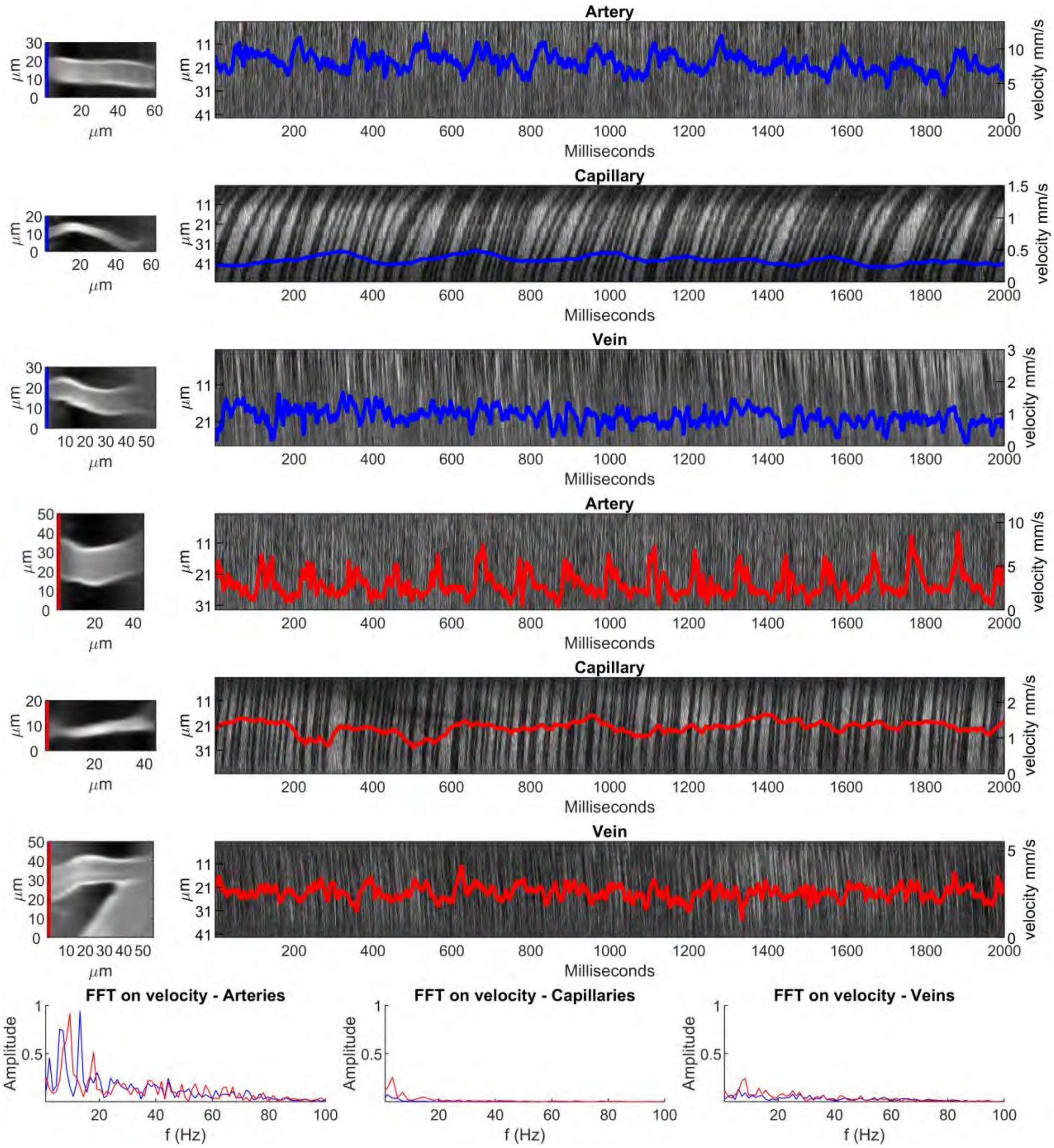

Figure 6.3: Kymographs of different vessels.

The 2D overview scan is depicted on the left, with the corresponding kymograph, as made with a linescan, is depicted on the right. The left axis of the kymograph depicts the width of the linescan, while the right axis corresponds to the estimated velocity, as plotted with a blue (sham) or red (TAC) line. Fast Fourier transform traces of these velocities are shown on the bottom.

6.5.2 2P FACED imaging

As in Meng et al. [261], we managed to get high quality kymographs, which allowed for velocity estimation of arteries, capillaries and veins (Figure 6.3). In both TAC and sham mice, a pulsatility that seemed to correspond with the heartbeat could be found in most arteries (Figure 6.3 and Appendix C.2 for a zoomed version), whereas the variability in velocity was much less apparent in capillaries and veins. The highest average estimated velocity was 20.7 mm/s, with peak velocity values around 40 mm/s (Appendix C.3).

Unsurprisingly, velocity is higher in arteries than in capillaries or veins (Figure 6.4A). Velocity estimations between Sham and TAC groups did not differ significantly (Arteries: $p = 0.22$, Capillaries: $p = 0.71$, Veins: $p = 0.52$, MWU).

In rare occasions there was a slight backflow of blood within the vessel, a backflow large enough to cancel out any forward movement, or even a reversal of flow (Appendix C.4). These were found in both TAC and Sham mice.

6.5.3 Pulsatility Sham vs TAC

Pulsatility in arteries is significantly higher in TAC mice (Figure 6.4B, $p = 0.000049$, MWU). The pulsatility of capillaries and veins does not differ between Sham and TAC mice ($p = 0.51$ and $p = 0.76$, respectively). Although the pulsatility index is an often used measure, it can become abnormally high in cases of very low average velocity blood flow. For this reason, Appendix C.5 shows pulse pressure plotted against velocity, which also seems to show a slightly higher pulse pressure in TAC mice.

To ensure differences in vessel diameter between the two groups do not influence the outcome measures, a scatter plot of velocity and diameter is included in Appendix C.5, and shows similar vessel sizes for the two groups.

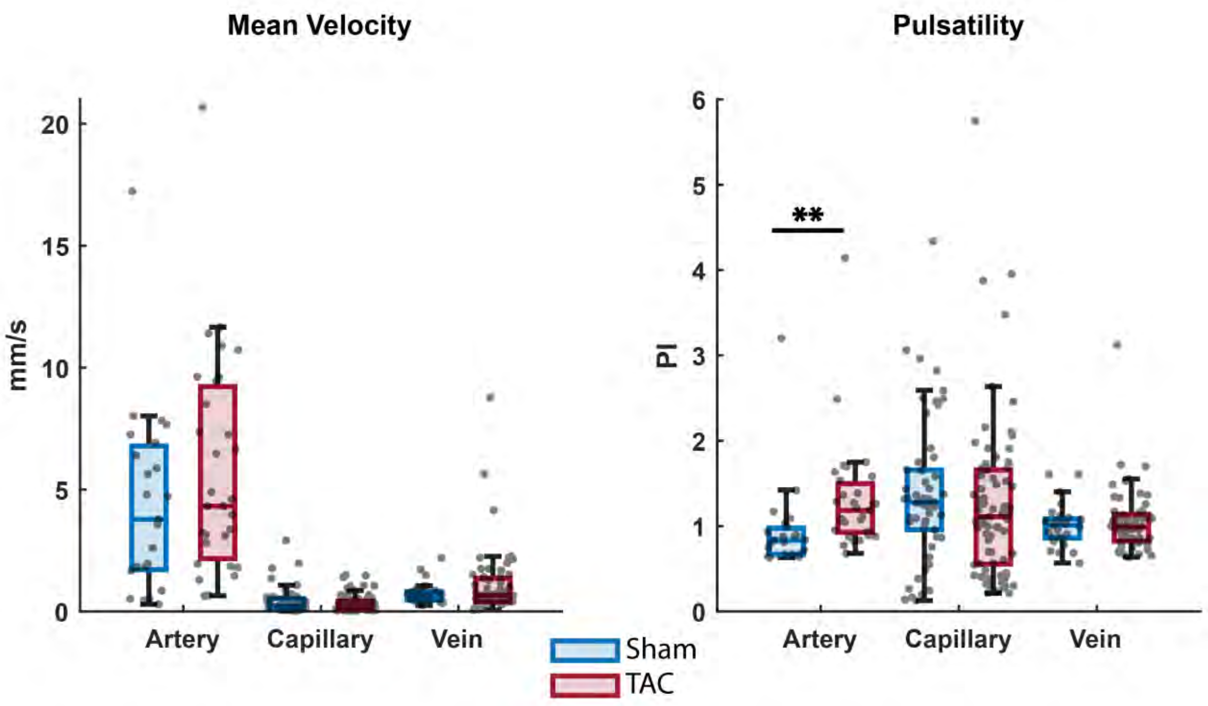

Figure 6.4: Boxplots of pulsatility and velocity.

Pulsatility and velocity measurements per acquisition (black dots) for TAC and Sham mice, grouped per vessel type. A significantly higher pulsatility index was found in arteries of TAC mice compared to Sham mice. Other parameters and groups did not differ significantly.

6.6 Upcoming results

6.6.1 Improvement of velocity calculation

A confounding factor is that RBCs are not always present in the kymograph in vessels with low velocity (Figure 6.1D, lines 500-700) or when stalling occurs. This will be improved by automatically detecting periods without RBC flux. Velocity and pulsatility can be estimated on parts where RBC flux is present for at least 0.5 continuous seconds, and these values can then be averaged so that acquisitions with stalling can be included in the analysis.

6.6.2 Microbleeds detection – Prussian blue

For microbleed detection, the protocol of Xie et al. [350] will be adapted for use. The brain will be cut in 1 mm thick slices and stained with Prussian blue iron stain kit (Sigma-Aldrich, USA). Slices will be submerged in a working stain solution (potassium ferrocyanide and hydrochloric acid 1:1) for 10 minutes, and stained with parasosaniline for 5 minutes, conform the manufacturer's instructions. The brain will be then cleared with the iDISCO protocol [351]. Imaging will be done with a confocal microscope.

Previous studies have found damages of the capillaries upon TAC surgery, and we expect to find the same outcome. However, if more microbleeds are found in TAC mice, without an increase in pulsatility in the capillaries, this could indicate that an increase in pulsatility in the capillaries is not in fact the underlying reason for capillary damage. Furthermore, this measurement will give an indication of which brain areas are most likely to be affected by the TAC surgery.

6.6.3 Light-sheet imaging of the heart

All hearts were kept after perfusion. A subset of hearts has already been cleared with the iDisco protocol [351], and imaged with a lightsheet microscope exploiting endogenous contrast to recover anatomy. The same will be done for the rest of the hearts. This will provide an extra measure for the impact of the TAC surgery.

6.7 Discussion

TAC surgery in mice and an increase in pulsatility in humans have been associated with cognitive decline [15, 17, 28, 35, 180, 186, 187, 190, 352]. The ongoing hypothesis for this is that the increased pulse wave penetrates into the microvasculature and creates damage in this manner [27]. Here, our preliminary results showed that the hypertrophy as induced by the TAC surgery increases pulsatility and velocity in arteries, but have no affect on capillaries. This implies that an increase in pulsatility does not reach the cerebral microvasculature within a timeframe of roughly 3 weeks. It is possible that the pulsatility does penetrate to the capillaries when the TAC surgery has had a longer time to take effect. For example, the study of Montgolfier et al. [15] waited for 6 weeks after TAC surgery to perform their tests, and studies in humans regarding increased PWV often investigate this in naturally occurring conditions that have a gradual onset, such as hypertension, atherosclerosis or old age [35, 190, 192, 353].

How our study fits with these results depends on the outcome of the microbleeds analysis as well. If we do not find a significant increase in microbleeds in the TAC mice like previous studies did

[15, 16], our model might not have had enough time to impact the microvasculature, showing that the effects of cardiac hypertrophy on capillary integrity can be mitigated in the early stages. However, if we do see an increase in microbleeds, this damage might not be caused by an increase in pulsatility, and instead could be caused by an increase in blood pressure (hypertension), which is also seen in this model. Hypertension and increased pulsatility are linked, since the former often leads to the latter. It is likely that they both contribute to damage of the microvasculature and cognitive decline.

CHAPTER 7 DISCUSSION

The studies in this thesis vary in their approach, imaging scale and methods. However, they come together in providing insights on the hemodynamic workings of the vascular system outside its normal parameters. Each project came with its unique challenges, which form lessons and inspiration for future studies.

7.1 Objective 1: Investigate the effect of global hypoxia on large-scale hemodynamics and neuronal activation (article 1)

Although global hypoxia as induced in our study does not mimic a particular cardiovascular disease, it does give insight into the mechanisms that kick in upon a lack of oxygen in the brain. Global oxygen delivery can be impaired in cases of cardiac arrest (disruption of general blood flow), anemia, or hypoperfusion. Here, we focused on the consequences of hypoxia itself, to be able to untangle the consequences of a lack of oxygen specifically compared to the bigger picture of the disease.

Unsurprisingly, global hypoxia of 8% oxygen has a large impact on both hemodynamics and neuronal activation in the brain. Interestingly, this occurred despite the oxygen saturation returning to baseline within the 10 minute hypoxic period. Especially the longer range connections between the anterior and posterior brain areas decrease in their functional connectivity.

7.1.1 Limitations and improvements

The combination of GCaMP and IOI brings a lot of benefits, allowing for simultaneous neuronal and hemodynamic measurements in vivo in awake animals, over a long period of time. However, one of the major drawbacks of this technique is that only the surface of the brain can be imaged, and thus it cannot inform about structures deeper in the brain. This also means that structures that are important in the DMN in human RSN, such as the cingulate cortex, cannot be properly investigated with GCaMP/IOI. This limitation applies to this objective as well as objective 2. Not many techniques allow for accurate imaging deep in the brain while informing on both neuronal and hemodynamic fluctuations, so overcoming this limitation will be a challenge. Studies combining electrophysiology and fMRI might give a clearer view on this, although these studies come with their own technical and ethical challenges.

An additional analysis that could be done with the data that is already collected is to investigate the NVC in a similar way as in the second article, with detection of spontaneous activation and comparison over brain areas. Hypothetically, hypoxia could decrease the neurovascular response, since the dilation of the blood vessels has an upper limit and the blood vessels are already dilated as a response to the hypoxia.

7.1.2 Future directions

The disconnection that seems to occur between the anterior and posterior parts of the brain could potentially be implicated in the effects of hypoxia, such as confusion or decreased cognitive ability. It would be interesting to follow this up by investigating anterior-posterior connectivity in other cases that affect cognition, such as mild cognitive impairment or Alzheimer’s.

The ability to return the oxygen saturation levels to baseline within minutes by increasing cerebral blood volume relies on intact cerebral vasculature. An interesting connection between hypoxia and increased pulse pressure exists in high performance athletes, that have a higher chance of cardiac hypertrophy because of the required output of the heart during intense exercise, and experience (mild) global hypoxia during high-altitude training (popular with cyclists for example). Although the hypoxic conditions during high-altitude training are much milder than the 8% oxygen in our study, it also consists for a much longer period of time. It would be interesting to investigate whether high performance athletes have the same response to hypoxia as regular people, or if hypertrophy in these otherwise healthy adults impairs the ability to compensate for lack of oxygen.

7.2 Objective 2: Investigate possible differences in neurovascular coupling as a result of a rigidified carotid artery (article 2)

This study showed a strong NVC in resting state, with a very consistent temporal profile for both calcium and hemodynamic components. Interestingly, this profile differed significantly over brain areas. Although this was not the main hypothesis of the study, it is both interesting and important to note this phenomenon.

7.2.1 Limitations and improvements

We initially expected to find that a calcified carotid artery would disturb the cerebral blood flow, and alter the hemodynamic RSN. However, we found no significant difference between the CaCl and Sham groups in this study. This might be partially due to the relatively mild effects of the calcification surgery. The diameter change of the carotid artery as measured with ultrasound was significantly different between the two groups, but barely. For future research, a good addition would be to determine the flexibility of the vessel both before and after the surgery, to be able to compare within individual. The differences in carotid artery stiffness per mouse might obfuscate the effect of the calcification surgery.

A challenge in this research was to determine the threshold for both spontaneous neuronal and hemodynamic "activations". Especially for the HbO measurement, there are a lot of global fluctuations. Although the threshold for HbO activations was set for each pixel individually, the slower oscillations of blood flow made the threshold as set by a z-score of 1.95 relatively high. This was chosen initially to make sure to err on the side of caution, and only label obvious increases in HbO as "activation". However, for future studies, a more sophisticated approach that takes into account the slower, more global activations is worth consideration.

In this study, we observed significant differences in spontaneous GCaMP activations between the left and right hemisphere. This could be an effect of the imaging set-up. Mice always faced the same direction, with the emission light and researcher always on the same side. Although measurements were taken in a dark room with the least amount of noise possible, not all confounding factors can be excluded. With the wisdom of hindsight, imaging the mice in the opposite direction as well could have given clarity on whether this left/right difference was due to intrinsic differences in the mouse, or an outside factor confounding the results.

The framerate of this study was 15 Hz, which limited the conclusions that we could draw on the timing of the HbO peak compared to the GCaMP peak. Although we see significant differences, the timing between both peaks was between ~0.73 and ~1.07 seconds, corresponding to 11 and 16 frames. In other words, the temporal resolution was not good enough to tease out the more subtle differences between areas. Lastly, similar to the first article, the restricted penetration depth of the IOI and GCaMP imaging is a limitation that can only be overcome by a different imaging method.

7.2.2 Future directions

The difference in NVC over brain areas in resting state is worth exploring in more detail. For example, the timing between the spontaneous activation and the influx of blood flow requires a more precise measurement than our study. An interesting approach would be to image the spontaneous activation of individual neurons and their effect on capillaries. Imaging the same kind of neurons over brain regions, and the dilatory effects that they have on the feeding capillaries could give a better insight into the differences between NVC on spontaneous activation.

Given the small effect of our calcification surgery, it would be interesting to investigate a potential neurovascular uncoupling over different intensities of rigidification and pulse pressure. If the pulse pressure causes capillary damage, then it would stand to reason that the NVC is hindered, which might be the explanatory factor in a difference found in RSN as measured by fMRI.

7.3 Objective 3: Ultrafast 2-photon imaging of cerebral vasculature in TAC mice (article 3)

Not all data for this study has been gathered yet. Interesting data that is still in the pipeline includes the microbleeds staining with Prussian blue.

7.3.1 Limitations and improvements

This study was done under isoflurane. As seen in Meng et al. [261], this can influence the measured dynamics. It might be worthwhile to repeat the study with awake mice that are trained for the head restriction necessary for 2P imaging.

Mice can also be imaged over time, by installing a chronic cranial window. This would allow for tracking the progression of damage that increased pulsatility brings to the microvasculature and give more insight as to the progression of diseases that increase the pulse pressure.

The imaging itself might damage the capillaries that we are looking into. Caution needs to be taken during imaging to not increase the laser strength by too much and thus burn the vessel. However, even with this caution, I have noticed during imaging that more and more white cells (presumably leukocytes) appear over time in the vessels, and that repeated imaging of a vessel seemed to increase the chances of it stalling. Without the flow of RBCs, the velocity and pulsatility cannot be determined. It could be that the capillaries that are the most damaged show the most stalling, hindering the calculation of velocity and pulsatility, and are thus not taken into the results of this study.

The opposite, where many RBCs flow through a vessel with little space between them, also limits the ability to calculate the velocity of the RBCs. If the space between the RBCs cannot be detected, and many RBCs are in close succession, then the start- and endpoint of an RBC in the kymograph cannot be determined, and thus the velocity cannot be calculated.

7.3.2 Future directions

The increased imaging speed that the FACED module offers in 2P imaging can open the door to research regarding the dynamics of faster vessels, such as arterioles and arteries. It would be interesting to combine the FACED 2P with neuronal measurements. This would give a very detailed look at the level of the individual neuron. The microbleed analysis could show us the regions in the brain that are most affected by the TAC surgery, which would allow for targeting a specific region and quantifying the NVC after increased pulsatility or blood pressure.

7.4 Broader implications

7.4.1 Results of the studies

Taking a step further, these results lead to new research questions regarding cerebral vasculature and neuronal activity. First, the changes in neuronal activity, despite a preserved cerebral oxygenation level, suggest that there are more mechanisms implicated than obvious at first glance. The results of hypoxia in the brain might not always be directly measurable with oxygenation levels, and thus the effects of this could be hidden from current imaging and diagnosis techniques. Interesting follow up on this could include methods to increase oxygenation of the brain, such as increasing the amount of exercise or administering extra oxygen to patients with cerebrovascular or cognitive diseases. If the “hidden” hypoxia in these cases alters neuronal activity, perhaps compensating for this might alleviate the symptoms experienced by patients.

Next, the second study showed that the neurovascular coupling differs over brain areas, raising the question of the cause and utility of this phenomenon. Do these differences arise from distinct needs of single neurons, neuronal groups, or functionality of brain areas? Or is it a consequence of the layout of the brain and the location of blood vessels? Investigations into the specifics of NVC, including whether a slower hemodynamic response comes with a cost to neuronal activity or whether any response under a maximum time limit would be sufficient, could be a useful addition to the field.

The second study also showed no changes in neurovascular coupling when increasing pulsatility, and our last study suggests the pulsatility does not reach the capillaries. This could indicate that another factor might be the link between cardiovascular diseases and cognitive decline. A potential suspect for this is an increase in blood pressure, which in patients often goes hand in hand with increased pulse pressure. Medication that decreases blood pressure might be beneficial not only for the vascular system, but potentially also for cognition.

7.4.2 Methodology

The work in this thesis has emphasised not only the potential pitfalls of assuming that NVC remains constant over both brain areas and physiological alterations, but also the benefit of the methodological developments in the field. The first two studies underline the importance of combining neuronal and hemodynamic measurements. A robust conclusion about NVC can only be drawn by measuring both components, and, as discussed in this thesis, one does not always accurately reflect the other.

The method of the third study are novel, and not yet often used in velocity estimation of cerebral blood flow. The 2P FACED opens up new possibilities in the field of NVC and cerebral blood flow, by significantly increasing the speed with which we can measure. Here, we have shown that the 2P FACED is reproducible, reliable and robust. Furthermore, by finetuning the analysis of the data acquired with this system, the results that can be obtained with this system are more exact and will more accurately show potential differences.

CHAPTER 8 CONCLUSION

This thesis started with the question:

> *How do the effects of cardiovascular diseases influence the resting state hemodynamics in the brain?*

Although my contribution to answering this question is modest, there are nevertheless interesting conclusions to draw from the three articles (one in progress) discussed.

The first article demonstrated a change in neuronal RSN in hypoxic conditions, even after reestablishing oxygenation of the tissue. The measured changes in neuronal RSN differed from those in hemodynamic RSN. This shows that alterations in the environment might reflect differently on neuronal versus hemodynamic connectivity, and thus raises the question whether the hemodynamic activity in resting state always accurately represent the neuronal activity in resting state.

In the second article, we expected to find a disconnect between the neuronal and hemodynamic RSN upon rigidification of the carotid artery. However, in this case, we found that hemodynamic activity in the resting state remains a stable indicator of neuronal activation, but that the specifics of neurovascular coupling differ over brain areas. This suggests that in situations where arteries rigidify, resting state evaluations from hemodynamic techniques, e.g. fMRI, potentially remain good indicators of brain function validating the approach.

Lastly, in our ongoing research, preliminary results point towards a minimum involvement of pulsatility in damage of cerebral microvasculature caused by TAC surgery. Proper conclusions cannot yet be drawn from this, but it might indicate that the penetration of the pulse wave into the microvasculature is not necessary for the damage of these vessels.

Overall, this thesis shows that although hemodynamic activity is often a good indicator of the underlying neuronal activity, this cannot be taken as a given. In certain situations, the cerebral hemodynamics might be affected differently than the neuronal activation patterns, and the relationship between hemodynamics and neuronal activity is not homogeneous over the brain either. Some consequences of cardiovascular diseases, such as a lack of oxygen in the tissue, can disturb the relationship between neurons and blood flow, whereas other factors, such as the rigidification of large arteries, might have less effect than previously thought. In order to use hemodynamic changes in resting state to inform on neuronal activity, it is important to take a case-to-case approach in the reliability of this method.

REFERENCES

[1] S. Prahl. "Optical Absorption of Hemoglobin." https://omlc.org/spectra/hemoglobin/index.html (accessed 2025).

[2] D. D. Clarke and L. Sokoloff, "Circulation and Energy Metabolism of the Brain," in *Basic Neurochemistry: Molecular, Cellular and Medical Aspects*, G. Siegel, B. Agranoff, R. Albers, S. Fisher, and M. Uhler Eds.: Lippincott-Raven Publishers, 1999, ch. 31, pp. 637-669.

[3] O. Paulson, S. Strandgaard, and L. Edvinsson, "Cerebral autoregulation," *Cerebrovascular and brain metabolism reviews,* vol. 2, pp. 161-92, 02/01 1990.

[4] J. E. Niven, "Neuronal energy consumption: biophysics, efficiency and evolution," *Curr Opin Neurobiol,* vol. 41, pp. 129-135, Dec 2016, doi: 10.1016/j.conb.2016.09.004.

[5] A. Silverman and N. H. Petersen, *Physiology, Cerebral Autoregulation*. StatPearls Publishing, Treasure Island (FL) (in eng), 2023.

[6] P. A. Chiarelli, D. P. Bulte, D. Gallichan, S. K. Piechnik, R. Wise, and P. Jezzard, "Flow-metabolism coupling in human visual, motor, and supplementary motor areas assessed by magnetic resonance imaging," *Magn Reson Med,* vol. 57, no. 3, pp. 538-47, Mar 2007, doi: 10.1002/mrm.21171.

[7] M. S. Vafaee and A. Gjedde, "Spatially dissociated flow-metabolism coupling in brain activation," *Neuroimage,* vol. 21, no. 2, pp. 507-15, Feb 2004, doi: 10.1016/j.neuroimage.2003.10.003.

[8] E. C. Peterson, Z. Wang, and G. Britz, "Regulation of cerebral blood flow," *Int J Vasc Med,* vol. 2011, p. 823525, 2011, doi: 10.1155/2011/823525.

[9] T. H. Adair, W. J. Gay, and J. P. Montani, "Growth regulation of the vascular system: evidence for a metabolic hypothesis," *American Journal of Physiology-Regulatory, Integrative and Comparative Physiology,* vol. 259, no. 3, pp. R393-R404, 1990, doi: 10.1152/ajpregu.1990.259.3.R393.

[10] A. R. Nippert, K. R. Biesecker, and E. A. Newman, "Mechanisms Mediating Functional Hyperemia in the Brain," *Neuroscientist,* vol. 24, no. 1, pp. 73-83, Feb 2018, doi: 10.1177/1073858417703033.

[11] R. L. Rungta, E. Chaigneau, B. F. Osmanski, and S. Charpak, "Vascular Compartmentalization of Functional Hyperemia from the Synapse to the Pia," *Neuron,* vol. 99, no. 2, pp. 362-375 e4, Jul 25 2018, doi: 10.1016/j.neuron.2018.06.012.

[12] F. Garcia-Polite *et al.*, "Pulsatility and high shear stress deteriorate barrier phenotype in brain microvascular endothelium," *J Cereb Blood Flow Metab,* vol. 37, no. 7, pp. 2614-2625, Jul 2017, doi: 10.1177/0271678X16672482.

[13] Y. Yang and G. A. Rosenberg, "Blood-brain barrier breakdown in acute and chronic cerebrovascular disease," *Stroke,* vol. 42, no. 11, pp. 3323-8, Nov 2011, doi: 10.1161/STROKEAHA.110.608257.

[14] S. V. S. Gangoda *et al.*, "Pulsatile stretch as a novel modulator of amyloid precursor protein processing and associated inflammatory markers in human cerebral endothelial cells," *Sci Rep,* vol. 8, no. 1, p. 1689, Jan 26 2018, doi: 10.1038/s41598-018-20117-6.

[15] O. de Montgolfier *et al.*, "High Systolic Blood Pressure Induces Cerebral Microvascular Endothelial Dysfunction, Neurovascular Unit Damage, and Cognitive Decline in Mice," *Hypertension,* vol. 73, no. 1, pp. 217-228, Jan 2019, doi: 10.1161/HYPERTENSIONAHA.118.12048.

[16] O. de Montgolfier *et al.*, "Systolic hypertension-induced neurovascular unit disruption magnifies vascular cognitive impairment in middle-age atherosclerotic LDLr(-/-):hApoB(+/+) mice," *Geroscience,* vol. 41, no. 5, pp. 511-532, Oct 2019, doi: 10.1007/s11357-019-00070-6.

[17] O. de Montgolfier, N. Thorin-Trescases, and E. Thorin, "Pathological Continuum From the Rise in Pulse Pressure to Impaired Neurovascular Coupling and Cognitive Decline," *Am J Hypertens,* vol. 33, no. 5, pp. 375-390, Apr 29 2020, doi: 10.1093/ajh/hpaa001.

[18] C. Iadecola, "The Neurovascular Unit Coming of Age: A Journey through Neurovascular Coupling in Health and Disease," *Neuron,* vol. 96, no. 1, pp. 17-42, Sep 27 2017, doi: 10.1016/j.neuron.2017.07.030.

[19] J. L. Presa, F. Saravia, Z. Bagi, and J. A. Filosa, "Vasculo-Neuronal Coupling and Neurovascular Coupling at the Neurovascular Unit: Impact of Hypertension," *Front Physiol,* vol. 11, p. 584135, 2020, doi: 10.3389/fphys.2020.584135.

[20] X. Liu *et al.*, "The role of neurovascular unit damage in the occurrence and development of Alzheimer's disease," *Rev Neurosci,* vol. 30, no. 5, pp. 477-484, Jul 26 2019, doi: 10.1515/revneuro-2018-0056.

[21] Q. Yang *et al.*, "Cerebral small vessel disease alters neurovascular unit regulation of microcirculation integrity involved in vascular cognitive impairment," *Neurobiol Dis,* vol. 170, p. 105750, Aug 2022, doi: 10.1016/j.nbd.2022.105750.

[22] S. Tarantini, C. H. T. Tran, G. R. Gordon, Z. Ungvari, and A. Csiszar, "Impaired neurovascular coupling in aging and Alzheimer's disease: Contribution of astrocyte dysfunction and endothelial impairment to cognitive decline," *Exp Gerontol,* vol. 94, pp. 52-58, Aug 2017, doi: 10.1016/j.exger.2016.11.004.

[23] H. Girouard and C. Iadecola, "Neurovascular coupling in the normal brain and in hypertension, stroke, and Alzheimer disease," *J Appl Physiol (1985),* vol. 100, no. 1, pp. 328-35, Jan 2006, doi: 10.1152/japplphysiol.00966.2005.

[24] O. Shabir, J. Berwick, and S. E. Francis, "Neurovascular dysfunction in vascular dementia, Alzheimer’s and atherosclerosis," *BMC Neuroscience,* vol. 19, no. 1, p. 62, 2018/10/17 2018, doi: 10.1186/s12868-018-0465-5.

[25] E. Farkas and P. G. M. Luiten, "Cerebral microvascular pathology in aging and Alzheimer's disease," *Progress in Neurobiology,* vol. 64, no. 6, pp. 575-611, 2001/08/01/ 2001, doi: https://doi.org/10.1016/S0301-0082(00)00068-X.

[26] C. Iadecola, "Neurovascular regulation in the normal brain and in Alzheimer's disease," *Nat Rev Neurosci,* vol. 5, no. 5, pp. 347-60, May 2004, doi: 10.1038/nrn1387.

[27] J. Stone, D. M. Johnstone, J. Mitrofanis, and M. O'Rourke, "The mechanical cause of age-related dementia (Alzheimer's disease): the brain is destroyed by the pulse," *J Alzheimers Dis,* vol. 44, no. 2, pp. 355-73, 2015, doi: 10.3233/JAD-141884.

[28] G. A. Bateman, "Pulse wave encephalopathy: a spectrum hypothesis incorporating Alzheimer's disease, vascular dementia and normal pressure hydrocephalus," *Med Hypotheses,* vol. 62, no. 2, pp. 182-7, 2004, doi: 10.1016/S0306-9877(03)00330-X.

[29] A. E. Roher *et al.*, "Circle of willis atherosclerosis is a risk factor for sporadic Alzheimer's disease," *Arterioscler Thromb Vasc Biol,* vol. 23, no. 11, pp. 2055-62, Nov 1 2003, doi: 10.1161/01.ATV.0000095973.42032.44.

[30] A. Csiszar *et al.*, "Hypertension impairs neurovascular coupling and promotes microvascular injury: role in exacerbation of Alzheimer's disease," *Geroscience,* vol. 39, no. 4, pp. 359-372, Aug 2017, doi: 10.1007/s11357-017-9991-9.

[31] U. K. Eriksson, A. M. Bennet, M. Gatz, P. W. Dickman, and N. L. Pedersen, "Nonstroke Cardiovascular Disease and Risk of Alzheimer Disease and Dementia," *Alzheimer Disease & Associated Disorders,* vol. 24, no. 3, pp. 213-219, 2010, doi: 10.1097/WAD.0b013e3181d1b99b.

[32] M. M. B. Breteler, "Vascular risk factors for Alzheimer’s disease:: An epidemiologic perspective," *Neurobiology of Aging,* vol. 21, no. 2, pp. 153-160, 2000/03/01/ 2000, doi: https://doi.org/10.1016/S0197-4580(99)00110-4.

[33] J.-H. Bae, J.-M. Kim, K.-Y. Park, and S.-H. Han, "Association between arterial stiffness and the presence of cerebral small vessel disease markers," *Brain and Behavior,* vol. 11, no. 1, p. e01935, 2021, doi: https://doi.org/10.1002/brb3.1935.

[34] A. H. Hainsworth, H. S. Markus, and J. A. Schneider, "Cerebral Small Vessel Disease, Hypertension, and Vascular Contributions to Cognitive Impairment and Dementia," *Hypertension,* vol. 81, no. 1, pp. 75-86, Jan 2024, doi: 10.1161/HYPERTENSIONAHA.123.19943.

[35] L. H. Henskens *et al.*, "Increased aortic pulse wave velocity is associated with silent cerebral small-vessel disease in hypertensive patients," *Hypertension,* vol. 52, no. 6, pp. 1120-6, Dec 2008, doi: 10.1161/HYPERTENSIONAHA.108.119024.

[36] M. M. F. Poels *et al.*, "Arterial Stiffness and Cerebral Small Vessel Disease," *Stroke,* vol. 43, no. 10, pp. 2637-2642, 2012, doi: doi:10.1161/STROKEAHA.111.642264.

[37] T. T. van Sloten, A. D. Protogerou, R. M. Henry, M. T. Schram, L. J. Launer, and C. D. Stehouwer, "Association between arterial stiffness, cerebral small vessel disease and cognitive impairment: A systematic review and meta-analysis," *Neurosci Biobehav Rev,* vol. 53, pp. 121-30, Jun 2015, doi: 10.1016/j.neubiorev.2015.03.011.

[38] J. S. Damoiseaux *et al.*, "Consistent resting-state networks across healthy subjects," *Proceedings of the National Academy of Sciences,* vol. 103, no. 37, pp. 13848-13853, 2006, doi: doi:10.1073/pnas.0601417103.

[39] B. Biswal, F. Z. Yetkin, V. M. Haughton, and J. S. Hyde, "Functional connectivity in the motor cortex of resting human brain using echo-planar MRI," (in eng), *Magn Reson Med,* vol. 34, no. 4, pp. 537-41, Oct 1995, doi: 10.1002/mrm.1910340409.

[40] T. T. Liu, "Neurovascular factors in resting-state functional MRI," *NeuroImage,* vol. 80, pp. 339-348, 2013, doi: 10.1016/j.neuroimage.2013.04.071.

[41] A. Savio *et al.*, "Resting-State Networks as Simultaneously Measured with Functional MRI and PET," *Journal of Nuclear Medicine,* vol. 58, no. 8, pp. 1314-1317, 2017, doi: 10.2967/jnumed.116.185835.

[42] S. Cho, M. van Es, M. Woolrich, and C. Gohil, "Comparison between EEG and MEG of static and dynamic resting-state networks," *Human Brain Mapping,* vol. 45, no. 13, p. e70018, 2024, doi: https://doi.org/10.1002/hbm.70018.

[43] P. W. Wright *et al.*, "Functional connectivity structure of cortical calcium dynamics in anesthetized and awake mice," *PLoS One,* vol. 12, no. 10, p. e0185759, 2017, doi: 10.1371/journal.pone.0185759.

[44] A. T. Winder, C. Echagarruga, Q. Zhang, and P. J. Drew, "Weak correlations between hemodynamic signals and ongoing neural activity during the resting state," *Nat Neurosci,* vol. 20, no. 12, pp. 1761-1769, Dec 2017, doi: 10.1038/s41593-017-0007-y.

[45] M. Bruyns-Haylett, S. Harris, L. Boorman, Y. Zheng, J. Berwick, and M. Jones, "The resting-state neurovascular coupling relationship: rapid changes in spontaneous neural activity in the somatosensory cortex are associated with haemodynamic fluctuations that resemble stimulus-evoked haemodynamics," *European Journal of Neuroscience,* vol. 38, no. 6, pp. 2902-2916, 2013, doi: https://doi.org/10.1111/ejn.12295.

[46] S. A. Rombouts, F. Barkhof, R. Goekoop, C. J. Stam, and P. Scheltens, "Altered resting state networks in mild cognitive impairment and mild Alzheimer's disease: an fMRI study," *Hum Brain Mapp,* vol. 26, no. 4, pp. 231-9, Dec 2005, doi: 10.1002/hbm.20160.

[47] A. Badhwar, A. Tam, C. Dansereau, P. Orban, F. Hoffstaedter, and P. Bellec, "Resting-state network dysfunction in Alzheimer's disease: A systematic review and meta-analysis," *Alzheimers Dement (Amst),* vol. 8, pp. 73-85, 2017, doi: 10.1016/j.dadm.2017.03.007.

[48] M. Schulz, C. Malherbe, B. Cheng, G. Thomalla, and E. Schlemm, "Functional connectivity changes in cerebral small vessel disease - a systematic review of the resting-state MRI literature," *BMC Med,* vol. 19, no. 1, p. 103, May 5 2021, doi: 10.1186/s12916-021-01962-1.

[49] V. L. Cherkassky, R. K. Kana, T. A. Keller, and M. A. Just, "Functional connectivity in a baseline resting-state network in autism," *NeuroReport,* vol. 17, no. 16, 2006. [Online]. Available: https://journals.lww.com/neuroreport/Fulltext/2006/11060/Functional_connectivity_in_a_baseline.6.aspx.

[50] B. Ibrahim *et al.*, "Diagnostic power of resting-state fMRI for detection of network connectivity in Alzheimer's disease and mild cognitive impairment: A systematic review," *Hum Brain Mapp,* vol. 42, no. 9, pp. 2941-2968, Jun 15 2021, doi: 10.1002/hbm.25369.

[51] D. Puttaert *et al.*, "Alterations in resting-state network dynamics along the Alzheimer's disease continuum," *Sci Rep,* vol. 10, no. 1, p. 21990, Dec 15 2020, doi: 10.1038/s41598-020-76201-3.

[52] B. S. Rauchmann *et al.*, "Resting-State Network Alterations Differ between Alzheimer's Disease Atrophy Subtypes," *Cereb Cortex,* vol. 31, no. 11, pp. 4901-4915, Oct 1 2021, doi: 10.1093/cercor/bhab130.

[53] R. Ju, C. Hu, z. p, and Q. Li, "Early Diagnosis of Alzheimer's Disease Based on Resting-State Brain Networks and Deep Learning," *IEEE/ACM Transactions on Computational Biology and Bioinformatics,* vol. 16, no. 1, pp. 244-257, 2019, doi: 10.1109/TCBB.2017.2776910.

[54] R. Cassani, M. Estarellas, R. San-Martin, F. J. Fraga, and T. H. Falk, "Systematic Review on Resting-State EEG for Alzheimer’s Disease Diagnosis and Progression Assessment," *Disease Markers,* vol. 2018, no. 1, p. 5174815, 2018, doi: https://doi.org/10.1155/2018/5174815.

[55] S. H. Hojjati, A. Ebrahimzadeh, A. Khazaee, A. Babajani-Feremi, and I. Alzheimer's Disease Neuroimaging, "Predicting conversion from MCI to AD using resting-state fMRI, graph theoretical approach and SVM," *J Neurosci Methods,* vol. 282, pp. 69-80, Apr 15 2017, doi: 10.1016/j.jneumeth.2017.03.006.

[56] M. Vanlandewijck *et al.*, "A molecular atlas of cell types and zonation in the brain vasculature," *Nature,* vol. 554, no. 7693, pp. 475-480, Feb 22 2018, doi: 10.1038/nature25739.

[57] S. Greenwald, "Ageing of the conduit arteries," *The Journal of Pathology,* vol. 211, no. 2, pp. 157-172, 2007, doi: https://doi.org/10.1002/path.2101.

[58] J. S. Bell *et al.*, "Microstructure and mechanics of human resistance arteries," *Am J Physiol Heart Circ Physiol,* vol. 311, no. 6, pp. H1560-H1568, Dec 1 2016, doi: 10.1152/ajpheart.00002.2016.

[59] W. F. Jackson, "Myogenic Tone in Peripheral Resistance Arteries and Arterioles: The Pressure Is On!," *Front Physiol,* vol. 12, p. 699517, 2021, doi: 10.3389/fphys.2021.699517.

[60] S. Schaeffer and C. Iadecola, "Revisiting the neurovascular unit," *Nat Neurosci,* vol. 24, no. 9, pp. 1198-1209, Sep 2021, doi: 10.1038/s41593-021-00904-7.

[61] K. Namdee, M. Carrasco-Teja, M. B. Fish, P. Charoenphol, and O. Eniola-Adefeso, "Effect of Variation in hemorheology between human and animal blood on the binding efficacy of vascular-targeted carriers," *Scientific Reports,* vol. 5, no. 1, p. 11631, 2015/06/26 2015, doi: 10.1038/srep11631.

[62] A. Chandra, W. A. Li, C. R. Stone, X. Geng, and Y. Ding, "The cerebral circulation and cerebrovascular disease I: Anatomy," *Brain Circ,* vol. 3, no. 2, pp. 45-56, Apr-Jun 2017, doi: 10.4103/bc.bc_10_17.

[63] B. Schaller, "Physiology of cerebral venous blood flow: from experimental data in animals to normal function in humans," *Brain Res Brain Res Rev,* vol. 46, no. 3, pp. 243-60, Nov 2004, doi: 10.1016/j.brainresrev.2004.04.005.

[64] N. A. Lassen, "Cerebral blood flow and oxygen consumption in man," (in eng), *Physiol Rev,* vol. 39, no. 2, pp. 183-238, Apr 1959, doi: 10.1152/physrev.1959.39.2.183.

[65] S. Fantini, A. Sassaroli, K. T. Tgavalekos, and J. Kornbluth, "Cerebral blood flow and autoregulation: current measurement techniques and prospects for noninvasive optical

methods," *Neurophotonics,* vol. 3, no. 3, p. 031411, Jul 2016, doi: 10.1117/1.NPh.3.3.031411.

[66] M. J. Davis, "Myogenic response gradient in an arteriolar network," (in eng), *Am J Physiol,* vol. 264, no. 6 Pt 2, pp. H2168-79, Jun 1993, doi: 10.1152/ajpheart.1993.264.6.H2168.

[67] D. Lidington, J. T. Kroetsch, and S. S. Bolz, "Cerebral artery myogenic reactivity: The next frontier in developing effective interventions for subarachnoid hemorrhage," *J Cereb Blood Flow Metab,* vol. 38, no. 1, pp. 17-37, Jan 2018, doi: 10.1177/0271678X17742548.

[68] E. L. Vu, C. H. t. Brown, K. M. Brady, and C. W. Hogue, "Monitoring of cerebral blood flow autoregulation: physiologic basis, measurement, and clinical implications," *Br J Anaesth,* vol. 132, no. 6, pp. 1260-1273, Jun 2024, doi: 10.1016/j.bja.2024.01.043.

[69] W. J. Gray and M. J. Rosner, "Pressure-volume index as a function of cerebral perfusion pressure: Part 2: The effects of low cerebral perfusion pressure and autoregulation," (in English), *Journal of Neurosurgery,* vol. 67, no. 3, pp. 377-380, 01 Jan. 1987 1987, doi: https://doi.org/10.3171/jns.1987.67.3.0377.

[70] M. J. Davis, J. A. Donovitz, and J. D. Hood, "Stretch-activated single-channel and whole cell currents in vascular smooth muscle cells," (in eng), *Am J Physiol,* vol. 262, no. 4 Pt 1, pp. C1083-8, Apr 1992, doi: 10.1152/ajpcell.1992.262.4.C1083.

[71] W. M. Bayliss, "On the local reactions of the arterial wall to changes of internal pressure," (in eng), *J Physiol,* vol. 28, no. 3, pp. 220-31, May 28 1902, doi: 10.1113/jphysiol.1902.sp000911.

[72] A. Koller, D. Sun, and G. Kaley, "Role of shear stress and endothelial prostaglandins in flow- and viscosity-induced dilation of arterioles in vitro," *Circulation Research,* vol. 72, no. 6, pp. 1276-1284, 1993, doi: doi:10.1161/01.RES.72.6.1276.

[73] A. Sandoo, J. J. van Zanten, G. S. Metsios, D. Carroll, and G. D. Kitas, "The endothelium and its role in regulating vascular tone," (in eng), *Open Cardiovasc Med J,* vol. 4, pp. 302-12, Dec 23 2010, doi: 10.2174/1874192401004010302.

[74] A. Wang, S. Ortega-Gutierrez, and N. H. Petersen, "Autoregulation in the Neuro ICU," *Curr Treat Options Neurol,* vol. 20, no. 6, p. 20, May 17 2018, doi: 10.1007/s11940-018-0501-x.

[75] C. Small *et al.*, "What are we measuring? A refined look at the process of disrupted autoregulation and the limitations of cerebral perfusion pressure in preventing secondary injury after traumatic brain injury," *Clin Neurol Neurosurg,* vol. 221, p. 107389, Oct 2022, doi: 10.1016/j.clineuro.2022.107389.

[76] A. Musso, "Sulla circolazione del cervello dell'uomo," *Atti R. Accad. Lincei,* vol. 5, pp. 237–358, 1880.

[77] E. Anenberg, A. W. Chan, Y. Xie, J. M. LeDue, and T. H. Murphy, "Optogenetic stimulation of GABA neurons can decrease local neuronal activity while increasing cortical blood flow," (in eng), *J Cereb Blood Flow Metab,* vol. 35, no. 10, pp. 1579-86, Oct 2015, doi: 10.1038/jcbfm.2015.140.

[78] H. Uhlirova *et al.*, "Cell type specificity of neurovascular coupling in cerebral cortex," *eLife,* vol. 5, p. e14315, 2016/05/31 2016, doi: 10.7554/eLife.14315.

[79] L. Kaplan, B. W. Chow, and C. Gu, "Neuronal regulation of the blood-brain barrier and neurovascular coupling," *Nat Rev Neurosci,* vol. 21, no. 8, pp. 416-432, Aug 2020, doi: 10.1038/s41583-020-0322-2.

[80] S. S. Segal, "Regulation of blood flow in the microcirculation," *Microcirculation,* vol. 12, no. 1, pp. 33-45, Jan-Feb 2005, doi: 10.1080/10739680590895028.

[81] S. Grubb *et al.*, "Precapillary sphincters maintain perfusion in the cerebral cortex," *Nat Commun,* vol. 11, no. 1, p. 395, Jan 20 2020, doi: 10.1038/s41467-020-14330-z.

[82] C. N. Hall *et al.*, "Capillary pericytes regulate cerebral blood flow in health and disease," *Nature,* vol. 508, no. 7494, pp. 55-60, Apr 3 2014, doi: 10.1038/nature13165.

[83] D. A. Hartmann *et al.*, "Brain capillary pericytes exert a substantial but slow influence on blood flow," *Nat Neurosci,* vol. 24, no. 5, pp. 633-645, May 2021, doi: 10.1038/s41593-020-00793-2.

[84] K. Kisler *et al.*, "Pericyte degeneration leads to neurovascular uncoupling and limits oxygen supply to brain," *Nat Neurosci,* vol. 20, no. 3, pp. 406-416, Mar 2017, doi: 10.1038/nn.4489.

[85] L. Alarcon-Martinez *et al.*, "Interpericyte tunnelling nanotubes regulate neurovascular coupling," *Nature*, vol. 585, no. 7823, pp. 91-95, Sep 2020, doi: 10.1038/s41586-020-2589-x.

[86] R. A. Hill, L. Tong, P. Yuan, S. Murikinati, S. Gupta, and J. Grutzendler, "Regional Blood Flow in the Normal and Ischemic Brain Is Controlled by Arteriolar Smooth Muscle Cell Contractility and Not by Capillary Pericytes," *Neuron,* vol. 87, no. 1, pp. 95-110, Jul 1 2015, doi: 10.1016/j.neuron.2015.06.001.

[87] A. L. Gonzales *et al.*, "Contractile pericytes determine the direction of blood flow at capillary junctions," *Proc Natl Acad Sci U S A,* vol. 117, no. 43, pp. 27022-27033, Oct 27 2020, doi: 10.1073/pnas.1922755117.

[88] B. A. MacVicar and E. A. Newman, "Astrocyte regulation of blood flow in the brain," *Cold Spring Harb Perspect Biol,* vol. 7, no. 5, Mar 27 2015, doi: 10.1101/cshperspect.a020388.

[89] B. R. Chen, M. G. Kozberg, M. B. Bouchard, M. A. Shaik, and E. M. C. Hillman, "A Critical Role for the Vascular Endothelium in Functional Neurovascular Coupling in the Brain," *Journal of the American Heart Association,* vol. 3, no. 3, p. e000787, 2014, doi: doi:10.1161/JAHA.114.000787.

[90] T. A. Longden *et al.*, "Capillary K(+)-sensing initiates retrograde hyperpolarization to increase local cerebral blood flow," (in eng), *Nat Neurosci,* vol. 20, no. 5, pp. 717-726, May 2017, doi: 10.1038/nn.4533.

[91] C. Iadecola, "Regulation of the cerebral microcirculation during neural activity: is nitric oxide the missing link?," *Trends in Neurosciences,* vol. 16, no. 6, pp. 206-214, 1993/06/01/ 1993, doi: https://doi.org/10.1016/0166-2236(93)90156-G.

[92] C. S. Roy and C. S. Sherrington, "On the regulation of the blood-supply of the brain," *The Journal of physiology,* vol. 11, no. 1-2, p. 85, 1890.

[93] R. L. Hoiland, J. A. Fisher, and P. N. Ainslie, "Regulation of the Cerebral Circulation by Arterial Carbon Dioxide," in *Comprehensive Physiology,* 2019, pp. 1101-1154.

[94] N. C. Lewis, L. Messinger, B. Monteleone, and P. N. Ainslie, "Effect of acute hypoxia on regional cerebral blood flow: effect of sympathetic nerve activity," *J Appl Physiol (1985),* vol. 116, no. 9, pp. 1189-96, May 1 2014, doi: 10.1152/japplphysiol.00114.2014.

[95] A. Mardimae *et al.*, "The interaction of carbon dioxide and hypoxia in the control of cerebral blood flow," (in eng), *Pflugers Arch,* vol. 464, no. 4, pp. 345-51, Oct 2012, doi: 10.1007/s00424-012-1148-1.

[96] U. Lindauer *et al.*, "Neurovascular coupling in rat brain operates independent of hemoglobin deoxygenation," *J Cereb Blood Flow Metab,* vol. 30, no. 4, pp. 757-68, Apr 2010, doi: 10.1038/jcbfm.2009.259.

[97] D. P. Cardenas, E. R. Muir, S. Huang, A. Boley, D. Lodge, and T. Q. Duong, "Functional MRI during hyperbaric oxygen: Effects of oxygen on neurovascular coupling and BOLD fMRI signals," *Neuroimage,* vol. 119, pp. 382-9, Oct 1 2015, doi: 10.1016/j.neuroimage.2015.06.082.

[98] D. Attwell and C. Iadecola, "The neural basis of functional brain imaging signals," *Trends in Neurosciences,* vol. 25, no. 12, pp. 621-625, 2002/12/01/ 2002, doi: https://doi.org/10.1016/S0166-2236(02)02264-6.

[99] G. H. Glover, "Overview of functional magnetic resonance imaging," *Neurosurg Clin N Am,* vol. 22, no. 2, pp. 133-9, vii, Apr 2011, doi: 10.1016/j.nec.2010.11.001.

[100] K. R. Thulborn, J. C. Waterton, P. M. Matthews, and G. K. Radda, "Oxygenation dependence of the transverse relaxation time of water protons in whole blood at high field," *Biochimica et Biophysica Acta (BBA) - General Subjects*, vol. 714, no. 2, pp. 265-270, 1982/02/02/ 1982, doi: https://doi.org/10.1016/0304-4165(82)90333-6.

[101] S. Agarwal, H. I. Sair, N. Yahyavi-Firouz-Abadi, R. Airan, and J. J. Pillai, "Neurovascular uncoupling in resting state fMRI demonstrated in patients with primary brain gliomas," *J Magn Reson Imaging,* vol. 43, no. 3, pp. 620-6, Mar 2016, doi: 10.1002/jmri.25012.

[102] B. Hu *et al.*, "Disturbed neurovascular coupling in type 2 diabetes mellitus patients: Evidence from a comprehensive fMRI analysis," *Neuroimage Clin,* vol. 22, p. 101802, 2019, doi: 10.1016/j.nicl.2019.101802.

[103] H. Li *et al.*, "Dysfunction of neurovascular coupling in patients with cerebral small vessel disease: A combined resting-state fMRI and arterial spin labeling study," *Exp Gerontol,* vol. 194, p. 112478, Sep 2024, doi: 10.1016/j.exger.2024.112478.

[104] P. Li *et al.*, "Neurovascular coupling dysfunction in end-stage renal disease patients related to cognitive impairment," (in eng), *J Cereb Blood Flow Metab,* vol. 41, no. 10, pp. 2593-2606, Oct 2021, doi: 10.1177/0271678x211007960.

[105] J. Chen *et al.*, "Increased Intraregional Synchronized Neural Activity in Adult Brain After Prolonged Adaptation to High-Altitude Hypoxia: A Resting-State fMRI Study," *High Alt Med Biol,* vol. 17, no. 1, pp. 16-24, Mar 2016, doi: 10.1089/ham.2015.0104.

[106] A. Rancillac, H. Geoffroy, and J. Rossier, "Impaired Neurovascular Coupling in the APPxPS1 Mouse Model of Alzheimer's Disease," *Current Alzheimer Research,* vol. 9, no. 10, pp. 1221-1230, 2012, doi: http://dx.doi.org/10.2174/156720512804142859.

[107] M. Fabiani *et al.*, "Neurovascular coupling in normal aging: a combined optical, ERP and fMRI study," *Neuroimage,* vol. 85 Pt 1, no. 0 1, pp. 592-607, Jan 15 2014, doi: 10.1016/j.neuroimage.2013.04.113.

[108] H. L. Sloan *et al.*, "Regional differences in neurovascular coupling in rat brain as determined by fMRI and electrophysiology," *Neuroimage,* vol. 53, no. 2, pp. 399-411, Nov 1 2010, doi: 10.1016/j.neuroimage.2010.07.014.

[109] O. J. Arthurs, T. Donovan, D. J. Spiegelhalter, J. D. Pickard, and S. J. Boniface, "Intracortically distributed neurovascular coupling relationships within and between human somatosensory cortices," (in eng), *Cereb Cortex,* vol. 17, no. 3, pp. 661-8, Mar 2007, doi: 10.1093/cercor/bhk014.

[110] N. Hewson-Stoate, M. Jones, J. Martindale, J. Berwick, and J. Mayhew, "Further nonlinearities in neurovascular coupling in rodent barrel cortex," (in eng), *Neuroimage,* vol. 24, no. 2, pp. 565-74, Jan 15 2005, doi: 10.1016/j.neuroimage.2004.08.040.

[111] I. S. Tigner A, Murray IV. "Histology, White Blood Cell." Treasure Island (FL): StatPearls Publishing. https://www.ncbi.nlm.nih.gov/books/NBK563148/ (accessed January, 2025).

[112] J. C. Palmer, H. M. Tayler, L. Dyer, P. G. Kehoe, J. F. R. Paton, and S. Love, "Zibotentan, an Endothelin A Receptor Antagonist, Prevents Amyloid-β-Induced Hypertension and Maintains Cerebral Perfusion," (in eng), *J Alzheimers Dis,* vol. 73, no. 3, pp. 1185-1199, 2020, doi: 10.3233/jad-190630.

[113] R. Crumpler, R. J. Roman, and F. Fan, "Capillary Stalling: A Mechanism of Decreased Cerebral Blood Flow in AD/ADRD," *J Exp Neurol,* vol. 2, no. 4, pp. 149-153, 2021, doi: 10.33696/neurol.2.048.

[114] S. Pantelakis, "[A particular type of senile angiopathy of the central nervous system: congophilic angiopathy, topography and frequency]," (in fre), *Monatsschr Psychiatr Neurol,* vol. 128, no. 4, pp. 219-56, Oct 1954. Un type particuliar d'angiopathie sénile du systeme nerveux central: l'angiopathie congophile; topographie et fréquence.

[115] A. Charidimou *et al.*, "Emerging concepts in sporadic cerebral amyloid angiopathy," *Brain,* vol. 140, no. 7, pp. 1829-1850, Jul 1 2017, doi: 10.1093/brain/awx047.

[116] H. H. Dietrich, C. Xiang, B. H. Han, G. J. Zipfel, and D. M. Holtzman, "Soluble amyloid-β, effect on cerebral arteriolar regulation and vascular cells," *Molecular Neurodegeneration,* vol. 5, no. 1, p. 15, 2010/04/13 2010, doi: 10.1186/1750-1326-5-15.

[117] F. Zhang, C. Eckman, S. Younkin, K. K. Hsiao, and C. Iadecola, "Increased susceptibility to ischemic brain damage in transgenic mice overexpressing the amyloid precursor protein," (in eng), *J Neurosci,* vol. 17, no. 20, pp. 7655-61, Oct 15 1997, doi: 10.1523/jneurosci.17-20-07655.1997.

[118] J. M. Price, E. T. Sutton, A. Hellermann, and T. Thomas, "beta-Amyloid induces cerebrovascular endothelial dysfunction in the rat brain," (in eng), *Neurol Res,* vol. 19, no. 5, pp. 534-8, Oct 1997, doi: 10.1080/01616412.1997.11740853.

[119] K. A. Jellinger, "Alzheimer disease and cerebrovascular pathology: an update," (in eng), *J Neural Transm (Vienna),* vol. 109, no. 5-6, pp. 813-36, May 2002, doi: 10.1007/s007020200068.

[120] A. C. Montezano, M. Dulak-Lis, S. Tsiropoulou, A. Harvey, A. M. Briones, and R. M. Touyz, "Oxidative stress and human hypertension: vascular mechanisms, biomarkers, and novel therapies," (in eng), *Can J Cardiol,* vol. 31, no. 5, pp. 631-41, May 2015, doi: 10.1016/j.cjca.2015.02.008.

[121] R. Chen, U. H. Lai, L. Zhu, A. Singh, M. Ahmed, and N. R. Forsyth, "Reactive Oxygen Species Formation in the Brain at Different Oxygen Levels: The Role of Hypoxia Inducible Factors," (in English), *Frontiers in Cell and Developmental Biology,* Review vol. Volume 6 - 2018, 2018-October-10 2018, doi: 10.3389/fcell.2018.00132.

[122] E. Mariani, M. C. Polidori, A. Cherubini, and P. Mecocci, "Oxidative stress in brain aging, neurodegenerative and vascular diseases: an overview," (in eng), *J Chromatogr B Analyt Technol Biomed Life Sci,* vol. 827, no. 1, pp. 65-75, Nov 15 2005, doi: 10.1016/j.jchromb.2005.04.023.

[123] O. Bracko, J. C. Cruz Hernandez, L. Park, N. Nishimura, and C. B. Schaffer, "Causes and consequences of baseline cerebral blood flow reductions in Alzheimer's disease," *J Cereb Blood Flow Metab,* vol. 41, no. 7, pp. 1501-1516, Jul 2021, doi: 10.1177/0271678X20982383.

[124] C. Grochowski, L. Jakub, K. Piotr, and R. and Maciejewski, "Oxidative stress in cerebral small vessel disease. Role of reactive species," *Free Radical Research,* vol. 52, no. 1, pp. 1-13, 2018/01/02 2018, doi: 10.1080/10715762.2017.1402304.

[125] A. A. Miller, T. M. De Silva, C. P. Judkins, H. Diep, G. R. Drummond, and C. G. Sobey, "Augmented superoxide production by Nox2-containing NADPH oxidase causes cerebral artery dysfunction during hypercholesterolemia," (in eng), *Stroke,* vol. 41, no. 4, pp. 784-9, Apr 2010, doi: 10.1161/strokeaha.109.575365.

[126] H. Girouard, L. Park, J. Anrather, P. Zhou, and C. Iadecola, "Cerebrovascular nitrosative stress mediates neurovascular and endothelial dysfunction induced by angiotensin II," (in eng), *Arterioscler Thromb Vasc Biol,* vol. 27, no. 2, pp. 303-9, Feb 2007, doi: 10.1161/01.Atv.0000253885.41509.25.

[127] W. R. Brown, "A review of string vessels or collapsed, empty basement membrane tubes," (in eng), *J Alzheimers Dis,* vol. 21, no. 3, pp. 725-39, 2010, doi: 10.3233/jad-2010-100219.

[128] B. J. Graff, S. L. Harrison, S. J. Payne, and W. K. El-Bouri, "Regional Cerebral Blood Flow Changes in Healthy Ageing and Alzheimer’s Disease: A Narrative Review," *Cerebrovascular Diseases,* vol. 52, no. 1, pp. 11-20, 2023, doi: 10.1159/000524797.

[129] J. J. Chen, H. D. Rosas, and D. H. Salat, "Age-associated reductions in cerebral blood flow are independent from regional atrophy," (in eng), *Neuroimage,* vol. 55, no. 2, pp. 468-78, Mar 15 2011, doi: 10.1016/j.neuroimage.2010.12.032.

[130] B. P. Austin *et al.*, "Effects of Hypoperfusion in Alzheimer's Disease," *Journal of Alzheimer’s Disease,* vol. 26, no. s3, pp. 123-133, 2011, doi: 10.3233/jad-2011-0010.

[131] C. C. Hays, Z. Z. Zlatar, and C. E. Wierenga, "The Utility of Cerebral Blood Flow as a Biomarker of Preclinical Alzheimer's Disease," (in eng), *Cell Mol Neurobiol,* vol. 36, no. 2, pp. 167-79, Mar 2016, doi: 10.1007/s10571-015-0261-z.

[132] H. J. Yoon, K. W. Park, Y. J. Jeong, and D. Y. Kang, "Significant correlation between cerebral hypoperfusion and neuropsychological assessment scores of patients with mild cognitive impairment," (in eng), *Nucl Med Commun,* vol. 33, no. 8, pp. 848-58, Aug 2012, doi: 10.1097/MNM.0b013e32835587f8.

[133] L. L. Chao *et al.*, "Patterns of cerebral hypoperfusion in amnestic and dysexecutive MCI," (in eng), *Alzheimer Dis Assoc Disord,* vol. 23, no. 3, pp. 245-52, Jul-Sep 2009, doi: 10.1097/WAD.0b013e318199ff46.

[134] P. M. Pimentel-Coelho, J. P. Michaud, and S. Rivest, "Effects of mild chronic cerebral hypoperfusion and early amyloid pathology on spatial learning and the cellular innate immune response in mice," (in eng), *Neurobiol Aging,* vol. 34, no. 3, pp. 679-93, Mar 2013, doi: 10.1016/j.neurobiolaging.2012.06.025.

[135] L. Qiu, G. Ng, E. K. Tan, P. Liao, N. Kandiah, and L. Zeng, "Chronic cerebral hypoperfusion enhances Tau hyperphosphorylation and reduces autophagy in Alzheimer's disease mice," (in eng), *Sci Rep,* vol. 6, p. 23964, Apr 6 2016, doi: 10.1038/srep23964.

[136] M. Yamada *et al.*, "The Influence of Chronic Cerebral Hypoperfusion on Cognitive Function and Amyloid β Metabolism in APP Overexpressing Mice," *PLOS ONE,* vol. 6, no. 1, p. e16567, 2011, doi: 10.1371/journal.pone.0016567.

[137] Y. Zhai *et al.*, "Chronic cerebral hypoperfusion accelerates Alzheimer’s disease pathology with cerebrovascular remodeling in a novel mouse model," *Journal of Alzheimer's Disease,* vol. 53, no. 3, pp. 893-905, 2016.

[138] J. S. Lee, D. S. Im, Y.-S. An, J. M. Hong, B. J. Gwag, and I. S. Joo, "Chronic cerebral hypoperfusion in a mouse model of Alzheimer's disease: an additional contributing factor of cognitive impairment," *Neuroscience letters,* vol. 489, no. 2, pp. 84-88, 2011.

[139] Q. Yang *et al.*, "Autophagy Regulation Attenuates Neuroinflammation and Cognitive Decline in an Alzheimer's Disease Mouse Model with Chronic Cerebral Hypoperfusion," *Inflammation,* Jun 29 2024, doi: 10.1007/s10753-024-02043-0.

[140] O. Bracko, B. N. Njiru, M. Swallow, M. Ali, M. Haft-Javaherian, and C. B. Schaffer, "Increasing cerebral blood flow improves cognition into late stages in Alzheimer's disease mice," (in eng), *J Cereb Blood Flow Metab,* vol. 40, no. 7, pp. 1441-1452, Jul 2020, doi: 10.1177/0271678x19873658.

[141] J. C. Cruz Hernandez *et al.*, "Neutrophil adhesion in brain capillaries reduces cortical blood flow and impairs memory function in Alzheimer's disease mouse models," *Nat Neurosci,* vol. 22, no. 3, pp. 413-420, Mar 2019, doi: 10.1038/s41593-018-0329-4.

[142] F. Fan and R. J. Roman, "Reversal of cerebral hypoperfusion: a novel therapeutic target for the treatment of AD/ADRD?," *Geroscience,* vol. 43, no. 2, pp. 1065-1067, Apr 2021, doi: 10.1007/s11357-021-00357-7.

[143] V. Rajeev *et al.*, "Pathophysiology of blood brain barrier dysfunction during chronic cerebral hypoperfusion in vascular cognitive impairment," *Theranostics,* vol. 12, no. 4, pp. 1639-1658, 2022, doi: 10.7150/thno.68304.

[144] H. Tayler, J. S. Miners, O. Guzel, R. MacLachlan, and S. Love, "Mediators of cerebral hypoperfusion and blood-brain barrier leakiness in Alzheimer's disease, vascular dementia

and mixed dementia," *Brain Pathol,* vol. 31, no. 4, p. e12935, Jul 2021, doi: 10.1111/bpa.12935.

[145] Y. Matsui *et al.*, "Brain-derived endothelial cells are neuroprotective in a chronic cerebral hypoperfusion mouse model," *Communications Biology,* vol. 7, no. 1, p. 338, 2024/03/18 2024, doi: 10.1038/s42003-024-06030-x.

[146] H. Liu and J. and Zhang, "Cerebral Hypoperfusion and Cognitive Impairment: The Pathogenic Role of Vascular Oxidative Stress," *International Journal of Neuroscience,* vol. 122, no. 9, pp. 494-499, 2012/07/17 2012, doi: 10.3109/00207454.2012.686543.

[147] S. Tarantini *et al.*, "Circulating IGF-1 deficiency exacerbates hypertension-induced microvascular rarefaction in the mouse hippocampus and retrosplenial cortex: implications for cerebromicrovascular and brain aging," *Age (Dordr),* vol. 38, no. 4, pp. 273-289, Aug 2016, doi: 10.1007/s11357-016-9931-0.

[148] W. G. Mayhan, "Disruption of blood-brain barrier during acute hypertension in adult and aged rats," (in eng), *Am J Physiol,* vol. 258, no. 6 Pt 2, pp. H1735-8, Jun 1990, doi: 10.1152/ajpheart.1990.258.6.H1735.

[149] P. Toth *et al.*, "Age-related autoregulatory dysfunction and cerebromicrovascular injury in mice with angiotensin II-induced hypertension," (in eng), *J Cereb Blood Flow Metab,* vol. 33, no. 11, pp. 1732-42, Nov 2013, doi: 10.1038/jcbfm.2013.143.

[150] C. S. Wilcox and W. J. Welch, "Oxidative Stress: Cause or Consequence of Hypertension," *Experimental Biology and Medicine,* vol. 226, no. 7, pp. 619-620, 2001, doi: 10.1177/153537020222600702.

[151] K. Takemori, T. Murakami, T. Kometani, and H. Ito, "Possible involvement of oxidative stress as a causative factor in blood–brain barrier dysfunction in stroke-prone spontaneously hypertensive rats," *Microvascular Research,* vol. 90, pp. 169-172, 2013/11/01/ 2013, doi: https://doi.org/10.1016/j.mvr.2013.08.005.

[152] N. Calcinaghi *et al.*, "Multimodal imaging in rats reveals impaired neurovascular coupling in sustained hypertension," *Stroke,* vol. 44, no. 7, pp. 1957-64, Jul 2013, doi: 10.1161/STROKEAHA.111.000185.

[153] J. C. Romero and J. F. Reckelhoff, "Role of Angiotensin and Oxidative Stress in Essential Hypertension," *Hypertension,* vol. 34, no. 4, pp. 943-949, 1999, doi: doi:10.1161/01.HYP.34.4.943.

[154] F. M. Faraci and D. D. Heistad, "Regulation of the Cerebral Circulation: Role of Endothelium and Potassium Channels," *Physiological Reviews,* vol. 78, no. 1, pp. 53-97, 1998, doi: 10.1152/physrev.1998.78.1.53.

[155] J. R. Jennings *et al.*, "Reduced cerebral blood flow response and compensation among patients with untreated hypertension," (in eng), *Neurology,* vol. 64, no. 8, pp. 1358-65, Apr 26 2005, doi: 10.1212/01.Wnl.0000158283.28251.3c.

[156] D. Weiss, J. J. Kools, and W. R. Taylor, "Angiotensin II–Induced Hypertension Accelerates the Development of Atherosclerosis in ApoE-Deficient Mice," *Circulation,* vol. 103, no. 3, pp. 448-454, 2001, doi: doi:10.1161/01.CIR.103.3.448.

[157] A. V. Poznyak *et al.*, "Hypertension as a risk factor for atherosclerosis: Cardiovascular risk assessment," *Front Cardiovasc Med,* vol. 9, p. 959285, 2022, doi: 10.3389/fcvm.2022.959285.

[158] S. E. Kjeldsen, "Hypertension and cardiovascular risk: General aspects," *Pharmacological Research,* vol. 129, pp. 95-99, 2018/03/01/ 2018, doi: https://doi.org/10.1016/j.phrs.2017.11.003.

[159] C. J. Dickinson, "Why are strokes related to hypertension? Classic studies and hypotheses revisited," (in eng), *J Hypertens,* vol. 19, no. 9, pp. 1515-21, Sep 2001, doi: 10.1097/00004872-200109000-00001.

[160] K. Rahimi *et al.*, "Age-stratified and blood-pressure-stratified effects of blood-pressure-lowering pharmacotherapy for the prevention of cardiovascular disease and death: an individual participant-level data meta-analysis," *The Lancet,* vol. 398, no. 10305, pp. 1053-1064, 2021/09/18/ 2021, doi: https://doi.org/10.1016/S0140-6736(21)01921-8.

[161] D. Carnevale and G. Lembo, "'Alzheimer-like' pathology in a murine model of arterial hypertension," *Biochemical Society Transactions,* vol. 39, no. 4, pp. 939-944, 2011, doi: 10.1042/bst0390939.

[162] C. Díaz-Ruiz *et al.*, "Role of Hypertension in Aggravating Abeta Neuropathology of AD Type and Tau-Mediated Motor Impairment," (in eng), *Cardiovasc Psychiatry Neurol,* vol. 2009, p. 107286, 2009, doi: 10.1155/2009/107286.

[163] T. Kurata *et al.*, "Telmisartan reduces progressive accumulation of cellular amyloid beta and phosphorylated tau with inflammatory responses in aged spontaneously hypertensive stroke resistant rat," (in eng), *J Stroke Cerebrovasc Dis,* vol. 23, no. 10, pp. 2580-2590, Nov-Dec 2014, doi: 10.1016/j.jstrokecerebrovasdis.2014.05.023.

[164] K. M. Bellew, J. G. Pigeon, P. E. Stang, W. Fleischman, R. M. Gardner, and W. W. Baker, "Hypertension and the Rate of Cognitive Decline in Patients With Dementia of the Alzheimer Type," *Alzheimer Disease & Associated Disorders,* vol. 18, no. 4, pp. 208-213, 2004. [Online]. Available: https://journals.lww.com/alzheimerjournal/fulltext/2004/10000/hypertension_and_the_rate_of_cognitive_decline_in.9.aspx.

[165] G. A. Fishbein and M. C. Fishbein, "Arteriosclerosis: rethinking the current classification," (in eng), *Arch Pathol Lab Med,* vol. 133, no. 8, pp. 1309-16, Aug 2009, doi: 10.5858/133.8.1309.

[166] S. E. Greenwald, "Pulse pressure and arterial elasticity," *QJM: An International Journal of Medicine,* vol. 95, no. 2, pp. 107-112, 2002, doi: 10.1093/qjmed/95.2.107.

[167] I. S. Mackenzie, I. B. Wilkinson, and J. R. Cockcroft, "Assessment of arterial stiffness in clinical practice," (in eng), *Qjm,* vol. 95, no. 2, pp. 67-74, Feb 2002, doi: 10.1093/qjmed/95.2.67.

[168] M. F. O'Rourke and M. G. Taylor, "Vascular Impedance of the Femoral Bed," *Circulation Research,* vol. 18, no. 2, pp. 126-139, 1966, doi: doi:10.1161/01.RES.18.2.126.

[169] E. D. Lehmann, "Noninvasive measurements of aortic stiffness: methodological considerations," (in eng), *Pathol Biol (Paris),* vol. 47, no. 7, pp. 716-30, Sep 1999.

[170] G. F. Mitchell *et al.*, "Arterial stiffness, pressure and flow pulsatility and brain structure and function: the Age, Gene/Environment Susceptibility--Reykjavik study," *Brain,* vol. 134, no. Pt 11, pp. 3398-407, Nov 2011, doi: 10.1093/brain/awr253.

[171] J. Janzen, "The microscopic transitional zone between elastic and muscular arteries," (in eng), *Arch Mal Coeur Vaiss,* vol. 97, no. 9, pp. 909-14, Sep 2004.

[172] M. Yildiz, A. A. Oktay, M. H. Stewart, R. V. Milani, H. O. Ventura, and C. J. Lavie, "Left ventricular hypertrophy and hypertension," *Prog Cardiovasc Dis,* vol. 63, no. 1, pp. 10-21, Jan-Feb 2020, doi: 10.1016/j.pcad.2019.11.009.

[173] A. Ganau *et al.*, "Patterns of left ventricular hypertrophy and geometric remodeling in essential hypertension," (in eng), *J Am Coll Cardiol,* vol. 19, no. 7, pp. 1550-8, Jun 1992, doi: 10.1016/0735-1097(92)90617-v.

[174] J. Rawlins, A. Bhan, and S. Sharma, "Left ventricular hypertrophy in athletes," *European Journal of Echocardiography,* vol. 10, no. 3, pp. 350-356, 2009, doi: 10.1093/ejechocard/jep017.

[175] C. S. Desai, H. Ning, and D. M. Lloyd-Jones, "Competing cardiovascular outcomes associated with electrocardiographic left ventricular hypertrophy: the Atherosclerosis Risk in Communities Study," *Heart,* vol. 98, no. 4, pp. 330-334, 2012, doi: 10.1136/heartjnl-2011-300819.

[176] M. Bikkina *et al.*, "Left Ventricular Mass and Risk of Stroke in an Elderly Cohort: The Framingham Heart Study," *JAMA,* vol. 272, no. 1, pp. 33-36, 1994, doi: 10.1001/jama.1994.03520010045030.

[177] S. K. Mehta *et al.*, "Left Ventricular Hypertrophy, Subclinical Atherosclerosis, and Inflammation," *Hypertension,* vol. 49, no. 6, pp. 1385-1391, 2007, doi: doi:10.1161/HYPERTENSIONAHA.107.087890.

[178] D. Watabe *et al.*, "Electrocardiographic Left Ventricular Hypertrophy and Arterial Stiffness: The Ohasama Study," *American Journal of Hypertension,* vol. 19, no. 12, pp. 1199-1205, 2006, doi: 10.1016/j.amjhyper.2006.05.001.

[179] S. Laurent *et al.*, "Aortic Stiffness Is an Independent Predictor of All-Cause and Cardiovascular Mortality in Hypertensive Patients," *Hypertension,* vol. 37, no. 5, pp. 1236-1241, 2001, doi: doi:10.1161/01.HYP.37.5.1236.

[180] L. L. Cooper *et al.*, "Cerebrovascular Damage Mediates Relations Between Aortic Stiffness and Memory," *Hypertension*, vol. 67, no. 1, pp. 176-82, Jan 2016, doi: 10.1161/HYPERTENSIONAHA.115.06398.

[181] C.-P. Chung, H.-Y. Lee, P.-C. Lin, and P.-N. Wang, "Cerebral Artery Pulsatility is Associated with Cognitive Impairment and Predicts Dementia in Individuals with Subjective Memory Decline or Mild Cognitive Impairment," *Journal of Alzheimer's Disease,* vol. 60, pp. 625-632, 2017, doi: 10.3233/JAD-170349.

[182] Y. Shi, Michael J. Thrippleton, I. Marshall, and Joanna M. Wardlaw, "Intracranial pulsatility in patients with cerebral small vessel disease: a systematic review," *Clinical Science,* vol. 132, no. 1, pp. 157-171, 2018, doi: 10.1042/cs20171280.

[183] F.-F. Zhai *et al.*, "Arterial Stiffness and Cerebral Small Vessel Disease," (in English), *Frontiers in Neurology*, Original Research vol. 9, 2018-August-28 2018, doi: 10.3389/fneur.2018.00723.

[184] A. Wahlin, K. Ambarki, R. Birgander, J. Malm, and A. Eklund, "Intracranial pulsatility is associated with regional brain volume in elderly individuals," *Neurobiol Aging*, vol. 35, no. 2, pp. 365-72, Feb 2014, doi: 10.1016/j.neurobiolaging.2013.08.026.

[185] S. R. Waldstein, S. C. Rice, J. F. Thayer, S. S. Najjar, A. Scuteri, and A. B. Zonderman, "Pulse Pressure and Pulse Wave Velocity Are Related to Cognitive Decline in the Baltimore Longitudinal Study of Aging," *Hypertension*, vol. 51, no. 1, pp. 99-104, 2008, doi: doi:10.1161/HYPERTENSIONAHA.107.093674.

[186] I. Hajjar, F. C. Goldstein, G. S. Martin, and A. A. Quyyumi, "Roles of Arterial Stiffness and Blood Pressure in Hypertension-Associated Cognitive Decline in Healthy Adults," *Hypertension*, vol. 67, no. 1, pp. 171-5, Jan 2016, doi: 10.1161/HYPERTENSIONAHA.115.06277.

[187] C. Alvarez-Bueno *et al.*, "Arterial Stiffness and Cognition Among Adults: A Systematic Review and Meta-Analysis of Observational and Longitudinal Studies," *J Am Heart Assoc*, vol. 9, no. 5, p. e014621, Mar 3 2020, doi: 10.1161/JAHA.119.014621.

[188] N. Thorin-Trescases *et al.*, "Impact of pulse pressure on cerebrovascular events leading to age-related cognitive decline," *Am J Physiol Heart Circ Physiol*, vol. 314, no. 6, pp. H1214-H1224, Jun 1 2018, doi: 10.1152/ajpheart.00637.2017.

[189] C. Qiu, B. Winblad, M. Viitanen, and L. Fratiglioni, "Pulse Pressure and Risk of Alzheimer Disease in Persons Aged 75 Years and Older," *Stroke*, vol. 34, no. 3, pp. 594-599, 2003, doi: doi:10.1161/01.STR.0000060127.96986.F4.

[190] R. A. Levin, M. H. Carnegie, and D. S. Celermajer, "Pulse Pressure: An Emerging Therapeutic Target for Dementia," *Front Neurosci*, vol. 14, p. 669, 2020, doi: 10.3389/fnins.2020.00669.

[191] F.-D. Liu *et al.*, "Pulse pressure as an independent predictor of stroke: a systematic review and a meta-analysis," *Clinical Research in Cardiology*, vol. 105, no. 8, pp. 677-686, 2016/08/01 2016, doi: 10.1007/s00392-016-0972-2.

[192] C. M. McEniery *et al.*, "Endothelial function is associated with pulse pressure, pulse wave velocity, and augmentation index in healthy humans," *Hypertension*, vol. 48, no. 4, pp. 602-8, Oct 2006, doi: 10.1161/01.HYP.0000239206.64270.5f.

[193] M. E. Wagshul, P. K. Eide, and J. R. Madsen, "The pulsating brain: A review of experimental and clinical studies of intracranial pulsatility," *Fluids Barriers CNS*, vol. 8, no. 1, p. 5, Jan 18 2011, doi: 10.1186/2045-8118-8-5.

[194] G. Muhire *et al.*, "Arterial Stiffness Due to Carotid Calcification Disrupts Cerebral Blood Flow Regulation and Leads to Cognitive Deficits," *J Am Heart Assoc*, vol. 8, no. 9, p. e011630, May 7 2019, doi: 10.1161/JAHA.118.011630.

[195] L. M. Van Bortel, H. A. Struijker-Boudier, and M. E. Safar, "Pulse pressure, arterial stiffness, and drug treatment of hypertension," (in eng), *Hypertension*, vol. 38, no. 4, pp. 914-21, Oct 2001, doi: 10.1161/hy1001.095773.

[196] B. B. Biswal, "Resting state fMRI: a personal history," *Neuroimage,* vol. 62, no. 2, pp. 938-44, Aug 15 2012, doi: 10.1016/j.neuroimage.2012.01.090.

[197] G. L. Shulman *et al.*, "Common Blood Flow Changes across Visual Tasks: II. Decreases in Cerebral Cortex," (in eng), *J Cogn Neurosci,* vol. 9, no. 5, pp. 648-63, Fall 1997, doi: 10.1162/jocn.1997.9.5.648.

[198] M. D. Fox, A. Z. Snyder, J. L. Vincent, M. Corbetta, D. C. Van Essen, and M. E. Raichle, "The Human Brain is Intrinsically Organized into Dynamic, Anticorrelated Functional Networks.," *PNAS,* vol. 102, no. 27, pp. 9673-9678, 2005.

[199] M. D. Greicius, B. Krasnow, A. L. Reiss, and V. Menon, "Functional connectivity in the resting brain: A network analysis of the default mode hypothesis," *Proceedings of the National Academy of Sciences,* vol. 100, no. 1, pp. 253-258, 2003, doi: doi:10.1073/pnas.0135058100.

[200] B. A. Seitzman, A. Z. Snyder, E. C. Leuthardt, and J. S. Shimony, "The State of Resting State Networks," *Top Magn Reson Imaging,* vol. 28, no. 4, pp. 189-196, Aug 2019, doi: 10.1097/RMR.0000000000000214.

[201] A. W. Bero *et al.*, "Bidirectional relationship between functional connectivity and amyloid-beta deposition in mouse brain," *J Neurosci,* vol. 32, no. 13, pp. 4334-40, Mar 28 2012, doi: 10.1523/JNEUROSCI.5845-11.2012.

[202] M. D. Greicius, G. Srivastava, A. L. Reiss, and V. Menon, "Default-mode network activity distinguishes Alzheimer's disease from healthy aging: evidence from functional MRI," (in eng), *Proc Natl Acad Sci U S A,* vol. 101, no. 13, pp. 4637-42, Mar 30 2004, doi: 10.1073/pnas.0308627101.

[203] M. P. van den Heuvel and H. E. Hulshoff Pol, "Exploring the brain network: a review on resting-state fMRI functional connectivity," *Eur Neuropsychopharmacol,* vol. 20, no. 8, pp. 519-34, Aug 2010, doi: 10.1016/j.euroneuro.2010.03.008.

[204] H.-C. Baggio *et al.*, "Cognitive impairment and resting-state network connectivity in Parkinson's disease," *Human Brain Mapping,* vol. 36, no. 1, pp. 199-212, 2015, doi: https://doi.org/10.1002/hbm.22622.

[205] O. Dekhil *et al.*, "Using resting state functional MRI to build a personalized autism diagnosis system," *PLOS ONE,* vol. 13, no. 10, p. e0206351, 2018, doi: 10.1371/journal.pone.0206351.

[206] Z. A. Huang, Z. Zhu, C. H. Yau, and K. C. Tan, "Identifying Autism Spectrum Disorder From Resting-State fMRI Using Deep Belief Network," *IEEE Trans Neural Netw Learn Syst*, vol. 32, no. 7, pp. 2847-2861, Jul 2021, doi: 10.1109/TNNLS.2020.3007943.

[207] J. Meng *et al.*, "Impairments in intrinsic functional networks in type 2 diabetes: A meta-analysis of resting-state functional connectivity," *Frontiers in Neuroendocrinology,* vol. 66, p. 100992, 2022/07/01/ 2022, doi: https://doi.org/10.1016/j.yfrne.2022.100992.

[208] D. S. Bassett, B. G. Nelson, B. A. Mueller, J. Camchong, and K. O. Lim, "Altered resting state complexity in schizophrenia," *Neuroimage,* vol. 59, no. 3, pp. 2196-207, Feb 1 2012, doi: 10.1016/j.neuroimage.2011.10.002.

[209] X. Chang, G. Collin, R. C. W. Mandl, W. Cahn, and R. S. Kahn, "Interhemispheric connectivity and hemispheric specialization in schizophrenia patients and their unaffected siblings," *Neuroimage Clin,* vol. 21, p. 101656, 2019, doi: 10.1016/j.nicl.2019.101656.

[210] T. E. Mwansisya *et al.*, "The diminished interhemispheric connectivity correlates with negative symptoms and cognitive impairment in first-episode schizophrenia," *Schizophr Res,* vol. 150, no. 1, pp. 144-50, Oct 2013, doi: 10.1016/j.schres.2013.07.018.

[211] J. M. Sheffield and D. M. Barch, "Cognition and resting-state functional connectivity in schizophrenia," *Neuroscience & Biobehavioral Reviews,* vol. 61, pp. 108-120, 2016/02/01/ 2016, doi: https://doi.org/10.1016/j.neubiorev.2015.12.007.

[212] M. Porcu *et al.*, "Extracranial Carotid Artery Stenosis: The Effects on Brain and Cognition with a Focus on Resting-State Functional Connectivity," *J Neuroimaging,* vol. 30, no. 6, pp. 736-745, Nov 2020, doi: 10.1111/jon.12777.

[213] M. Porcu *et al.*, "Reorganization of brain networks following carotid endarterectomy: an exploratory study using resting state functional connectivity with a focus on the changes in Default Mode Network connectivity," *Eur J Radiol,* vol. 110, pp. 233-241, Jan 2019, doi: 10.1016/j.ejrad.2018.12.007.

[214] S. J. Son *et al.*, "Effect of hypertension on the resting-state functional connectivity in patients with Alzheimer's disease (AD)," *Archives of Gerontology and Geriatrics,* vol. 60, no. 1, pp. 210-216, 2015/01/01/ 2015, doi: https://doi.org/10.1016/j.archger.2014.09.012.

[215] T.-H. Hung *et al.*, "Investigating the effect of hypertension on vascular cognitive impairment by using the resting-state functional connectome," *Scientific Reports,* vol. 14, no. 1, p. 4580, 2024/02/25 2024, doi: 10.1038/s41598-024-54996-9.

[216] L. Carnevale, A. Maffei, A. Landolfi, G. Grillea, D. Carnevale, and G. Lembo, "Brain Functional Magnetic Resonance Imaging Highlights Altered Connections and Functional Networks in Patients With Hypertension," *Hypertension,* vol. 76, no. 5, pp. 1480-1490, 2020, doi: doi:10.1161/HYPERTENSIONAHA.120.15296.

[217] B. Zhang *et al.*, "Abnormal brain functional connectivity coupled with hypoperfusion measured by Resting-State fMRI: An additional contributing factor for cognitive impairment in patients with Alzheimer's disease," *Psychiatry Research: Neuroimaging,* vol. 289, pp. 18-25, 2019/07/30/ 2019, doi: https://doi.org/10.1016/j.pscychresns.2019.04.007.

[218] J.-Y. Hu *et al.*, "A novel approach for assessing hypoperfusion in stroke using spatial independent component analysis of resting-state fMRI," *Human Brain Mapping,* vol. 42, no. 16, pp. 5204-5216, 2021, doi: https://doi.org/10.1002/hbm.25610.

[219] H. Obrig *et al.*, "Spontaneous low frequency oscillations of cerebral hemodynamics and metabolism in human adults," *Neuroimage,* vol. 12, no. 6, pp. 623-39, Dec 2000, doi: 10.1006/nimg.2000.0657.

[220] E. van Diessen *et al.*, "Opportunities and methodological challenges in EEG and MEG resting state functional brain network research," *Clin Neurophysiol,* vol. 126, no. 8, pp. 1468-81, Aug 2015, doi: 10.1016/j.clinph.2014.11.018.

[221] M. J. Brookes *et al.*, "Investigating the electrophysiological basis of resting state networks using magnetoencephalography," *Proc Natl Acad Sci U S A,* vol. 108, no. 40, pp. 16783-8, Oct 4 2011, doi: 10.1073/pnas.1112685108.

[222] S. Belanger, B. O. de Souza, C. Casanova, and F. Lesage, "Correlation of hemodynamic and fluorescence signals under resting state conditions in mice's barrel field cortex," *Neurosci Lett,* vol. 616, pp. 177-81, Mar 11 2016, doi: 10.1016/j.neulet.2016.01.067.

[223] C. Tong, J. K. Dai, Y. Chen, K. Zhang, Y. Feng, and Z. Liang, "Differential coupling between subcortical calcium and BOLD signals during evoked and resting state through simultaneous calcium fiber photometry and fMRI," *Neuroimage,* vol. 200, pp. 405-413, Oct 15 2019, doi: 10.1016/j.neuroimage.2019.07.006.

[224] M. C. Murphy, K. C. Chan, S. G. Kim, and A. L. Vazquez, "Macroscale variation in resting-state neuronal activity and connectivity assessed by simultaneous calcium imaging, hemodynamic imaging and electrophysiology," *Neuroimage,* vol. 169, pp. 352-362, Apr 1 2018, doi: 10.1016/j.neuroimage.2017.12.070.

[225] T. Matsui, T. Murakami, and K. Ohki, "Neuronal Origin of the Temporal Dynamics of Spontaneous BOLD Activity Correlation," *Cereb Cortex,* vol. 29, no. 4, pp. 1496-1508, Apr 1 2019, doi: 10.1093/cercor/bhy045.

[226] A. Shmuel and D. A. Leopold, "Neuronal correlates of spontaneous fluctuations in fMRI signals in monkey visual cortex: Implications for functional connectivity at rest," *Hum Brain Mapp,* vol. 29, no. 7, pp. 751-61, Jul 2008, doi: 10.1002/hbm.20580.

[227] J. Britz, D. Van De Ville, and C. M. Michel, "BOLD correlates of EEG topography reveal rapid resting-state network dynamics," *Neuroimage,* vol. 52, no. 4, pp. 1162-70, Oct 1 2010, doi: 10.1016/j.neuroimage.2010.02.052.

[228] T. Hiltunen *et al.*, "Infra-slow EEG fluctuations are correlated with resting-state network dynamics in fMRI," *J Neurosci,* vol. 34, no. 2, pp. 356-62, Jan 8 2014, doi: 10.1523/JNEUROSCI.0276-13.2014.

[229] C. D. Hacker, A. Z. Snyder, M. Pahwa, M. Corbetta, and E. C. Leuthardt, "Frequency-specific electrophysiologic correlates of resting state fMRI networks," *Neuroimage,* vol. 149, pp. 446-457, Apr 1 2017, doi: 10.1016/j.neuroimage.2017.01.054.

[230] X. Gu, W. Chen, N. D. Volkow, A. P. Koretsky, C. Du, and Y. Pan, "Synchronized Astrocytic Ca(2+) Responses in Neurovascular Coupling during Somatosensory Stimulation and for the Resting State," *Cell Rep,* vol. 23, no. 13, pp. 3878-3890, Jun 26 2018, doi: 10.1016/j.celrep.2018.05.091.

[231] A. Q. Bauer, A. W. Kraft, P. W. Wright, A. Z. Snyder, J. M. Lee, and J. P. Culver, "Optical imaging of disrupted functional connectivity following ischemic stroke in mice," *Neuroimage,* vol. 99, pp. 388-401, Oct 1 2014, doi: 10.1016/j.neuroimage.2014.05.051.

[232] F.-J. Hsiao, F.-Y. Hsieh, W.-T. Chen, D.-C. Chu, and Y.-Y. Lin, "Altered Resting-State Cortical EEG Oscillations in Patients With Severe Asymptomatic Carotid Stenosis," *Clinical EEG and Neuroscience,* vol. 47, no. 2, pp. 142-149, 2016, doi: 10.1177/1550059414560396.

[233] N. Sadekova, D. Vallerand, E. Guevara, F. Lesage, and H. Girouard, "Carotid calcification in mice: a new model to study the effects of arterial stiffness on the brain," *J Am Heart Assoc,* vol. 2, no. 3, p. e000224, Jun 19 2013, doi: 10.1161/JAHA.113.000224.

[234] N. Sadekova *et al.*, "Arterial stiffness induced by carotid calcification leads to cerebral gliosis mediated by oxidative stress," *J Hypertens,* vol. 36, no. 2, pp. 286-298, Feb 2018, doi: 10.1097/HJH.0000000000001557.

[235] E. Guevara, N. Sadekova, H. Girouard, and F. Lesage, "Optical imaging of resting-state functional connectivity in a novel arterial stiffness model," *Biomed. Opt. Express,* vol. 4, no. 11, pp. 2332-2346, 2013/11/01 2013, doi: 10.1364/BOE.4.002332.

[236] Q. Li, H. Guo, D. W. Chou, A. Berndt, J. P. Sundberg, and J. Uitto, "Mutant Enpp1asj mice as a model for generalized arterial calcification of infancy," *Dis Model Mech,* vol. 6, no. 5, pp. 1227-35, Sep 2013, doi: 10.1242/dmm.012765.

[237] R. H. Zhou *et al.*, "Mitochondrial oxidative stress in aortic stiffening with age: the role of smooth muscle cell function," *Arterioscler Thromb Vasc Biol,* vol. 32, no. 3, pp. 745-55, Mar 2012, doi: 10.1161/ATVBAHA.111.243121.

[238] H. A. Rockman *et al.*, "Segregation of atrial-specific and inducible expression of an atrial natriuretic factor transgene in an in vivo murine model of cardiac hypertrophy," (in eng), *Proc Natl Acad Sci U S A,* vol. 88, no. 18, pp. 8277-81, Sep 15 1991, doi: 10.1073/pnas.88.18.8277.

[239] C. Ruwhof and A. van der Laarse, "Mechanical stress-induced cardiac hypertrophy: mechanisms and signal transduction pathways," (in eng), *Cardiovasc Res,* vol. 47, no. 1, pp. 23-37, Jul 2000, doi: 10.1016/s0008-6363(00)00076-6.

[240] C. J. Hartley *et al.*, "Vascular adaptations to transverse aortic banding in mice," presented at the 2001 Conference Proceedings of the 23rd Annual International Conference of the IEEE Engineering in Medicine and Biology Society, 2001.

[241] T. Furihata *et al.*, "The experimental model of transition from compensated cardiac hypertrophy to failure created by transverse aortic constriction in mice," *Int J Cardiol Heart Vasc,* vol. 11, pp. 24-28, Jun 2016, doi: 10.1016/j.ijcha.2016.03.007.

[242] L. Bosch *et al.*, "The transverse aortic constriction heart failure animal model: a systematic review and meta-analysis," *Heart Fail Rev,* vol. 26, no. 6, pp. 1515-1524, Nov 2021, doi: 10.1007/s10741-020-09960-w.

[243] D. A. Richards *et al.*, "Distinct Phenotypes Induced by Three Degrees of Transverse Aortic Constriction in Mice," *Sci Rep,* vol. 9, no. 1, p. 5844, Apr 10 2019, doi: 10.1038/s41598-019-42209-7.

[244] M. Skavdahl *et al.*, "Estrogen receptor-beta mediates male-female differences in the development of pressure overload hypertrophy," *Am J Physiol Heart Circ Physiol,* vol. 288, no. 2, pp. H469-76, Feb 2005, doi: 10.1152/ajpheart.00723.2004.

[245] D. Merino *et al.*, "Experimental modelling of cardiac pressure overload hypertrophy: Modified technique for precise, reproducible, safe and easy aortic arch banding-debanding in mice," *Sci Rep,* vol. 8, no. 1, p. 3167, Feb 16 2018, doi: 10.1038/s41598-018-21548-x.

[246] Y. Zhang *et al.*, "Fast and sensitive GCaMP calcium indicators for imaging neural populations," *Nature,* vol. 615, no. 7954, pp. 884-891, Mar 2023, doi: 10.1038/s41586-023-05828-9.

[247] T. W. Chen *et al.*, "Ultrasensitive fluorescent proteins for imaging neuronal activity," *Nature,* vol. 499, no. 7458, pp. 295-300, Jul 18 2013, doi: 10.1038/nature12354.

[248] H. H. Yang and F. St-Pierre, "Genetically Encoded Voltage Indicators: Opportunities and Challenges," *J Neurosci,* vol. 36, no. 39, pp. 9977-89, Sep 28 2016, doi: 10.1523/JNEUROSCI.1095-16.2016.

[249] Y. Xie *et al.*, "Resolution of High-Frequency Mesoscale Intracortical Maps Using the Genetically Encoded Glutamate Sensor iGluSnFR," *J Neurosci,* vol. 36, no. 4, pp. 1261-72, Jan 27 2016, doi: 10.1523/JNEUROSCI.2744-15.2016.

[250] M. T. Valley *et al.*, "Separation of hemodynamic signals from GCaMP fluorescence measured with wide-field imaging," *J Neurophysiol,* vol. 123, no. 1, pp. 356-366, Jan 1 2020, doi: 10.1152/jn.00304.2019.

[251] M. P. Vanni and T. H. Murphy, "Mesoscale transcranial spontaneous activity mapping in GCaMP3 transgenic mice reveals extensive reciprocal connections between areas of somatomotor cortex," *J Neurosci,* vol. 34, no. 48, pp. 15931-46, Nov 26 2014, doi: 10.1523/JNEUROSCI.1818-14.2014.

[252] M. P. Vanni, A. W. Chan, M. Balbi, G. Silasi, and T. H. Murphy, "Mesoscale Mapping of Mouse Cortex Reveals Frequency-Dependent Cycling between Distinct Macroscale Functional Modules," *J Neurosci,* vol. 37, no. 31, pp. 7513-7533, Aug 2 2017, doi: 10.1523/JNEUROSCI.3560-16.2017.

[253] S. L. Jacques, "Optical properties of biological tissues: a review," *Phys Med Biol,* vol. 58, no. 11, pp. R37-61, Jun 7 2013, doi: 10.1088/0031-9155/58/11/R37.

[254] Y. Ma *et al.,* "Wide-field optical mapping of neural activity and brain haemodynamics: considerations and novel approaches," *Philos Trans R Soc Lond B Biol Sci,* vol. 371, no. 1705, Oct 5 2016, doi: 10.1098/rstb.2015.0360.

[255] F. Helmchen and W. Denk, "Deep tissue two-photon microscopy," *Nat Methods,* vol. 2, no. 12, pp. 932-40, Dec 2005, doi: 10.1038/nmeth818.

[256] H. Cheng *et al.*, "Deep-brain 2-photon fluorescence microscopy in vivo excited at the1700 nm window," *Opt. Lett.*, vol. 44, no. 17, pp. 4432-4435, 2019/09/01 2019, doi: 10.1364/OL.44.004432.

[257] A. Y. Shih, J. D. Driscoll, P. J. Drew, N. Nishimura, C. B. Schaffer, and D. Kleinfeld, "Two-photon microscopy as a tool to study blood flow and neurovascular coupling in the rodent brain," *J Cereb Blood Flow Metab,* vol. 32, no. 7, pp. 1277-309, Jul 2012, doi: 10.1038/jcbfm.2011.196.

[258] W. Denk, J. H. Strickler, and W. W. Webb, "Two-Photon Laser Scanning Fluorescence Microscopy," *Science,* vol. 248, no. 4951, pp. 73-76, 1990, doi: doi:10.1126/science.2321027.

[259] J. L. Wu *et al.*, "Ultrafast laser-scanning time-stretch imaging at visible wavelengths," *Light Sci Appl,* vol. 6, no. 1, p. e16196, Jan 2017, doi: 10.1038/lsa.2016.196.

[260] J. Wu *et al.*, "Kilohertz two-photon fluorescence microscopy imaging of neural activity in vivo," *Nat Methods,* vol. 17, no. 3, pp. 287-290, Mar 2020, doi: 10.1038/s41592-020-0762-7.

[261] G. Meng *et al.*, "Ultrafast two-photon fluorescence imaging of cerebral blood circulation in the mouse brain in vivo," *Proc Natl Acad Sci U S A,* vol. 119, no. 23, p. e2117346119, Jun 7 2022, doi: 10.1073/pnas.2117346119.

[262] A. Nieto-Posadas *et al.*, "Change in network connectivity during fictive-gasping generation in hypoxia: prevention by a metabolic intermediate," *Front Physiol,* vol. 5, p. 265, 2014, doi: 10.3389/fphys.2014.00265.

[263] A. M. Baig, "Computing the Effects of SARS-CoV-2 on Respiration Regulatory Mechanisms in COVID-19," *ACS Chemical Neuroscience,* vol. 11, no. 16, pp. 2416-2421, 2020/08/19 2020, doi: 10.1021/acschemneuro.0c00349.

[264] F. Peña and J. M. Ramirez, "Hypoxia-induced changes in neuronal network properties," (in eng), *Mol Neurobiol,* vol. 32, no. 3, pp. 251-83, Dec 2005, doi: 10.1385/mn:32:3:251.

[265] J. Van der Post, L. A. W. Noordzij, M. L. de Kam, G. J. Blauw, A. F. Cohen, and J. M. A. van Gerven, "Evaluation of tests of central nervous system performance after hypoxemia for a model for cognitive impairment," *Journal of Psychopharmacology,* vol. 16, no. 4, pp. 337-343, 2002, doi: 10.1177/026988110201600408.

[266] N. Tsarouchas, K. Benedek, A. Bezerianos, G. Benedek, and S. Keri, "Effects of moderate hypobaric hypoxia on evoked categorical visuocognitive responses," *Clinical Neurophysiology,* vol. 119, no. 7, pp. 1475-1485, 2008/07/01/ 2008, doi: https://doi.org/10.1016/j.clinph.2008.02.021.

[267] T. McMorris, B. J. Hale, M. Barwood, J. Costello, and J. Corbett, "Effect of acute hypoxia on cognition: A systematic review and meta-regression analysis," *Neuroscience & Biobehavioral Reviews,* vol. 74, pp. 225-232, 2017/03/01/ 2017, doi: https://doi.org/10.1016/j.neubiorev.2017.01.019.

[268] J. V. Brugniaux, A. N. Hodges, P. J. Hanly, and M. J. Poulin, "Cerebrovascular responses to altitude," *Respir Physiol Neurobiol,* vol. 158, no. 2-3, pp. 212-23, Sep 30 2007, doi: 10.1016/j.resp.2007.04.008.

[269] S. S. Kety and C. F. Schmidt, "The effects of altered arterial tensions of carbon dioxide and oxygen on cerebral blood flow and cerebral oxygen consumption of normal young men," *The Journal of clinical investigation,* vol. 27, no. 4, pp. 484-492, 1948.

[270] A. D. Harris *et al.*, "Cerebral blood flow response to acute hypoxic hypoxia," *NMR Biomed,* vol. 26, no. 12, pp. 1844-52, Dec 2013, doi: 10.1002/nbm.3026.

[271] P. N. Ainslie and A. W. Subudhi, "Cerebral blood flow at high altitude," (in eng), *High Alt Med Biol,* vol. 15, no. 2, pp. 133-40, Jun 2014, doi: 10.1089/ham.2013.1138.

[272] A. P. Binks, V. J. Cunningham, L. Adams, and R. B. Banzett, "Gray matter blood flow change is unevenly distributed during moderate isocapnic hypoxia in humans," *J Appl Physiol (1985),* vol. 104, no. 1, pp. 212-7, Jan 2008, doi: 10.1152/japplphysiol.00069.2007.

[273] J. S. Lawley, J. H. Macdonald, S. J. Oliver, and P. G. Mullins, "Unexpected reductions in regional cerebral perfusion during prolonged hypoxia," *J Physiol,* vol. 595, no. 3, pp. 935-947, Feb 1 2017, doi: 10.1113/JP272557.

[274] P. J. Cohen, S. C. Alexander, T. C. Smith, M. Reivich, and H. Wollman, "Effects of hypoxia and normocarbia on cerebral blood flow and metabolism in conscious man," (in eng), *J Appl Physiol,* vol. 23, no. 2, pp. 183-9, Aug 1967, doi: 10.1152/jappl.1967.23.2.183.

[275] C. K. Willie *et al.*, "Regional brain blood flow in man during acute changes in arterial blood gases," (in eng), *J Physiol,* vol. 590, no. 14, pp. 3261-75, Jul 15 2012, doi: 10.1113/jphysiol.2012.228551.

[276] I. Fukushi *et al.*, "Effects of arundic acid, an astrocytic modulator, on the cerebral and respiratory functions in severe hypoxia," *Respir Physiol Neurobiol,* vol. 226, pp. 24-9, Jun 2016, doi: 10.1016/j.resp.2015.11.011.

[277] W. Feng, C. Zhang, and D. Zhu, "Comparison of Cortical and Cutaneous Vascular Hemodynamic Changes in Hypoxia by Using in Vivo Skull and Skin Optical Clearing Techniques," *IEEE Journal of Selected Topics in Quantum Electronics,* vol. 27, no. 4, pp. 1-7, 2021, doi: 10.1109/jstqe.2021.3062595.

[278] U. Noth, F. Kotajima, R. Deichmann, R. Turner, and D. R. Corfield, "Mapping of the cerebral vascular response to hypoxia and hypercapnia using quantitative perfusion MRI at 3 T," *NMR Biomed,* vol. 21, no. 5, pp. 464-72, Jun 2008, doi: 10.1002/nbm.1210.

[279] D. De Bels *et al.*, "Variation of Cognitive Function During a Short Stay at Hypobaric Hypoxia Chamber (Altitude: 3842 M)," *Front Physiol,* vol. 10, p. 806, 2019, doi: 10.3389/fphys.2019.00806.

[280] J. Virués-Ortega, G. Buela-Casal, E. Garrido, and B. Alcázar, "Neuropsychological functioning associated with high-altitude exposure," *Neuropsychology review,* vol. 14, no. 4, pp. 197-224, 2004.

[281] P. Maiti, S. B. Singh, B. Mallick, S. Muthuraju, and G. Ilavazhagan, "High altitude memory impairment is due to neuronal apoptosis in hippocampus, cortex and striatum," *Journal of Chemical Neuroanatomy,* vol. 36, no. 3, pp. 227-238, 2008/12/01/ 2008, doi: https://doi.org/10.1016/j.jchemneu.2008.07.003.

[282] P. Lipton and T. S. Whittingham, "The effect of hypoxia on evoked potentials in the in vitro hippocampus," (in eng), *J Physiol,* vol. 287, pp. 427-38, Feb 1979, doi: 10.1113/jphysiol.1979.sp012668.

[283] H. J. Luhmann and U. Heinemann, "Hypoxia-induced functional alterations in adult rat neocortex," *Journal of Neurophysiology,* vol. 67, no. 4, pp. 798-811, 1992, doi: 10.1152/jn.1992.67.4.798.

[284] J. A. Neubauer and J. Sunderram, "Oxygen-sensing neurons in the central nervous system," *Journal of Applied Physiology,* vol. 96, no. 1, pp. 367-374, 2004, doi: 10.1152/japplphysiol.00831.2003.

[285] E. J. Gonzalez-Rothi, K. Z. Lee, E. A. Dale, P. J. Reier, G. S. Mitchell, and D. D. Fuller, "Intermittent hypoxia and neurorehabilitation," *J Appl Physiol (1985),* vol. 119, no. 12, pp. 1455-65, Dec 15 2015, doi: 10.1152/japplphysiol.00235.2015.

[286] M. D. Fox and M. E. Raichle, "Spontaneous fluctuations in brain activity observed with functional magnetic resonance imaging," *Nature Reviews Neuroscience,* vol. 8, no. 9, pp. 700-711, 2007/09/01 2007, doi: 10.1038/nrn2201.

[287] A. Badhwar, A. Tam, C. Dansereau, P. Orban, F. Hoffstaedter, and P. Bellec, "Resting-state network dysfunction in Alzheimer's disease: A systematic review and meta-analysis," *Alzheimer's & Dementia: Diagnosis, Assessment & Disease Monitoring,* vol. 8, pp. 73-85, 2017/01/01/ 2017, doi: https://doi.org/10.1016/j.dadm.2017.03.007.

[288] J. Zhang *et al.*, "Alteration of Spontaneous Brain Activity After Hypoxia-Reoxygenation: A Resting-State fMRI Study," *High Alt Med Biol,* vol. 18, no. 1, pp. 20-26, Mar 2017, doi: 10.1089/ham.2016.0083.

[289] H. J. Li, X. J. Dai, H. H. Gong, X. Nie, W. Zhang, and D. C. Peng, "Aberrant spontaneous low-frequency brain activity in male patients with severe obstructive sleep apnea revealed by resting-state functional MRI," *Neuropsychiatr Dis Treat,* vol. 11, pp. 207-14, 2015, doi: 10.2147/NDT.S73730.

[290] H. J. Li, X. Nie, H. H. Gong, W. Zhang, S. Nie, and D. C. Peng, "Abnormal resting-state functional connectivity within the default mode network subregions in male patients with obstructive sleep apnea," *Neuropsychiatr Dis Treat,* vol. 12, pp. 203-12, 2016, doi: 10.2147/NDT.S97449.

[291] C. M. Hill *et al.*, "Cognitive performance in high-altitude Andean residents compared with low-altitude populations: From childhood to older age," *Neuropsychology,* vol. 28, no. 5, pp. 752-760, 2014, doi: 10.1037/neu0000065.

[292] K. Gagnon *et al.*, "Cognitive impairment in obstructive sleep apnea," *Pathologie Biologie,* vol. 62, no. 5, pp. 233-240, 2014/10/01/ 2014, doi: https://doi.org/10.1016/j.patbio.2014.05.015.

[293] L. J. Findley, J. T. Barth, D. C. Powers, S. C. Wilhoit, D. G. Boyd, and P. M. Suratt, "Cognitive Impairment in Patients with Obstructive Sleep Apnea and Associated Hypoxemia," *Chest,* vol. 90, no. 5, pp. 686-690, 1986/11/01/ 1986, doi: https://doi.org/10.1378/chest.90.5.686.

[294] M. Nasiriavanaki, J. Xia, H. Wan, A. Q. Bauer, J. P. Culver, and L. V. Wang, "High-resolution photoacoustic tomography of resting-state functional connectivity in the mouse brain," *Proceedings of the National Academy of Sciences,* vol. 111, no. 1, pp. 21-26, 2014, doi: doi:10.1073/pnas.1311868111.

[295] M. P. Vanni and T. H. Murphy, "Mesoscale transcranial spontaneous activity mapping in GCaMP3 transgenic mice reveals extensive reciprocal connections between areas of somatomotor cortex," *Journal of Neuroscience,* vol. 34, no. 48, pp. 15931-15946, 2014.

[296] D. Bereczki *et al.*, "Hypoxia Increases Velocity of Blood Flow through Parenchymal Microvascular Systems in Rat Brain," *Journal of Cerebral Blood Flow & Metabolism,* vol. 13, no. 3, pp. 475-486, 1993, doi: 10.1038/jcbfm.1993.62.

[297] J. Hofmeijer, A. T. Mulder, A. C. Farinha, M. J. van Putten, and J. le Feber, "Mild hypoxia affects synaptic connectivity in cultured neuronal networks," *Brain Res,* vol. 1557, pp. 180-9, Apr 4 2014, doi: 10.1016/j.brainres.2014.02.027.

[298] K. Y. Chan *et al.*, "Engineered AAVs for efficient noninvasive gene delivery to the central and peripheral nervous systems," (in eng), *Nat Neurosci,* vol. 20, no. 8, pp. 1172-1179, Aug 2017, doi: 10.1038/nn.4593.

[299] G. Silasi, D. Xiao, M. P. Vanni, A. C. Chen, and T. H. Murphy, "Intact skull chronic windows for mesoscopic wide-field imaging in awake mice," (in eng), *J Neurosci Methods,* vol. 267, pp. 141-9, Jul 15 2016, doi: 10.1016/j.jneumeth.2016.04.012.

[300] T. Q. Duong, C. Iadecola, and S. G. Kim, "Effect of Hyperoxia, Hypercapnia, and Hypoxia on Cerebral Interstitial Oxygen Tension and Cerebral Blood Flow," *Magnetic Resonance in Medicine,* vol. 45, pp. 61-70, 2001.

[301] F. A. Nasrallah, H. C. Tay, and K. H. Chuang, "Detection of functional connectivity in the resting mouse brain," *Neuroimage,* vol. 86, pp. 417-24, Feb 1 2014, doi: 10.1016/j.neuroimage.2013.10.025.

[302] A. K. Dunn, A. Devor, A. M. Dale, and D. A. Boas, "Spatial extent of oxygen metabolism and hemodynamic changes during functional activation of the rat somatosensory cortex," *NeuroImage,* vol. 27, no. 2, pp. 279-290, 2005/08/15/ 2005, doi: https://doi.org/10.1016/j.neuroimage.2005.04.024.

[303] M. Jones, J. Berwick, and J. Mayhew, "Changes in Blood Flow, Oxygenation, and Volume Following Extended Stimulation of Rodent Barrel Cortex," *NeuroImage,* vol. 15, no. 3, pp. 474-487, 2002/03/01/ 2002, doi: https://doi.org/10.1006/nimg.2001.1000.

[304] J. Mayhew, D. Johnston, J. Berwick, M. Jones, P. Coffey, and Y. Zheng, "Spectroscopic Analysis of Neural Activity in Brain: Increased Oxygen Consumption Following Activation of Barrel Cortex," *NeuroImage,* vol. 12, no. 6, pp. 664-675, 2000/12/01/ 2000, doi: https://doi.org/10.1006/nimg.2000.0656.

[305] Q. Wang *et al.*, "The Allen Mouse Brain Common Coordinate Framework: A 3D Reference Atlas," *Cell,* vol. 181, no. 4, pp. 936-953.e20, 2020/05/14/ 2020, doi: https://doi.org/10.1016/j.cell.2020.04.007.

[306] Y. Benjamini and Y. Hochberg, "Controlling the False Discovery Rate: A Practical and Powerful Approach to Multiple Testing," *Journal of the Royal Statistical Society. Series B (Methodological),* vol. 57, no. 1, pp. 289-300, 1995. [Online]. Available: http://www.jstor.org/stable/2346101.

[307] C. Julien-Dolbec *et al.*, "Regional response of cerebral blood volume to graded hypoxic hypoxia in rat brain," *British Journal of Anaesthesia,* vol. 89, no. 2, pp. 287-293, 2002/08/01/ 2002, doi: https://doi.org/10.1093/bja/aef182.

[308] D. M. Bailey *et al.*, "Increased cerebral output of free radicals during hypoxia: implications for acute mountain sickness?," (in eng), *Am J Physiol Regul Integr Comp Physiol,* vol. 297, no. 5, pp. R1283-92, Nov 2009, doi: 10.1152/ajpregu.00366.2009.

[309] C. Constantinides, R. Mean, and B. J. Janssen, "Effects of isoflurane anesthesia on the cardiovascular function of the C57BL/6 mouse," (in eng), *Ilar j,* vol. 52, no. 3, pp. e21-31, 2011.

[310] Y. Xu and Q. Fan, "Relationship between chronic hypoxia and seizure susceptibility," *CNS Neurosci Ther,* vol. 28, no. 11, pp. 1689-1705, Nov 2022, doi: 10.1111/cns.13942.

[311] E. P. Ott *et al.*, "Sympathetic neural recruitment strategies following acute intermittent hypoxia in humans," *Am J Physiol Regul Integr Comp Physiol,* vol. 318, no. 5, pp. R961-R971, May 1 2020, doi: 10.1152/ajpregu.00004.2020.

[312] H. T. Finn *et al.*, "The effect of acute intermittent hypoxia on human limb motoneurone output," (in eng), *Exp Physiol,* vol. 107, no. 6, pp. 615-630, Jun 2022, doi: 10.1113/ep090099.

[313] L. Xu, Q. Li, Y. Ke, and W. H. Yung, "Chronic Intermittent Hypoxia-Induced Aberrant Neural Activities in the Hippocampus of Male Rats Revealed by Long-Term in vivo Recording," *Front Cell Neurosci,* vol. 15, p. 784045, 2021, doi: 10.3389/fncel.2021.784045.

[314] Y. Ma *et al.*, "Resting-state hemodynamics are spatiotemporally coupled to synchronized and symmetric neural activity in excitatory neurons," *Proc Natl Acad Sci U S A,* vol. 113, no. 52, pp. E8463-E8471, Dec 27 2016, doi: 10.1073/pnas.1525369113.

[315] M. De Luca, C. F. Beckmann, N. De Stefano, P. M. Matthews, and S. M. Smith, "fMRI resting state networks define distinct modes of long-distance interactions in the human brain," *Neuroimage,* vol. 29, no. 4, pp. 1359-67, Feb 15 2006, doi: 10.1016/j.neuroimage.2005.08.035.

[316] I. M. Devonshire *et al.*, "Neurovascular coupling is brain region-dependent," *Neuroimage,* vol. 59, no. 3, pp. 1997-2006, Feb 1 2012, doi: 10.1016/j.neuroimage.2011.09.050.

[317] K. Shaw *et al.*, "Neurovascular coupling and oxygenation are decreased in hippocampus compared to neocortex because of microvascular differences," *Nat Commun,* vol. 12, no. 1, p. 3190, May 27 2021, doi: 10.1038/s41467-021-23508-y.

[318] E. L. Fletcher, M. A. Dixon, S. A. Mills, and A. I. Jobling, "Anomalies in neurovascular coupling during early diabetes: A review," *Clin Exp Ophthalmol,* vol. 51, no. 1, pp. 81-91, Jan 2023, doi: 10.1111/ceo.14190.

[319] P. Wang *et al.*, "Altered resting-state neurovascular coupling in patients with pontine infarction," *Exp Gerontol,* vol. 179, p. 112241, Aug 2023, doi: 10.1016/j.exger.2023.112241.

[320] S. Bloch, D. Obari, and H. Girouard, "Angiotensin and Neurovascular Coupling: Beyond Hypertension," *Microcirculation,* vol. 22, no. 3, pp. 159-167, 2015, doi: https://doi.org/10.1111/micc.12193.

[321] K. Kazama *et al.*, "Angiotensin II impairs neurovascular coupling in neocortex through NADPH oxidase-derived radicals," (in eng), *Circ Res,* vol. 95, no. 10, pp. 1019-26, Nov 12 2004, doi: 10.1161/01.RES.0000148637.85595.c5.

[322] K. Kazama, G. Wang, K. Frys, J. Anrather, and C. Iadecola, "Angiotensin II attenuates functional hyperemia in the mouse somatosensory cortex," (in eng), *Am J Physiol Heart Circ Physiol,* vol. 285, no. 5, pp. H1890-9, Nov 2003, doi: 10.1152/ajpheart.00464.2003.

[323] A. J. Lusis, "Atherosclerosis," (in eng), *Nature,* vol. 407, no. 6801, pp. 233-41, Sep 14 2000, doi: 10.1038/35025203.

[324] R. Moretti and P. Caruso, "Small Vessel Disease-Related Dementia: An Invalid Neurovascular Coupling?," *Int J Mol Sci,* vol. 21, no. 3, Feb 7 2020, doi: 10.3390/ijms21031095.

[325] W. H. Lin, Q. Hao, B. Rosengarten, W. H. Leung, and K. S. Wong, "Impaired neurovascular coupling in ischaemic stroke patients with large or small vessel disease," (in eng), *Eur J Neurol,* vol. 18, no. 5, pp. 731-6, May 2011, doi: 10.1111/j.1468-1331.2010.03262.x.

[326] B. Johnson *et al.*, "Alteration of brain default network in subacute phase of injury in concussed individuals: resting-state fMRI study," *Neuroimage,* vol. 59, no. 1, pp. 511-8, Jan 2 2012, doi: 10.1016/j.neuroimage.2011.07.081.

[327] A. Messe *et al.*, "Specific and evolving resting-state network alterations in post-concussion syndrome following mild traumatic brain injury," *PLoS One,* vol. 8, no. 6, p. e65470, 2013, doi: 10.1371/journal.pone.0065470.

[328] G. A. Mack and J. H. Skillings, "A Friedman-Type Rank Test for Main Effects in a Two-Factor ANOVA," *Journal of the American Statistical Association,* vol. 75, no. 372, pp. 947-951, 1980/12/01 1980, doi: 10.1080/01621459.1980.10477577.

[329] T. J. Pingel, "The Mack-Skillings Statistical Test https://github.com/thomaspingel/mackskill-matlab," *Department of Geography, University of California, Santa Barbara,* 2010. [Online]. Available: https://github.com/thomaspingel/mackskill-matlab.

[330] K. Murphy and M. D. Fox, "Towards a consensus regarding global signal regression for resting state functional connectivity MRI," *NeuroImage,* vol. 154, pp. 169-173, 2017, doi: 10.1016/j.neuroimage.2016.11.052.

[331] R. A. Fisher, "Frequency Distribution of the Values of the Correlation Coefficient in Samples from an Indefinitely Large Population.," *Biometrika,* vol. 10, pp. 507-521, 1915, doi: http://dx.doi.org/10.2307/2331838.

[332] Z. Liang, Y. Ma, G. D. R. Watson, and N. Zhang, "Simultaneous GCaMP6-based fiber photometry and fMRI in rats," *J Neurosci Methods,* vol. 289, pp. 31-38, Sep 1 2017, doi: 10.1016/j.jneumeth.2017.07.002.

[333] E. Bullmore and O. Sporns, "The economy of brain network organization," *Nat Rev Neurosci,* vol. 13, no. 5, pp. 336-49, Apr 13 2012, doi: 10.1038/nrn3214.

[334] C. Martin, J. Martindale, J. Berwick, and J. Mayhew, "Investigating neural-hemodynamic coupling and the hemodynamic response function in the awake rat," *Neuroimage,* vol. 32, no. 1, pp. 33-48, Aug 1 2006, doi: 10.1016/j.neuroimage.2006.02.021.

[335] Y. Hirano, B. Stefanovic, and A. C. Silva, "Spatiotemporal evolution of the functional magnetic resonance imaging response to ultrashort stimuli," *J Neurosci,* vol. 31, no. 4, pp. 1440-7, Jan 26 2011, doi: 10.1523/JNEUROSCI.3986-10.2011.

[336] S. Sunil *et al.*, "Neurovascular coupling is preserved in chronic stroke recovery after targeted photothrombosis," *Neuroimage Clin,* vol. 38, p. 103377, 2023, doi: 10.1016/j.nicl.2023.103377.

[337] J. Berwick *et al.*, "Fine detail of neurovascular coupling revealed by spatiotemporal analysis of the hemodynamic response to single whisker stimulation in rat barrel cortex," *J Neurophysiol,* vol. 99, no. 2, pp. 787-98, Feb 2008, doi: 10.1152/jn.00658.2007.

[338] D. A. Soltysik, K. K. Peck, K. D. White, B. Crosson, and R. W. Briggs, "Comparison of hemodynamic response nonlinearity across primary cortical areas," *Neuroimage,* vol. 22, no. 3, pp. 1117-27, Jul 2004, doi: 10.1016/j.neuroimage.2004.03.024.

[339] B. Xiong *et al.*, "Precise Cerebral Vascular Atlas in Stereotaxic Coordinates of Whole Mouse Brain," *Front Neuroanat,* vol. 11, p. 128, 2017, doi: 10.3389/fnana.2017.00128.

[340] M. Scherr *et al.*, "Effective connectivity in the default mode network is distinctively disrupted in Alzheimer's disease-A simultaneous resting-state FDG-PET/fMRI study," *Hum Brain Mapp,* Jan 30 2019, doi: 10.1002/hbm.24517.

[341] G. F. Mitchell, "Aortic stiffness, pressure and flow pulsatility, and target organ damage," *J Appl Physiol (1985),* vol. 125, no. 6, pp. 1871-1880, Dec 1 2018, doi: 10.1152/japplphysiol.00108.2018.

[342] A. Raignault, V. Bolduc, F. Lesage, and E. Thorin, "Pulse pressure-dependent cerebrovascular eNOS regulation in mice," *J Cereb Blood Flow Metab,* vol. 37, no. 2, pp. 413-424, Feb 2017, doi: 10.1177/0271678X16629155.

[343] A. Papadopoulos, K. Palaiopanos, A. P. Protogerou, G. P. Paraskevas, G. Tsivgoulis, and M. K. Georgakis, "Left Ventricular Hypertrophy and Cerebral Small Vessel Disease: A Systematic Review and Meta-Analysis," *J Stroke,* vol. 22, no. 2, pp. 206-224, May 2020, doi: 10.5853/jos.2019.03335.

[344] N. Saji, K. Toba, and T. Sakurai, "Cerebral Small Vessel Disease and Arterial Stiffness: Tsunami Effect in the Brain?," *Pulse (Basel),* vol. 3, no. 3-4, pp. 182-9, Apr 2016, doi: 10.1159/000443614.

[345] S. Harris, T. Reyhan, Y. Ramli, J. Prihartono, and M. Kurniawan, "Middle Cerebral Artery Pulsatility Index as Predictor of Cognitive Impairment in Hypertensive Patients," (in English), *Frontiers in Neurology,* Original Research vol. 9, 2018-July-20 2018, doi: 10.3389/fneur.2018.00538.

[346] A. Scuteri, M. Tesauro, S. Appolloni, F. Preziosi, A. M. Brancati, and M. Volpe, "Arterial stiffness as an independent predictor of longitudinal changes in cognitive function in the older individual," (in eng), *J Hypertens,* vol. 25, no. 5, pp. 1035-40, May 2007, doi: 10.1097/HJH.0b013e3280895b55.

[347] Z. Shirzadi *et al.*, "Brain tissue pulsatility is related to clinical features of Parkinson's disease," *Neuroimage Clin,* vol. 20, pp. 222-227, 2018, doi: 10.1016/j.nicl.2018.07.017.

[348] S. Frenzel *et al.*, "Left ventricular hypertrophy as a risk factor for accelerated brain aging: Results from the Study of Health in Pomerania," *Hum Brain Mapp,* vol. 45, no. 3, p. e26567, Feb 15 2024, doi: 10.1002/hbm.26567.

[349] G. Selvetella *et al.*, "Left ventricular hypertrophy is associated with asymptomatic cerebral damage in hypertensive patients," *Stroke,* vol. 34, no. 7, pp. 1766-70, Jul 2003, doi: 10.1161/01.STR.0000078310.98444.1D.

[350] D. F. Xie *et al.*, "Semi-automated protocol to quantify and characterize fluorescent three-dimensional vascular images," *PLoS One,* vol. 19, no. 5, p. e0289109, 2024, doi: 10.1371/journal.pone.0289109.

[351] N. Renier, Z. Wu, D. J. Simon, J. Yang, P. Ariel, and M. Tessier-Lavigne, "iDISCO: a simple, rapid method to immunolabel large tissue samples for volume imaging," *Cell,* vol. 159, no. 4, pp. 896-910, Nov 6 2014, doi: 10.1016/j.cell.2014.10.010.

[352] A. Badji, D. Sabra, L. Bherer, J. Cohen-Adad, H. Girouard, and C. J. Gauthier, "Arterial stiffness and brain integrity: A review of MRI findings," *Ageing Res Rev,* vol. 53, p. 100907, Aug 2019, doi: 10.1016/j.arr.2019.05.001.

[353] T. J. Niiranen, B. Kalesan, G. F. Mitchell, and R. S. Vasan, "Relative Contributions of Pulse Pressure and Arterial Stiffness to Cardiovascular Disease," *Hypertension,* vol. 73, no. 3, pp. 712-717, Mar 2019, doi: 10.1161/HYPERTENSIONAHA.118.12289.

APPENDIX A APPENDIX OF ARTICLE 1: ALTERATION OF FUNCTIONAL CONNECTIVITY DESPITE PRESERVED CEREBRAL OXYGENATION DURING ACUTE HYPOXIA

1. Methods activation seed pairs

Appendix 1.1. To be able to look at the activation of the seeds and to compare the amount of activation over time, the timecourses of the seeds were recalculated without normalisation and GSR. This means the images were co-registered and corrected for hemodynamics, and the timecourses were taken from the centroids of the regions of interests. Mice had a different level of fluorescence expression, either because of the succes rate of the virus injection or because of biological differences. This resulted in different amounts of fluorescence expression between mice. In order to compare between mice, we calculated the mean of minutes 2.5-7.5 of each seed for each mouse, and divided the whole timecourse by that number. Then, the mean over mice for each seed was taken and plotted (Appendix 1.2). The steep decline at the start of the acquisition is caused by the exponential decay from the illumination source warming up.

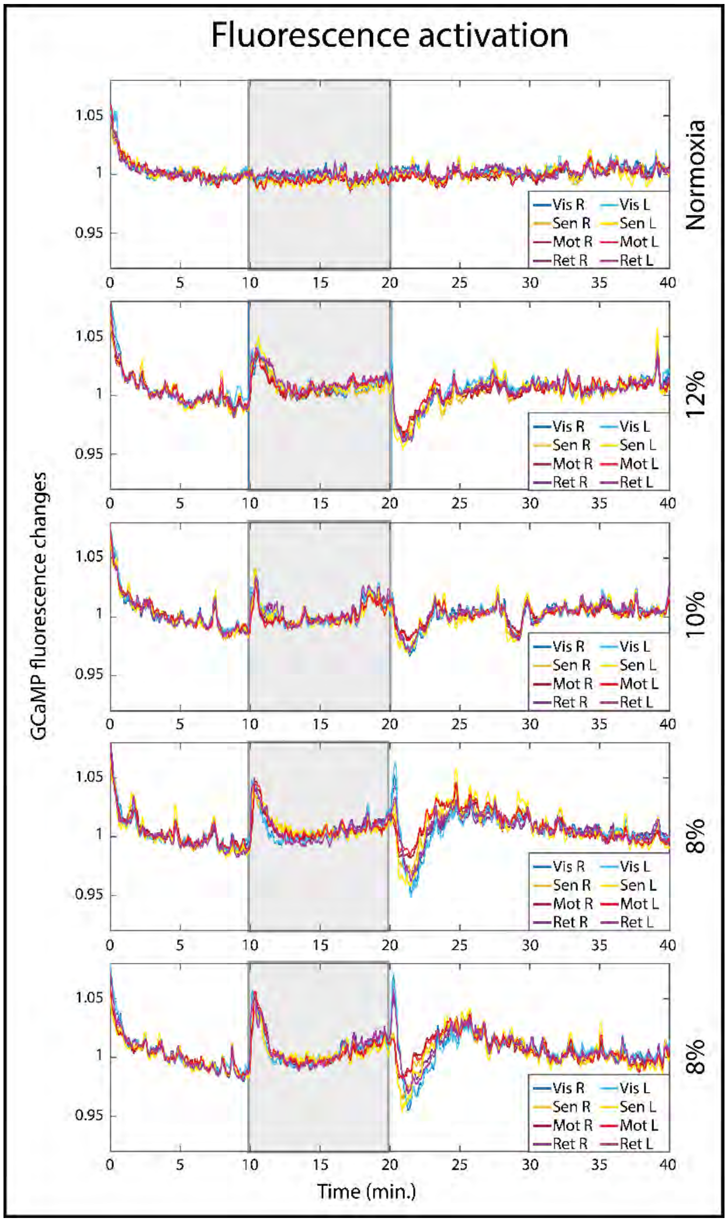

Appendix 1.2. Fluorescence activation over time, depicted per seed, averaged over all mice (n=7). Grey areas indicate the timing of the hypoxia period.

2. Seed pixel correlation maps without GSR

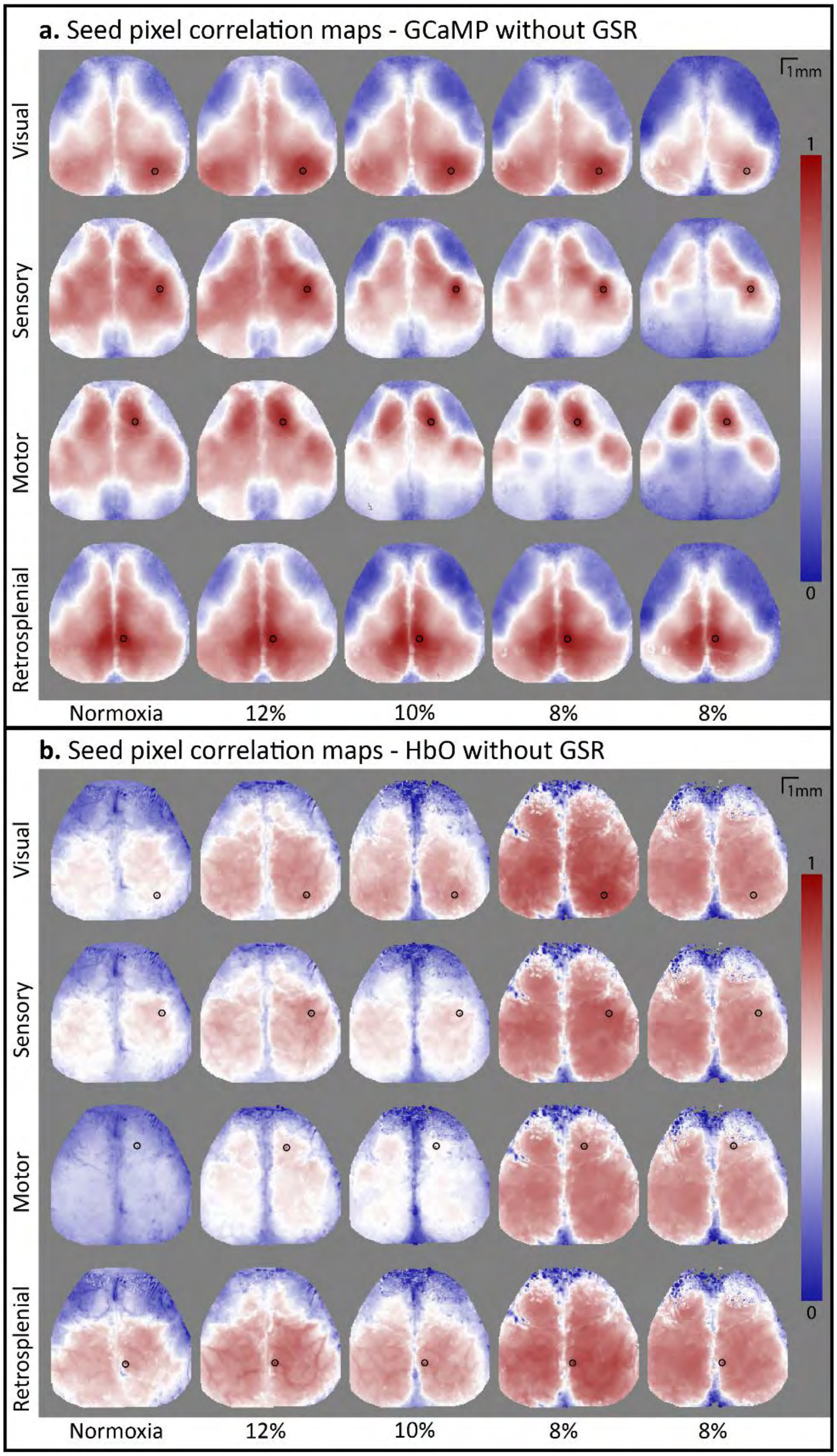

Appendix 2. Seed pixel correlation maps without GSR. Maps represent correlation over minute 12.5 to 17.5 of the first normoxia, and all hypoxia periods (n=1). The black circle indicates the chosen seed; the centroid of the region of interest. Red indicates positive correlation of the seeds timecourse to the corresponding pixel, blue indicates negative correlation. a. Maps based on GCaMP data. b. Maps based on HbO data.

3. Statistics

Appendix 3. Q-values for the differences in correlation, based on GCaMP data. Values were computed by comparing correlation z-scores during hypoxia (8% oxygen, minute 12.5 to 17.5) to the period before (minute 2.5 to 7.5). The bottom left triangle shows values for the first acquisition, the top right for the second.

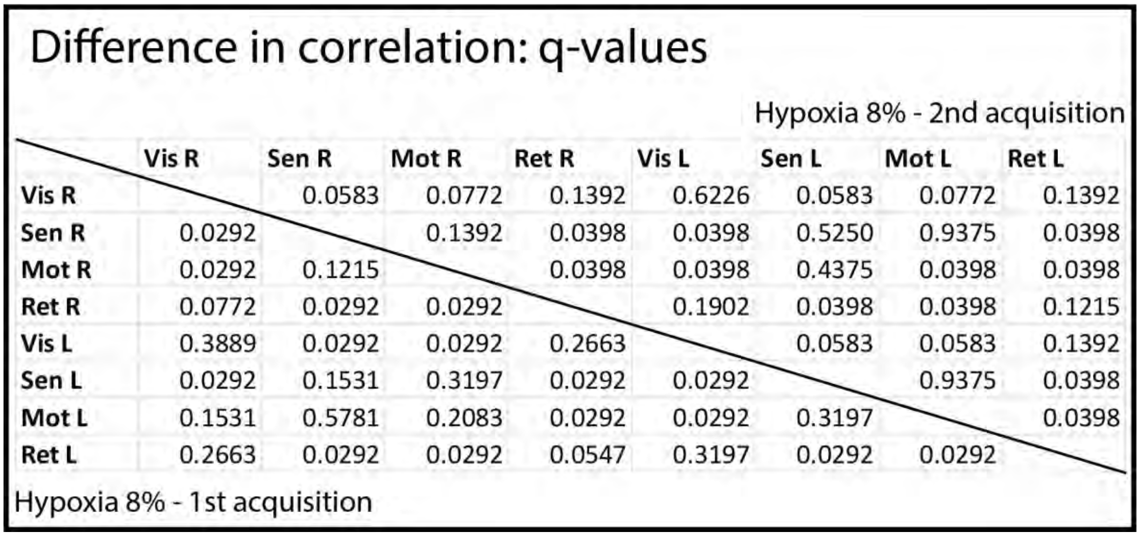

Difference in correlation: q-values

Hypoxia 8% - 2nd acquisition

	Vis R	Sen R	Mot R	Ret R	Vis L	Sen L	Mot L	Ret L
Vis R		0.0583	0.0772	0.1392	0.6226	0.0583	0.0772	0.1392
Sen R	0.0292		0.1392	0.0398	0.0398	0.5250	0.9375	0.0398
Mot R	0.0292	0.1215		0.0398	0.0398	0.4375	0.0398	0.0398
Ret R	0.0772	0.0292	0.0292		0.1902	0.0398	0.0398	0.1215
Vis L	0.3889	0.0292	0.0292	0.2663		0.0583	0.0583	0.1392
Sen L	0.0292	0.1531	0.3197	0.0292	0.0292		0.9375	0.0398
Mot L	0.1531	0.5781	0.2083	0.0292	0.0292	0.3197		0.0398
Ret L	0.2663	0.0292	0.0292	0.0547	0.3197	0.0292	0.0292	

Hypoxia 8% - 1st acquisition

APPENDIX B APPENDIX OF ARTICLE 2: NEUROVASCULAR COUPLING OVER CORTICAL BRAIN AREAS AND RESTING STATE NETWORK CONNECTIVITY WITH AND WITHOUT RIGIDIFIED CAROTID ARTERY

1. Movement - Plot

Appendix 1. Number of frames where the mouse was moving the treadmill. Acquisitions existed of 9000 frames in total. Movement did not differ significantly between groups in the GCaMP acquisitions (A1: p = 0.37, A2: p = 0.39, A3: p = 0.32), as tested with Kruskal Wallis tests.

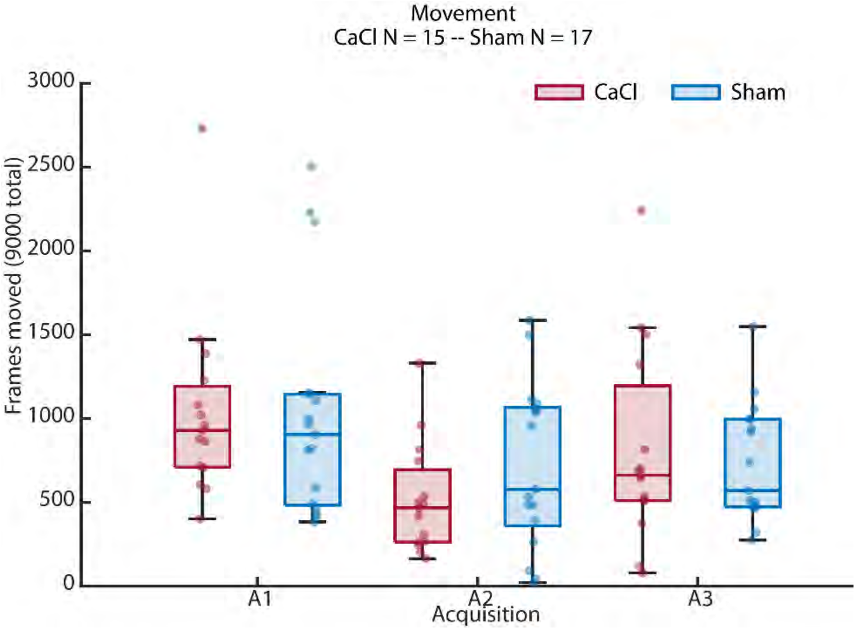

2. Detected GCaMP and HbO activations

Appendix 2. Number of spontaneous activations per brain region during Acquisition 1, detected on GCaMP data (A) or HbO data (B). Per detected GCaMP activation, the percentage activations that were followed by the HbO timecourse reaching the detection threshold within 2 seconds is shown in C. Conversely, D shows the percentage of detected HbO activations that were preceded (within 2 seconds) by a GCaMP peak that crossed the detection threshold. E: The number of detected GCaMP activations of A was taken, but timepoints were randomized in order to fabricate a control group for C. F: Similar situation as E, where the number of HbO-detected activations from B were randomized and checked for a corresponding GCaMP activation.

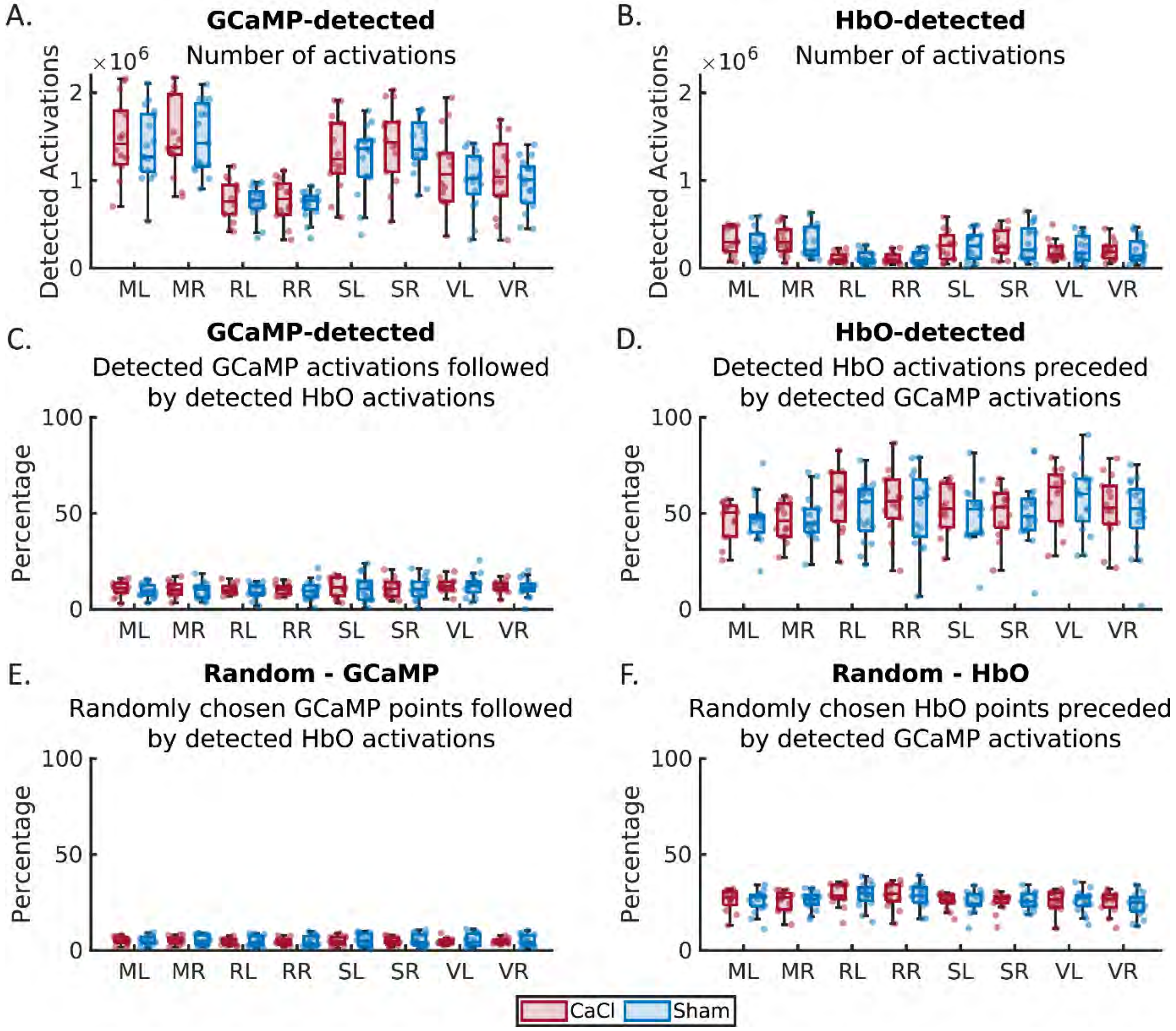

3. Verification rigidification surgery

Appendix 3. A. Representative frame of an ultrasound recording in m-mode. B. Diameter change of the right carotid artery. Dots indicate individual samples. N = 7 for the CaCl group, and N = 6 for the sham group. P = 0.04.

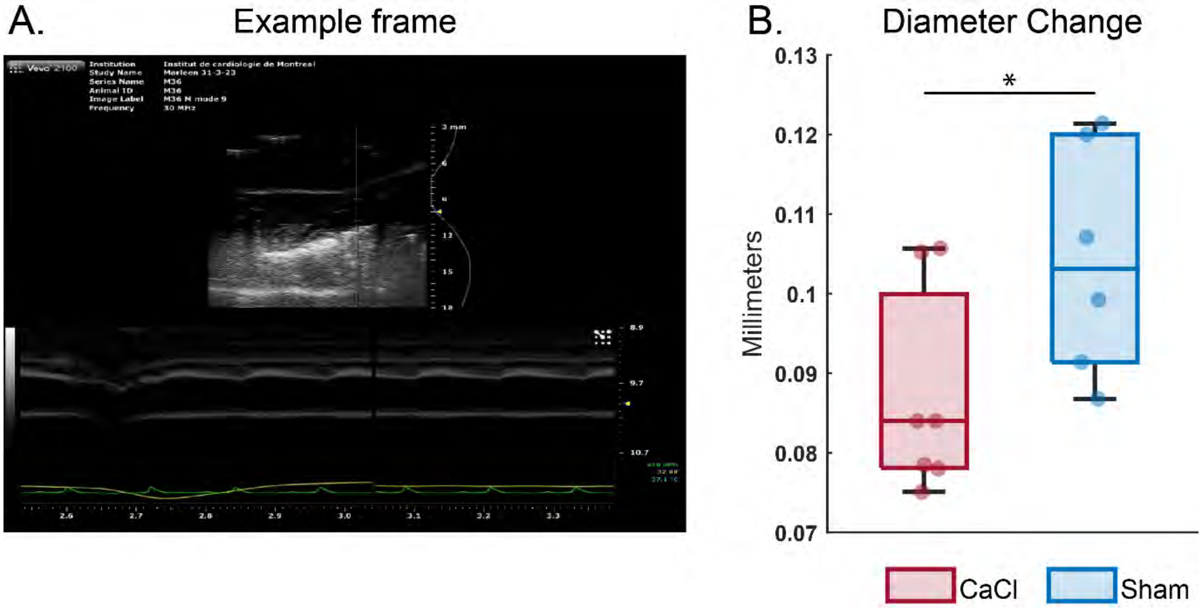

4. NVC in RS Sham - Statistics

Appendix 4. Statistics on neurovascular coupling parameters during resting state, in sham mice on the first acquisition. Grey boxes indicate values <0.05. Q-values are FDR-corrected p-values. A. Tests that were performed per parameter to see if there was a significant difference between ROIs. All parameters showed significant. B. Post-hoc test results, showing which ROIs differed significantly per parameter.

A.

Parameter	**Testtype**	**p**	**q**
GCaMP Peak	rANOVA - Greenhouse-Geisser corrected	5.02E-12	2.17E-11
HbO Peak	rANOVA - Greenhouse-Geisser corrected	1.52E-09	2.28E-09
HbR Peak	Friedman	2.27E-12	2.04E-11
GCaMP Increase	rANOVA - Greenhouse-Geisser corrected	7.23E-12	2.17E-11
HbO Increase	Friedman	3.66E-11	8.22E-11
HbR Decrease	rANOVA	1.94E-06	1.94E-06
Delay (sec)	Friedman	2.93E-09	3.76E-09
Response Strength	Friedman	4.85E-08	5.45E-08
Response Strength Increase	Friedman	7.22E-10	1.30E-09

B.

ROI 1	ROI 2	GCaMP Peak	HbO Peak	HbR Peak	GCaMP Increase	HbO Increase	HbR Decrease	Delay (sec.)	Response Strength	Response Strength Increase
ML	MR	4.65E-04	1.00E+00	1.00E+00	9.71E-04	1.00E+00	1.00E+00	9.99E-01	6.06E-01	4.31E-02
ML	RL	2.83E-04	9.99E-01	7.44E-01	2.28E-01	9.35E-01	9.95E-01	7.63E-02	5.09E-01	1.00E+00
ML	RR	4.24E-04	9.38E-01	1.59E-01	3.13E-02	1.87E-01	6.54E-01	5.47E-02	6.48E-02	9.95E-01
ML	SL	2.88E-02	8.87E-01	3.49E-02	1.66E-02	2.00E-04	2.17E-01	9.64E-01	1.00E+00	2.88E-01
ML	SR	5.96E-08	8.68E-01	1.77E-02	5.96E-08	1.44E-04	3.49E-02	8.48E-01	2.24E-02	1.87E-01
ML	VL	2.70E-01	1.96E-02	5.09E-01	1.98E-01	2.76E-04	7.00E-01	9.98E-01	2.88E-01	1.87E-01
ML	VR	1.47E-04	2.92E-01	2.88E-01	1.49E-03	1.84E-05	9.35E-01	2.57E-01	9.67E-01	9.77E-01
MR	RL	6.24E-01	9.50E-01	8.23E-01	9.31E-01	9.35E-01	9.97E-01	2.99E-01	1.00E+00	4.31E-02
MR	RR	1.94E-02	6.96E-01	2.17E-01	7.00E-01	1.87E-01	7.00E-01	2.37E-01	9.53E-01	2.88E-01
MR	SL	9.99E-01	7.77E-01	2.24E-02	9.81E-01	2.00E-04	1.87E-01	7.15E-01	5.58E-01	1.99E-06
MR	SR	5.66E-06	6.28E-01	1.10E-02	1.43E-05	1.44E-04	2.80E-02	4.73E-01	8.23E-01	9.99E-01
MR	VL	1.00E+00	1.73E-03	4.15E-01	1.00E+00	2.76E-04	6.54E-01	9.12E-01	9.44E-04	6.39E-07
MR	VR	8.36E-03	1.78E-01	2.17E-01	3.86E-02	1.84E-05	9.13E-01	6.12E-02	9.95E-01	4.15E-01
RL	RR	4.21E-03	7.71E-01	9.77E-01	2.89E-02	8.88E-01	9.77E-01	1.00E+00	9.77E-01	9.95E-01
RL	SL	9.82E-01	9.48E-01	5.26E-05	5.01E-01	2.24E-02	2.80E-02	2.02E-03	4.61E-01	2.88E-01
RL	SR	2.29E-04	9.55E-01	1.84E-05	9.54E-07	1.77E-02	2.25E-03	4.48E-04	8.88E-01	1.87E-01
RL	VL	3.08E-01	7.34E-05	8.53E-03	9.04E-01	2.80E-02	2.17E-01	9.10E-03	5.16E-04	1.87E-01
RL	VR	4.79E-03	1.95E-01	2.25E-03	1.90E-03	3.90E-03	5.09E-01	4.19E-06	9.85E-01	9.77E-01
RR	SL	3.62E-02	1.00E+00	3.03E-07	9.46E-01	5.09E-01	7.00E-04	1.24E-03	5.30E-02	4.31E-02
RR	SR	5.25E-01	1.00E+00	1.20E-07	2.98E-02	4.61E-01	2.62E-05	2.63E-04	1.00E+00	6.54E-01
RR	VL	3.37E-04	7.20E-02	1.44E-04	3.41E-01	5.58E-01	1.40E-02	5.90E-03	4.17E-06	2.24E-02
RR	VR	2.81E-01	3.04E-01	2.62E-05	2.73E-02	2.17E-01	6.48E-02	2.19E-06	5.58E-01	1.00E+00
SL	SR	3.24E-05	1.00E+00	1.00E+00	1.16E-04	1.00E+00	9.97E-01	1.00E+00	1.77E-02	3.72E-05
SL	VL	9.74E-01	6.54E-01	9.35E-01	9.68E-01	1.00E+00	9.95E-01	1.00E+00	3.27E-01	1.00E+00
SL	VR	2.38E-02	8.84E-01	9.91E-01	1.08E-01	1.00E+00	9.13E-01	8.98E-01	9.53E-01	2.24E-02
SR	VL	7.30E-05	4.43E-01	8.58E-01	1.90E-04	1.00E+00	8.23E-01	9.95E-01	5.85E-07	1.28E-05
SR	VR	1.00E+00	7.99E-01	9.67E-01	1.00E+00	1.00E+00	5.09E-01	9.81E-01	3.27E-01	7.86E-01
VL	VR	1.54E-04	1.00E+00	1.00E+00	2.21E-03	9.99E-01	1.00E+00	6.89E-01	1.77E-02	1.10E-02

5. NVC in RS Sham – Plots

Appendix 5. GCaMP (depicted in green) corresponds to the left y-axis, while hemodynamics (HbO in red and HbR in blue) correspond to the right y-axis. X-axis shows time in seconds, with 0 being the time of the detected spontaneous GCaMP activation. A. Curves of GCaMP and hemodynamics per mouse, per region of interest. For clarity, HbT curves are not depicted. Each line shows the average curve over a region of interest of one mouse. B. Curves of GCaMP and hemodynamics of one mouse, over the whole brain, with filtered and unfiltered data. C. Neurovascular coupling curves per mouse. Unfiltered version of Figure 2A. D. Group average of mice depicted in C. Dark line shows the group average, patches show standard error of the mean (SEM). Unfiltered version of Figure 2B.

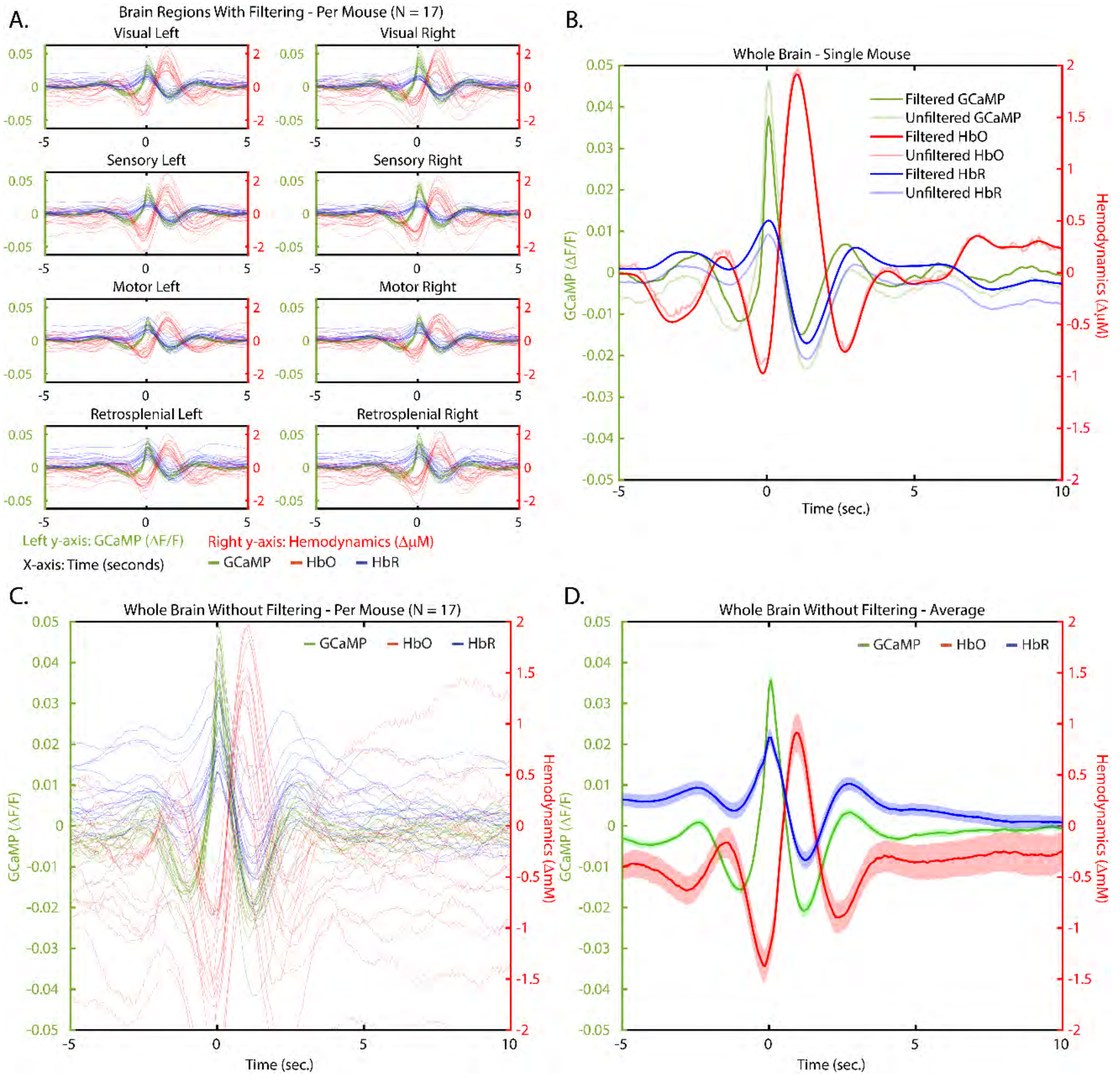

6. NVC CaCl vs Sham ROI – Figures

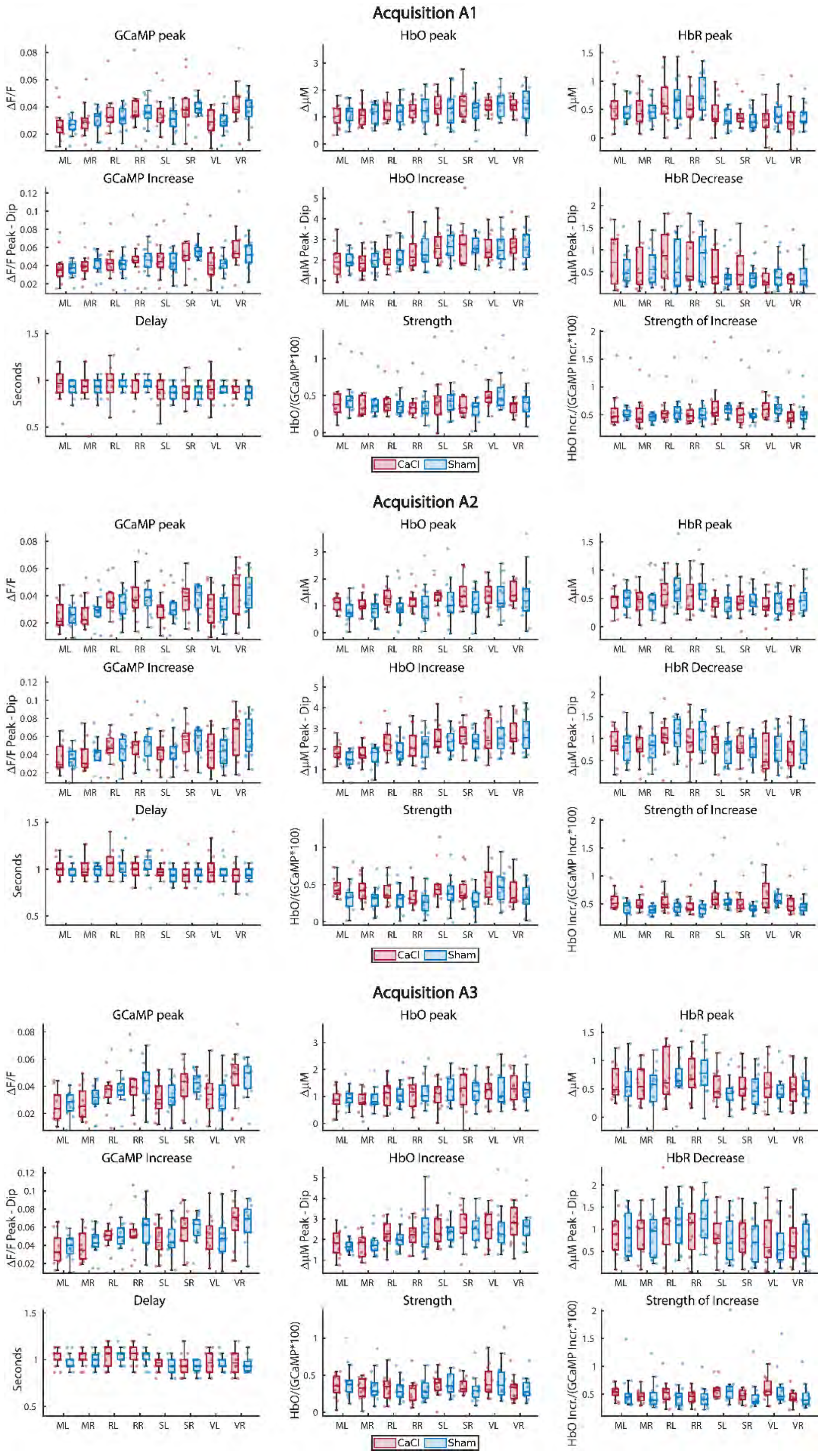

Appendix 6. Neurovascular coupling parameters for all brain areas over the three acquisitions. For statistics on the difference between CaCl and Sham groups over the right hemisphere, see Appendix 7.

7. NVC in CaCl vs Sham right hemisphere - Statistics

Appendix 7. Statistics for the neurovascular coupling parameters of the Sham versus CaCl groups. Q-values are FDR-corrected p-values. No significant differences were found, and thus no post-hoc testing was done.

Parameter	Testtype	p	q
GCaMP Peak	rANOVA	9.44E-01	9.79E-01
HbO Peak	rANOVA	4.91E-01	9.79E-01
HbR Peak	MackSkillings	3.40E-01	9.79E-01
GCaMP Increase	rANOVA	9.79E-01	9.79E-01
HbO Increase	rANOVA	7.15E-01	9.79E-01
HbR Decrease	MackSkillings	5.43E-01	9.79E-01
Delay (sec)	MackSkillings	4.34E-01	9.79E-01
Response Strength	MackSkillings	8.77E-01	9.79E-01
Response Strength Increase	MackSkillings	7.63E-01	9.79E-01

8. Correlation Matrices without GSR

Appendix 8. Correlation matrices of GCaMP (A), HbO (B) and HbR (C). Rows depict different acquisitions (A1, A2 and A3 for week 3, 4 and 5 after surgery, respectively). First column shows the average correlation between seeds of the CaCl group, second column of the Sham group, and the third column shows the difference between Sham and CaCl (CaCl minus Sham average correlation). Differences were not significant (see Appendix 10 for statistics).

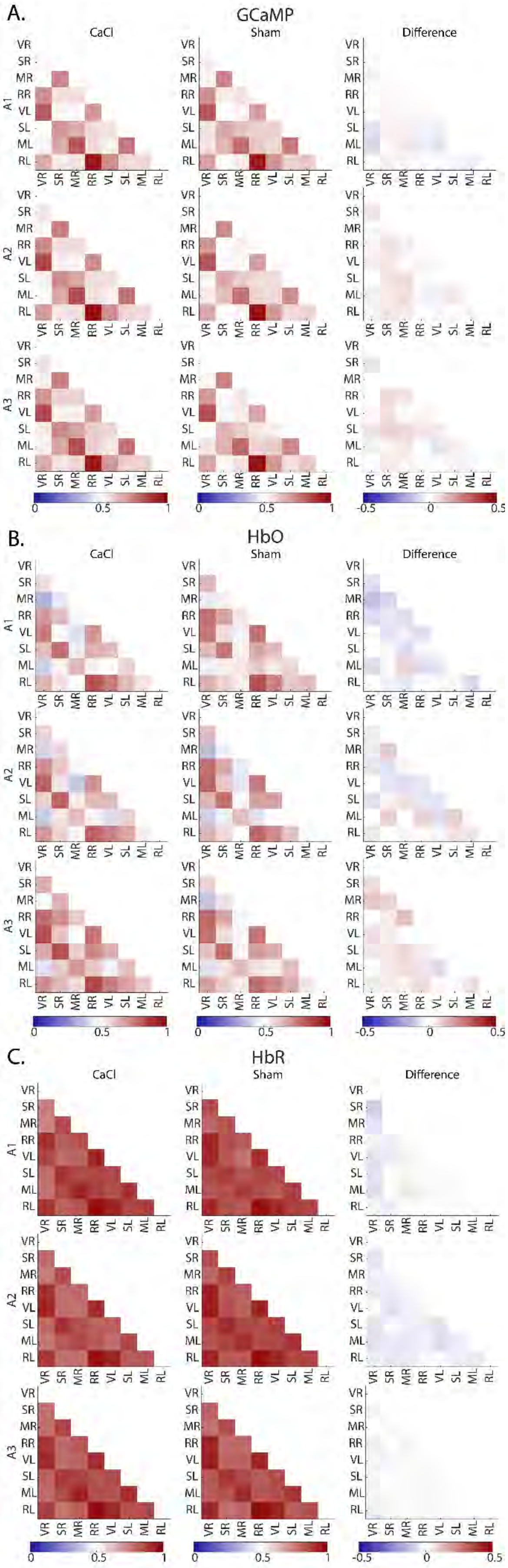

9. Correlation Matrices with GSR

Appendix 9. Correlation matrices of GCaMP (A), HbO (B) and HbR (C) with GSR. Rows depict different acquisitions (A1, A2 and A3 for week 3, 4 and 5 after surgery, respectively). First column shows the average correlation between seeds of the CaCl group, second column of the Sham group, and the third column shows the difference between Sham and CaCl (CaCl minus Sham average correlation).

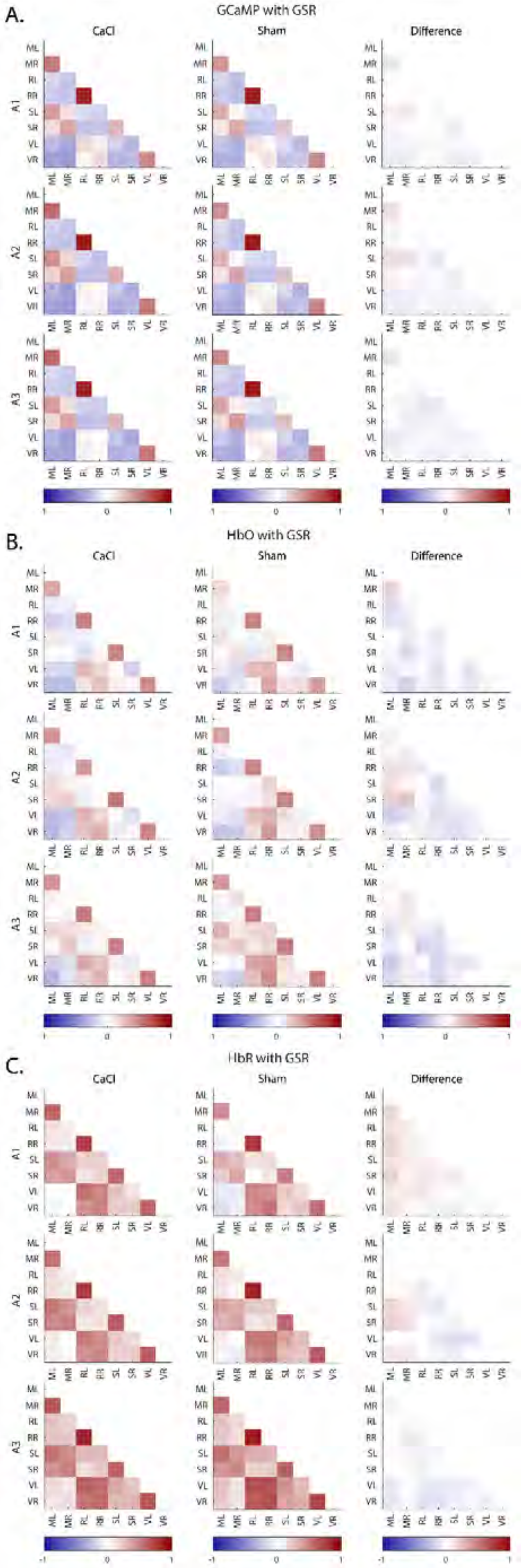

10. Correlation Matrices – CaCl vs Sham Statistics

Appendix 10. Statistics of the difference between correlation matrices of CaCl and Sham groups, of GCaMP (A), HbO (B) and HbR (C), as shown in Appendix 8 (right columns). No GSR was performed on this data. P-values were calculated with Mann Whitney U tests. Grey boxes indicate values <0.05. The upper triangle (grey text) shows p-values, the lower triangle (black text) shows the FDR-corrected p-values; q-values.

A.

GCaMP		ML	MR	RL	RR	SL	SR	VL	VR
A1	ML		0.258	0.706	0.603	0.620	0.706	0.439	0.147
	MR	0.918		0.592	0.787	0.416	1.000	0.890	0.487
	RL	0.918	0.918		0.755	0.620	0.620	0.736	0.565
	RR	0.918	0.918	0.918		0.633	0.633	0.418	0.884
	SL	0.918	0.918	0.918	0.918		0.311	0.620	0.226
	SR	0.918	1.000	0.918	0.918	0.918		0.736	0.677
	VL	0.918	0.955	0.918	0.918	0.918	0.918		0.921
	VR	0.918	0.918	0.918	0.955	0.918	0.918	0.955	

A2		ML	MR	RL	RR	SL	SR	VL	VR
	ML		0.054	0.706	0.858	0.159	0.226	0.463	0.706
	MR	0.741		0.293	0.293	0.159	0.463	0.890	0.858
	RL	0.890	0.744		0.487	0.827	0.331	0.565	0.372
	RR	0.890	0.744	0.758		0.890	0.117	0.311	0.416
	SL	0.741	0.741	0.890	0.890		0.108	0.796	0.796
	SR	0.744	0.758	0.744	0.741	0.741		0.372	0.258
	VL	0.758	0.890	0.832	0.744	0.890	0.744		0.099
	VR	0.890	0.890	0.744	0.758	0.890	0.744	0.741	

A3		ML	MR	RL	RR	SL	SR	VL	VR
	ML		0.059	0.819	0.827	0.171	0.439	0.184	0.512
	MR	0.554		0.917	0.487	0.137	0.890	0.620	0.858
	RL	1.000	1.000		1.000	0.394	0.289	0.983	0.724

RR	1.000	0.844	1.000		0.147	0.049	0.439	0.984
SL	0.734	0.734	0.844	0.734		0.028	0.706	0.487
SR	0.844	1.000	0.844	0.554	0.554		0.439	0.211
VL	0.734	0.964	1.000	0.844	1.000	0.844		0.487
VR	0.844	1.000	1.000	1.000	0.844	0.739	0.844	

B.

HbO		ML	MR	RL	RR	SL	SR	VL	VR
A1	ML		0.260	0.064	0.333	0.647	0.777	0.323	0.132
	MR	0.732		0.481	0.326	0.431	0.481	0.305	0.056
	RL	0.732	0.748		0.442	0.767	0.828	0.340	0.567
	RR	0.732	0.732	0.748		0.724	0.205	0.285	0.109
	SL	0.862	0.748	0.906	0.906		0.921	0.934	0.953
	SR	0.906	0.748	0.927	0.732	0.953		0.619	0.213
	VL	0.732	0.732	0.732	0.732	0.953	0.862		0.455
	VR	0.732	0.732	0.835	0.732	0.953	0.732	0.748	

A2		ML	MR	RL	RR	SL	SR	VL	VR
	ML		0.348	0.418	0.220	0.260	0.169	0.369	0.859
	MR	0.688		0.777	0.945	0.305	0.148	0.320	0.983
	RL	0.688	0.946		0.662	0.395	0.879	0.645	0.109
	RR	0.688	0.980	0.905		0.350	0.183	0.067	0.329
	SL	0.688	0.688	0.688	0.688		0.678	0.263	0.374
	SR	0.688	0.688	0.946	0.688	0.905		0.826	0.879
	VL	0.688	0.688	0.905	0.688	0.688	0.946		0.469
	VR	0.946	0.983	0.688	0.688	0.688	0.946	0.730	

A3		ML	MR	RL	RR	SL	SR	VL	VR
	ML		0.369	0.182	0.344	0.939	0.544	0.320	0.865
	MR	0.854		0.678	0.140	0.421	0.182	0.818	0.088
	RL	0.788	0.863		0.128	0.678	0.580	0.782	0.249

RR	0.854	0.788	0.788		0.643	0.434	0.311	0.712
SL	0.973	0.854	0.863	0.863		0.479	0.981	0.510
SR	0.854	0.788	0.855	0.854	0.854		0.549	0.197
VL	0.854	0.916	0.913	0.854	0.981	0.854		0.097
VR	0.932	0.788	0.854	0.867	0.854	0.788	0.788	

C.

HbR		ML	MR	RL	RR	SL	SR	VL	VR
A1	ML		0.649	0.177	0.525	0.707	0.567	0.767	0.109
	MR	0.957		0.493	0.878	0.921	0.489	0.465	0.072
	RL	0.644	0.908		0.584	0.819	0.350	0.253	0.152
	RR	0.908	0.992	0.908		0.983	0.142	0.196	0.228
	SL	0.990	0.992	0.992	1.000		1.000	0.797	0.244
	SR	0.908	0.908	0.816	0.644	1.000		0.118	0.101
	VL	0.992	0.908	0.644	0.644	0.992	0.644		0.890
	VR	0.644	0.644	0.644	0.644	0.644	0.644	0.992	

A2		ML	MR	RL	RR	SL	SR	VL	VR
	ML		0.323	0.182	0.452	0.301	0.482	0.085	0.077
	MR	0.503		0.216	0.512	0.206	0.297	0.320	0.323
	RL	0.503	0.503		0.182	0.115	0.442	0.554	0.234
	RR	0.574	0.574	0.503		0.198	0.538	0.190	0.062
	SL	0.503	0.503	0.503	0.503		0.512	0.062	0.070
	SR	0.574	0.503	0.574	0.575	0.574		0.412	0.716
	VL	0.476	0.503	0.575	0.503	0.476	0.574		0.344
	VR	0.476	0.503	0.503	0.476	0.476	0.716	0.507	

A3		ML	MR	RL	RR	SL	SR	VL	VR
	ML		0.305	0.743	0.647	0.913	0.445	0.678	0.711
	MR	0.946		0.678	0.305	0.214	0.102	1.000	0.616

RL	0.946	0.946		0.585	0.743	0.743	0.395	0.111
RR	0.946	0.946	0.946		0.585	0.743	0.395	0.169
SL	0.947	0.946	0.946	0.946		0.585	0.711	0.844
SR	0.946	0.946	0.946	0.946	0.946		0.913	0.810
VL	0.946	1.000	0.946	0.946	0.946	0.947		0.879
VR	0.946	0.946	0.946	0.946	0.947	0.947	0.947	

11. Correlation Matrices – Comparisons over timepoints A1 – A2 – A3

Appendix 11. Statistics of the difference between correlation matrices over timepoints (A1, A2 and A3), of GCaMP (A), HbO (B) and HbR (C). P-values were calculated with Friedman tests. Grey boxes indicate values <0.05. The upper triangle (grey text) shows p-values, the lower triangle (black text) shows the FDR-corrected p-values; q-values. Since no q-values showed significant, no post-hoc testing was performed.

A.

GCaMP	ML	MR	RL	RR	SL	SR	VL	VR
ML		0.159	0.356	0.875	0.798	0.879	0.405	0.405
MR	0.968		0.531	0.435	0.542	0.405	0.798	0.879
RL	0.968	0.968		0.015	0.875	0.792	0.905	0.875
RR	0.968	0.968	0.406		0.905	0.967	0.435	0.648
SL	0.968	0.968	0.968	0.968		0.748	0.968	0.748
SR	0.968	0.968	0.968	0.968	0.968		0.657	0.679
VL	0.968	0.968	0.968	0.968	0.968	0.968		0.078
VR	0.968	0.968	0.968	0.968	0.968	0.968	0.968	

B.

HbO	ML	MR	RL	RR	SL	SR	VL	VR
ML		0.241	0.459	0.040	0.651	0.026	0.340	0.852
MR	0.701		0.630	0.018	0.891	0.102	0.499	0.197
RL	0.960	0.960		0.236	0.867	0.607	0.607	0.895
RR	0.369	0.368	0.701		0.862	0.250	0.882	0.482
SL	0.960	0.962	0.962	0.962		0.158	0.962	0.891
SR	0.368	0.701	0.960	0.701	0.701		0.568	0.962
VL	0.864	0.960	0.960	0.962	0.962	0.960		0.214
VR	0.962	0.701	0.962	0.960	0.962	0.962	0.701	

C.

HbR	ML	MR	RL	RR	SL	SR	VL	VR

ML		0.088	0.020	0.054	0.393	0.519	0.104	0.540
MR	0.266		0.020	0.025	0.301	0.519	0.236	0.446
RL	0.114	0.114		0.862	0.005	0.104	0.595	0.595
RR	0.214	0.115	0.862		0.004	0.008	0.607	0.417
SL	0.679	0.602	0.071	0.071		0.639	0.495	0.482
SR	0.679	0.679	0.266	0.071	0.688		0.764	0.080
VL	0.266	0.508	0.679	0.679	0.679	0.792		0.228
VR	0.679	0.679	0.679	0.679	0.679	0.266	0.508	

APPENDIX C APPENDIX OF CHAPTER 6: ULTRAFAST 2-PHOTON IMAGING OF CEREBRAL VASCULATURE IN TAC MICE

1. Weight and Heart Weight for TAC and Sham

Body weight at the day of imaging and heart weight after sacrifice of the mice, grouped by sex. Asterix (*) symbol depicts mice that were unfit for imaging and are thus not included in other results. Symbols correspond to those in Figure 2.

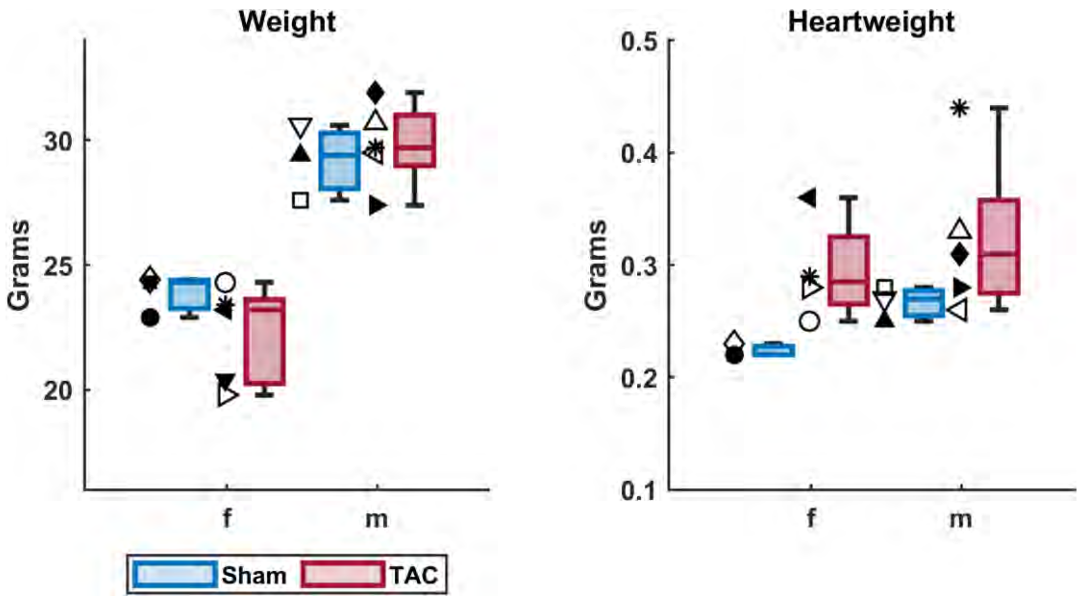

2. Kymographs of Arteries and Veins

Zoom-in of Figure 3 of arteries and veins. The 2D overview scan is depicted on the left, with the corresponding kymograph, as made with a linescan, is depicted on the right. The left axis of the kymograph depicts the width of the linescan, while the right axis corresponds to the estimated velocity, as plotted with a blue (sham) or red (TAC) line.

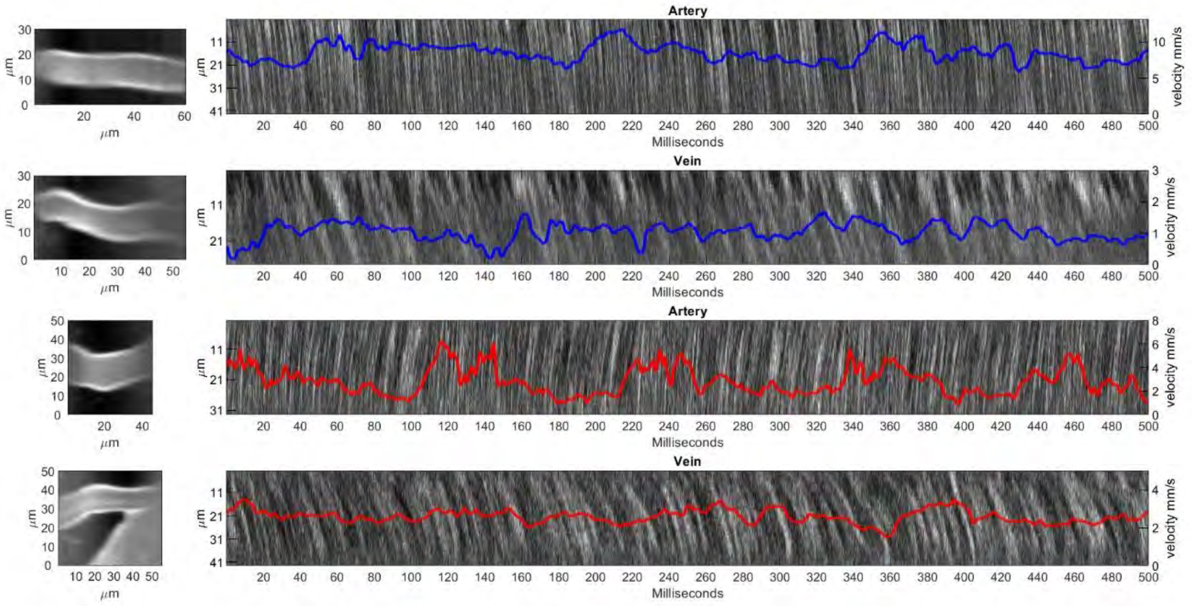

3. Kymographs of High Pulsatility Vessels

Acquisitions with a very high pulsatility (top 3 acquisitions) and the acquisition with the highest velocity that we measured in this article (bottom). The 2D overview scan is depicted on the left, with the corresponding kymograph, as made with a linescan, is depicted on the right. The left axis of the kymograph depicts the width of the linescan, while the right axis corresponds to the estimated velocity, as plotted with a blue (sham) or red (TAC) line, with a white line depicting the fitted velocity trace.

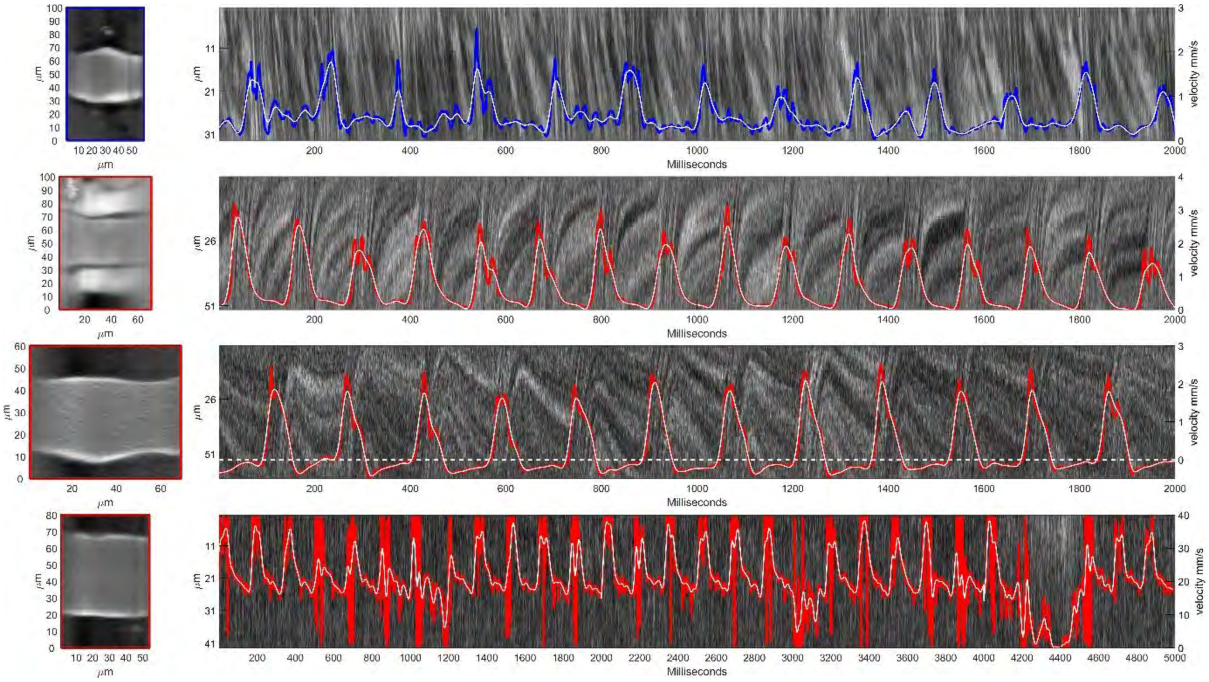

4. Remarkable Kymographs

Kymographs of remarkable situations. The 2D overview scan is depicted on the left, with the corresponding kymograph, as made with a linescan, is depicted on the right. 2D images with red borders depict TAC mice, images with blue borders depict Sham mice.

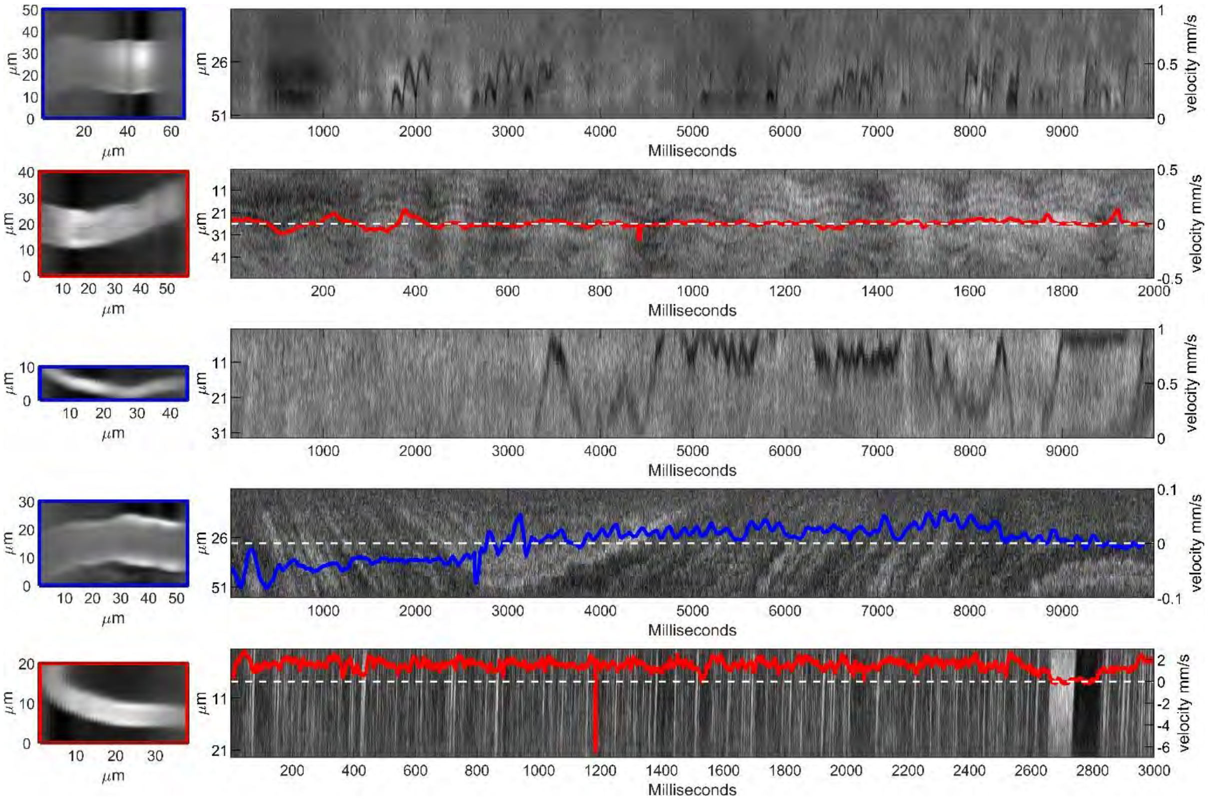

5. Scatterplots of Velocity, Diameter and Pulse Pressure

Scatterplots of average velocity versus vessel diameter (top row) and pulse pressure as calculated by the maximum velocity minus the minimum velocity per heartbeat versus the mean velocity (bottom row).